Fluid-induced seismicity: insights from laboratory experiments and implications for geohazard management systems

FADUL AHMED FADUL DAWOOD

How to cite:

DAWOOD, FADUL AHMED FADUL (2025) Fluid-induced seismicity: insights from laboratory experiments and implications for geohazard management systems. Doctoral thesis, Durham University.

Fluid-induced seismicity: insights from laboratory experiments and implications for geohazard management systems

Fadul Ahmed Fadul Dawood

This thesis is submitted in partial fulfilment of the
requirements for the degree of Doctor of Philosophy (PhD) at Durham
University

Rock Mechanics Laboratory
Department of Earth Sciences, Durham University, Durham, UK
December 2024

Fluid-induced seismicity: insights from laboratory experiments and implications for geohazard management systems

By Fadul Dawood

Abstract

Fluid-induced seismicity is a significant geohazard in industrial activities involving subsurface fluid injection, such as hydraulic fracturing, carbon sequestration, wastewater disposal, and enhanced geothermal systems. Current risk management strategies often rely on empirical relationships between fluid injection volumes and cumulative seismic moment. However, field observations show that some induced earthquakes exceed forecasted maximum magnitudes, highlighting limitations in existing predictive models. This thesis investigates the correlation between the spatial and temporal evolution of faulting and measured physical properties of shale reservoir and underburden rocks, and seismic parameters from laboratory earthquakes.

Two experimental sets were conducted. First, intact core samples from the Horn River Basin shale in British Columbia, Canada, were characterised for their elastic moduli, ultrasonic wave velocity, and seismic anisotropy. These samples were loaded to failure under reservoir conditions in a triaxial apparatus, with acoustic emissions (AE) monitoring. Three deformation stages were observed: (i) an elastic stage with low AE rates, relatively small magnitudes, and distributed seismic events; (ii) a prefailure stage with increasing AE rates and moderate relative magnitudes AE events; and (iii) a failure stage with high AE rates, larger magnitudes, and AE localization. Progressive deformation was associated with decreases in the frequency-magnitude distribution parameter, *b*-value and P-wave velocity. AE events location shows that the evolution of seismic parameters at the transition between pre- to co-failure corresponds to the development of a larger, throughgoing fault.

In the second set, fluid was injected into a composite sample consisting of shale overlying a granite sawcut, simulating a pre-existing fault in the reservoir underburden. Fault reactivation patterns were strongly influenced by the strength heterogeneity of the composite sample. Initially, complex conjugate faulting developed in the underburden. At constant pore pressure, AE locations show progressive fault reactivation and throughgoing fault growth into the reservoir. The development of the throughgoing fault was accompanied by a reduction in P-wave velocity, an increase in seismicity rate, and larger seismic event magnitudes. Progressive fault reactivation and growth were also associated with a reduction in the *b*-value. The results reveal a clear relationship between the evolving fault structure, its growth, and the magnitudes of associated seismic events.

These findings demonstrate that real-time monitoring of systematic changes in physical properties and seismic parameters can inform proactive risk mitigation strategies, offering a more comprehensive approach to managing fluid-induced seismicity.

Declaration

The work in this thesis is based on the research carried out by the author, at the Rock Mechanics Laboratory, Department of Earth Sciences, Durham University. No part of this thesis has been submitted elsewhere for any other degree or qualification, and it is all the author's work unless referenced to the contrary in the text.

Acknowledgements

Growing up, I knew very few people who had attended university, let alone considered PhD research as an option. Reaching this milestone would not have been possible without the help and support of many people. First and foremost, I would like to express my deepest gratitude to the Rock Mechanics Laboratory management team—Prof. Nicola De Paola, Prof. Stefan Nielsen, and Prof. Bob Holdsworth. Your unwavering support, from securing the necessary funding to providing the flexibility to balance my work commitments and studies, has been invaluable. Beyond financial assistance, your encouragement allowed me to attend national and international conferences, significantly enriching my personal and professional development throughout this PhD journey. I will always be grateful for your support.

To my supervisory team: Prof. Nicola De Paola, Prof. Stefan Nielsen, and Prof. Andrew Aplin, thank you for your invaluable guidance and support throughout my studies. Nic, your remarkable ability to recall the finest details, even during casual and rambling conversations, never ceased to amaze me. Your attention to detail has significantly improved this manuscript. Stefan, your patience and willingness to entertain all my unfiltered ideas has been truly inspirational. And thank you for gently nudging me towards Python for plotting graphs. Andy, your steady guidance and constant encouragement have been a source of motivation and reassurance throughout this journey.

I would like to express my sincere thanks to the staff in the Earth Sciences department for their continuous support, and to the Technical Support Staff team for their camaraderie and countless tea breaks that provided much-needed respite. A special thanks to my PhD examiners, Professor Sergio Vinciguerra, Professor Fabio Trippetta, and Professor Mark Allen for taking the time to review this work and for providing insightful feedback. Your kind and engaging discussion during my viva made it much more relaxed experience than I had anticipated.

To my amazing wife, Safa, and my precious son, Hashim: thank you both for your patience, love, and understanding during the countless late nights and weekends spent on my PhD. Safa, your unwavering love, support, care, and belief in me have made this achievement possible —this accomplishment is as much yours as mine. Hashim, thank you for reminding me of what truly matters in life and bringing me joy through it all. I love you both beyond words.

Finally, to my parents, siblings, and extended family: your unconditional support throughout my years of study, especially during my time away from home, has been invaluable. Thank you all.

Dedication

To my mother, Noora Hashim, and my late father, Ahmed Fadul, who taught me the values of perseverance, kindness, and the courage to pursue my dreams.

إلى والِدَتي نورةَ هاشمَ ووالِدي الراحلِ أحمدَ فضل، اللَّذَيْنِ علَّماني قِيَمَ المثابرةِ، واللُّطفِ، وشجاعةَ السَّعيِ لتحقيقِ أحلامي.

Table of Contents

Abstract ii

Declaration iii

Acknowledgements iv

Dedication v

Table of Contents vi

List of Figures x

1 Thesis introduction 1

1.1 Fluid injection and induced seismicity 1

1.1.1 Mechanism of induced seismicity 4

1.2 Natural versus human-induced seismicity: scaling parameters 6

1.3 Managing fluid-injection induced geohazards 8

1.3.1 Traffic light protocols 11

1.4 Induced seismicity in Horn River basin: a case study 13

1.5 Laboratory acoustic emissions as analogues for earthquakes 14

1.6 Aims of the PhD thesis 17

1.7 Structure of the thesis 18

2 Methods 20

2.1 Introduction 20

2.2 Triaxial deformation apparatus 21

2.2.1 Sample assembly 24

2.2.2 Data logging and servo control systems 26

2.3 Sample preparation 27

2.3.1 New protocol for shale cores preparation 27

2.3.2 Composite sample preparation 30

2.3.3 Installation of sensors 30
2.4 Bulk density measurement 32
2.5 Benchtop ultrasonic velocity measurement 33
2.5.1 Measurement setup 33
2.5.2 Dynamic moduli calculation 35
2.5.3 Anisotropy parameters calculation 37
2.5.4 Error estimation 37
2.6 Acoustic emissions (AE) data acquisition system 39
2.6.1 Continuous data acquisition 39
2.6.2 AE data processing 41
2.6.2.1 Filtering and events harvesting 41
2.6.2.2 AE source location 42
2.6.2.3 Ultrasonic velocity estimation 45
2.6.2.4 Seismic parameters calculation 47
2.7 Computed tomography (CT) data acquisition and processing 49

3 Geomechanical properties and seismic anisotropy of Horn River shales 50
3.1 Introduction 50
3.2 Geological background 52
3.3 Samples characterisation 54
3.3.1 Petrophysical and mineralogical characterisation 54
3.3.2 Total organic carbon and density 56
3.3.3 Microstructure and textural anisotropy 57
3.4 Experimental techniques 60
3.4.1 Triaxial loading experiments. 60
3.4.2 Loading protocol, measured and calculated parameters 61
3.4.3 Wave velocity measurements and anisotropy calculations 62
3.5 Results 62
3.5.1 Physical properties (Vp/Vs, density) 62
3.5.2 Mechanical strength and static young’s modulus 63
3.5.3 Dynamic stiffness coefficients, Young’s moduli, and Poisson’s ratios 65
3.5.4 Seismic anisotropy 68
3.6 Discussion 72
3.6.1 Effect of shale composition on anisotropic properties 72
3.6.2 Implications for hydraulic fracturing operations in HRB 75

3.7 Conclusion 78

4 Temporal and spatial evolution of acoustic emission and seismic parameters of Horn River shales during shear faulting 80

4.1 Introduction..80
4.1.1 Hydraulic fracturing, faulting and induced microseismicity...................................80
4.1.2 Hydraulic fracturing induced seismicity in the HRB: a case study..........................82
4.2 Experimental techniques..86
4.2.1 Triaxial loading experiments..86
4.2.2 Loading protocol, measured and calculated parameters.......................................88
4.2.3 Acoustic emissions data recording and processing..88
4.2.4 Post-deformation computerized tomography (CT) scan 89
4.3 Results 89
4.3.1 Mechanical data 89
4.3.1.1 Experiment Dutff 348 (sample A12)...89
4.3.1.2 Experiment Dutff 350 (sample A14)...91
4.3.1.3 Experiment Dutff 351 (sample A15)...92
4.3.2 Acoustic emission data...93
4.3.2.1 Linear elastic deformation stage 94
4.3.2.2 Pre-failure stage 95
4.3.2.3 Failure stage 97
4.3.2.4 Fluid-induced fault reactivation and microseismicity 97
4.3.3 Post-mortem CT scan data 98
4.3.4 Seismic parameters 103
4.3.4.1 P-wave velocity...103
4.3.4.2 b-value and D-value..104
4.4 Discussion 106
4.4.1 Faults structure evolution during loading to failure...106
4.4.2 Fault structure controls the evolution of physical and seismic parameters..........108
4.4.3 Implications for microseismic monitoring..110
4.5 Conclusion 111

5 Fault reactivation and induced seismicity during fluid injection............................ 113

5.1 Introduction...113
5.1.1 Fluid injection during industrial activity and seismicity 113

5.1.2 Managing induced seismicity hazard 116
5.2 Experimental techniques 119
5.2.1 Reactivation experiment in triaxial loading apparatus 119
5.2.2 Loading protocol, measured and calculated parameters 121
5.2.3 Acoustic emissions data recording and processing 122
5.3 Results 122
5.3.1 Mechanical data 122
5.3.1.1 Intact shale, intact Westerly granite, and Westerly granite sawcut 122
5.3.1.2 Composite reactivation experiment: intact WG and WG sawcut 123
5.3.1.3 Composite reactivation experiment: intact shale and WG sawcut 124
5.3.2 Slip event mechanical characteristics 125
5.3.3 Acoustic emission data 126
5.3.4 Evolution of seismic parameters 128
5.4 Discussion 131
5.4.1 Heterogeneous mechanical properties control the complexity of reactivated fault patterns. 131
5.4.2 The role of fluid injection during fault reactivation 131
5.4.3 Evolution of seismic parameters during fluid induced seismic sequences 132
5.4.4 Implications for hazard management of fluid induced seismicity 134
5.5 Conclusion 135

6 Discussion and conclusions 137
6.1 Introduction 137
6.2 Key controls on fault slip modes 137
6.3 Implications for natural and fluid induced earthquakes 139
6.4 Implications for geohazards management and mitigation systems of fluid induced seismicity 140
6.5 Further research 142
6.6 Conclusion 143

References 144

Appendices 162
Appendix A 162
Appendix B 163

List of Figures

Figure 1.1. Schematic illustration of geo-energy applications associated with induced seismicity. Not to scale. Seismic events have been triggered by hydraulic fracturing in tight shale gas formations, conventional oil and gas extraction, deep disposal of wastewater, geological sequestration of CO_2, exploitation of geothermal energy, and mining operations. Modified from Kivi et al. (2023). 1

Figure 1.2. Global map showing the distribution of reported fluid-induced seismicity due to geo-energy activity. Data collated from the Human-Induced Earthquake Database (HiQuake), (www.inducedearthquakes.org). Last accessed 20/10/2024..2

Figure 1.3. Mohr circle diagram showing the effect of increased fluid pressure on a fault. The black semicircle represents the initial stress condition, with the maximum and minimum principal normal stresses ($\sigma 1$ and $\sigma 3$). When fluid pressure (Pf) is increased, normal stresses are reduced by Pf, resulting in effective normal stresses $\sigma 1'$and $\sigma 3'$, moving the Mohr circle to the left by Pf (red semicircle). Shear failure occurs when the shear stress equals the shear strength (yelllow star). Any perturbation of the solid matrix stress can change the radius and expand the Mohr circle, moving it closer to the shear strength (blue semicircle). If the minimum effective normal stress ($\sigma 3'$) is less than the tensile strength (T) of the rock, the rock will fail in tension (green semicircle). The red, blue, and green semicircles represent the three primary mechanisms of fluid-injection induced failure (1), (2), and (3), respectively (see description in the text). 5

Figure 1.4. Source parameters scaling relationship plot for tectonic earthquakes and induced seismicity. Both tectonic earthquakes and induced seismicity exhibit a linear scale between seismic moment and source radius, and an inverse relationship with the corner frequency. The dashed lines are constant stress drop lines. The hydraulic fracturing induced seismicity in the Horn River Basin shows significantly smaller stress drop compared to tectonic, EGS and mining-induced seismicity. Adapted from Kwiatek et al. (2011). The Horn River data is from Bosman et al. (2016)...................7

Figure 1.5. Maximum seismic moment and magnitude as a function of total volume of injected fluid from the start of injection until the time of largest induced earthquake. Solid line is estimated upper bound for McGarr (2014) model...10

Figure 1.6. Traffic light protocol thresholds for various regions across the world. The event magnitudes necessary to activate amber or red scenarios vary widely between different regions and within the geo-energy industries. Modified from Atkinson et al. (2020). 12

Figure 1.7. Cumulative seismicity in two major hydrocarbon plays (HRB and Montney) in British Columbia. The cumulative seismicity graph shows changes in seismicity rate, transitioning from background rate to development of the HRB and then development of the Montney play (Schultz et al., 2020b). Inserts A and B display the stratigraphic column and location of HRB, respectively, modified from Dong et al. (2017b). 13

Figure 2.1. Schematic diagram shows the experimental program for data acquisition and processing. 20

Figure 2.2. Scale drawing of the triaxial deformation apparatus used for conducting loading experiments (Bedford, 2017). 22

Figure 2.3. Photograph of the axial load system. The gear train is driven by a printed motor works GM12 pancake servo motor. Axial displacement is measured using an LVDT mounted at the base of the loading column. 23

Figure 2.4. A diagram and picture showing the main components of the force gauge. 24

Figure 2.5. (A) Scale drawing of the sample assembly. (B) Photograph of the sample assembly with the sample mounted. (C) Sample inserted into a PVC jacket, with sensor lead wires extracted. 25

Figure 2.6. Schematic illustration of triaxial deformation apparatus components, data logging and control systems (modified from Harbord, 2018). Not to scale. 27

Figure 2.7. Photos showing stages of cutting and grinding procedures. (A) Initial shale block, (B) Intermediate cutting stage, (C) Polygonal prism, (D) Grinding stage: the grinding wheel moves left-right (black double-headed arrow) while rotating to cut along the prism axis. Then the grinding wheel moves in-out (green double-headed arrow) to square the end faces (see the text for details). The polygonal prism is rotating along its axis during the cutting process. 28

Figure 2.8. (a) Schematic of a polygonal prism showing the intended dimension of the core plug. (b) A photograph of specimen at an intermediate stage. (c) Photograph of the final product. 29

Figure 2.9. Pictures of core plugs obtained using the technique developed during the course of the PhD. These core plugs will be utilized in intact samples experiments in Chapter 4 and reactivation experiments in Chapter 5. 29

Figure 2.10. a) A granite sawcut with a drilled bore for fluid injection. b) An assembled granite sawcut. c) An intact shale core. d) Schematic showing the assembled granite sawcut and intact shale core on top. The red curve represents the simulated fault plane, and the blue dashed line indicate the drilled bore for fluid injection. 30

Figure 2.11. A) Sensor installation tools. B) Picture of sample with sensor installed. C) Sample jacketed in PVC and sensor lead wires extracted. 31

Figure 2.12**.** Density measurement setup. The picture shows a test sample suspended in distilled water and placed on a digital scale. This setup allows for the measurement of the sample's mass in the fluid to determine its density. 32

Figure 2.13. Schematic illustration shows the setup for ultrasonic wave velocity measurements. Not to scale. 33

Figure 2.14. Ultrasonic wave velocity measurement setup. 34

Figure 2.15. A) Schematic diagram showing the location of five pairs of piezoelectric transducers on the sample. The subscripts indicate the direction with respect to the bedding plane (grey horizontal lines). The dashed lines represent the direction of wave propagation. B) Picture of test specimen cut

into prism. C) Schematic of a VTI rock with a presumed axis of rotational symmetry parallel to the x3. The oblique orientation measurements are taken at a 45° angle to the x1-x2 plane. 35

Figure 2.16. AE data acquisition setup. Not to scale. Indicated on the test sample is a sensor S_i at location (X_i, Y_i, Z_i), distance D_i from the sensor S_i to an AE source location with the coordinates (X_0, Y_0, Z_0). 39

Figure 2.17. Picture of the AE data acquisition system. 40

Figure 2.18. A) 90 seconds (3 files) of continuous data stream showing recorded AE events and the background noise level. B) Continuous data in the frequency domain enables the design of a filter to remove the background noise level. Refer to the text for explanation. C) A discrete event harvested and filtered. The blue line represents the arrival time of the P-wave. 42

Figure 2.19. An example of a triaxial experiment shows identified deformation stages. The cluster of events recorded at each stage is used to estimate the P-wave velocity. Further details about this experiment are presented in Chapter 4. 46

Figure 2.20. An example of a log-log plot of C(r) versus r. The D-value corresponds to the slope of a least-squares fit to the linear portion of the plot. The error represents the deviation of the slope at the end-member points of the AE events relative to the slope determined at the centre of the range. 49

Figure 3.1. Parameters derived from well logs for reservoir formations. Elastic properties (Young's modulus and Poisson's ratio) were computed from V_p, V_s, and density logs. Total organic carbon (TOC) was measured from core samples. TOC curve shows approximate mirror image of the V_p/V_s curve. Adapted from Mo et al. (2018). 51

Figure 3.2. 1D anisotropic velocity model showing: (A) vertical V_P and V_S velocities, and (B) Thomsen’s anisotropic parameters (ε, γ). The Fort Simpson shale exhibits high anisotropy, with Thomsen’s parameter showing a sharp drop at the top of the reservoir formation (Muskwa) before recovering in the lower reservoir formations (Otter Park and Evie). Adapted from Baird et al. (2017). 52

Figure 3.3. (A) Map of Horn River basin, along with the adjacent areas of Liard basin and Cordova embayment, indicating the location of Well A100B/94. Insert: map showing the location of Horn River basin in Western Canada. (B) Middle and upper Devonian stratigraphy. Modified from Charlton et al. (2023) and Dong et al. (2017b). 53

Figure 3.4. TOC plotted against density for overburden and reservoir samples. Overburden samples show higher densities and lower TOC compared to reservoir samples. While a distinct linear correlation exists between TOC and density for both overburden and reservoir samples, the nature of this correlation differs between the two. 56

Figure 3.5. SEM images along with corresponding radial profiles of the Autocorrelation Function (ACF). (A) Overburden sample A2 displays an illite-dominated clay (Cly) matrix with scattered quartz (Qtz) and pyrite (Py) grains. (C) Overburden sample A6 exhibits a texture similar to A2, but with less pronounced alignment of clay minerals and the inclusion of dolomite (Dol) grains. (E) Reservoir

sample A16 consists of angular dolomite grains with dispersed quartz grains and a minor clay/organic phase. For each of these samples, azimuthal profiles of the corresponding ACF from 0 to 180 degrees are shown in (B), (D), and (F). The lag value, where the correlation function reaches $1/e$ of its maximum value at zero lag, is used to measure the correlation length at each azimuth. The ratio between the maximum and minimum correlation lengths obtained over all azimuths provides a measure of anisotropy. A broader spread of ACF with azimuth indicates higher textural anisotropy. For example, sample A2 exhibits highly aligned, elongated clay fabrics (sub-horizontal orientation) with a lower Str value (52%), while sample A6 shows less pronounced fabric alignment and a higher Str value (72%). 59

Figure 3.6. Textural anisotropy of HRB shale samples as function of TOC. The smaller the percentage on the textural anisotropy scale the more anisotropic is the sample. 60

Figure 3.7. An example of a triaxial loading experiment, in which the confining pressure was increased stepwise from 10 MPa to 80 MPa without unloading between stages. At each pressure level, axial loading was applied until the axial stress equalled the confining pressure, after which the next confining pressure increment was introduced. The red mark on the stress-strain curve indicates the portion used to calculate the static Young's modulus (refer to the text for details). 64

Figure 3.8. Static Young's modulus versus confining pressure. The triangular markers all belong to sample A15 (see Figure 3.7 for details). 65

Figure 3.9. Dynamic stiffness coefficients as function of TOC. The maximum uncertainty is 4%. Solid markers correspond to overburden samples and open markers show reservoir samples. 66

Figure 3.10. Relationship between dynamic Young's moduli E1 and E3. The colour coding represents TOC. The crosses are data from Higgins et al. (2008), and the dashed line indicates a 1:1 ratio between E1 and E3. 67

Figure 3.11. Dynamic Poisson ratio. Solid markers correspond to overburden samples and open markers show reservoir samples. 68

Figure 3.12. Thomsen anisotropy parameters as function of TOC. Solid markers correspond to overburden samples and open markers show reservoir samples. 69

Figure 3.13. Cross-plot of Thomsen anisotropy parameters and textural anisotropy measured from SEM images. 70

Figure 3.14. Comparison of anisotropy parameters with P-wave and S-wave velocities measured parallel to the bedding plane (Vp (0), Vsh (0)). (a) Epsilon versus Vp (0). (b) Gamma versus Vsh (0). Crosses are data from previous studies (Vernik and Liu, 1997; Sone and Zoback, 2013). 70

Figure 3.15. Cross-plot between Thomsen's anisotropy parameters: (a) epsilon and gamma, (b) delta and gamma, (c) delta and epsilon. Crosses are data from previous studies (Vernik and Liu, 1997; Sone and Zoback, 2013). 71

Figure 3.16. Plot of Thomsen's ε versus γ for varying coefficients $W400$ (colour) and $W200$ (thin isolines) of the ODF of clay platelets for a model composed of 60% clays (36% illite, 8% chlorite, and

16% kaolinite), and 40% quartz. The experimentally measured anisotropy of Horn River shales is superimposed on the plot. Circular markers represent overburden samples, and diamond markers represent reservoir samples. The green line indicates textures where $W400\,/\,W200 = W400max\,/\,W200max$. Natural textures are expected to plot to the right of this line. 74

Figure 3.17. A cross-plot of Young's modulus and Poisson's ratio. High Young's modulus and low Poisson's ratio values indicate more brittle rock. In this study, overburden samples are represented by red-filled square symbols, while reservoir samples are shown with black-filled square symbols. The plot includes data derived from wireline logs of Vp and Vs (Labani and Rezaee, 2015; Dong et al., 2017b) alongside data from laboratory measurements. Note that the Young's modulus and Poisson's ratio values are generally higher in wireline logs and laboratory measurements under confinement compared to laboratory measurements conducted at ambient pressure. This discrepancy is primarily attributed to the consistently lower Vs values recorded in core samples, likely caused by pressure release during core retrieval. 76

Figure 4.1. Microseismic magnitudes recorded in hydraulic fracturing operation in major North American shale basins. Each data point represents the maximum microseismicity stimulated by a hydraulic fracture treatment (Zhao et al., 2018). 81

Figure 4.2. (A) Map showing the location of the HRB in British Columbia and the samples well location; (B) Stratigraphic column of HRB shales. Assembled from Dong et al. (2015), and Mo et al. (2018). 82

Figure 4.3. Locations and timings of HF-induced events in British Columbia (BC). (a) A map showing seismicity in BC (red circles). This map includes larger seismic events (ML ≥ 2.5) recorded from October 2006 to September 2017. The seismicity cluster in Horn River Basin is labelled as number 1. (b) Graphs showing cumulative seismicity in BC (upper panel) and the number of horizontal HF wells in BC (lower panel). The cumulative seismicity graph shows changes in the seismicity rate, transitioning from background levels to increased activity during the development of the HRB and then development of the Montney play. The number of hydraulically fractured wells in BC show a relatively steady rate starting in 2010 (Schultz et al., 2020b). 83

Figure 4.4. Cross-section view of events recorded during hydraulic fracturing in the HRB. Events are colour-coded by moment magnitude (Mw). Three reservoir units— Muskwa, Otter Park, and Evie— are targeted for hydraulic fracturing stimulation (solid horizontal lines). The dashed black box indicates the area of "good microseismicity" within the stimulated reservoir volume. Higher-magnitude events are recorded below the target formations, outside the reservoir volume (red dashed box). Modified from Kettlety et al. (2019)...84

Figure 4.5. *b*-values variation in the target reservoir formations of the HRB (Snelling et al., 2013). 85

Figure 4.6. A photograph of the sample assembly with the sample jacketed in PVC and mounted, and a shale core plug with piezoelectric sensor attached. The AE recording system and graphs of examples of the mechanical and AE data recorded. 87

Figure 4.7. A) A shale sample inserted into a PVC tube with sensor lead wires extracted. B) A shale core with attached piezoelectric sensors. C) Schematic shows the locations of the sensors. 88

Figure 4.8. Stress vs. strain evolution for experiment Dutff 348 conducted at 10 MPa confining pressure. No fluid injection after the macroscopic failure of the sample. Three deformation stages are identified: 1) linear elastic deformation stage (grey coloured area); 2) prefailure stage (pink coloured area), and 3) failure stage (yellow coloured area). The insert shows the sample before and after deformation. 90

Figure 4.9. Stress vs. strain, and pore pressure evolution for Dutff 350. Similar to Dutff 348, three loading stages are identified. After macroscopic failure, fluid is injected into the newly formed fault. Pictures on the right shows the sample before and after deformation. LED: linear elastic deformation; F: Failure. 91

Figure 4.10. Evolution of stress-strain, confining pressure, and pore fluid pressure during experiment Dutff 351. The sample was loaded under stepwise increases in confining pressure from 10 MPa to 80 MPa, in increment of 10 MPa, without unloading between stages. See the text for details. As Dutff 348 and Dutff 350, three loading stages are identified. The insert shows pictures of the sample before and after deformation. 93

Figure 4.11. A) Evolution of differential stress, axial shortening, and cumulative number of AE events for Experiment Dutff 348. B) Snapshot showing the spatial and temporal distribution of microseismic events corresponding to the three identified deformation stages. The post-deformation image of the sample shows the formation of a main fault with a dip of approximately 30 degrees relative to the specimen’s axis. Three minor faults branch off from the main fault, each dipping at about 30 degrees to the main fault (green dashed lines). 95

Figure 4.12. A) Evolution of differential stress, axial shortening, and cumulative number of AE events for Experiment Dutff 350. B) Snapshot showing the spatial and temporal distribution of microseismic events corresponding to the identified deformation stages. Note that the time scale is relative to each deformation stage. 96

Figure 4.13. A) Evolution of differential stress, axial shortening, and cumulative number of AE events for Experiment Dutff 351. B) Snapshot showing the spatial and temporal distribution of microseismic events corresponding to the three identified deformation stages. The post-deformation image of the sample shows the formation of a main fault with a dip of approximately 45 degrees relative to the specimen’s axis. A minor fault branches off from the main fault, dipping about 30 degrees relative to the main fault (green dashed lines). 98

Figure 4.14. Reconstructed 3D grayscale images from X-ray scans. The brighter areas in Dutff 348 are bedding planes showing inclusion of a higher density minerals. B, D, and F are 2D cross-sectional view looking at the centre of the samples. The axes animations indicate the viewing plane. 99

Figure 4.15. Snapshot of spatial and temporal distribution of microseismic events corresponding to the three identified deformation stages (see Figure 4.8). a) linear elastic deformation, b) prefailure, c) failure stage, and d) all three stages together. 100

Figure 4.16. Snapshot of spatial and temporal distribution of microseismic events of experiment Dutff 350. a) prefailure, b) failure, c) fluid injection stages and d) all stages together (see Figure 4.9). 101

Figure 4.17. Snapshot of spatial and temporal distribution of microseismic events of experiment Dutff 351. a) prefailure, b) failure, c) fluid injection stage and d) all three stages together (see Figure 4.10). 102

Figure 4.18. P-wave velocity change during deformation compared to initial velocity. The data point at time 0 represents the benchtop measurement (see Chapter 3 for details). The colour code is the same as in Figure 4.8. Abbreviations: Pref - prefailure, F - failure, FI - fluid injection, and Re - reactivation. 104

Figure 4.19. Evolution of *b*-value and D-value during deformation for experiments Dutff 348, Dutff 350, and Dutff 351. The *b*-values are represented by diamond markers, and the D-values by circle markers. The abbreviations are the same as in Figure 4.18. 105

Figure 4.20. Schematic model of the evolution of cracks and failure as a function of differential stress acting perpendicular to the bedding planes (A-D). Modified from Dewhurst et al. (2008). (E) CT scan image of a shale sample loaded to failure (Experiment Dutff 351). 107

Figure 4.21. A) Schematic demonstrating the role of competence layering on brittle failure mode, modified from Sibson (2000). B) Cross- section of the sample shown in Figure 4.12E displaying dilational jogs. 108

Figure 5.1. Schematic showing shale gas resource play targeted by injection borehole for hydraulic fracturing. Pre-existing faults located outside the reservoir that potentially can be reactivated resulting in large magnitude seismic event. Not to scale. 114

Figure 5.2. (A) Cross-sectional view of event hypocentres recorded during hydraulic stimulation of the Muskwa, Otter Park, and Evie formations in the HRB. Events are color-coded by moment magnitude (Mw). Higher-magnitude events occur in the basement below the stimulated reservoir formations (highlighted by the red dashed box), while lower-magnitude events, or “good seismicity,” are mostly contained within the stimulated reservoir volume (outlined by the black dashed box). (B) Pre-existing faults associated with the higher-magnitude events shown in the red dashed box in (A). Modified from Kettlety et al. (2019). 115

Figure 5.3. Relationship between cumulative injected volume and seismic moment. Purple diamonds indicate proposed cases of runaway rupture: Pohang, Korea (enhanced geothermal system) (diamond 1), Pawnee, Oklahoma, USA (wastewater disposal) (diamond 2), Prague, Oklahoma, USA (wastewater disposal) (diamond 3), Fort St. John, Canada (hydraulic fracturing) (diamond 4) and Fox Creek, Canada (hydraulic fracturing) (diamond 5). Grey and black lines illustrate the scaling relationship between cumulative volume and total seismic moment as proposed by McGarr (2014) and Galis et al. (2017), respectively. Background colours represent the nature of triggered activity relative to injected volume: events in the pale orange–white zone align with mechanisms where magnitude scales with cumulative volume, while events in the orange zone exceed volume-based predictions. The intermediate region represents ambiguous rupture types. Modified from Atkinson et al. (2020). 117

Figure 5.4. End-member components tested: (a) intact shale (Chapter 4, Experiment Dutff 348), (b) Intact Westerly granite, (c) WG sawcut, and (d) a composite sample with intact WG on top of a WG sawcut. Mechanical results are presented in the Results section below. 119

Figure 5.5. Components of a composite sample with intact shale on top of a WG sawcut: (a) granite sawcut with a drilled borehole for fluid injection, (b) assembled granite sawcut, (c) intact shale core, and (d) schematic showing the assembly of the composite sample. 120

Figure 5.6. Map of PTZ sensor locations on the composite sample plotted against sample height and angles around the circumference. The dashed curve represents the edge of the pre-existing fault plane. The image on the right shows the composite sample with attached sensors. 121

Figure 5.7. Differential stress vs strain graphs for end-member components of the composite test. A) Intact shale and intact WG samples loaded at 10 MPa confining pressure. B) Westerly granite sawcut loaded at 10 MPa and 50 MPa. 123

Figure 5.8. Differential stress vs. strain curve for a composite sample (intact WG on top of a WG sawcut). The plane-polarized light (PPL) and crossed-polarized light (XPL) images are courtesy of Nicola De Paola. 123

Figure 5.9. Evolution of stress, pore fluid pressure, axial shortening, and slip rate during the reactivation experiment. The light grey background represents the mechanical loading stage, while the light green background indicates the fluid injection/extraction stage (see text for description). The white circles on the pore fluid curve indicate pore pressure level at the onset of fault slip. The dark green dashed ellipses highlight episodes that are shown in detail in Figure 5.10 A and B, respectively. 124

Figure 5.10. A) Slip event in Cycle 2b: The fault starts slipping at a slow rate, accelerates to dynamic slip and then deceleration to steady slip. B) Slip event in Cycle 10: multiple slips at slow slip rates (< 5 µm s^{-1}). 126

Figure 5.11. A) Effective axial stress, fluid pressure, and cumulative number of events plotted as a function of time across multiple reactivation cycles. The emission rate remains steady during the reactivation stage. Reactivation at high fluid pressure results in a higher emission rate compared to reactivation at lower fluid pressure (Cycle 8). B) The spatial and temporal evolution of microseismic events. The magnitude of the events increases progressively with each successive reactivation cycle. C) A post-mortem picture of the test specimen, showing creation of a conjugate fault that propagated into the top seal. 127

Figure 5.12. The fractal dimension (D-value) of event hypocentres and velocity variation for each reactivation cycle. Velocity measured at the benchtop is shown as at cycle zero. 129

Figure 5.13. The frequency-magnitude distribution for event clusters recorded in the reactivation experiment. In Figure 5.13A, each line corresponds to events cluster, with the colour scale indicating the *b*-value obtained for each cluster. In Figure 5.13B, each line representing the cumulative number of events recorded in all previous cycles. 130

1 Thesis introduction

1.1 Fluid injection and induced seismicity

A strong causal correlation has been established between industrial activities involving subsurface fluid injection and the occurrence of induced seismicity. This phenomenon has become global, affecting various regions across diverse tectonic environments, and impacting both the geo-energy industry and society. Figure 1.1 provides a schematic overview of geo-energy projects that trigger seismicity. It is important to note that some of these industries play a key role in the transition to a net-zero economy.

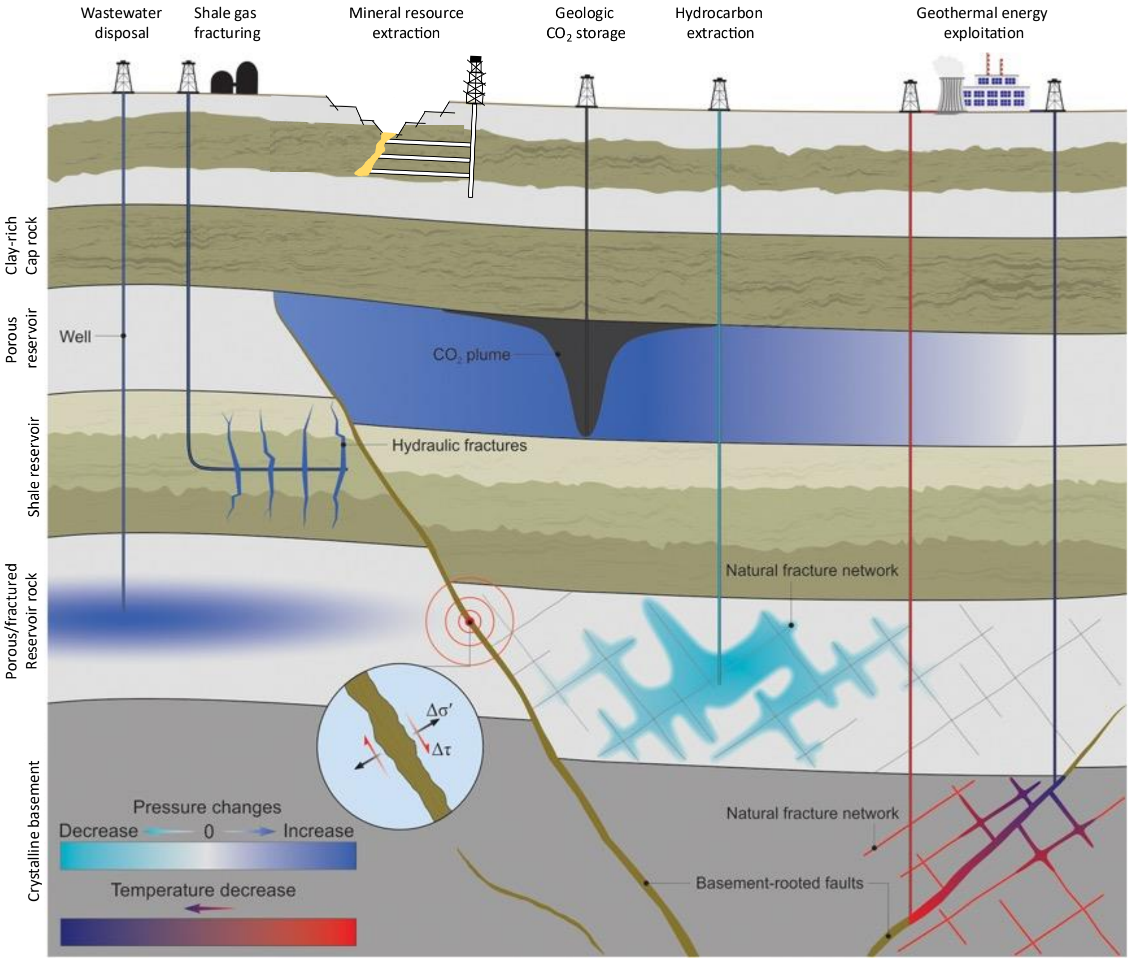

Figure 1.1. Schematic illustration of geo-energy applications associated with induced seismicity. Not to scale. Seismic events have been triggered by hydraulic fracturing in tight shale gas formations, conventional oil and gas extraction, deep disposal of wastewater, geological sequestration of CO_2, exploitation of geothermal energy, and mining operations. Modified from Kivi et al. (2023).

Figure 1.2 illustrates the global distribution and magnitude of fluid injection-induced seismicity resulting from wastewater disposal, hydraulic fracturing, carbon capture and storage, and geothermal energy exploitation. In western Canada, induced earthquakes exceeding magnitudes of M > 3 have tripled in the last decade (Atkinson et al., 2020) , primarily linked to hydraulic fracturing projects (Bao and Eaton, 2016). Similarly, wastewater disposal by injection in deep formations (Ake et al., 2005; Keranen et al., 2013) has led to a tenfold increase in seismicity in the Midwest United States (Ellsworth, 2013). Additionally, geothermal energy exploitation has triggered several large earthquakes, notably the Mw 5.5 earthquake that occurred in Pohang, South Korea, on 15 November 2017. This earthquake was triggered by fluid injection into a low-permeability crystalline basement to develop an enhanced geothermal system (EGS) (Ellsworth et al., 2019).

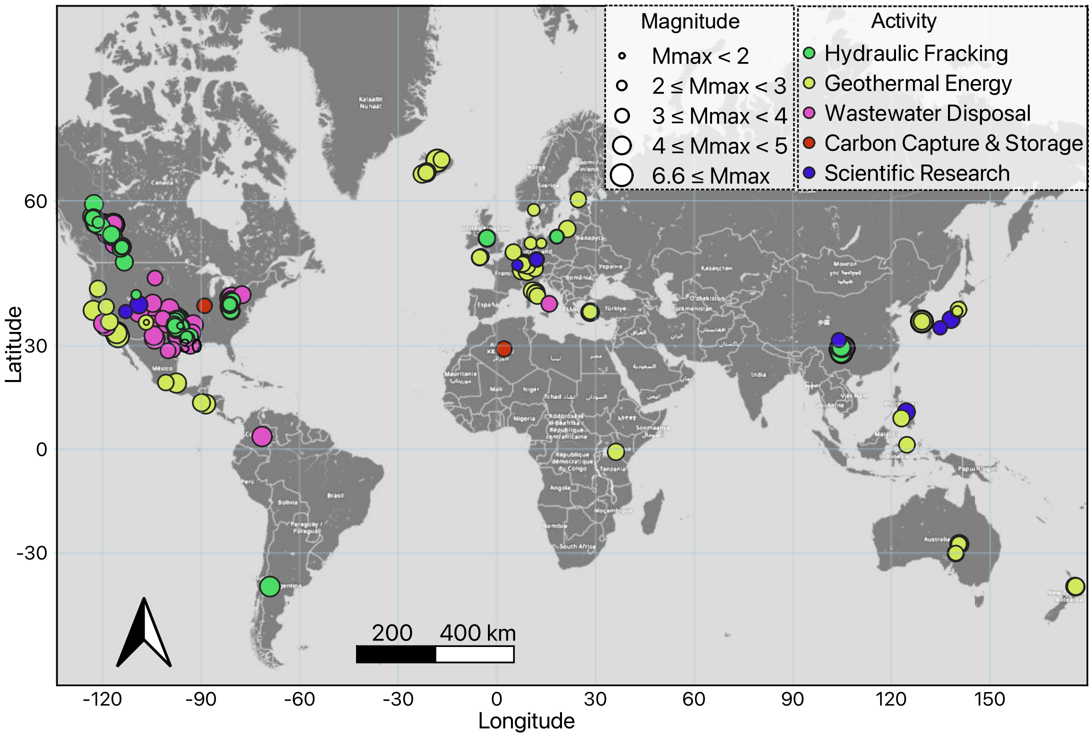

Figure 1.2. Global map showing the distribution of reported fluid-induced seismicity due to geo-energy activity. Data collated from the Human-Induced Earthquake Database (HiQuake), (www.inducedearthquakes.org). Last accessed 20/10/2024.

The recent surge in the number of injection-induced earthquakes, particularly those associated with hydraulic fracturing, has garnered significant scientific interest and public concern due to its potential implications for seismic hazard, infrastructure integrity, and public safety. Hydraulic fracturing (HF) techniques involve injecting fluids at high pressure into tight, unconventional hydrocarbon reservoirs to increase their permeability by creating new fractures or extending pre-existing ones. These generated fractures within the reservoir volume enhance permeability and increase the hydrocarbon production rate (Schultz et al., 2020b). In most HF operations, induced events within the stimulated reservoir typically have a magnitude of Mw ≤ 3 (Li et al., 2019) and are categorized as microseismicity.

Artificially created microseismicity generally does not cause ground motion and is not felt at the surface (Rubinstein and Mahani, 2015; Verdon and Budge, 2018). However, there have been instances where larger, felt-induced seismic events, with magnitude exceeding M > 4, have been linked to HF operations (Lei et al., 2017; Wang et al., 2017; Wang et al., 2020a). For example, in the Changning shale gas reservoir in the Sichuan Basin, China, HF has been associated with two events of magnitudes greater than 5: a M_L 5.7 event in December 2018 and a M_L 5.3 event in January 2019 (Li et al., 2019). Additionally, the Western Canadian Sedimentary Basin (WCSB) has experienced several seismic events with magnitudes exceeding M_L 4, which have been linked to HF operations (Atkinson et al., 2015; Farahbod et al., 2015; Bao and Eaton, 2016).

In many cases, the relatively large (M > 4), felt, and sometimes damaging induced events are associated with the reactivation of pre-existing faults in the underburden region located outside the stimulated reservoir (Lei et al., 2017; Kettlety et al., 2019; Wang et al., 2021). For example, the largest recorded HF-induced event in Canada, which occurred during the stimulation of a tight-shale gas reservoir at a depth of 1.9 km, is attributed to the reactivation of a pre-existing fault in the Lower Montney Formation (Wang et al., 2020a). This event, registering Mw 4.6 on 17 August 2015, occurred five days after the initiation of fluid injection. Wang et al. (2020a) used the source parameters of the Mw 4.6 sequence to estimate stress drops, reporting a range from 1 to 35 MPa, which is a typical value for tectonic earthquakes. However, they also reported a lower *b*-value of 0.78, where the *b* parameter is a key seismic parameter indicating the ratio between large and small earthquakes in a seismic sequence. They suggested that pre-existing faults are an important factor controlling the potential seismic hazard associated with HF operations (Wang et al., 2020a).

In Europe, the first felt induced seismicity associated with HF operations is linked to the reactivation of a pre-existing fault during shale reservoir stimulation in the Carboniferous Bowland Shale (Clarke et al., 2014). The M_L 2.3 earthquake detected in Lancashire, UK, in 2011 resulted from the fluid-induced reactivation of an optimally oriented, critically stressed reverse fault. The epicentre of the event was reported to be 1.8 km from the injection well and at a depth of 3.6 km.

1.1.1 Mechanism of induced seismicity

The injection of fluid perturbs the subsurface stress regime, potentially leading to the reactivation of pre-existing faults or the creation of new fractures, which can ultimately result in seismic events (Hubbert and Rubey, 1959; Sibson, 1992). The shear strength of a fault, represented by the shear stress required for failure (τ), can be defined by the Mohr-Coulomb failure criterion, expressed as

$$\tau = C + \mu\left(\sigma_n - P_f\right) \text{..............} 1.1$$

where τ is the shear stress, C is the cohesion, μ is the sliding friction coefficient (which typically ranges from 0.6 to 1, (Byerlee, 1978)), σ_n is the normal stress (considered positive for compression), P_f is the pore fluid pressure, and the difference between normal stress and pore pressure, i.e. $\sigma_n - P_f$, is defined as the effective normal stress, σ_n'. Therefore, according to equation 1.1, an increase in pore pressure during fluid injection can reduce the shear strength of faults, causing their reactivation when the tectonic shear stress τ is equal to their shear strength. Based on the effective stress principles (Byerlee, 1978; Sibson, 1998), three primary mechanisms are identified for fluid-injection induced seismicity, as graphically illustrated in Figure 1.3.

The first mechanism is pore fluid pressure change. When fluid injection increases pore fluid pressure, it reduces the effective normal stress and shifts the Mohr circle closer to the failure criterion, triggering a failure or fault reactivation (Shapiro and Dinske, 2009; Ge and Saar, 2022). Perturbations in pore pressure can propagate far beyond the injection zone, reaching distances of tens of kilometres in highly permeable formations (Hennings et al., 2021). The primary cause of induced earthquakes from wastewater disposal, often occurring many kilometres away from the injection site, is recognized as pore-pressure diffusion. This can lead to significant seismic activity, which might be delayed for months or even longer (Keranen et al., 2014). Similarly, the initiation of seismic events during EGS stimulations is mainly due to pore pressure diffusion (Yeo et al., 2020).

In hydraulic fracturing of shales, the pressure front outside the fractures is impeded by the low permeability of the reservoir. Therefore, a hydrologic connection is required to transmit pressure diffusion from the injection region to critically stressed faults, whose reactivation will result in dynamic rupture. This connection is typically facilitated by pre-existing fracture corridors that enable fluid-pressure perturbations to communicate with larger pre-existing faults, even at distances exceeding 1 km (Schultz et al., 2020b; Igonin et al., 2021). In most hydraulic fracturing case histories, induced events with a magnitude M > 3 are attributed to the pore-pressure diffusion from the reservoir to nearby hydraulically connected pre-existing faults (Atkinson et al., 2015; Schultz et al., 2017).

The second mechanism is poroelastic stress transfer. When fluid injection causes changes in solid matrix stresses through poroelastic stress transfer, leading to an increase in shear stress, the Mohr circle expands towards the failure criterion (Figure 1.3), resulting in fault reactivation (Segall and Lu, 2015). Poroelastic stress transfer occurs at the speed of seismic waves and can perturb the strength balance on distant fractures and faults without any hydraulic communication. This mechanism is invoked to explain scenarios where seismic activity begins ~1 km from the injection site within 2–3 hours from the beginning of fluid injection. Furthermore, it offers a viable account for shut-in phenomena, such as increases in earthquake rate or the occurrence of the largest-magnitude event after hydraulic fracturing completion (Schultz et al., 2020b). Investigations have indicated that shear stress changes as small as 0.01 – 0.1 MPa can trigger seismic events (Lockner and Beeler, 1999; McGarr et al., 2002). Poroelastic stress transfer has been identified as a contributing factor in EGS (Chang et al., 2020) and hydraulic fracturing operations (Bao and Eaton, 2016).

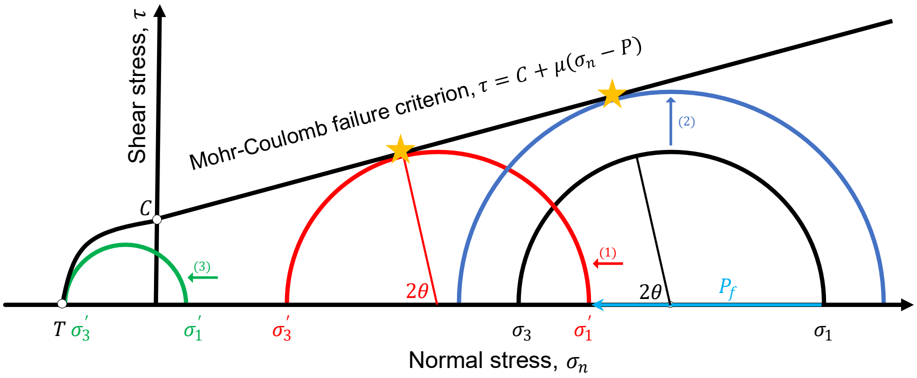

Figure 1.3. Mohr circle diagram showing the effect of increased fluid pressure on a fault. The black semicircle represents the initial stress condition, with the maximum and minimum principal normal stresses (σ_1 and σ_3). When fluid pressure (P_f) is increased, normal stresses are reduced by P_f, resulting in effective normal stresses $\sigma_1'$and σ_3', moving the Mohr circle to the left by P_f (red semicircle). Shear failure occurs when the shear stress equals the shear strength (yelllow star). Any perturbation of the solid matrix stress can change the radius and expand the Mohr circle, moving it closer to the shear strength (blue semicircle). If the minimum effective normal stress (σ_3') is less than the tensile strength (T) of the rock, the rock will fail in tension (green semicircle). The red, blue, and green semicircles represent the three primary mechanisms of fluid-injection induced failure (1), (2), and (3), respectively (see description in the text).

The third mechanism occurs when fluid injection pressure causes tensile stresses in the reservoir, leading to tensile fracturing when the minimum effective normal stress (σ_3') is equal to the tensile strength of the rocks (Figure 1.3). An analysis of the microseismic events spectra, recorded during a multistage hydraulic fracturing field experiment in western Canada in 2011, reveals event characteristics consistent with tensile rupture (Eaton et al., 2014b).

In summary, all the discussed mechanisms can contribute to the stress perturbation that can trigger failure and induce seismicity. Studies using multiphysical modelling at well-characterised injection and extraction sites revealed that the relative significance of triggering mechanisms can vary between sites (Hajati et al., 2015; Duboeuf et al., 2017). This variation depends on several factors including the rock physical properties, reservoir structure, operational parameters, fault geometry, seismotectonic conditions and proximity to injection and extraction sites (Hajati et al., 2015; Amini et al., 2022; Moein et al., 2023). Nevertheless, pore-pressure change is considered the primary mechanism for injection-induced seismicity (Keranen and Weingarten, 2018; Ge and Saar, 2022).

1.2 Natural versus human-induced seismicity: scaling parameters

Injection-induced seismicity and natural or tectonic earthquakes share common features but also demonstrate significant differences. For instance, both exhibit similar rupture mechanics (Moein et al., 2023) and scaling relations between source magnitude and source area (Kwiatek et al., 2011). The magnitude of seismic events linearly scales with the size of the failure area (see Figure 1.4). The stress drop in tectonic events is usually higher than in fluid injection-induced seismicity (Schultz et al., 2017; Yang et al., 2017). However, stress drops due to fluid injection vary significantly (Schultz et al., 2020b). For instance, in the Western Canadian Sedimentary Basin, events in the Horn River Basin show lower stress drops than those in the Duvernay Basin by a factor of 10 to 20. The anomalously low stress drop in the Horn River Basin is attributed to the region's specific stress conditions, where higher stress areas tend to release a greater amount of stored elastic strain through higher stress drop (Viegas et al., 2017). Earthquakes with higher stress drops play a significant role in seismic hazard by generating stronger ground motions at higher frequencies, thereby posing an increased seismic risk. Additionally, unlike the typical foreshock-mainshock-aftershock sequence observed in tectonic earthquakes, injection-induced seismicity tends to manifest with swarm-like patterns (Skoumal et al., 2015). The swarm-like characteristic can be used as a criterion for differentiating between the two types of earthquakes, especially in seismically inactive regions.

The most significant difference between tectonic and induced seismicity lies in their recurrence statistics. The classic Gutenberg-Richter relationship (Gutenberg and Richter, 1944) provides a fundamental model for earthquake magnitude-frequency distribution in a given region

$$log_{10}N(M) = a - bM \ \ldots\ldots\ldots\ldots\ldots\ldots\ldots\ldots 1.2$$

where $N(M)$ defines the cumulative number of earthquakes larger than magnitude M, 'a' defines the overall rate of seismic activity, and 'b' quantifies the proportion of large to small events. Tectonic seismicity usually exhibits a 'b' value around 1 (Frohlich and Davis, 1993), whereas numerous studies on fluid-induced seismicity have reported considerably higher values, as high as 3 (Roche et al., 2015; Mousavi et al., 2017; Mahani, 2021). This implies that induced seismicity is dominated by numerous small-magnitude events, with few relatively large or felt earthquakes. Therefore, characterizing 'b' values is crucial for predicting the likelihood of larger, potentially hazardous seismic events. A lower 'b' values indicates a higher frequency of larger events compared to that of a typical population with b ~ 1.0.

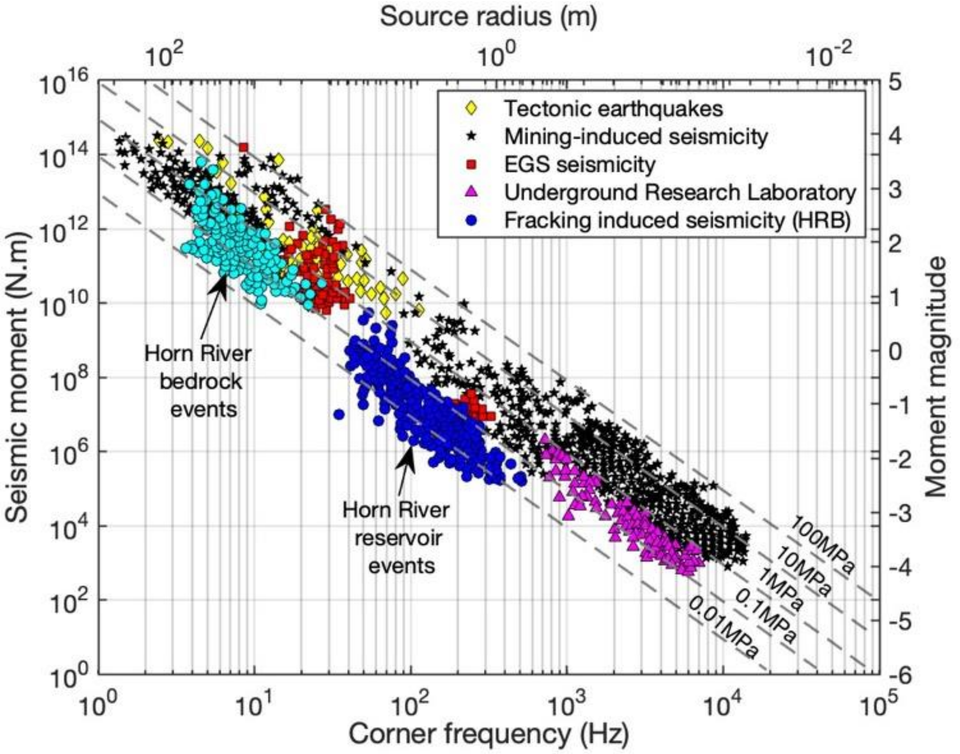

Figure 1.4. Source parameters scaling relationship plot for tectonic earthquakes and induced seismicity. Both tectonic earthquakes and induced seismicity exhibit a linear scale between seismic moment and source radius, and an inverse relationship with the corner frequency. The dashed lines are constant stress drop lines. The hydraulic fracturing induced seismicity in the Horn River Basin shows significantly smaller stress drop compared to tectonic, EGS and mining-induced seismicity. Adapted from Kwiatek et al. (2011). The Horn River data is from Bosman et al. (2016).

Deviation from the typical *‘b’* value can be attributed to various physical phenomena (El-Isa and Eaton, 2014). Studies in areas with underground fluid injection show that changes in the *'b'* value correlate with changes in pressure gradient or shear stress (Bachmann et al., 2012; Mousavi et al., 2017). These findings highlight the connection between '*b*' values and external factors, providing insights into the mechanics of induced seismicity. Moreover, the spatial distribution and focal mechanisms of microseismic event clusters suggest an association between high *b*-value seismicity and widespread microfracture development, while low *b*-value seismicity appears to originate from localised structures during the reactivation of pre-existing faults (Kettlety et al., 2019).

Several hypotheses have been proposed to explain the observed high *b*-value characteristic in fluid injection-induced microseismicity. One prominent theory suggests that, in the absence of large-scale fault activation, the microseismic magnitude distribution exhibits a tapering curvature, resulting in fewer large events than expected from a linear relationship (Eaton et al., 2014a; Kozłowska et al., 2018). This tapering could be due to limitations in the seismic source dimensions, where microseismic events are associated with the reactivation of strata-bound fracture networks. Notably, the slope within the tapered portion of the frequency distribution consistently appears steeper than the main distribution’s slope (Eaton and Maghsoudi, 2015). This phenomenon is likely due to the observed microseismic event source dimensions approaching the maximum fracture size. As a result, only the tapered portion becomes observable, leading to an elevated apparent *b*-value.

Understanding the connection between fault age, smoothness, and earthquake size is crucial. Evidence suggests that mature faults with smoother surfaces can accommodate larger earthquakes and exhibit gentler magnitude distributions, unlike younger, rougher faults. This implies that fault characteristics like age and smoothness can control the maximum earthquake size a fault can produce, potentially influencing the ‘*b*’ value (Perrin et al., 2016; Goebel et al., 2017; Kozłowska et al., 2018). The Gutenberg-Richter *‘b’* value serves as a powerful tool for differentiating and understanding tectonic and induced seismicity. Its deviation from the typical value of 1.0 provides key insights into the underlying physical processes and potential hazards associated with both type of earthquakes.

1.3 Managing fluid-injection induced geohazards

Induced seismicity presents significant challenges in geohazard management. Despite advances in understanding the mechanisms driving fluid injection-induced seismicity, accurately forecasting the seismic response to such activities remains a complex task. In certain regions, the rate and magnitude of seismicity triggered by fluid injection raise concerns, while other areas experience minimal seismic activity, even with comparable injection or extraction volumes of fluids. This variability in the seismic response is influenced by both geological factors and operational parameters (Keranen and Weingarten, 2018; Fasola et al., 2019).

Geological factors play a crucial role in determining the nature and magnitude of induced seismic events. These factors include regional tectonic stress conditions, the number, size, and orientation of pre-existing fractures and faults, local stratigraphy, and the presence of hydraulic conduits. For instance, Schultz et al. (2016) observed a correlation between the depth of induced seismic events and potentially basement-controlled faults in the central Western Canada Sedimentary Basin (WCSB). Additionally, their research noted spatial associations between seismic events and fossil reef structures, providing deeper insights into the mechanisms of induced earthquakes and identifying areas with higher seismogenic potential.

In addition to geological factors, operational parameters such as injection rate and volume significantly influence the likelihood and magnitude of induced seismic events (Schultz et al., 2020b). While some studies emphasize injection rate as a critical factor, others like Schultz et al. (2018) have identified injection volume as a stronger predictor of seismic activity in the Canadian Duvernay play. This contrasts with a previous suggestion by Atkinson et al. (2016), who posited that the total volume of injected fluid might not heavily influence the maximum magnitude of hydraulic fracturing-induced seismicity in the WCSB.

A fundamental challenge in managing induced seismicity lies in establishing reliable relationships between operational parameters in each geological setting and the potential magnitude of seismic events. Several studies have attempted to estimate the maximum magnitudes based on assumptions about source processes and operational parameters (McGarr, 2014; Dieterich et al., 2015; McGarr and Barbour, 2018; Ge and Saar, 2022). For instance, McGarr (2014) proposed that the maximum moment of an induced earthquake is proportional to the total injection volume ($M_0^{max} = G\Delta V$), where G represents the shear modulus and ΔV the injected volume of fluids. McGarr's proposal relies on three key assumptions: first, that induced earthquakes experience shear stress drops proportional to the increase in pore pressure driven by injected fluid volume; second, that induced seismicity follows the Gutenberg-Richter magnitude-frequency distribution; and third, that the strain change within a specific volume is proportional to the total moment released by all earthquakes within that volume. While McGarr's proposed relationship initially aligns with data from certain activities such as wastewater disposal, hydraulic fracturing, and enhanced geothermal systems (Figure 1.5), subsequent studies have revealed instances where fracturing-induced earthquakes released seismic moments up to 100 times greater than McGarr's upper limit (Atkinson et al., 2016).

Large-scale hydraulic fracturing experiment by Guglielmi et al. (2015) revealed that a significant amount of energy is dissipated by an initial aseismic deformation phase before seismic deformation commences. The findings of Guglielmi et al. (2015) suggest that McGarr's proposed limit significantly underestimates the magnitude of induced events. Therefore, focusing solely on injection volume might not be sufficient, and the injection rate could be a more relevant parameter in certain cases. Studies like Weingarten et al. (2015) in the US mid-continent region support this notion, emphasizing the potential of managing injection rates as a tool for mitigating induced seismicity risk. Additionally, the seismic moment released by the 2017 Mw 5.5 Pohang main shock from enhanced geothermal system is 10 orders of magnitude bigger than moment expected by McGarr's relationship (Kim et al., 2018). The Pohang injection was into a fault zone dominated by patches of clay-rich low-permeability layers. These patches act as flow barriers, and thus pore pressure can locally reach a critical value for fault failure after a relatively small volume of fluid is injected (Kim et al., 2018) .

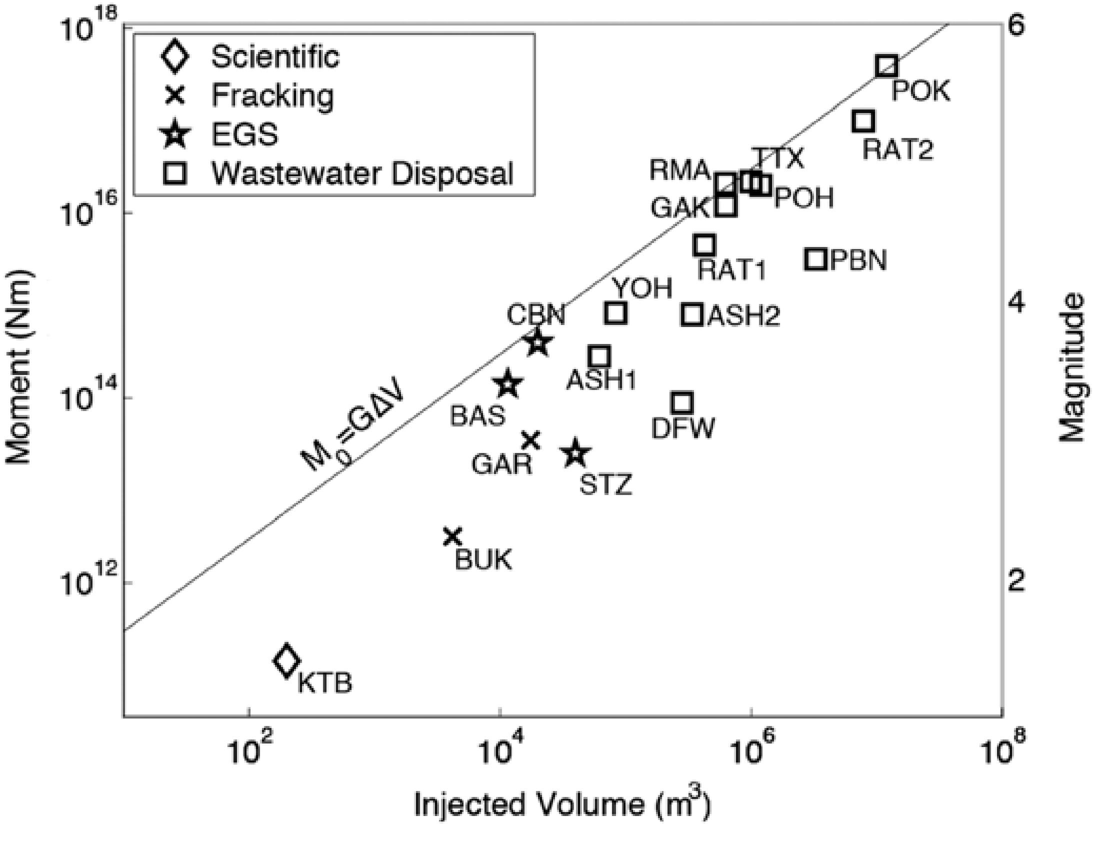

Figure 1.5. Maximum seismic moment and magnitude as a function of total volume of injected fluid from the start of injection until the time of largest induced earthquake. Solid line is estimated upper bound for McGarr (2014) model.

The absence of a universal, deterministic limit for induced seismic events underscores the importance of thorough assessments of geological and operational parameters. Furthermore, the review of current practices in managing these risks highlights a significant reliance on real-time monitoring systems and responsive protocols to mitigate the impacts of such seismic activities (Atkinson et al., 2020). A key component of these management strategies involves Traffic Light Systems, detailed below, which are designed to provide operational guidelines based on the real-time monitoring of seismic activity.

1.3.1 Traffic light protocols

Several jurisdictions have adopted magnitude-based Traffic Light Protocols (TLP) as a decision-making process to manage risks associated with induced seismicity. These protocols operate on two main principles: near-real-time monitoring of microseismic activities and execution of predefined responses once seismic events exceed threshold magnitudes (Atkinson et al., 2020). Figure 1.6 depicts the threshold magnitudes used in various jurisdictions. In the red range, any seismic event triggers an immediate halt to field operations for any well within a specified radius of the event's epicentre. Operations can only resume after consultation with the relevant regulatory bodies and the implementation of an approved mitigation and monitoring plan. For the intermediate 'amber light' threshold, operational modifications are required to reduce the risk of large-magnitude seismic events. For magnitudes below the 'amber light' threshold, considered the green range, operations proceed as planned.

Despite the straightforward concept and implementation of TLP systems, their effectiveness varies across different geo-energy industries. A notable limitation is the inconsistency in criteria and cut-off thresholds for TLP among various countries and regions (Figure 1.6). Moreover, these protocols typically favour the local magnitude scale over others, such as the moment magnitude scale, due to its suitability in near-real-time applications. However, local magnitude estimates can vary based on the monitoring systems deployed (Kendall et al., 2019). For instance, discrepancies in local magnitude readings for a seismic event can range by up to a unit when recorded at nearby stations (< 5 km) compared with those at greater distances (> 50 km) (Butcher et al., 2017). Furthermore, events characterised using near-surface arrays also tend to underestimate magnitudes relative to those characterised by downhole arrays (Baig, 2014).

A primary critique of TLPs lies in their retroactive nature, as they only initiate precautionary measures following a seismic event. Additionally, the implementation of TLP systems carries inherent risks. For instance, measures taken in response to specific mechanisms, as outlined in the *Mechanisms of Induced Seismicity* section, can inadvertently contribute to the occurrence of further seismic activity, such as the shut-in phenomena prompted by poroelastic stress transfer. There is also the possibility that by the time the predefined measures are enacted, it might already be too late to prevent a damaging seismic event. For example, the Mw 5.5 Pohang earthquake occurred two months of the cessation of injection activity (Yeo et al., 2020).

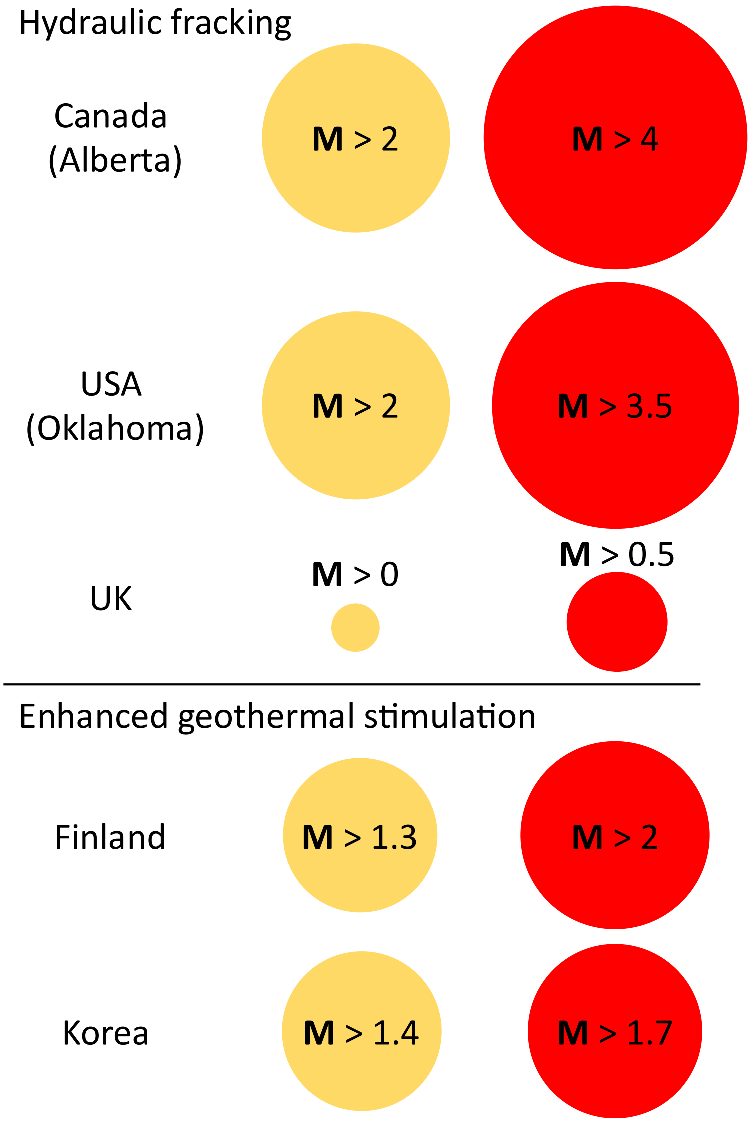

Figure 1.6. Traffic light protocol thresholds for various regions across the world. The event magnitudes necessary to activate amber or red scenarios vary widely between different regions and within the geo-energy industries. Modified from Atkinson et al. (2020).

Another significant oversight is the lack of consideration for site-specific geological factors in the establishment of magnitude thresholds (Schultz et al., 2020a). As indicated in earlier discussions, factors such as local stratigraphy, stress conditions and orientation, and the presence of faults and fracture corridors are crucial. The failure to account for the existence of faults can have particularly detrimental consequences, as demonstrated in the 2017 M_w 5.5 Pohang earthquake case (Kaown et al., 2021; Shapiro et al., 2021). Recent studies suggest a probabilistic approach to setting thresholds, which considers not only geological and operational data but also demographic and infrastructural vulnerabilities, could enhance the predictive capabilities and responsiveness of TLP systems (Schultz et al., 2021).

1.4 Induced seismicity in Horn River basin: a case study

The exact mechanisms at play when it comes to induced seismicity are influenced by local geology and the presence of pre-existing structures within the reservoir and/or the underlying underburden. This thesis focuses on fluid injection during hydraulic stimulation of tight shales from the Horn River Basin (HRB), British Columbia, Canada, as a case study. Initially, borehole samples from the basin will be characterised in terms of their petrophysical and geomechanical properties. Subsequently, these samples will undergo laboratory loading tests under reservoir conditions, with acoustic emission (AE) recording. The AE signature will be analysed in the context of the recorded microseismic activity in the HRB. This section provides an introductory overview of the HRB and the microseismic activity induced by hydraulic fracturing.

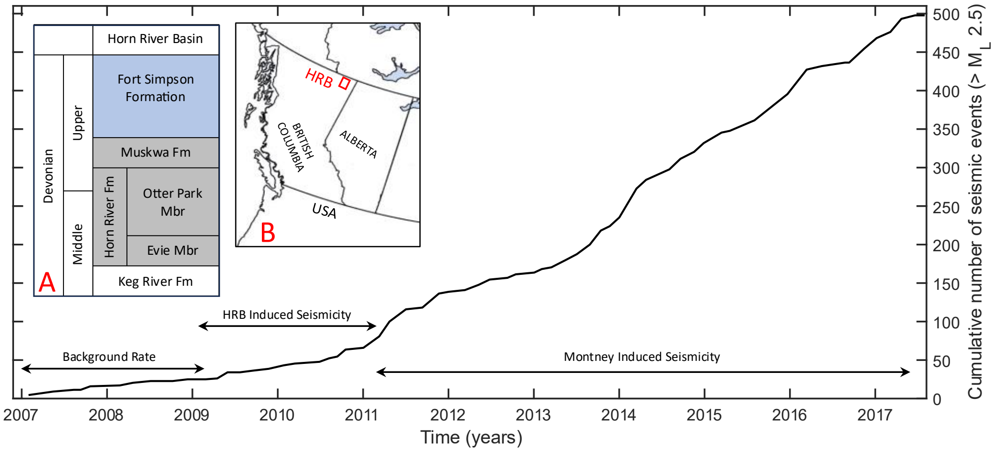

Figure 1.7. Cumulative seismicity in two major hydrocarbon plays (HRB and Montney) in British Columbia. The cumulative seismicity graph shows changes in seismicity rate, transitioning from background rate to development of the HRB and then development of the Montney play (Schultz et al., 2020b). Inserts A and B display the stratigraphic column and location of HRB, respectively, modified from Dong et al. (2017b).

The HRB, located in northeast British Columbia, is one of the largest shale gas fields in North America (Farahbod et al., 2014). It consists of three distinct overpressured, organic-rich shale formations: Muskwa, Otter Park, and Evie, which are overlain by the Fort Simpson shale — a calcareous shale with little organic content — and underlain by the Keg River carbonate (Dong et al., 2017b). The inserts in Figure 1.7 show the stratigraphic column of HRB shales (Insert A) and the location of HRB in British Columbia (red square, Insert B). Exploration and development activities started in 2006 and peaked in 2011 (Farahbod et al., 2015). Studies in British Columbia revealed an increase in the background seismicity rate associated with the commencement of the hydraulic fracturing operations in the area (Figure 1.7) (Schultz et al., 2020b).This has raised concerns from governments and local communities on various environmental and public safety issues. Among them, it is the possibility of increasing seismic hazards due to earthquakes induced by the hydraulic fracturing (HF) treatment of shale gas formations.

Farahbod et al. (2015) analysed historical seismogram data recorded in the HRB. They observed a clear correlation between increased HF operations and seismicity rates. In addition, they have reported a shift in the average maximum magnitude of events from M_L 2.9 to M_L 3.6 as the scale of HF operation expanded from 2006 to 2011. The *b*-value of the earthquake catalogue is estimated to be 1.21, higher than the typical tectonic/natural earthquakes of about 1, suggesting a physical correlation between HF operations and induced seismicity in the area.

Verdon and Budge (2018) conducted a study examining the spatial distribution of over 232,000 events detected during hydraulic fracturing in the HRB. Their examination revealed evidence of interaction between fluid-induced seismicity and pre-existing faults. They identified several events with magnitudes up to Mw 1.3 — larger than typically observed when hydraulic fractures propagate through shale gas reservoirs, where magnitudes are generally less than Mw 0. In a separate study, Kettlety et al. (2019) investigated the role of elastic stress transfer in the reactivation of pre-existing faults, analysing a microseismic dataset and quantifying the cumulative stress release associated with the reactivation of pre-existing faults. They concluded that the stress change alone did not significantly contribute to fault reactivation, instead, failure may have been initiated by fault interaction with the injected pressurized fluid.

1.5 Laboratory acoustic emissions as analogues for earthquakes

The study of earthquakes presents numerous challenges, as they inherently occur under complex and unconstrained natural conditions. To overcome these limitations, laboratory recorded acoustic emissions (AE) have long been utilised as analogues for tectonic earthquakes, providing a controlled environment to investigate seismic processes (Scholz, 1968; Lockner and

Byerlee, 1977). AE events are transient elastic waves generated by the rapid release of stress during microfracturing in rock samples. Although these AE events are orders of magnitude smaller, they share fundamental characteristics with natural earthquakes, including sudden failure, energy release, and elastic wave propagation (Lockner et al., 1991).

In laboratory settings, AE events are typically induced by subjecting rock samples to controlled loading conditions that lead to fracture, mimicking the natural accumulation and release of tectonic stress. High-frequency sensors, such as piezoelectric transducers, are used to record AE signals associated with crack initiation and propagation (Goodfellow and Young, 2014; McLaskey et al., 2015). The recorded AE events provide valuable insights into the timing, location, and magnitude of microfractures and help elucidate the mechanisms of crack coalescence and rupture. They also support the interpretation of larger-scale seismicity, as both the microseismic events and tectonic earthquakes exhibit similar statistical behaviour in key seismic parameters, such as the Gutenberg–Richter b-value (see Section 1.2).

On a field scale, microseismic monitoring has become a widely adopted seismic technique, particularly in contexts such as hydraulic fracturing, where it assists in visualizing the initiation and propagation of fractures (Rodríguez-Pradilla, 2015; Waldron and Camac, 2016). The hypocentre location of microseismic events enables the mapping of fracture growth within the stimulated reservoir and the reactivation of pre-existing faults in the surrounding region. Additionally, microseismic sequences have been utilised to infer failure mechanisms (Kettlety et al., 2019; Kettlety and Verdon, 2021).

Microseismic data can also play a vital role in mitigating and managing seismic risks. For example, near-real-time monitoring of microseismic data enabled the effective control of induced earthquakes and safe stimulation of a 6.1-km-deep geothermal well near Helsinki, Finland, in 2018 (Kwiatek et al., 2019). This was achieved by analysing seismicity rates, events locations, magnitudes, and the evolution of injection pressure. Operational parameters, such as pumping flow rate and wellhead pressures, were then adapted to maintain the induced seismicity within the thresholds prescribed by the regional traffic light system (TLS).

Furthermore, Verdon and Budge (2018) developed a statistical model using a microseismic dataset to forecast the largest induced event within specific time windows. Predicting the magnitude of induced events is vital for mitigating geohazard risks. Clarke et al. (2019) further demonstrated the use of microseismic monitoring for making real-time operational decisions during hydraulic fracturing operations.

While field-scale microseismic monitoring provides valuable operational and hazard mitigation insights, laboratory AE experiments offer a complementary approach by enabling detailed, controlled investigation of fundamental fracture processes. However, extrapolating laboratory AE observations to natural seismicity presents several challenges due to differences in scale, stress conditions, and signal frequency (McLaskey et al., 2012). A particularly significant difference lies in the frequency content of recorded AE signals (Burlini et al., 2007). Natural earthquakes are typically observed at frequencies below 100 Hz, whereas AE signals occur in the ultrasonic range—from tens of kHz to MHz (Brantut et al., 2011; Pignalberi et al., 2024). The elastic properties of rocks, such as wave velocity and attenuation, are known to be frequency-dependent due to dispersion and pore-fluid interactions, particularly in high-porosity, fine-grained rocks (Vinciguerra et al., 2006; Mavko et al., 2009; Trippetta et al., 2013). Theoretical models, including Biot-Gassmann formulations (Mavko and Bandyopadhyay, 2008), describe these behaviours and show that mechanical properties measured at ultrasonic frequencies often differ from those relevant at field scale.

Furthermore, the scaling between frequency and source dimension (Figure 1.4) implies that AE events arise from fracture processes operating at the grain or micrometre scale, whereas natural earthquakes involve slip over fault planes ranging from centimetres to kilometres. Differences in boundary conditions and stress states also limit direct comparability. Laboratory experiments typically involve relatively high strain rates and well-defined boundary constraints. In contrast, natural faulting evolves under variable and complex boundary conditions over geologic timescales. Nonetheless, laboratory recorded AE events remain a powerful means of probing the fundamental mechanics of crack initiation, coalescence, and failure—processes integral to all scales of seismicity.

Another potential source of uncertainty is the sensor array configuration and sensor calibration adopted in laboratory experiments (McLaskey and Glaser, 2012). Adequate volumetric coverage of the test specimen is required to ensure that AE events representative of the whole sample behaviour is recorded. Uncalibrated AE systems can catalogue AE occurrences, locations, relative amplitudes, and sometimes focal mechanisms, allowing insightful interpretations to be drawn of the seismic evolution during loading and failure (Goebel et al., 2012; Goebel et al., 2013; Khajehdehi et al., 2024; Zhang et al., 2025). However, to obtain absolute magnitudes and to characterise the source parameters of the AE events, sensor calibration is required, as amplitudes and frequency content depend on sensor sensitivity and response characteristics (Pignalberi et al., 2024).

The role of rock microstructure is also critical in bridging the scale gap. In fine-grained sedimentary rocks such as shales, features like bedding-parallel lamination, aligned clay minerals, microcrack networks, and organic inclusions influence both mechanical behaviour and wave propagation (Li et al., 2017; Sarout et al., 2017). These microstructural features control anisotropy, pore pressure evolution, and fracture toughness (Dewhurst and Siggins, 2006;

Ougier-Simonin et al., 2016). While laboratory AE studies can characterise such effects in detail, their influence does not necessarily scale uniformly to field-scale rock masses. Therefore, interpretation of AE data demands integration with upscaling methods and rock physics models that account for frequency dispersion and poroelastic effects (Hajati et al., 2015; De Barros et al., 2019).

In summary, despite differences in scale and signal frequency, laboratory recorded AE provides a robust framework for investigating fracture and seismic processes in controlled settings—including the evolution of failure, timing and source location, seismic parameters such as b-value, P-wave velocity, and event clustering. In this thesis, AE monitoring provides a critical tool for investigating how microseismicity evolves during deformation of fine-grained, low-porosity shales, enabling detailed analysis of behavioural changes as the rock transitions through different loading and failure stages.

1.6 Aims of the PhD thesis

The overarching goal of this PhD thesis is to advance our understanding of key controls that trigger fluid-induced seismicity. This complex phenomenon, increasingly recognized due to its association with industrial activities such as hydraulic fracturing and enhanced geothermal stimulation, poses significant safety challenges in terms of both prediction and management. The thesis aims to dissect the critical controls and interactions that lead to seismic events caused by fluid injections into the Earth's crust. The specific research questions addressed in this thesis are outlined below:

- **Pore fluid and fracturing/faulting processes:** What role does pore fluid pressure play in controlling the reactivation and slip mode of pre-existing faults?
- **Systematic variations of seismic parameters:** Is it possible to detect and measure systematic variations of seismic parameters before major induced events, such as the b-value, P-wave velocity, source location, and fractal dimension?
- **Microseismic monitoring strategies:** How can we improve microseismic monitoring strategies and address current limitations in managing hazards associated with induced seismicity?

To address these questions, the thesis will employ a range of laboratory experimentation techniques. Laboratory work will include the development of a protocol for obtaining shales core at a centimetre scale and conducting triaxial loading experiments with acoustic emission (AE) recordings. These methods are designed to simulate and analyse the conditions under which fluid injections can induce fracturing, faulting processes, and seismic activities. Through these experiments, the thesis aims to provide insights into the mechanics of these seismic events.

1.7 Structure of the thesis

This thesis is divided into 6 chapters. Following the introduction (this Chapter), Chapter 2 describes the essential methodology and tools used throughout the thesis. Chapters 3 to 5 present the main results of the experimental work carried out during the study. A final discussion and conclusions are presented in Chapter 6, integrating the thesis's main findings. Below is an overview of the contents of each chapter.

Chapter 1: Thesis introduction

This chapter provides a background of the project, offering a brief introduction to the physical processes that cause induced seismicity. It also provides an overview of risk management and mitigation strategies for induced seismicity. Finally, it outlines the aims and structure of this thesis.

Chapter 2: Methods

This chapter details the methods used during this PhD study, covering the range of experimental techniques used to acquire datasets. A particular focus is given to describe the: 1) new protocol to obtain shale core plugs; 2) various techniques used to measure the physical properties of shales; 3) triaxial deformation apparatus used to perform loading experiments; 4) acquisition and processing of the acoustic emissions (AE) data recorded during loading experiments.

Chapter 3: Geomechanical properties and seismic anisotropy of Horn River shales

This chapter is dedicated to the characterization of Horn River (HR) shale samples in terms of mechanical, petrophysical, and anisotropic properties. Measurements of density, ultrasonic wave velocity (V_P/V_S), elastic moduli and anisotropy are reported. The mineralogical composition and microstructural characteristics influencing these properties are identified, and their role in the observed induced seismicity of HR is discussed.

Chapter 4: Temporal and spatial evolution of acoustic emission and seismic parameters of Horn River shales during shear faulting

This chapter presents the results of acoustic emissions (AE) from triaxial loading experiments to failure, conducted on borehole samples from Horn River Basin (HRB) shales. The study explores the relationship between AE rate, the evolution of *b*-value and P-wave velocity (V_P) to the progressive shear-induced degradation of the sample, eventually leading to macroscopic failure. The aim is to calibrate progressive deformation leading to failure with microseismic response of HRB shales under reservoir conditions.

Chapter 5: Fault reactivation and induced seismicity during fluid injection

This chapter reports the results of loading experiment conducted on borehole sample from HRB with a simulated pre-existing fault. The aim is to study the role of fault heterogeneity and pore fluid control on fault reactivation and fault slip modes. This Chapter complements the results of Chapter 4, where the microseismic signature is obtained for an initially intact shale material.

Chapter 6: Discussion and conclusions

This chapter integrates the results from chapters 3 to 5. First, it discusses the key controls on fault reactivation and earthquakes slip modes (e.g., slow vs fast earthquakes). Then, it explores the implications of these results in the broader context of natural and fluid-induced seismicity, including their potential application for geohazard management and mitigation systems. Finally, it identifies potential further research topics arising from this thesis.

2 Methods

2.1 Introduction

This chapter describes the triaxial loading apparatus, sample preparation, and data acquisition systems. A schematic diagram illustrating the experimental workflow is presented in Figure 2.1. Borehole samples obtained from Horn River basin in British Columbia, Canada, underwent non-destructive characterization, including density and elastic wave velocity measurements. Subsequently, a novel protocol was developed for the preparation of shale core samples. These sample cores were subjected to triaxial loading, and mechanical and acoustic emission (AE) data were collected. Fragments from the coring process were used for total organic content measurements. The post triaxial loading experiment cores underwent X-ray scanning to identify fracture geometry. Finally, specialized software was employed for data processing and visualization.

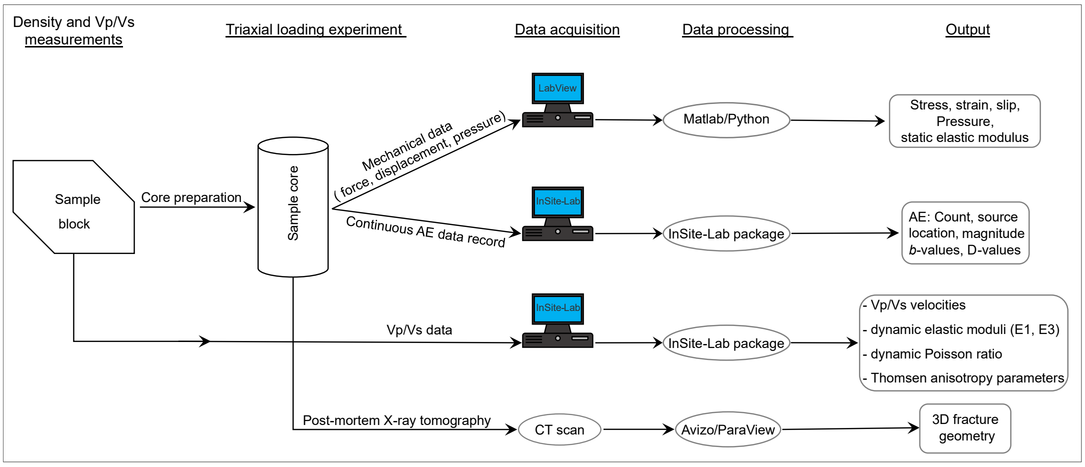

Figure 2.1. Schematic diagram shows the experimental program for data acquisition and processing.

The following sections provide a comprehensive overview of the experimental techniques and methods employed to implement the workflow. The discussion will primarily focus on three key aspects: 1) the development of a novel protocol for preparing shale core plugs; 2) the utilization of a triaxial deformation apparatus for conducting the experiments; and 3) the acquisition and processing of the acoustic emission (AE) data recorded during these experiments.

2.2 Triaxial deformation apparatus

The Durham University triaxial apparatus with fluid flow (Dutff) is designed for triaxial loading ($\sigma_1 > \sigma_2 = \sigma_3$) experiments. It has the capability to apply up to 250 MPa of confining pressure, 200 MPa of pore fluid pressure, and temperatures of up to 200°C. The pressure vessel is cylindrical, with an outer diameter of 180 mm and an internal bore of 60 mm (Figure 2.2). To ensure corrosion prevention and enhance vessel longevity, a low viscosity (0.01 Pa. s) silicone oil is used as the confining medium. The oil is introduced into the vessel through a pipe located at the top of a sample assembly (see Figure 2.5). The pressure increase is achieved using an air-driven hydraulic pump, which can be isolated from the vessel once the target pressure is attained. Pressure measurements are obtained using an analogue gauge and an RDPE-J type transducer manufactured by Honeywell, with an accuracy level of approximately 0.01 MPa.

A servo-controlled electromechanical loading system enables the application of a differential load of up to 300 kN to the sample. The loading system comprises several components, including a force gauge block, force gauge, spacer, loading column, and drive gear (Figures 2.2, 2.3, and 2.4). In experiments involving high temperatures, the spacer on top of the force gauge can be replaced with a cooling plate (Figure 2.2). This cooling plate acts as a thermal insulation to minimize the influence of elevated temperatures on the force gauge measurements. To ensure proper sealing, a dynamic Variseal, manufactured by Trelleborg Ltd., is utilized for the force gauge. The Variseal effectively prevents the leakage of confining oil from the bottom of the vessel (Figures 2.2 and 2.4).

The loading column of the apparatus is driven by a Printed Motor Works GM12 pancake-type servo motor and gear train (Figure 2.3). The gear train consists of a Parvalux gearbox connected in series with a Hydro-mec worm gearbox, located at the bottom of the apparatus (Figures 2.2 and 2.3). The combined gear train is then coupled to the main drive gear, which has a gear ratio of 5:1. Consequently, a final gear ratio of 20700:1 is achieved between the motor and the loading column. The motor has a maximum speed of 3000 rpm, resulting in a rotational speed of 0.14 rpm at the drive gear. Considering that the loading column has a lead of 10 mm, the maximum loading velocity is $23\ \mu m\ s^{-1}$. For the majority of experiments conducted in this thesis, a loading velocity of $1\ \mathrm{\mu m\ s^{-1}}$was employed, and the maximum loading velocity never exceeded $14\ \mathrm{\mu m\ s^{-1}}$. A linear variable displacement transducer (LVDT) is mounted at the base of the loading column to measure its axial displacement (Figure 2.2 and 2.3). This measurement is used to calculate the strain of the test specimen (see the next section for details).

The force is transmitted to the sample through a threaded force gauge extension block (Figure 2.4). Force measurements are obtained by measuring the elastic distortion of the force gauge column. A LVDT is located internally within the loading column below the pressure vessel column (Figure 2.2). The LVDT insert is pressed against a shoulder within the force gauge housing, positioned above the level of the Variseal (Figure 2.3). As a result, the actively deforming length of the gauge is situated above the seal, eliminating the need for friction correction. The force gauge column is fabricated from M300 maraging steel, which has a yield strength of approximately 2 GPa. The overall resolution of the force gauge is approximately ±10 N. During the loading process, the insertion of the axial loading column into the pressure vessel leads to an increase in pressure due to volume loss within the vessel.

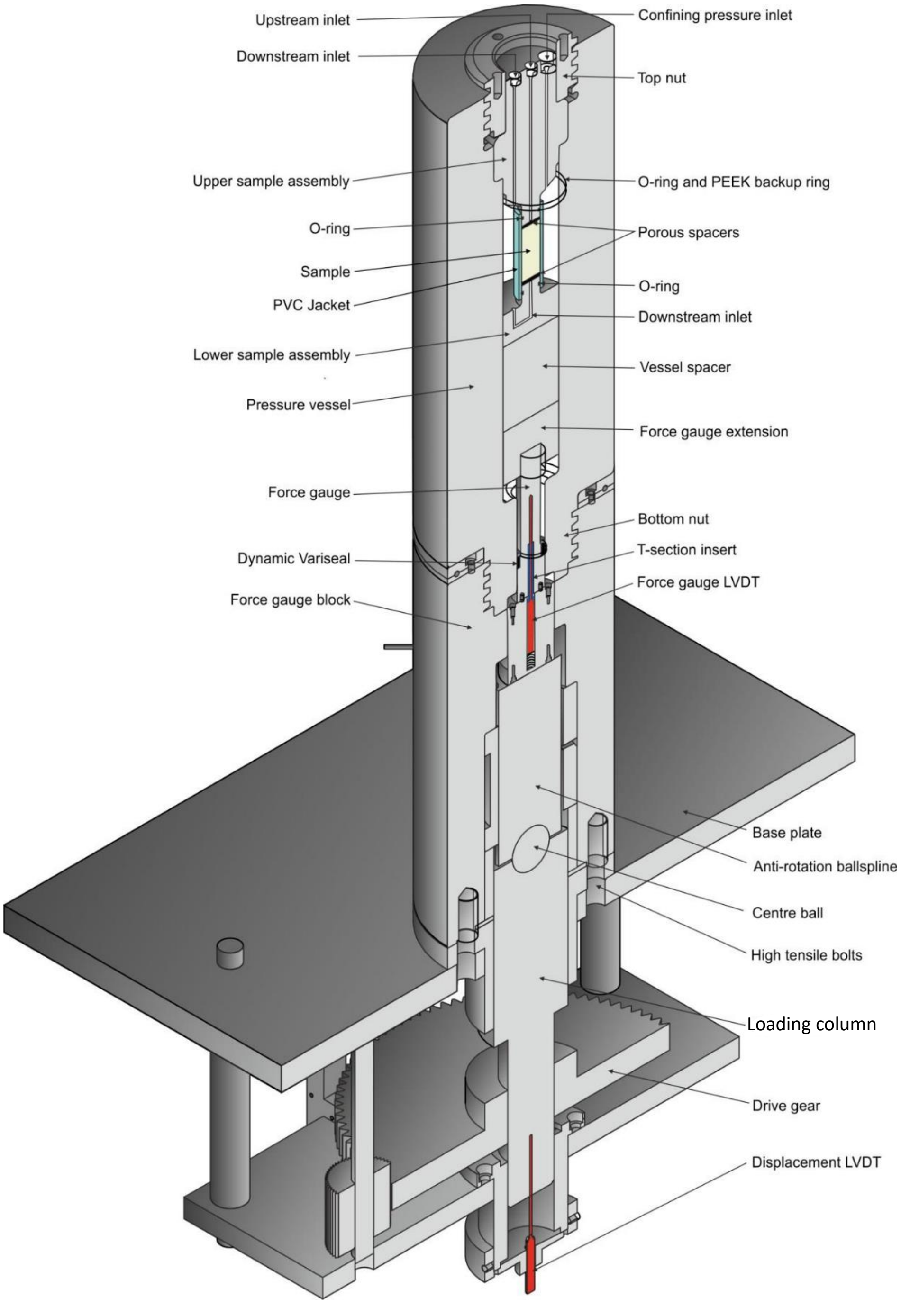

Figure 2.2. Scale drawing of the triaxial deformation apparatus used for conducting loading experiments (Bedford, 2017).

To maintain a constant confinement pressure, a Nova Swiss 10 cc syringe pump is employed. Throughout the loading phase, the syringe pump is manually retracted to compensate for the lost volume. Generally, this approach allows for pressure maintenance during the loading experiments within ± 0.1 MPa of the target pressure.

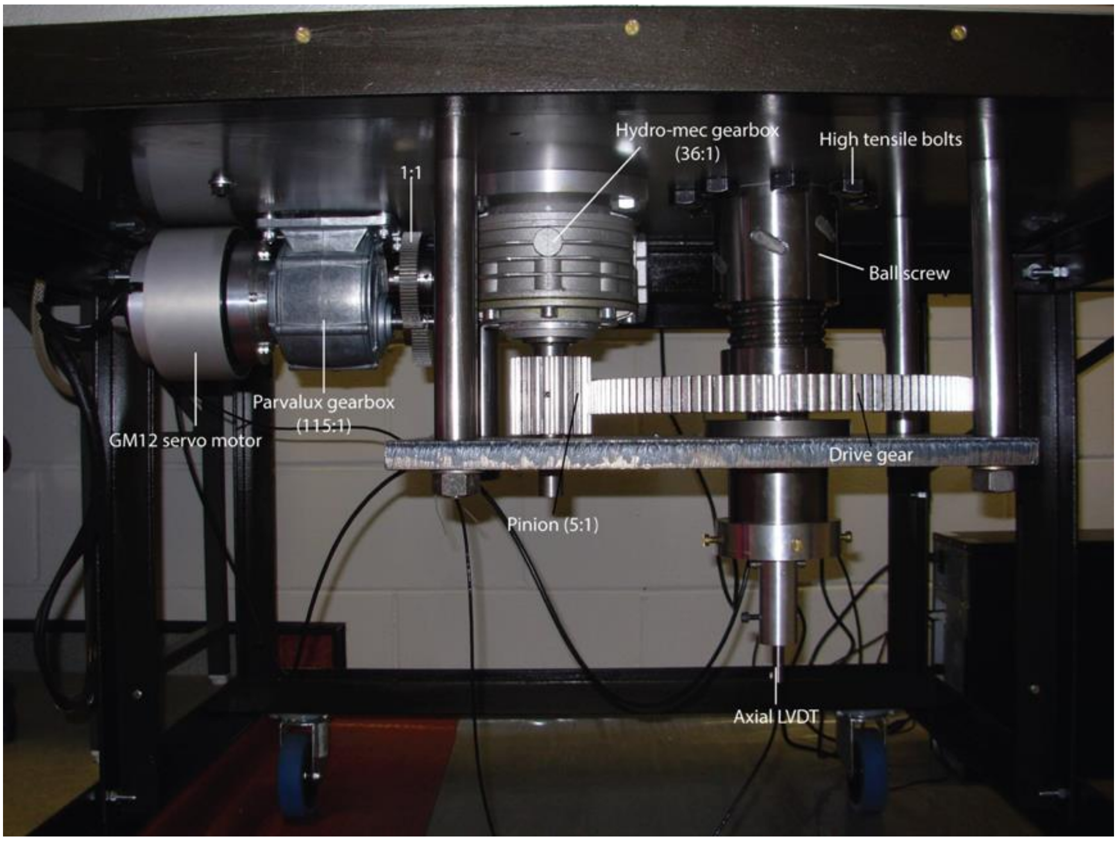

Figure 2.3. Photograph of the axial load system. The gear train is driven by a printed motor works GM12 pancake servo motor. Axial displacement is measured using an LVDT mounted at the base of the loading column.

Pore fluid pressure in the apparatus is controlled by a servo-controlled pump, enabling precise application of the pore fluid at both the top (upstream) and bottom (downstream) of the test specimen (see Figure 2.5). The upstream and downstream ends of the sample are connected through a volumometer with a measurement precision of 0.1 mm^3. This volumometer monitors relative changes in pore volume during experiments by measuring the displacement of the pump piston using an LVDT (De Paola et al., 2009). By isolating the upstream and downstream reservoirs so they are connected solely through the sample, this configuration facilitates permeability measurements using techniques such as transient pulse decay (Brace et al., 1968) or pore pressure oscillation methods (Fischer, 1992). However, permeability monitoring was not conducted in the experiments reported in this thesis. Instead, pore pressure was applied using a manual Nova Swiss 10 cm^3 pump connected to the upstream and down reservoirs. The pore fluid pressure was measured during the experiments using an analogue gauge and an RDPE-J type transducer manufactured by Honeywell, with an accuracy of approximately 0.01 MPa.

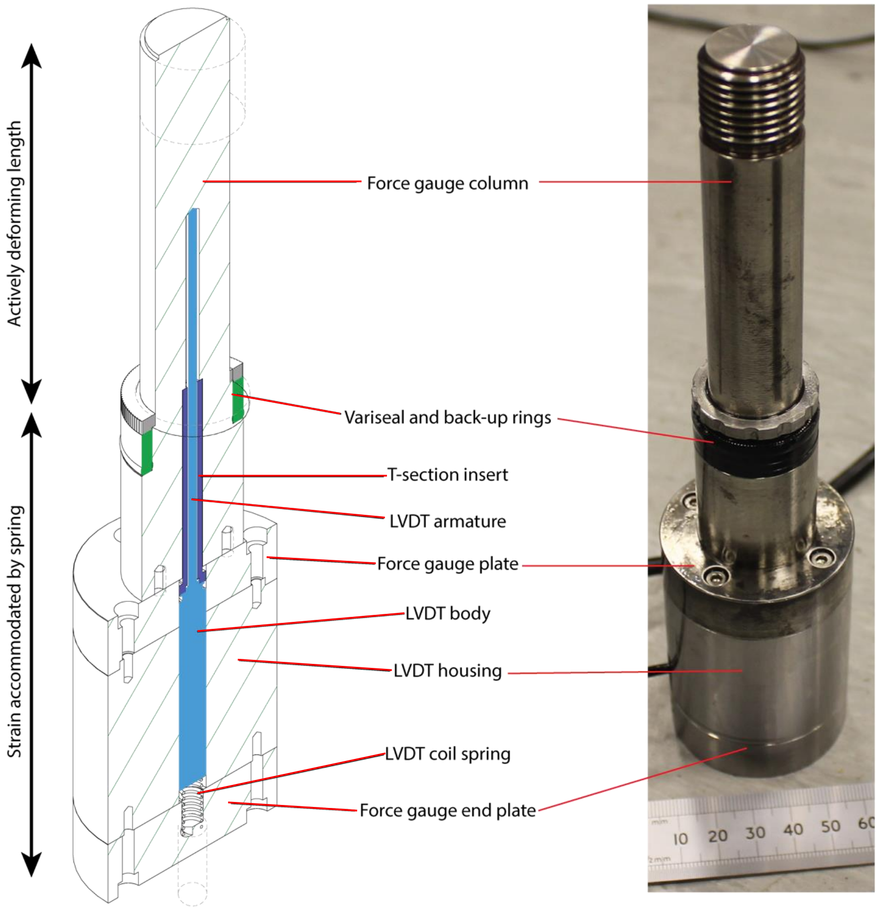

Figure 2.4. A diagram and picture showing the main components of the force gauge.

2.2.1 Sample assembly

The sample assembly utilized in these experiments comprises an upper and lower part, with the experimental sample positioned between them (Figure 2.5). It is specifically designed to accommodate cylindrical samples measuring 20 mm diameter by 60 mm length. Once the sensors are attached to the sample (attachment procedures is described in section 2.3.3), the sample is wrapped with Teflon tape and inserted into a PVC jacket. The PVC jacket serves to isolate the test sample from the silicone oil confining medium. The PVC jackets are constructed using PVC tubing, featuring an inner diameter of 19 mm and an outer diameter of 25 mm. The jacket is sealed using O-rings located on the upper and lower parts of the sample assembly (Figure 2.5). The Teflon tape facilitates smooth insertion of the sample into the jacket and helps minimize friction.

To allow for the extraction of sensor lead wires, a hole is created in the jacket's wall, which is subsequently sealed with Loctite Hysol 9455 flexible epoxy to prevent oil leakage into the jacket. Additionally, two 17-4 PH stainless steel spacers, equipped with machined grooves, are positioned above and below the sample. These spacers ensure a uniform distribution of pore fluid pressure across the surfaces of the sample ends. Once the jacketed sample is mounted onto the assembly, it is prepared for insertion in the pressure vessel.

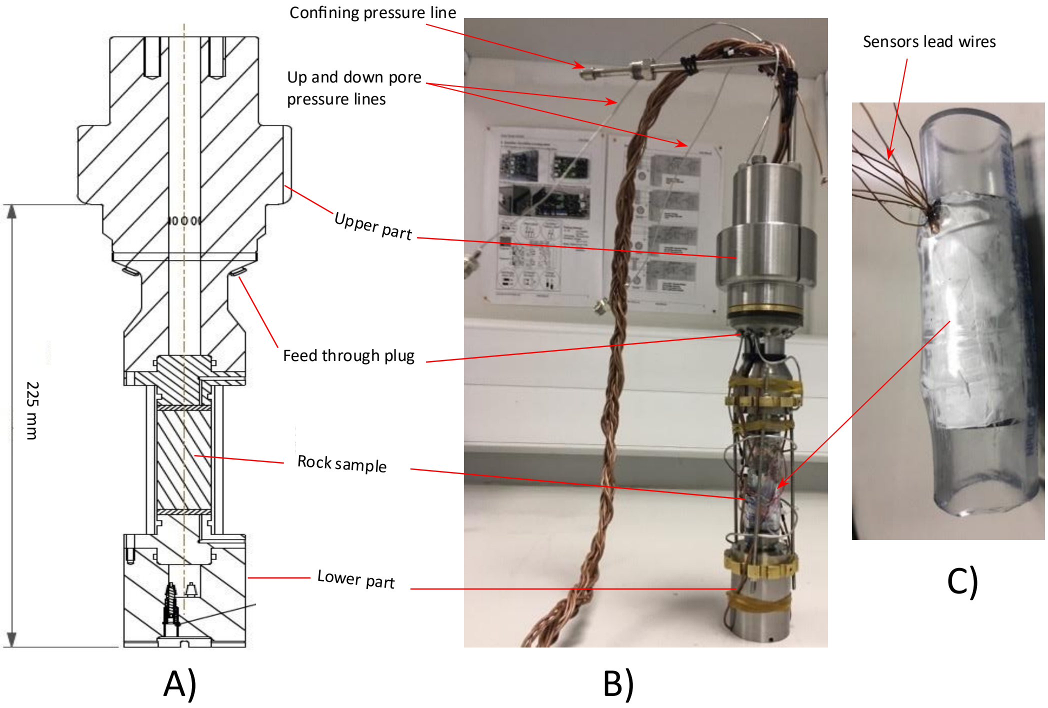

Figure 2.5. (A) Scale drawing of the sample assembly. (B) Photograph of the sample assembly with the sample mounted. (C) Sample inserted into a PVC jacket, with sensor lead wires extracted.

Measurement signals from the sensors are transferred to and from the pressure vessel through a specialized arrangement. This arrangement involves the drilling of 12 narrow boreholes that intersect a wider, longer central borehole located in the top part of the assembly (Figure 2.5). The narrow boreholes are tapered inward, creating a sealing surface against the confining pressure. To facilitate the transmission of signals, shielded cables are soldered onto insulated sliver feedthroughs, which are then connected to the sensors on the pressure vessel side. These cables run through the central borehole of the sample assembly and are routed to external amplifiers and a data acquisition system. It is important to note that while the borehole sealing, and connection performance is generally reliable, regular maintenance is necessary due to occasional electrical shortcuts that occur during operations. For more comprehensive information on connection wires, soldering, and the sealing mechanism, refer to the work by Harbord (2018).

After the test sample is mounted on the sample assembly (Figure 2.5 B), the entire assembly is inserted into the pressure vessel through a threaded top opening (Figure 2.2). A threaded top nut is used to tightly secure the assembly in place within the vessel. The sealing of the vessel is achieved through a combination of a Viton O-ring and a PEEK delta backup ring. The Viton O-ring is positioned to prevent any extrusion of the O-ring material between the sample assembly and the vessel (Figure 2.2). This O-ring serves as the primary sealing element. Additionally, a PEEK delta backup ring is utilized to provide additional support and stability to the O-ring, further preventing extrusion and maintaining the integrity of the seal (Figure 2.2).

By employing both the Viton O-ring on the sample assembly and the dynamic Variseal on the force gauge (described in the previous section; Figure 2.3), an effective sealing mechanism is established, ensuring that the pressure vessel remains tightly sealed during the experimental procedures.

2.2.2 Data logging and servo control systems

Figure 2.6 presents a schematic illustration of the triaxial deformation apparatus components, data logging, and control systems. The apparatus is operated using LabView software, which serves as a control interface in conjunction with a series of servo control boxes. These control boxes convert the DC voltage output from a National Instrument (NI) digital input/output interface. The control script was developed by D. Faulkner (Harbord, 2018). Two sets of data were collected for each triaxial experiment: mechanical data (force, displacement, and pressure) and acoustic emission (AE) data (Figure 2.1).

Three linear variable differential transformers (LVDTs) record the position of the pore fluid pump piston in the volumeter, the axial shortening of the loading column, and the linear deformation of the force gauge. The raw voltage signals from the LVDTs are fed into an RDP Modular 600 multi-channel signal conditioning system, which amplifies the analogue signals at a bandwidth of 10 kHz. Additionally, three Honeywell pressure transducers monitor the confining pressure as well as the upstream and downstream pore fluid pressures. The outputs from the pressure transducers are also amplified using the RDP 600 amplifier.

The analogue signals from the LVDTs and pressure transducers are transmitted via coaxial cables to an NI 9215 analogue-to-digital converter (ADC). The ADC converts the signals into digital format, which is then transmitted to the LabView PC via USB. On the LabView PC, these digital signals are converted from raw voltages to physical units using machine calibrations (Harbord, 2018). The converted physical units recorded by the LVDTs, and pressure transducers are saved as a text files (. ascii) on the LabView PC at a sampling rate of 10 samples per second. This data is later processed using algorithms developed in MATLAB by the author to extract the mechanical parameters. In contrast, acoustic emission (AE) signals are recorded using a separate high-frequency acquisition system, as described in Section 2.6, and processed using ITASCA's proprietary software, InSite-Lab.

In all the experiments, the macroscopic failure time is manually noted to serve as a reference point for synchronization procedures during data processing. The synchronization is crucial to ensure accurate alignment of the timing between the mechanical and AE data, as these are logged on separate PCs at different sampling rates.

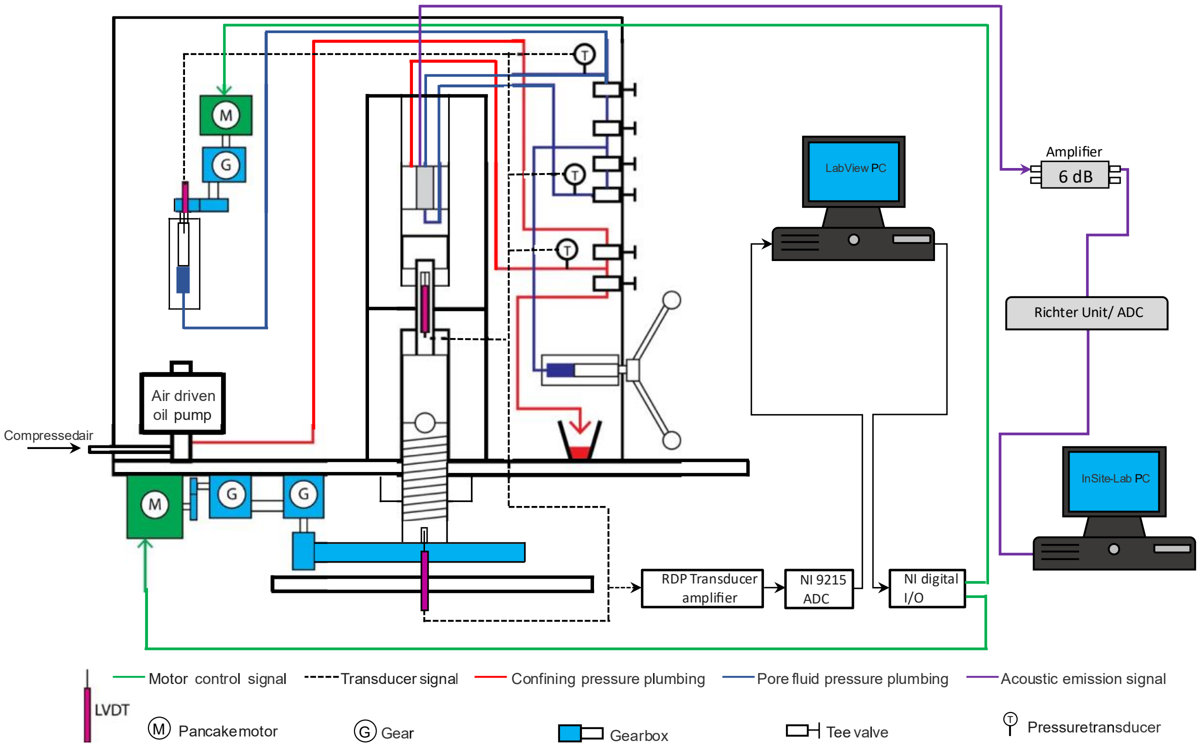

Figure 2.6. Schematic illustration of triaxial deformation apparatus components, data logging and control systems (modified from Harbord, 2018). Not to scale.

2.3 Sample preparation

2.3.1 New protocol for shale cores preparation

Obtaining shale core plugs, at centimetre scale, represents the biggest challenge facing the experimental aspects of this project. Shales inherently contain weakness planes. Moreover, shales have a tendency to swell and disintegrate upon contact with water (Chandler et al., 2016). Therefore, considerable effort was dedicated to developing a protocol to obtain shale core plugs (Figures 2.7,2.8, and 2.9). The following steps outline the procedures involved in obtaining a core plug with a diameter of 20 mm and a length of 60 mm, starting from a block measuring approximately 50 mm by 100 mm.

1. Using a tile saw with a thin blade (1 mm thick), cut the block into an approximate polygonal prism with a diameter of 24 mm (Figure 2.7 A-C). Use a minimal amount of water as cooling fluid to cool the cutting blade and dampen the dust.
2. Mount the polygonal prism on a grinder tool jaw, ensuring that about 70 mm of the polygonal prism sticking out of the grinder jaw (Figure 2.7D).
3. While the prism is rotating on its axis, slowly introduce a grinding wheel along the long axis, cutting off a thin layer of the rock piece at a time (100 – 200 micron).
4. Repeat the cutting process until a cylindrical core with diameter of 20 mm is obtained.
5. Once the desired diameter is achieved, cut the core plug to the required length by introducing the grinding wheel across the face of the specimen, removing a minimal layer of the rock at a time (100 – 200 micron).
6. Repeat this cutting process until the end of the specimen is flattened and perpendicular to the plug axis.
7. Mount the specimen from the flattened end and repeat the perpendicular cutting process until the second end of the specimen is flattened and the required length of the core plug is obtained.
8. Use a minimal amount of water to cool the grinding wheel during the cutting processes.

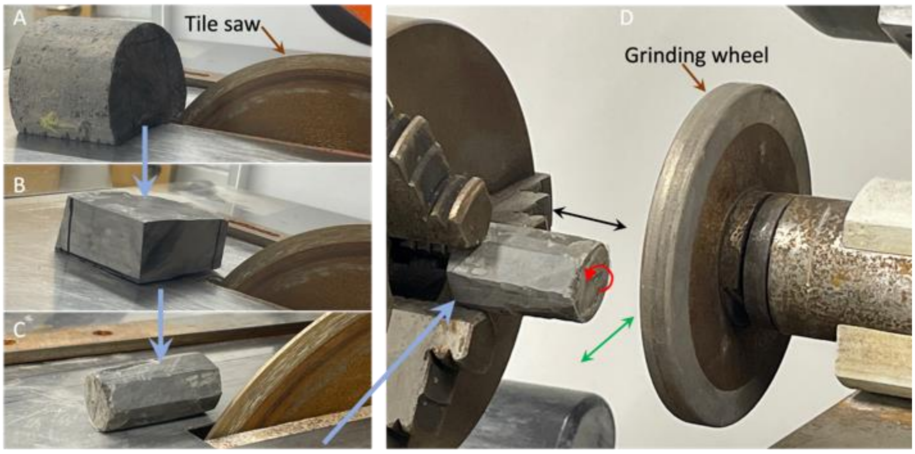

Figure 2.7. Photos showing stages of cutting and grinding procedures. (A) Initial shale block, (B) Intermediate cutting stage, (C) Polygonal prism, (D) Grinding stage: the grinding wheel moves left-right (black double-headed arrow) while rotating to cut along the prism axis. Then the grinding wheel moves in-out (green double-headed arrow) to square the end faces (see the text for details). The polygonal prism is rotating along its axis during the cutting process.

The technique described above has been successfully used to obtain core plugs from shale samples collected from the Horn River Basin in Western Canada (Figure 2.9). The Horn River formation is siliceous, organic-rich shale comprising 67% silicate minerals, 3% total organic carbon (TOC), and porosity of 5% (Dong et al., 2015). For a detailed description of the lithology and depositional environments of Horn River shales, see Chapter 3.

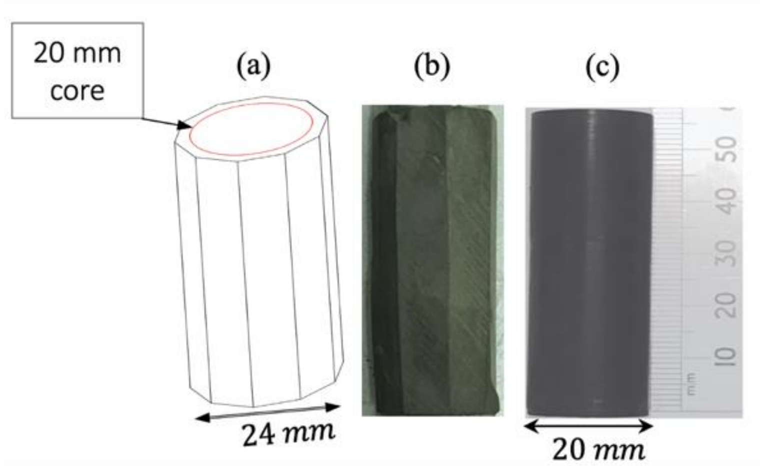

Figure 2.8. (a) Schematic of a polygonal prism showing the intended dimension of the core plug. (b) A photograph of specimen at an intermediate stage. (c) Photograph of the final product.

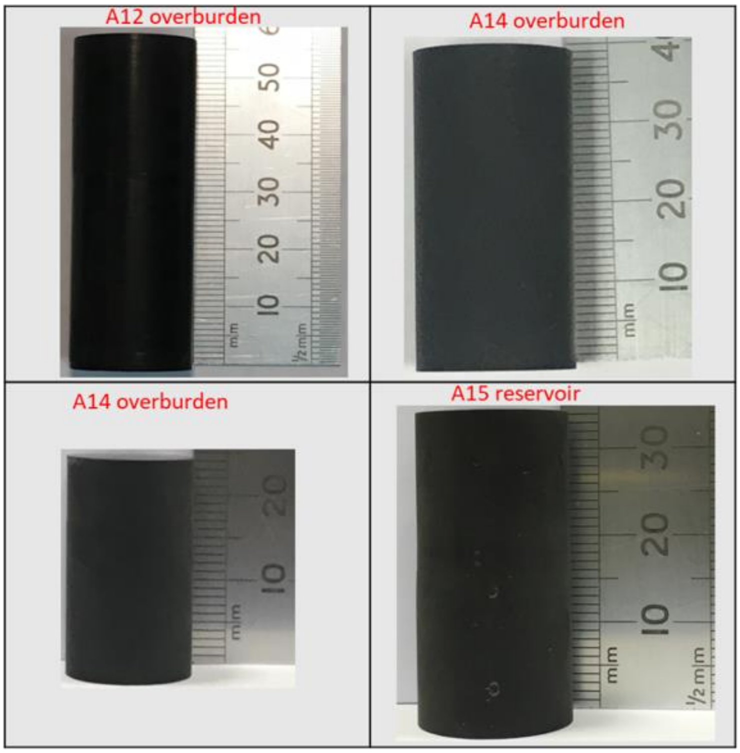

Figure 2.9. Pictures of core plugs obtained using the technique developed during the course of the PhD. These core plugs will be utilized in intact samples experiments in Chapter 4 and reactivation experiments in Chapter 5.

2.3.2 Composite sample preparation

To investigate fluid-induced reactivation of a pre-existing fault within the reservoir underburden, I conducted a reactivation experiment on a composite sample. The Horn River Basin reservoir units overlie carbonates (limestones and dolostones, see Chapter 3), therefore a composite sample is used to simulate this geological heterogeneity. The sample comprises an intact shale core on top of a Westerly granite sawcut. The shale core plug is prepared following the protocol described in the preceding section. The Westerly granite is chosen due to its homogeneity and well-characterised microseismic response (Further details about its selection are provided in Chapter 5). To create the granite sawcut, a 20-mm diameter and 25-mm long granite core plug is utilized. Initially, a 3 mm diameter bore that is concentric with the core is drilled to a depth of two-thirds of the core height. This bore serves as a channel for injecting fluids directly into the simulated fault plane.

Next, the simulated pre-existing fault plane is achieved by cutting the core at a 30-degree angle to its axis using a diamond saw (Figure 2.10). The resulting cross-section of the cut matches the core's diameter, resulting in a simulated fault plane that is 20-mm long. Finally, both sides of the fault surfaces are carefully ground using a grinder to ensure a precise fit between the two components. The surfaces are then roughened with #800-grit sandpaper (approximately 10 µm particle size).

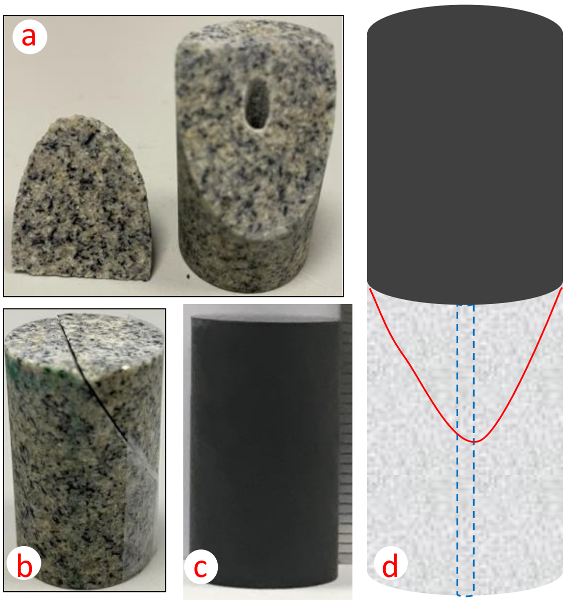

Figure 2.10. a) A granite sawcut with a drilled bore for fluid injection. b) An assembled granite sawcut. c) An intact shale core. d) Schematic showing the assembled granite sawcut and intact shale core on top. The red curve represents the simulated fault plane, and the blue dashed line indicate the drilled bore for fluid injection.

2.3.3 Installation of sensors

Piezoelectric sensors manufactured by PI (Physik Instrumente Ltd) were used to record acoustic emissions (AE) during triaxial loading experiments. These sensors are made of lead zirconate titanate (PZT) and have dimensions of 3x3x0.75 mm (Figure 2.11A), with a resonant frequency of 4 MHz. The minimum number of sensors needed to form an array depends on the spatial dimension that needs to be covered. In general, for an N-dimensional problem where the wave velocity of the rock is known and constant, a minimum of N-1 sensors is required in the array. In the case of a cylindrical rock specimen, at least four sensors are necessary to accurately locate sources within the rock volume. For the majority of triaxial loading experiments reported in this thesis, nine piezoelectric sensors are used.

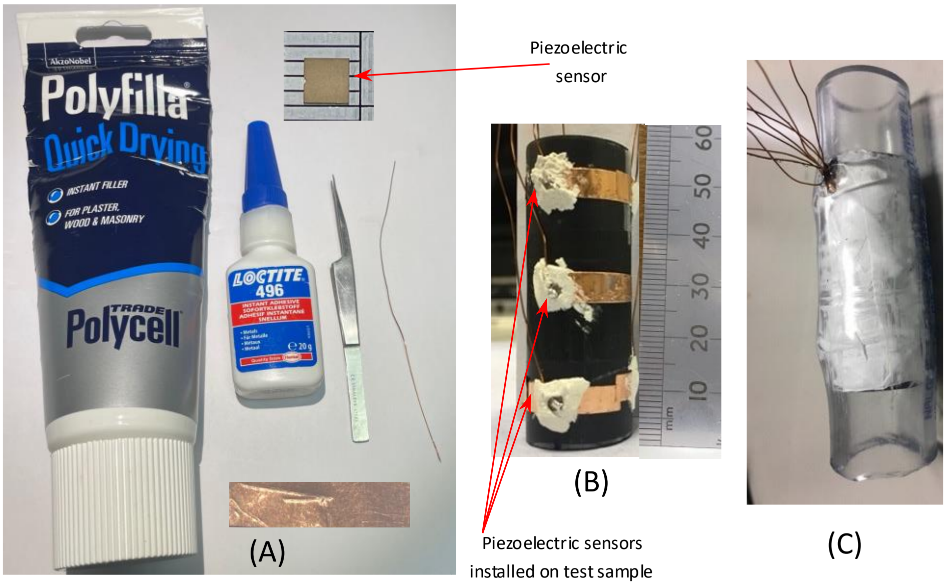

Figure 2.11. A) Sensor installation tools. B) Picture of sample with sensor installed. C) Sample jacketed in PVC and sensor lead wires extracted.

The installation process for piezoelectric sensors involves several steps (Figure 2.11). First, a piezoelectric sensor is glued onto a thin copper sheet using Superglue. The copper sheet serves as the ground connection for the sensors. Then, a layer of Polyfilla is applied to the test specimen where the sensor will be attached. The Polyfilla layer acts as a support, filling the gap between the flat edge of the sensor plate and the curved surface of the cylindrical sample. Next, the copper sheet with the sensor glued on is placed on top of the Polyfilla layer and pressed firmly. This action spreads the Polyfilla layer underneath and fills the gap between the flat end of the sensor and the curved surface of the test sample (Figure 2.11B). Once the Polyfilla sets, the copper sheets are arranged in a local grid pattern, allowing a single channel to be used as a common ground connection for the entire sensor network.

To connect the sensors, a single-threaded anodized wire is soldered directly onto the upper face of each piezoelectric sensor. The wire is then extracted through a hole in the PVC jacket (Figure 2.11C). The other end of the anodized wire is soldered onto the sample assembly feedthrough channel and passed out of the pressure vessel through the feedthrough, ultimately connecting to the data acquisition system.

2.4 Bulk density measurement

The bulk density of the sample is measured using the buoyancy method (ASTM, 2009). In this method, a dry mass of the sample m_s is weighed using an electronic balance under ambient conditions. The sample is then suspended to a thin wire and immersed in a beaker containing water of known density ρ_f (Figure 2.12). The change of mass of the beaker and water is measured upon immersion of the sample. The measured change of mass (m_f) is proportional to the volume of the displaced fluid (i.e., the volume V_s of the immersed sample), which can be computed as $V_s = m_f/\rho_f$. Finally, the density of the sample is calculated as $\rho_s = \frac{m_s}{V_s} = \frac{m_s}{m_f} \times \rho_f$.

For this measurement, distilled water with a density $\rho_f = 1.0 \text{ g } cm^{-3}$ was used. The volume of the suspension wire is considered negligible in this calculation. The resolution of the balance used is 0.1 g. The measurement error is estimated by taking into account the upper and lower bounds of the resolution of the measurement devices used.

$$\text{Upper bound, } \rho_u = \frac{m_s\, reading + device\ resolution}{m_f\, reading - device\ resolution},$$

$$\text{Lower bound, } \rho_l = \frac{m_s\, reading - device\ resolution}{m_f\, reading + device\ resolution},$$

$$\text{Error} = \pm\left(\frac{\rho_u - \rho_l}{2}\right)$$

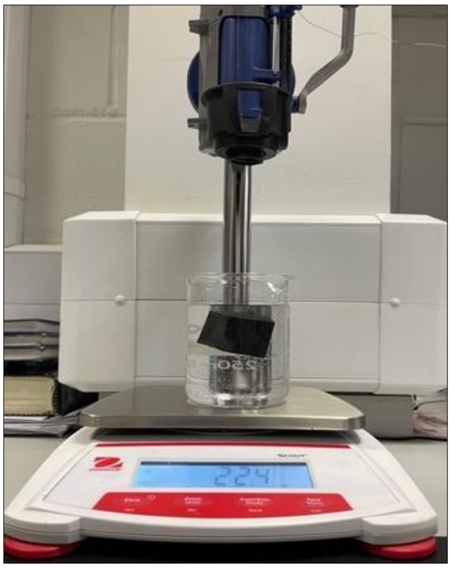

Figure 2.12. Density measurement setup. The picture shows a test sample suspended in distilled water and placed on a digital scale. This setup allows for the measurement of the sample's mass in the fluid to determine its density.

2.5 Benchtop ultrasonic velocity measurement

2.5.1 Measurement setup

Benchtop (room temperature and pressure) ultrasonic velocity measurements were made using the classical ultrasonic pulse transmission technique (Birch, 1960; Culshaw, 2015). This technique involves sending a high-frequency pulse through the rock sample and measuring the time it takes for the wave to travel a known distance, which corresponds to the distance between the pulse and receiver sensors. It assumes straight ray paths for the propagation of the wave in the medium. The measurement setup consists of a transducer assembly, a pulse generator, an amplifier, and a signal recording unit. Figure 2.13 shows a schematic illustration of the measurement setup.

The active electromechanical converter used is a lead zirconate titanate piezoceramic (PZT) transducers (manufactured by Boston Piezo-Optics Inc). The compressional (P) wave transducers are 10-mm-diameter semi-circular discs with a thickness of 1.4 mm. The shear (S) wave transducers are 10-mm-diameter semi-circular discs with a thickness of 0.6 mm. Both compressional and shear wave transducers have a central resonant frequency of 1.5 MHz. The polarization direction of the shear wave transducer is indicated with white lines engraved on the transducer’s surface (Figure 2.14a).

Thin copper sheets with thickness of $50\ \mu m$ were placed beneath and on top of the transducers. These copper sheets acted as electrodes for the transducers. A pair of P- or S-wave transducers, consisting of one transmitter and one receiver, were attached on opposite faces of the test specimen, and held tightly in place by a clamp, as illustrated in Figure 2.13. Insulated electrical wires were soldered to the electrodes and connected to the pulser/receiver PAD unit. The pulser PAD was connected to a pulse generator, while the receiver PAD was connected to Richter Unit. The Richter Unit acted as an analogue-to-digital converter (ADC), digitizing the signal at 16 bits resolution. The waveform was then sampled at a rate of 10 MHz. All waveforms were transferred to a computer running InSite-Lab software and stored for processing.

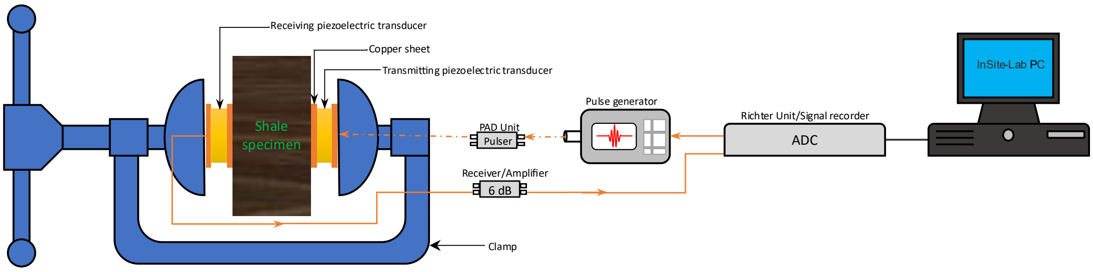

Figure 2.13. Schematic illustration shows the setup for ultrasonic wave velocity measurements. Not to scale.

In the measurement sequence, a sinusoidal pulse is generated by a pulse generator with a peak-to-peak amplitude of 400 V and a frequency of 1 MHz. The pulse is then converted into a P-wave or S-wave perturbation, depending on the transmitting transducer used. This perturbation is transmitted through the test sample. As it propagates through the sample, the perturbation is received by a receiving transducer. The receiving transducer converts the received perturbation into an electrical signal, which is then amplified with a gain of 6 dB (equivalent to 2 times the input amplitude). This amplified signal is digitized by the Richter Unit, an analogue-to-digital converter (ADC) and sampled at 10 MHz.

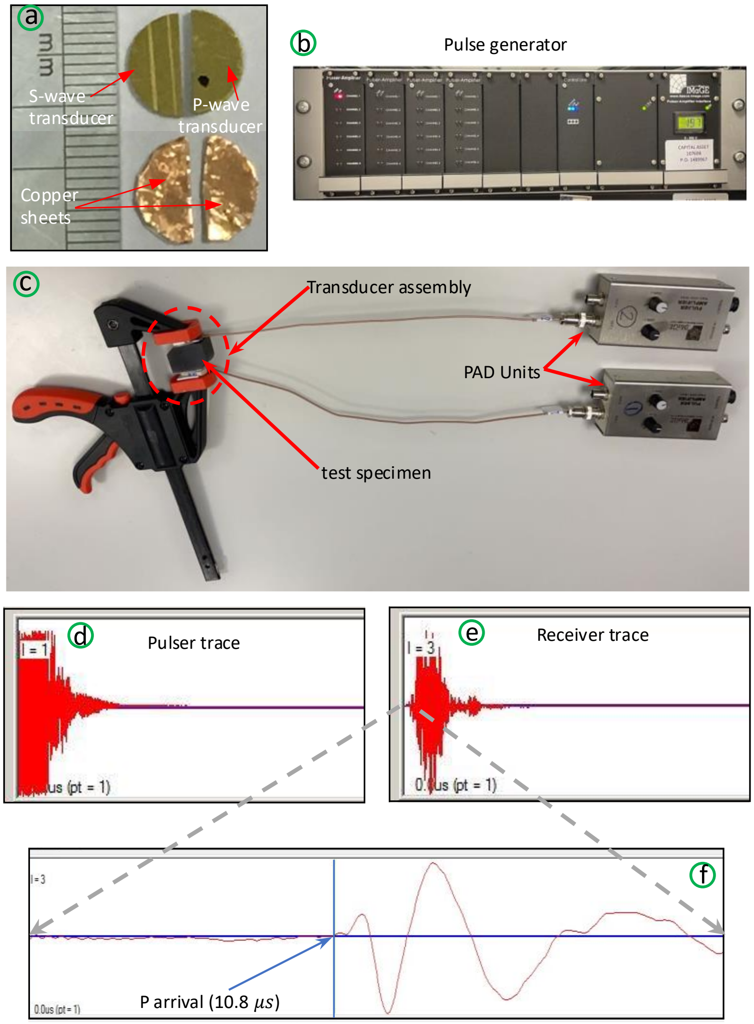

Figure 2.14. Ultrasonic wave velocity measurement setup.

Both the transmitted and received waveforms are recorded by the InSite-Lab PC on the same time basis (Figure 2.14d-e). To determine the transit times of the P-wave or S-wave, the first extremum value of the digitized waveforms is manually picked (Figure 2.14e-f). Finally, the velocity is calculated as the ratio between the length of the wave path and the transit time.

2.5.2 Dynamic moduli calculation

To obtain a full set of dynamic elastic moduli, I measure wave velocities in several strategic directions relative to the axis of symmetry of the shale material. Shales can be approximated as vertically transverse isotropic (VTI) materials, both under in situ and ambient conditions (Johnston and Christensen, 1995; Vernik and Liu, 1997; Hornby, 1998; Sondergeld and Rai, 2011; Horne, 2013). To fully characterize a VTI medium, at least five independent velocities are required. These include two P-wave velocities (Vp) with polarization in the vertical and horizontal direction, two S-wave velocities (Vs) with polarization in the vertical and horizontal direction, and an additional velocity at an oblique angle. This additional velocity is usually denoted as Vp(45), where 45 is the angle between the polarization direction and the horizontal plane.

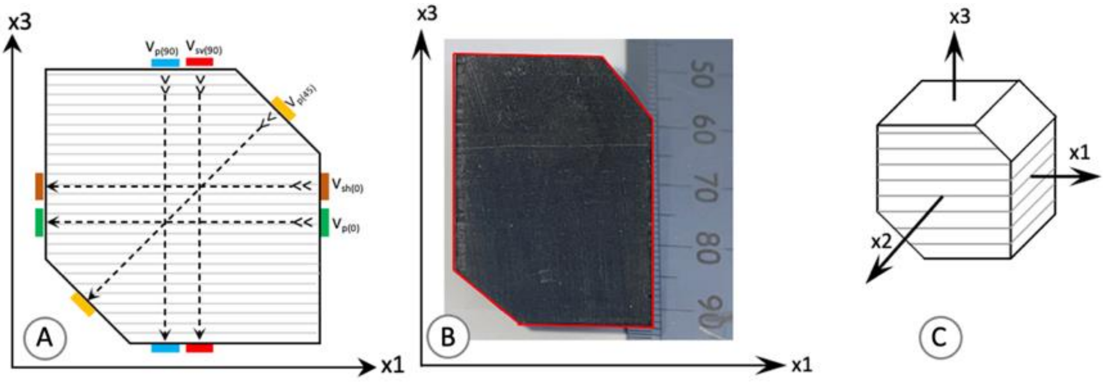

Figure 2.15. A) Schematic diagram showing the location of five pairs of piezoelectric transducers on the sample. The subscripts indicate the direction with respect to the bedding plane (grey horizontal lines). The dashed lines represent the direction of wave propagation. B) Picture of test specimen cut into prism. C) Schematic of a VTI rock with a presumed axis of rotational symmetry parallel to the x3. The oblique orientation measurements are taken at a 45° angle to the x1-x2 plane.

Our shale samples (Figure 2.15 B) were machined into prism-like geometries where the opposing faces allow wave propagation along the vertical and horizontal directions, as well as at an oblique angle. Each opposing face of the prism is carefully ground parallel to within 1 mm and polished with fine sandpaper to ensure proper transducer adhesion. This specific geometry, adapted from Wong et al. (2008), differs from the conventional cylindrical cores typically used for measuring the dynamic properties and anisotropy of rocks. However, it offers several advantages. One key advantage is that the transmitting and receiving piezoelectric transducers always directly face each other across the sample. This approach eliminates the need to conduct measurements on differently oriented samples typically required for characterizing the dynamic properties of a transversely isotropic rock. An additional advantage of measuring five velocities on a single sample is the minimization of errors that may arise from differences between two supposedly similar samples in terms of lithology, and physical state (such as stress, hydration, and saturation histories since recovery).

Figure 2.15 C shows a reference frame where x1-x2 represents the horizontal bedding plane. X3 is the axis of symmetry for the transversely isotropic cubical shale sample. In this reference frame, I measure three compressional velocities (V_P) and two shear velocities (V_S) in three different directions. The velocities are referenced with respect to the bedding plane, i.e., $V_P(0)$ for the bedding-parallel compressional velocity, $V_P(45)$ for the compressional velocity at a 45-degree angle to the bedding, $V_P(90)$ for the bedding-perpendicular compressional velocity, $V_{SH}(0)$ for the horizontally polarized, bedding-parallel shear velocity, and $V_{SV}(90)$ for the vertically polarized bedding-parallel shear velocity (Figure 2.15).

The five independent velocities obtained from the measurements can be readily converted into elastic stiffness coefficients, as demonstrated by various authors (Dewhurst and Siggins, 2006; Sarout and Guéguen, 2008; Chan and Schmitt, 2015). The relationship between velocities and elastic constants is described by the following equations.

$$\begin{aligned} c_{11} &= \rho V_{p0}^2 \\ c_{33} &= \rho V_{p90}^2 \\ c_{44} &= \rho V_{sv90}^2 \\ c_{66} &= \rho V_{sh0}^2 \\ c_{13} &= -c_{44} + \left[\left(c_{11} + c_{44} - 2\rho\, V_{p45}^2\right) \times \left(c_{33} + c_{44} - 2\rho V_{p45}^2\right)\right]^{0.5} \end{aligned} \tag{1}$$

where ρ is sample density; $c_{12} = c_{11} - 2c_{66}$, referring to the orientation of axes with respect to the symmetry of transversely isotropic medium. The independent stiffness coefficient, C_{ij} can be uniquely related to the five classical engineering elastic constants of a transversely isotropic medium (Meléndez-Martínez and Schmitt, 2016), as shown below

$$\begin{aligned} E_1 &= c_{11} + \frac{c_{13}^2(-2c_{11} + c_{12}) + c_{12}(-c_{33}c_{12} + c_{13}^2)}{c_{33}c_{11} - c_{13}^2} \\ E_3 &= c_{33} - \frac{2c_{13}^2}{c_{11} + c_{12}} \end{aligned} \tag{2}$$

$$\begin{aligned} \nu_{33} &= \frac{c_{12}c_{33} - c_{13}^2}{c_{11}c_{33} - c_{13}^2} \\ \nu_{31} &= \frac{c_{13}(c_{11} - c_{12})}{c_{11}c_{33} - c_{13}^2} \\ \nu_{13} &= \frac{c_{13}}{c_{11}+c_{12}} \end{aligned} \tag{3}$$

where $E1$ is the horizontal Young's modulus, $E3$ is the vertical Young's modulus, ν_{33} is the Poisson's ratio for the vertical strain induced when applying a vertical directed uniaxial stress, ν_{31} is the Poisson's ratio for the horizontal strain induced when applying a vertical directed uniaxial stress and ν_{13} is the Poisson's ratio for the vertical strain induced when applying a horizontal directed uniaxial stress.

2.5.3 Anisotropy parameters calculation

Anisotropy is defined as variation of a physical property depending on the direction in which it is measured. In the case of a vertically transverse isotropic (VTI) medium, Thomsen parameters are commonly used to characterize the anisotropy (Thomsen, 1986). The Thomsen parameters (epsilon, gamma, and delta) are defined by the equations

$$\varepsilon = \frac{c_{11}-c_{33}}{2c_{33}},$$

$$\gamma = \frac{c_{66}-c_{44}}{2c_{44}}, \qquad (4)$$

$$\delta = \frac{(c_{13}+c_{44})^2-(c_{33}-c_{44})^2}{2c_{33}(c_{33}-c_{44})}$$

Parameters ε and γ reflect the fractional differences in P- and S-wave velocities between vertical and horizontal directions. In contrast, parameter δ does not have a clear physical interpretation and tends to dominate the near-vertical P wave response for weakly anisotropic material. Laboratory measurements of shale anisotropy consistently demonstrate that Thomsen parameters ε and γ are almost always positive and exhibit strong correlations with each other. Parameter δ can have both positive and negative values and tends to scatter within a relatively narrow limit around zero. It does not show a clear correlation with ε or γ.

2.5.4 Error estimation

To estimate the relative error in the elastic stiffness coefficient (C) measurement, I follow an analysis similar to that used by Hornby (1998) and Yin (1992). In this method, the error is estimated by decomposing the measured parameter to its constituents using partial derivatives. These derivatives allow the evaluation of the sensitivity of the measured parameter to variations in constituents' measurement. For the elastic stiffness coefficient (C) measurement, it requires measuring the velocity (V) and the density (ρ) of the medium. To measure the velocity (V) of an elastic wave in a medium, it involves determining both the time-of-flight t and the distance travelled(L). Similarly, for measuring the density (ρ), it requires measuring the mass (m_s) and volume (v) of the rock sample ($v = m_f$, where m_f is the mass of the sample suspended in fluid of density 1 g cm^{-3}, as described in section 2.4).

To quantify the systematic relative error $\left(\frac{\Delta C}{C}\right)$ in the measurement of C, partial derivatives are taken. The error $\frac{\Delta C}{C}$ can then be derived from these partial derivatives

$$C = \rho V^2 \Rightarrow \frac{\Delta C}{C} = \sqrt{\left(\frac{\Delta\rho}{\rho}\right)^2 + \left(\frac{2\Delta V}{V}\right)^2},$$

$$V = \frac{L}{t} \Rightarrow \frac{\Delta V}{V} = \sqrt{\left(\frac{\Delta L}{L}\right)^2 + \left(\frac{\Delta t}{t}\right)^2},$$

$$\rho = \frac{m_s}{v} = \frac{m_s}{m_f} \Rightarrow \frac{\Delta\rho}{\rho} = \sqrt{\left(\frac{\Delta m_s}{m_s}\right)^2 + \left(\frac{\Delta m_f}{m_f}\right)^2},$$

From the above we have

$$\frac{\Delta C}{C} = \sqrt{\left(\frac{\Delta m_s}{m_s}\right)^2 + \left(\frac{\Delta m_f}{m_f}\right)^2 + \left(\frac{2\Delta L}{L}\right)^2 + \left(\frac{2\Delta t}{t}\right)^2} \ldots\ldots\ldots\ldots\ldots.\ldots(5)$$

The level of decomposition of sources of error in this context is somewhat arbitrary as it relies on our ability to estimate each individual component. Equation (5) indicates that $\frac{\Delta L}{L}, \frac{\Delta t}{t}$, and $\frac{\Delta m}{m}$ are the fundamental components of the measurement chain. Therefore, we can estimate the accumulated error by considering the smallest and largest errors in each component. Length measurements are carried out using a digital calliper with a resolution of 0.01 mm. The range of lengths measured is from 15 to 38 mm. Therefore, the error in length measurements is

$$\left(\frac{\Delta L}{L}\right)_{min} = \frac{0.01}{38} \; and \; \left(\frac{\Delta L}{L}\right)_{max} = \frac{0.01}{15}$$

The error in the mass measurement is determined by the laboratory scale used, which has a resolution of 0.1 g. For the dry samples, the range is 15 to 100 g, while for samples suspended in fluid, it is 7 to 45 g.

$$\left(\frac{\Delta m_s}{m_s}\right)_{min} = \frac{0.1}{110} \; and \; \left(\frac{\Delta m_s}{m_s}\right)_{max} = \frac{0.1}{15}$$

$$\left(\frac{\Delta m_f}{m_f}\right)_{min} = \frac{0.1}{45} \; and \; \left(\frac{\Delta m_f}{m_f}\right)_{max} = \frac{0.1}{7}$$

Finally, the relative error in picking the arrival time of an elastic wave depends on several factors: (i) the type of polarization of the P or S wave, (ii) the direction of propagation in the anisotropic medium, and (iii) the physical state of the environment. The error in the picking of arrival time is taken as equal to the sampling frequency (Δt) in the measurements, which is 10 MHz (or 0.1 µs). During the tests, the typical flight times ranged from $t_{min} = 6\ \mu s$ to $t_{max} = 15\ \mu s$. Hence, the range of relative errors in the time of arrival would be:

$$\left(\frac{\Delta t}{t}\right)_{min} = \frac{0.1}{15} \; and \; \left(\frac{\Delta t}{t}\right)_{max} = \frac{0.1}{6}$$

Combining the results shown above, I can estimate the upper and lower bounds of the relative error $\frac{\Delta C}{C}$ as

$$\left(\frac{\Delta C}{C}\right)_{min} = 1.4\%\ and\ \left(\frac{\Delta C}{C}\right)_{max} = 4\%$$

The most unfavourable case of maximum error is particularly linked to the modulus C13 calculated from $V_p(45^\circ)$. Indeed, among the five typical signals transmitted during the experiments, it is that of $V_p(45)$ which is of poorer quality (lowest signal/noise ratio), and therefore likely to be the least precise.

2.6 Acoustic emissions (AE) data acquisition system

An acoustic emission (AE) data acquisition system is a setup used to detect and record acoustic emission signals generated by rocks under stress or deformation. It consists of various components designed to detect, amplify, digitize, and record the AE signals. Figure 2.16 shows a schematic of the main stages of AE acquisition and processing. This section describes the hardware and techniques used to acquire and process AE data.

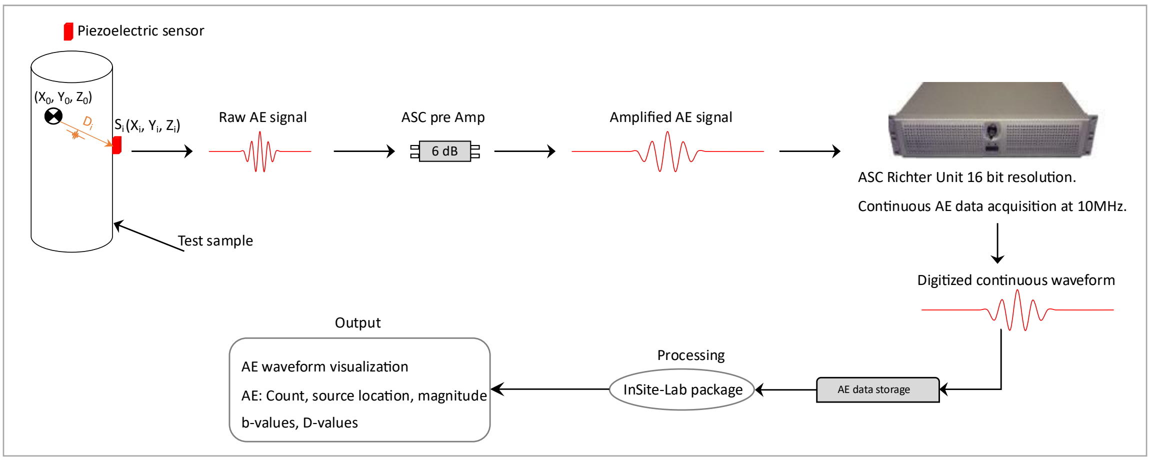

Figure 2.16. AE data acquisition setup. Not to scale. Indicated on the test sample is a sensor S_i at location (X_i, Y_i, Z_i), distance D_i from the sensor S_i to an AE source location with the coordinates (X_0, Y_0, Z_0).

2.6.1 Continuous data acquisition

There are two types of acquisition systems for acquiring AE signals: trigger systems and continuous systems. Trigger systems employ a predefined criterion to initiate acquisition. For instance, if four or more channels record a voltage exceeding 100 mV within a window length of 256 sample points (equivalent to 25.6 µs), a waveform of 512 data points is acquired (25% before the trigger and 75% after it) and saved for each channel in a file. This system is ideal for slow loading rate experiments that take a longer time. However, when the event occurrence rate exceeds the capture rate capability of the recording system, without additional measures, information loss may occur.

Continuous systems, on the other hand, operate by continuously streaming the AE signal at a predetermined sampling rate. This acquisition system offers several advantages: (1) data is always available in its raw form for reprocessing, and (2) there is no missing data for the entire recording time interval. For typical triaxial deformation experiments lasting from 1 to 4 hours, nearly 2 TB of data was recorded, posing challenges for long-term storage. For all the experiments described in this thesis, the continuous system was utilized for data acquisition.

The acquisition system used in this study consists of six Richter units and nine pre-amplifiers known as Pulser Amplifier Desktops (PADs) (Figure 2.17). The Richter units, designed and manufactured by Applied Seismology Consultants (ASC), offer a dynamic range of 10 V. Each Richter unit can sample four channels at a resolution of 16 bits and a sampling rate of 10 MHz. When an incident AE wavefront interacts with an AE sensor, the piezoelectric element undergoes mechanical deformation, inducing a variation in its output voltage. All piezoelectric elements used in this research were made of lead zirconate titanate (PZT), as described in Section 2.3.3.

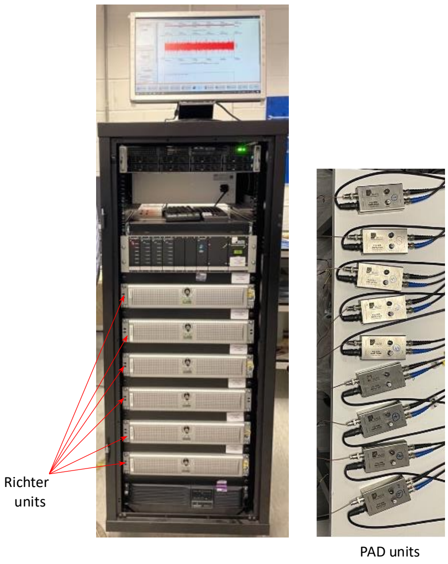

Figure 2.17. Picture of the AE data acquisition system.

Initially, the incoming signals from the AE sensors are transmitted via shielded cables to a PAD where they are amplified by 6 dB. Typically, preamplifiers have a built-in filter to remove unwanted noise. However, in this case, the filtering function is disabled, and all filtering is done post-recording. The amplified signals are then transmitted to the Richter units using shielded BNC to BNC cables. Subsequently, the Richter units digitize the signals at a resolution of 16 bits. Finally, the digitized signals are sampled at a rate of 10 MHz and continuously streamed and stored on a hard drive in HDF5 (.h5) format for further processing. To facilitate data handling, the data is stored in separate files, each with a duration of 30 seconds.

The acquisition system is operated using InSite-Lab software, proprietary to ITASCA. InSite-Lab is a comprehensive software package that includes specialized modules for continuous data streaming, post-acquisition processing, and visualization.

2.6.2 AE data processing

The acoustic emission (AE) data processing involves data formatting, filtering, procedures for extracting discrete AE events, calculating source locations, *b*-values, D-values calculations, and Vp estimation. The following sections describe the processing steps outlined.

2.6.2.1 Filtering and events harvesting

The raw, continuous dataset, stored as an .h5 digital file, is formatted using InSite-Lab software (Figure 2.18). This enables basic visualization of the data for each channel in both the time and frequency domain. The visualization serves two main purposes. Firstly, it allows initial data analysis for determining the failure time, which is crucial for data synchronization. Since the mechanical and AE data are recorded using different logging systems and at different sampling rates, time synchronization is necessary before further analysis can be conducted. Time synchronization is performed based on the macroscopic failure event time (see section 2.2.2). Once the time synchronization value is determined, it is applied to the mechanical dataset to correct the time offset. The time synchronization procedure is carried out using MATLAB.

The second purpose of visualization is to determine the background noise level and identify the frequency characteristics of electrical noise pulses across all channels. Based on this assessment, a bandpass filter is designed to suppress both high-frequency electrical pulses and low-frequency background noise. Through experimentation, a filter range of 200 kHz to 1.5 MHz is found to be the most effective for the experiments reported in this thesis.

After filtering, discrete events are harvested using a triggering algorithm implemented in InSite-Lab (Figure 2.18C). A trigger is activated when the signal amplitude exceeds 10% above the mean background noise level of 200 mV within a 10 µs window and is simultaneously detected on at least 3 channels. When these conditions are satisfied, a waveform of 1024 points (equivalent to 102.4 µs) is extracted and stored for further analysis. This waveform length ensures the complete capture of both the P-wave onset and its coda. The selected parameters represent a trade-off between sensitivity and data quality. All triggered events are manually reviewed, and any false positives (e.g., electrical noises) are discarded from further analysis. For each valid event, the P-wave arrival time is determined using an autopicking routine or manually (see the next section), and is subsequently used for source location analysis, as described in Section 2.6.2.2.

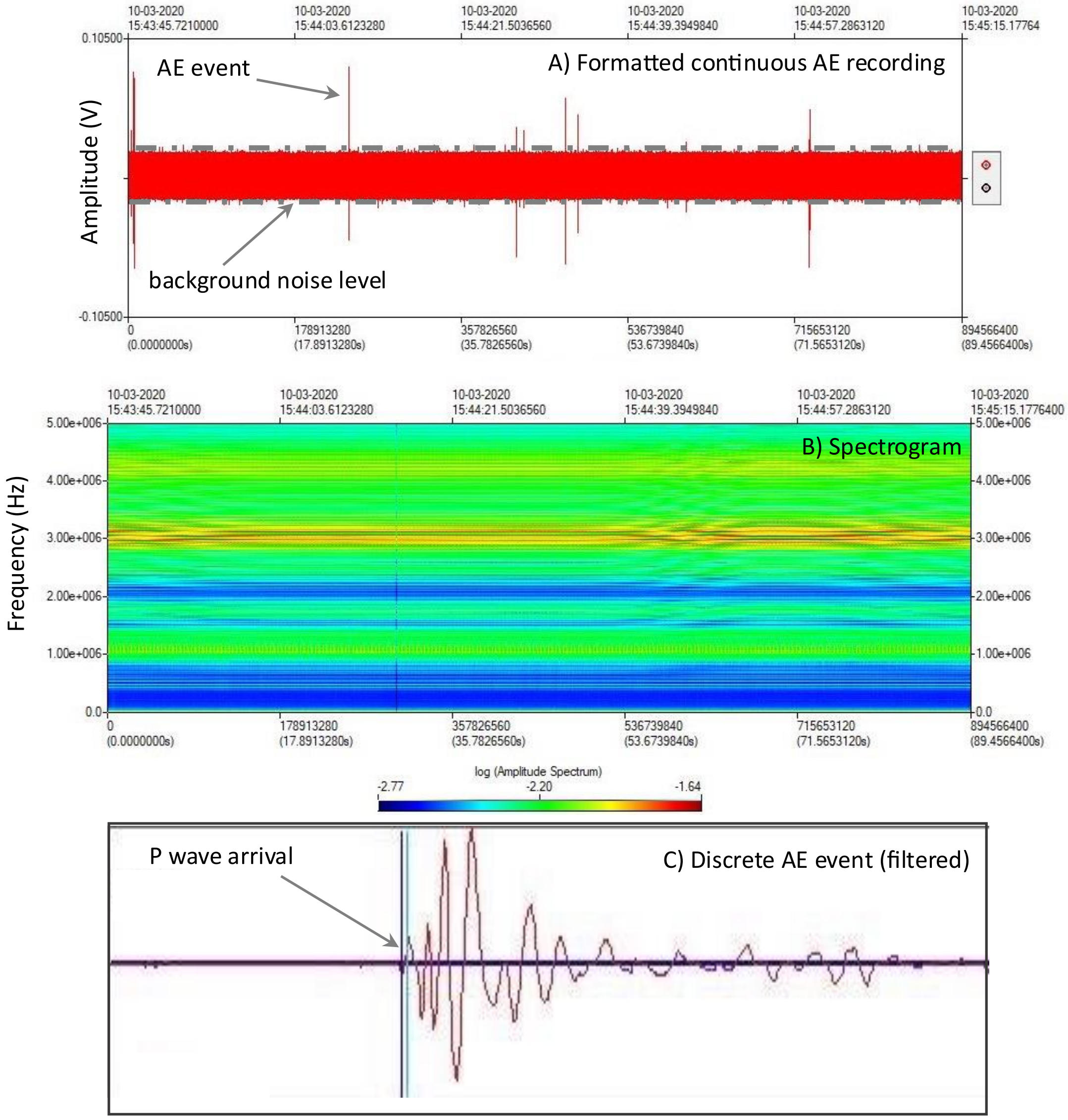

Figure 2.18. A) 90 seconds (3 files) of continuous data stream showing recorded AE events and the background noise level. B) Continuous data in the frequency domain enables the design of a filter to remove the background noise level. Refer to the text for explanation. C) A discrete event harvested and filtered. The blue line represents the arrival time of the P-wave.

2.6.2.2 AE source location

Acoustic emission source location analysis is one of the most frequently used techniques in AE studies (Goodfellow, 2015). By knowing the locations of the sensors and having information about the seismic velocities in the medium, the location of the microfracture source can be calculated with a certain level of certainty. In general, we have N AE sensors located around the rock specimen with known coordinates (X_i, Y_i, Z_i) as shown in Figure 2.16. For most of the experiments discussed in this thesis, I use 9 AE sensors (i = 1 - 9).

The measured arrival time of the P-wave (T_i^M) at sensor i, is picked using an autopicking algorithm for each channel. The algorithm operates by calculating the square mean root (RMS) of the waveform using a moving window approach. At every data point, i, of the waveform, two windows are generated: a front window and a back window. The value of the auto-picking function, F_i, is calculated by

$$F_i = \frac{\sum_{j=i+1}^{i+NF} A_j^n}{\sum_{j=i-1}^{i-NB} A_j^n} \quad (6)$$

where A_j is the amplitude, NF, is the length of the front-window in data points, NB, is the length of the back-window in data points and $n = 2$.

The autopicking function represents a difference in energy contained in the front window compared to the back window. Peaks occur in the function where waveform signals suddenly increase in amplitude relative to data behind it (Figure 2.18 C). These peaks can then be used to estimate the arrival time of the different phases. The P-wave arrival can often be picked with high certainty as it emerges from just a background noise level. However, for some events in certain channels, the algorithm mis-picks the arrival time, which has to be adjusted manually.

The P-wave velocity within the medium is measured under ambient conditions, as discussed in section 2.5. These measurements are used to construct the velocity structure of the medium. In shales, the velocity structure can be approximated as transversely isotropic with

$$V = \frac{(Vaxial + Vradial)}{2} - \frac{(Vaxial - Vradial)}{2} cos(180 - 2\theta) \quad (7)$$

where $Vaxial$ is the velocity along the axis of symmetry. $Vradial$ is the velocity perpendicular to the axis of symmetry and is calculated using $V_{radial} = \alpha V_{axial}$, where α is the anisotropy factor. θ is the angle between axis of symmetry and ray path.

In our shale samples, V_{axial} is P wave velocity in the vertical direction (along the axis of symmetry) and V_{radial} is the velocity in the horizontal plane (refer to schematic diagram in Figure 2.15 for reference). Since the P-wave velocity is known, only four unknowns are left in the AE source location estimation, namely source location coordinates (X_0, Y_0, Z_0) and the source time T_0. This problem can be solved by the following steps. First, the distance D_i, between an AE source with coordinates (X_0, Y_0, Z_0) and any sensor at the sample surface with coordinates (X_i, Y_i, Z_i) is given by

$$D_i = \sqrt{(X_0 - X_i)^2 + (Y_0 - Y_i)^2 + (Z_0 - Z_i)^2} \quad (8)$$

and the velocity along any source-receiver ray path is represented by equation

$$V_i = \sqrt{\frac{V^2{}_{radial}(X_0 - X_i)^2 + V^2{}_{radial}(Y_0 - Y_i)^2 + V^2{}_{axial}(Z_0 - Z_i)^2}{(X_0 - X_i)^2 + (Y_0 - Y_i)^2 + (Z_0 - Z_i)^2}} \qquad (9)$$

The P wave travel time between the source (X_0, Y_0, Z_0) and sensor (X_i, Y_i, Z_i) is calculated using equations

$$dT_i = \frac{D_i}{V_i}$$

$$dT_i = \frac{(X_0 - X_i)^2 + (Y_0 - Y_i)^2 + (Z_0 - Z_i)^2}{\sqrt{V^2 radial(X_0 - X_i)^2 + V^2 raial(Y_0 - Y_i)^2 + V^2 axial(Z_0 - Z_i)^2}} \tag{10}$$

The theoretical arrival time of the P wave at any sensor is calculated by equation

$$T_i^T = T_0 + \frac{(X_0 - X_i)^2 + (Y_0 - Y_i)^2 + (Z_0 - Z_i)^2}{\sqrt{V^2 radial(X_0 - X_i)^2 + V^2 raial(Y_0 - Y_i)^2 + V^2 axial(Z_0 - Z_i)^2}} \qquad (11)$$

where T_i^T is the theoretical P wave arrival time and T_0 is the source time. The residual time (T_{res_i}), which is the difference between the theoretical (T_i^T) and measured (T_i^M) arrival times, is calculated from equation

$$T_{res_i} = \left|T_i^M - T_i^T\right| \qquad (12)$$

Lastly the sum of all residual times (T_{res}) is calculated from equation

$$T_{res} = \sum_{i=1}^{N} \left|T_i^M - T_i^T\right| \qquad (13)$$

I proceed to find a set of X_0, Y_0, Z_0 , and T_0 that minimizes T_{res} . To solve this minimization problem, I utilized the downhill simplex method implemented in the InSite-Lab software. The Downhill Simplex Method (Nelder and Mead, 1965) is an iterative procedure that searches the error space to locate the minimum. It employs a geometrical shape called a Simplex, which, in three dimensions, can be visualized as a tetrahedron with each vertex defined by its spatial coordinates (x, y, z). At each vertex, the error space is calculated and based on the relative values of the error space, the simplex is instructed to move or contract for the next iteration. In this manner, the simplex moves around the error space until it converges to a minimum.

In InSite-Lab, the Simplex algorithm is implemented through a series of steps designed to ensure accurate and reliable source location results. A vertically transversely isotropic (VTI) velocity model is used. The algorithm requires input parameters including P-wave arrival times (picked either automatically or manually, as described earlier), the P-wave velocity in the shale measured at room temperature and pressure (see next section for details), the anisotropy factor, and a tolerance value. This tolerance defines the fractional change in the error space across the Simplex at which the algorithm stops iterating.

An outlier identification procedure is then applied to remove arrivals with the highest error above an error threshold defined by the Arrival Error Factor. The is based on the residual difference between the measured and theoretical travel times from the source to each sensor. If a sensor's arrival error exceeds the threshold, it is excluded from the location algorithm. The process repeats until no remaining arrivals exceed the threshold, at which point the location solution is considered final. Source locations computed using fewer than six independent arrivals are discarded.

For each located AE event, the algorithm calculates the RMS error using only the sensors included in the final location (Manual, 2019). The average hypocentre location error across the dataset is estimated at ±3 mm, based on an average of six sensors per event. This estimate is obtained by multiplying the P-wave velocity and its uncertainty ($\sim$ 2%) by the RMS of the time residuals between the measured and theoretical arrival times, averaged over the number of sensors used. The error accounts for uncertainties in first arrival picking and sensor position measurements.

2.6.2.3 Ultrasonic velocity estimation

For the procedure described in the previous section, the P-wave velocities measured at ambient conditions were used as inputs for source location calculations. Although our experiments are conducted under confinement pressure, the use of P-wave velocities and anisotropy parameters measured at ambient conditions is justified for these particular shales. Experimental measurements show that the dependence of P-wave velocity on confinement pressure is primarily controlled by factors such as porosity, microfracture density and loading orientation, rather than the pressure itself (Dewhurst et al., 2011; Bonnelye et al., 2017a).

For example, Vernik and Nur (1992) conducted extensive laboratory measurements on Mississippian-Devonian shales with porosities less than 4%. They observed two distinct behaviors in P-wave velocity. The first behavior showed little sensitivity to confinement pressure, while the other exhibited a significant increase in P-wave velocity with increasing confining pressure. They concluded that the insensitivity and velocity increase are influenced by microfracture density in the shales.

Sarout and Guéguen (2008) performed measurements on Callovo-Oxfordian shales (47.4% clay, porosity about 10%) and reported that gamma and delta were almost insensitive to pressure. However, the epsilon value decreased from 0.5 (ambient measurement) to 0.37 (at 55 MPa confinement). Dewhurst and Siggins (2006) reported an increase in P-wave velocity measured parallel to the bedding plane for Muderong shale (65% clay, 17% porosity) with increasing mean effective pressure. The velocity was found to increase by approximately 17% for a mean effective pressure increase from 5 to 60 MPa. On the other hand, Sarout et al. (2007) reported a decrease in P-wave velocity measured parallel to bedding as a function of axial stress, indicative of deformation, for Callovo-Oxfordian shale at a confining pressure of 15 MPa. It decreased by approximately 6% at peak stress (50 MPa). In our samples, which consist of clay-rich, quartz/carbonate-rich and quartz-rich shales with a porosity of 5% (Dong et al., 2015), the influence of confinement pressure on P-wave velocity is expected to be minimal.

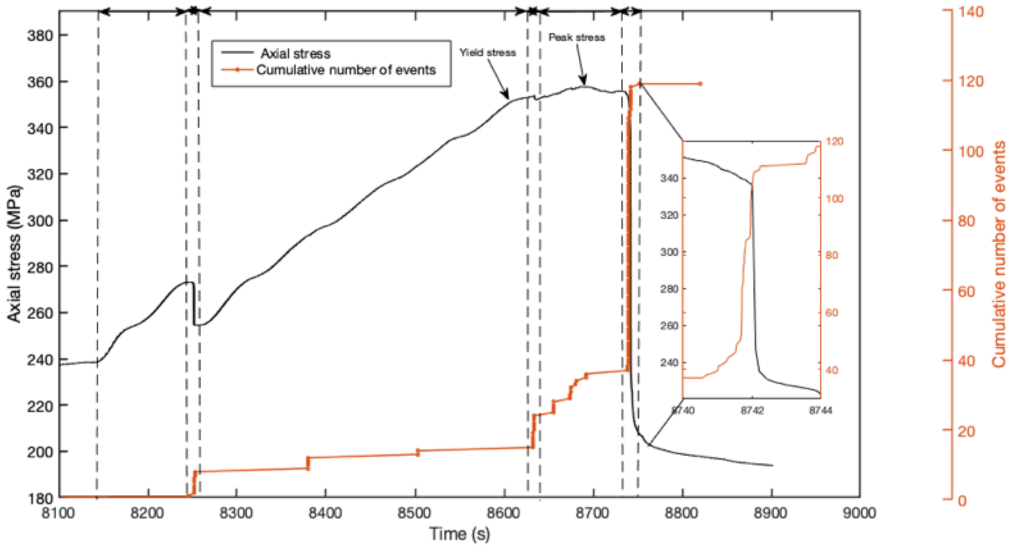

Figure 2.19. An example of a triaxial experiment shows identified deformation stages. The cluster of events recorded at each stage is used to estimate the P-wave velocity. Further details about this experiment are presented in Chapter 4.

Since the source location algorithm provides an RMS error for each located event (as discussed in the previous section), this information can be used to estimate the P-wave velocity at different stages of shale deformation. To do this, I select a cluster of AE events recorded during a particular deformation stage and vary the input velocity in increments of 5%, recalculating the source locations each time. Each recalculation yields a corresponding RMS error. The input velocity that results in the lowest RMS error is taken as the P-wave velocity of the shale at that deformation stage. The uncertainty in the estimated P-wave velocity is calculated based on the average location error, weighted by the average distance between the source location and the sensors used. Figure 2.19 illustrates a triaxial experiment in which different deformation stages are identified. The cumulative AE event count highlights clusters corresponding to each stage.

2.6.2.4 Seismic parameters calculation

For each located event, a relative magnitude — referred to as the Location Magnitude (M_L) — is calculated. For clusters of located events, both the b-value and fractal dimension (D-value) are subsequently estimated. The relative magnitude is specific to the sensor array configuration and is based on the amplitude of the recorded signal, weighted by the distance between each sensor and the event hypocentre. This weighted amplitude is then averaged over all the sensors used in the hypocentre calculation (equation 14). The Location Magnitude (M_L) is estimated within the Simplex algorithm in InSite-Lab using the following equation:

$$M_L = \log\left(\frac{\sum_{m=1}^{n}\left(W_{RMS_m}.d_m\right)}{n}\right) \qquad (14)$$

Where:

- W_{RMS_m} is the root mean square amplitude of the waveform at sensor m,
- d_m is the distance between the source location and sensor m,
- n is the number of sensors used in the location calculation.

The RMS of the waveform is calculated as: $W_{RMS} = \sqrt{\frac{\sum_{i=1}^{x} W_{mi}^2}{x}}$ (15)

Where: W_{mi} is the waveform amplitude on channel m at point i, x is the number of points in the waveform. The Location Magnitude provides a simple estimate of the relative magnitudes of events recorded using the same sensor array. It indicates the relative size of AE events but is not directly calibrated to their physical size.

The relative magnitude distribtion in my experiments can be desribed by the Gutenberg–Richter relation, characterised by an exponent *b* (Gutenberg and Richter, 1944). This b-value represents the relative proportion of large to small magnitude events in a catalogue and is estimated using the maximum likelihood method for a binned catalogue (Aki, 1965; Roberts et al., 2015):

$$b = \frac{\log_{10}(e)}{\bar{M}-\left(M_c-\frac{\Delta M}{2}\right)} \qquad (16)$$

Where:

- M_c is the magnitude of completeness, determined from the point of maximum curvature of the frequency-magnitude distribution (Gutenberg and Richter, 1944),
- $\overline{M}$ is the average magnitude of events with M $\geq M_c$,
- ΔM is the magnitude bin size, set to 0.1 following Roberts et al. (2015) and Marzocchi and Sandri (2003).

The standard deviation (uncertainty) in the b-value is estimated using the formulation of Shi and Bolt (1982), corrected for small sample sizes:

$$\sigma_b = 2.30b^2\sqrt{\frac{\sum_{i=1}^{n}(M_i-\overline{M})^2}{N(N-1)}} \tag{17}$$

Where:

- b is the b-value esitmated from equation (16),
- N is the number of events in the cluster,
- M_i are the individual magnitudes of the event.

Finally, a two-point correlation integral was estimated to examine the spatial clustering of the hypocentres of AE events. The two-point correlation is defined as

$$C(r) = \frac{2N_r(R<r)}{N(N-1)} \tag{18}$$

where $2N_r(R < r)$ represents the number of hypocentre pairs with separation distance less than r, and N is the total number of AE events analysed. If the hypocentre distribution is self-similar

$$C(r) \propto r^D$$

where D is the fractal dimension, corresponding to the slope of a least-squares fit to the linear portion of the log-log plot of $C(r)$ versus r (Figure 2.20). The D-value reflects the spatial distribution and clustering of events (Hirata et al., 1987). A D-value of 0 indicates that the events map onto a point; a value of 1 represents a linear distribution; 2 corresponds to a planar distribution; and 3 indicates a volumetric uniform distribution. The spatial resolution of fractal dimension maps is limited by location accuracy, geometric and boundary effects (Wyss et al., 2004; Kagan, 2007).

The uncertainty in D in these calculations is computed based on the uncertainty in the fit, without accounting for the uncertainties in hypocentre locations or in the estimate of the fitting range. As a results, the uncertainties estimated using this method are underestimated. A more comprehensive uncertainty estimate, incorporating epistemic contributions, would be larger but would also reflect a combination of different sources of uncertainty, including assumptions about hypocentre location errors and range estimates (Kagan, 2007). Thus, it is appropriate to report the formal errors of the fit. Because the differences in D discussed in this thesis are highly significant, they cannot be attributed to uncertainties in the estimation of D.

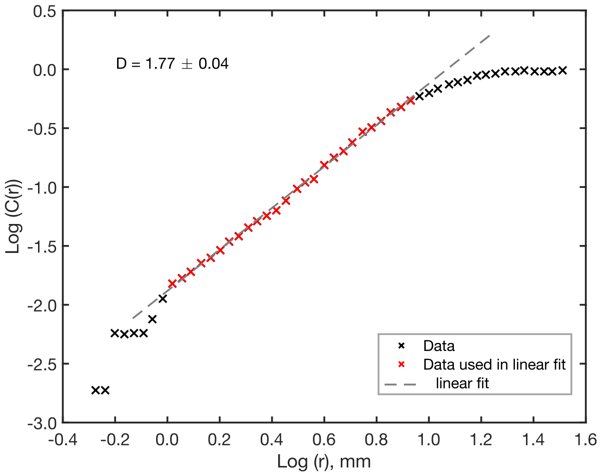

Figure 2.20. An example of a log-log plot of C(r) versus r. The D-value corresponds to the slope of a least-squares fit to the linear portion of the plot. The error represents the deviation of the slope at the end-member points of the AE events relative to the slope determined at the centre of the range.

2.7 Computed tomography (CT) data acquisition and processing

After the loading experiments, the broken samples were imaged using an X-ray computed tomography (CT) scanner. This technique employs X-rays to generate a 3D image of a sample by stacking cross-sectional 2D X-ray attenuation projections. This enables examination of fracture distribution, fault geometry, and the damage zone within the sample's volume. To maintain the condition of the deformed samples and minimize damage during scanning, they were wrapped in adhesive tape after extraction from the Triaxial loading apparatus.

The Phoenix Nanotom NF180 scanner was used for the scans. The scanner can operate at a maximum voltage of 180 kV, electric current of 0.5 mA, and has a maximum resolution of 0.5-1.0 microns. To achieve high-resolution images, the optimal scanning parameters were set based on the sample size and material type. The parameters used for these samples were 110-140 kV and a current of 190-240 μA. A total of 1440 2D images were taken per sample. The images have a voxel size of 300 × 300 × 300 μm with a resolution of 20 µm and were visualized using Avizo software.

The X-ray scans were conducted by staff at the Laboratory of Geoscience and Engineering, Faculty of Civil Engineering and Geosciences, Delft University of Technology, Netherlands. The CT scan data was synchronized with the AE data using ParaView. The visualization and synchronization were performed by the author.

3 Geomechanical properties and seismic anisotropy of Horn River shales

3.1 Introduction

The Horn River Basin (HRB), located in north-eastern British Columbia, Canada, is renowned for its rich shale gas resources (Schultz et al., 2020b). Hydraulic fracturing techniques have been used to extract hydrocarbon resources from these low-permeability, organic-rich shale rocks. However, HRB shale formations exhibit complex mechanical behaviour due to their anisotropic nature (Figures 3.1 and 3.2) (Dong et al., 2017b). They possess different strengths and stiffnesses along different orientations, which are linked to their mineral composition and diagenetic processes through their burial history (Figure 3.1). To facilitate effective hydraulic fracturing, it is essential to assess the orientation-dependent mechanical properties of the rock, such as Young's modulus and Poisson's ratio.

Additionally, HRB shales exhibit significant variation in elastic wave velocity anisotropies (Baird et al., 2017). The uppermost clay-rich formation of Fort Simpson displays significant anisotropy, while the organic-rich lower formations of Muskwa, Otter Park, and Evie are less anisotropic (Figure 3.2). These elastic wave velocities are important indicators of rock properties and can provide valuable insights into reservoir characteristics such as porosity, fracture distribution, and fluid saturation. Anisotropy also plays a crucial role in several geophysical techniques, including depth conversion for seismic exploration, imaging of subsurface structures, and amplitude variation with offset (AVO) analysis (Sayers et al., 2015). Therefore, detecting and characterizing anisotropy is crucial, as they strongly impact the analyses and interpretations of seismic surveys, sonic logs, and microseismic monitoring (Sone and Zoback, 2013).

Laboratory measurements of the geomechanical and anisotropic properties of shales are limited (Vernik and Nur, 1992; Johnston and Christensen, 1995; Hornby, 1998; Wang, 2002; Dewhurst et al., 2011). These studies demonstrate that shales are typically transversely isotropic (TI), with the degree of anisotropy dependent on factors such as porosity, clay content, organic matter, thermal maturity, and microfractures (Dewhurst and Siggins, 2006; Sone and Zoback, 2013). Furthermore, previous studies on HRB shales have provided valuable insights into their composition and geomechanical properties, particularly in understanding how factors such as clay content influence parameters like Young's modulus and Poisson's ratio (Figure 3.1). For instance, Dong et al. (2017b) evaluated the Young’s modulus and Poisson’s ratio using dipole sonic and density log data, revealing notable geographic and stratigraphic variations in both

Young's modulus and Poisson's ratio within HRB shales. They identified clay content as the primary controlling factor influencing the magnitude of these parameters.

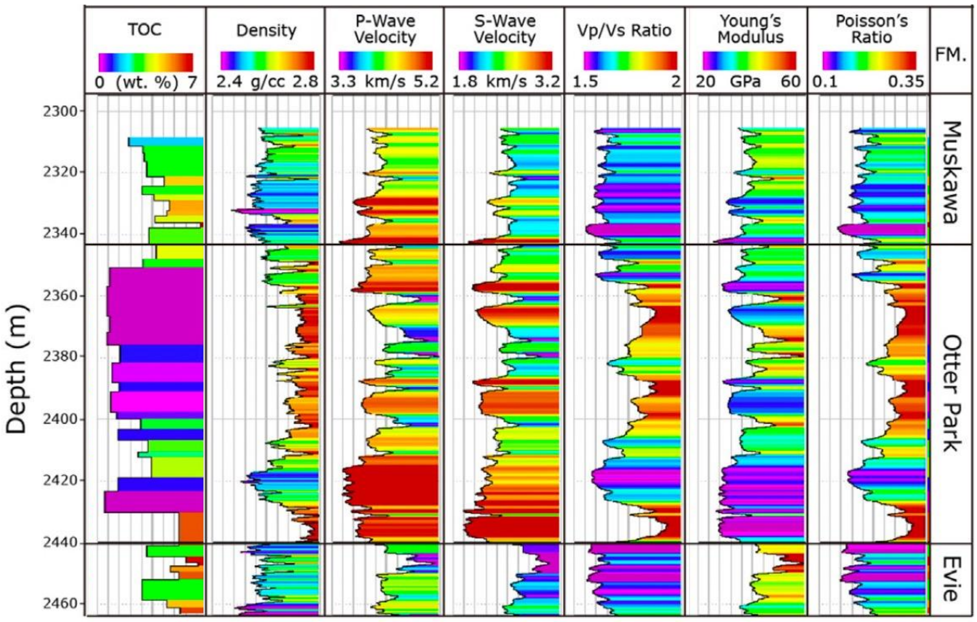

Figure 3.1. Parameters derived from well logs for reservoir formations. Elastic properties (Young's modulus and Poisson's ratio) were computed from V_p, V_s, and density logs. Total organic carbon (TOC) was measured from core samples. TOC curve shows approximate mirror image of the V_p/V_s curve. Adapted from Mo et al. (2018).

Moghadam et al. (2019) reported measurements of static and dynamic Young's modulus and Poisson's ratio, highlighting significant differences between the static and dynamic modulus values and the lack of a clear trend between dynamic and static Poisson's ratio. Similarly, Baird et al. (2017) investigated HRB shales anisotropy using S-wave splitting in a microseismic dataset. Their findings indicated a significant anisotropy in the Fort Simpson (Figure 3.2), primarily exhibiting vertical transverse isotropy (VTI) symmetry. They attributed a substantial portion of the observed anisotropy to the presence of aligned clays and emphasized the importance of limited hydraulic connectivity for VTI to occur. Additionally, Sayers et al. (2015) used kriged predictions of density, P-wave velocity, and S-wave velocity in vertical wells in the Horn River resource play, comparing them with measured logs to estimate anisotropy parameters.

Despite these valuable insights, a comprehensive laboratory determination of elastic stiffnesses and anisotropic parameters of HRB shales remains unavailable. Therefore, this study aims to bridge this gap by independently determining the full set of dynamic elastic stiffnesses, dynamic Young’s moduli, and the anisotropic parameters of HRB shales through ultrasonic wave velocity measurements. In addition, a subset of the samples is subjected to triaxial loading tests to determine the static Young’s modulus and mechanical strength. Subsequently, the laboratory data is analysed in the context of mineralogy, total organic carbon, and texture, to gain a better understanding of the impact of diagenetic processes on shale properties.

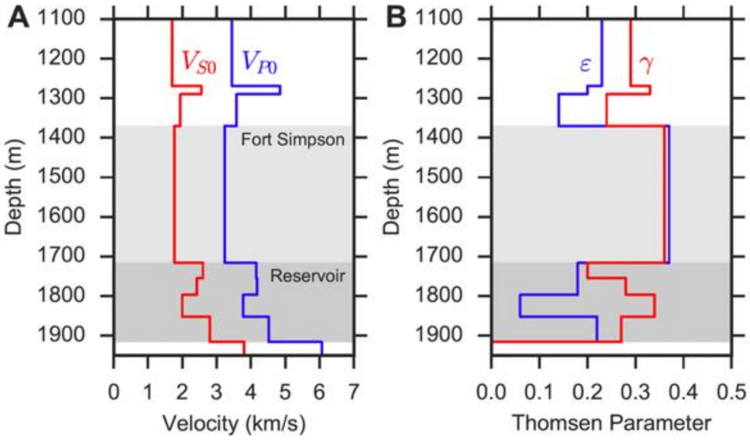

Figure 3.2. 1D anisotropic velocity model showing: (A) vertical V_P and V_S velocities, and (B) Thomsen’s anisotropic parameters (ε, γ). The Fort Simpson shale exhibits high anisotropy, with Thomsen’s parameter showing a sharp drop at the top of the reservoir formation (Muskwa) before recovering in the lower reservoir formations (Otter Park and Evie). Adapted from Baird et al. (2017).

This work sheds light on fundamental controls on the mechanics and physical properties of low porosity, fine-grained sediments. More specifically, the findings contribute significantly to the broader knowledge of shale gas reservoir characterization and provide valuable guidance for hydraulic fracturing operations in unconventional shale gas reservoirs.

3.2 Geological background

The Horn River Basin, spanning an area of approximately 12,000 km^2, is located in northeast British Columbia, Canada (Figure 3.3A). It is situated in the northwest segment of the expansive Western Canada Sedimentary Basin (WCSB), where predominately carbonates and marine shales were deposited during the Middle and Late Devonian periods (Dong et al., 2017b). On its eastern and southern boundaries, the HRB is bounded by the Presqu'ile reef carbonate platform. Towards the west, it is separated from the Liard Basin by the Bovie Fault zone.

The Horn River Group shale consists of the Evie and Otter Park Members of the Horn River Formation and the Muskwa Formation (Figure 3.3B). Its age ranges from late Givetian (ca.

393 Ma) to early Frasnian (ca.383 Ma; Dong et al., 2017a). The Evie Member overlies the lower Keg River Formation, which primarily comprises limestones and dolostones from shallow marine carbonates. The Evie Member is a dark grey to black calcareous mudstone. Its thickness ranges from 40 to 750 m, and it becomes more argillaceous towards the top. Notably, it contains the highest total organic carbon (TOC) among the Horn River Group shale (Figure 3.1), averaging 3.65 weight percent (wt. %) (Dong et al., 2015).

The Otter Park Member, situated above the Evie Member, is characterised by dark-grey, pyritic, noncalcareous to calcareous or siliceous mudstone. It reaches a maximum thickness of 270 m in the southeast (McPhail et al., 2008). Typically, it contains less organic matter compared to the Evie Member and Muskwa Formation, averaging 2.35 wt. % TOC (Dong et al., 2015).

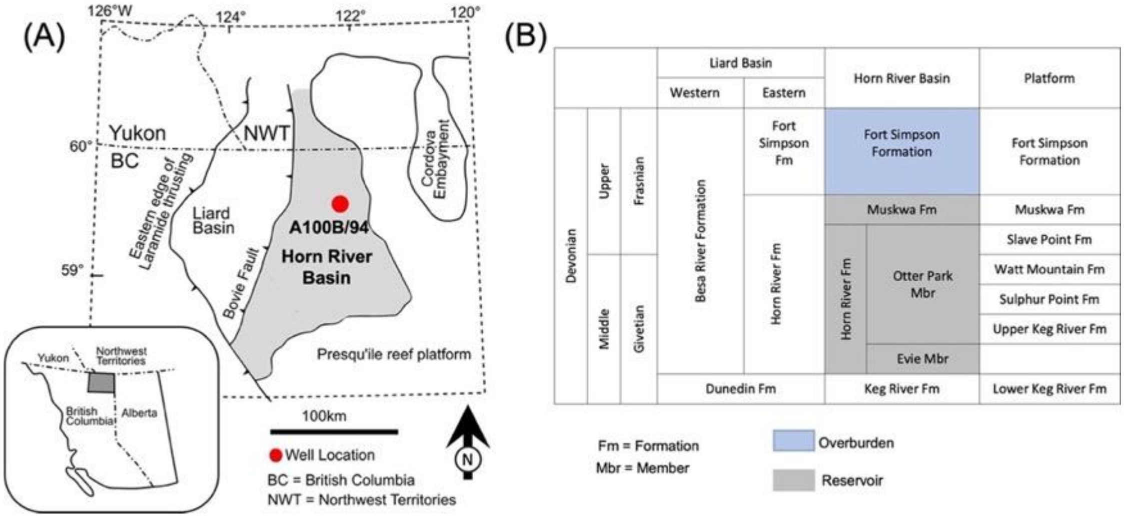

Figure 3.3. (A) Map of Horn River basin, along with the adjacent areas of Liard basin and Cordova embayment, indicating the location of Well A100B/94. Insert: map showing the location of Horn River basin in Western Canada. (B) Middle and upper Devonian stratigraphy. Modified from Charlton et al. (2023) and Dong et al. (2017b).

The Muskwa Formation overlays the Otter Park Member and consists of grey to black, siliceous, pyritic, radioactive, and organic-rich mudstone. Its thickness ranges from 30 to 60 m, with a thickening trend towards the west. Dong et al. (2015) reported a high organic carbon enrichment in the Muskwa Formation, averaging 3.41 wt. % TOC. The top of the Muskwa Formation is found at depths ranging from 2175 m to approximately 3000 m. The Muskwa Formation is conformably overlain by the argillaceous shale of the Fort Simpson Formation, which reaches thicknesses of over 1000 m (Figure 3.3B).

The Fort Simpson Formation has a gradational contact with the Muskwa Formation and acts as an effective fracture barrier during fracking operations (Yu and Shapiro, 2014; Charlton et al., 2023). The porosity of HRB shales ranges from 0.62% to 12.04%, while the measured matrix permeability values show an increasing trend as porosity increases, ranging from 1.7 to 42.8 nanoDarcy (Dong et al., 2017a). The Horn River Group shale was buried into the dry gas window, with thermal maturities ranging from 1.6% to 2.5% Ro (vitrinite reflectance; Ross and Bustin, 2008). The Muskwa, Otter Park, and Evie formations have been targeted for hydraulic fracturing to produce gas. Henceforth, samples from these formations are referred to as reservoir samples, while samples from the overlying Fort Simpson Formation are designated as overburden samples.

3.3 Samples characterisation

3.3.1 Petrophysical and mineralogical characterisation

In this study, samples were collected from a well (A100B/94) drilled in the eastern part of the basin (Figure 3.1A). The well was drilled to a total vertical depth of 2743 m. Table 3.1 details the depths at which the samples were retrieved, and the laboratory measurements conducted on each sample. Results from the acoustic emission measurements will be presented in Chapters 4 and 5.

Table 3.1. Samples collected from Horn River Basin (Well A100B/94) and the laboratory measurements performed on each sample. Abbreviations: Fm: Formation; FSMP, Fort Simpson; MSKW, Muskwa; OPRK, Otter Park; SEM, Scanning Electron Microscopy; ACF, Autocorrelation Function; TOC, Total Organic Carbon; XRD, X-ray Diffraction; Vp/Vs, P- and S-wave velocity; and AE, Acoustic Emission.

Sample ID	Depth (m)	Fm	Laboratory measurement								
			SEM	ACF	Density	TOC	Porosity	XRD	Vp/Vs	Mechanical loading	AE
A2	2535.2	FSMP	√	√	√	√	√	√	√		
A6	2542.2	FSMP	√	√	√	√	√	√	√		
A8	2543.75	FSMP	√	√	√	√			√		
A11	2570.5	FSMP	√	√	√	√	√		√		
A12	2571.9	FSMP	√	√	√	√			√	√	√
A14	2575.9	FSMP	√	√	√	√			√	√	√
A15	2589.5	MSKW	√	√	√	√			√	√√	√√
A16	2665.25	OPRK	√	√	√	√	√	√	√		
A18	2691	OPRK	√	√	√	√			√		
A21	2706.5	EVIE			√	√			√		

The bulk composition was analysed using X-Ray Diffraction (XRD), and the effective (connected) porosity was estimated through Mercury Injection Porosimetry (MIP) (Charlton et al., 2023). Shale cubes, measuring 1–1.5 cm^3, extracted from the core samples, underwent MIP testing. These samples were dried in a humidity-controlled oven at 90°C until a stable weight was achieved. Analysis was performed using a Micromeritics Series V mercury injection porosimeter. The MIP tests comprised 40 pressure increments ranging from 2 to 55,000 psi (pounds per square inch). Initially, pressure increments were spaced at 3 psi, gradually increasing to 5,000 psi increments at higher-pressure intervals. The MIP data underwent conformance correction, followed by the calculation of effective porosity (ϕ) using the equation: $\phi = \frac{V_{Hg}}{V_b}$, where V_{Hg} represents the total volume of mercury injected into the sample, and V_b denotes the bulk volume.

Table 3.2. Sample bulk composition (wt. %) and porosity (%).

Source	Overburden		Reservoir
Formation	Fort Simpson		Otter Park
Sample ID	A2	A6	A16
Quartz	28.7	31.6	20.8
Albite	5.3	5.7	6.6
Microcline	-	-	-
Calcite	-	-	-
Dolomite	-	2.9	66.3
Siderite	2.2	2.5	-
Pyrite	2.1	2.2	1.43
Illite	39.6	32.3	4.8
Illite-smectite	10.3	13	-
Kaolinite	3.8	2.2	-
Chlorite	8	7.7	-
TOC	1.97	1.08	1.97
Total clays	61.7	55.2	4.8
Porosity	3.0	1.4	0.1
Note: Total clays include mica, illite-smectite, kaolinite, and chlorite.			

Table 3.2 shows the bulk composition of samples A2, A6 (Fort Simpson, overburden), and A16 (Otter Park, reservoir) expressed as weight percent (wt. %) of each mineral. The overburden samples are clay-rich; for example, A2 contains 61.7% total clays, with illite and illite-smectite as the dominant clay minerals at 39.6% and 10.3%, respectively. The other major mineral in A2 is quartz (28.7%), with minor amounts of albite, pyrite, and siderite, and a porosity of 3%. A6 is similar in composition to A2 but with lower total clay content (55.2%) and more quartz (31.6%). Similar to A2, the dominant clay minerals in A6 are Illite and illite-smectite, comprising 32.3% and 13% respectively. In addition to quartz, A6 contains minor amounts of albite, pyrite, and carbonates such as dolomite and siderite. Sample A6 has a lower porosity compared to A2, measuring 1.4%.

The reservoir sample is compositionally distinct to the overburden. For example, sample A16 originates from a lithology rich in carbonates within the Otter Park member, dominated by dolomite (66.3%). The fine-grained materials consist of a mixture of quartz and albite, with a small presence of illite and pyrite. The measured porosity of sample A16 is minimal, at 0.1%.

3.3.2 Total organic carbon and density

Total organic carbon (TOC) and density measurements were performed on all samples. Density was determined using the buoyancy technique, where a dry mass of the sample was weighed under ambient conditions. The sample was then submerged in water, and the density was calculated using the volume of the displaced fluid. For further details about density measurements, refer to Chapter 2. TOC analysis was conducted at the Stable Isotope Biogeochemistry Laboratory (SIBL) at Durham University. Each sample, weighing 4-5 grams, was powdered, and treated with a 3 M hydrochloric acid leach at room temperature for 24 hours to remove any carbonate. Subsequently, the samples were rinsed with deionized water and centrifuged until neutrality was achieved. Following this, they were oven-dried at 60°C for 48 hours. The resulting pellets were then re-homogenized using a mortar and pestle. Approximately 2-2.5 mg of powder was loaded into tin capsules. TOC was determined by thermal oxygen combustion at 1010 °C in a Costech Elemental Analyser (ECS 4010).

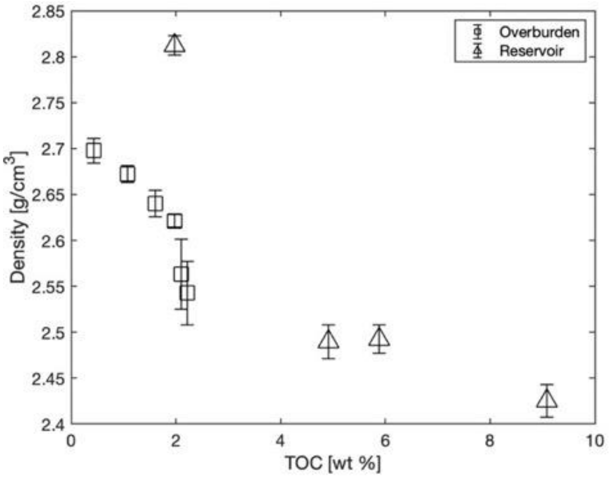

Figure 3.4. TOC plotted against density for overburden and reservoir samples. Overburden samples show higher densities and lower TOC compared to reservoir samples. While a distinct linear correlation exists between TOC and density for both overburden and reservoir samples, the nature of this correlation differs between the two.

Figure 3.4 displays the TOC and density results. Overburden samples have densities ranging from 2.54 to 2.70 g cm^{-3}, with an average density of 2.62 g cm^{-3}. In contrast, the reservoir samples generally exhibit lower densities, except for sample A16, which has a density of 2.81 g cm^{-3}. These findings align with the densities reported from wireline logs for the Horn River Basin (Figure 3.1) (Ross and Bustin, 2008; Mo et al., 2018). It is worth noting that Ross and Bustin

(2008) reported a slight density increase with depth in the basin, attributed to a rising trend in quartz contents in the reservoir compared to clay-rich overburden shales.

The TOC values show an inverse linear correlation with density, with lower values observed in the overburden and an increasing trend in the reservoir. Overburden samples exhibit TOC ranges from 0.43 to 2.21 wt.%, with an average of 1.57%, while reservoir samples range from 1.97 to 9.08 wt.% with an average of 5.46%. These patterns align with measurements reported by Dong et al. (2015), wherein reservoir units (Muskwa, Otter Park, and Evie) consistently display moderate to high TOC levels, with an increasing trend observed at greater depths. In contrast, the Fort Simpson formation exhibits minimal TOC.

3.3.3 Microstructure and textural anisotropy

The textures of the samples were analysed using scanning electron microscopy (SEM). Microscope specifications and scanning conditions are described in Charlton et al. (2023). Figure 3.5 shows examples of images captured in back-scattered electron (BSE) mode. The microstructures of the overburden samples predominantly consist of an extremely fine-grained clayey and/or calcareous matrix, silt-sized detrital grains, and solid organic materials with varying aspect ratios.

For instance, in sample A2 (Figure 3.5A), the matrix is very fine-grained, with small amounts of visible pyrite. Notably, this sample exhibited a distinct alignment of clay minerals within the porous matrix, accompanied by scattered detrital quartz grains. Similarly, sample A6 (Figure 3.5C) displays a texture similar to A2, characterised by a clay matrix containing pyrite inclusions. Sample A6 showed a noticeable presence of dolomite, observed as individual scattered grains within the matrix (Figure 3.5C). Additionally, in comparison to A2, the quartz in sample A6 is generally coarser. Lastly, Figure 3.3C suggests that the alignment of clay minerals is less pronounced in contrast to the strongly oriented minerals observed in A2.

The reservoir samples are primarily composed of carbonates (dolomite). For example, the microstructure of sample A16 (Figure 3.5E) consists of angular dolomite grains sparsely interspersed with pyrite, along with scattered quartz grains and a clay/organic phase. Figure 3.5E highlights the limited orientation of the clay minerals in this sample, particularly when contrasted with the overburden samples.

The textural (fabric) anisotropy of the samples was quantified using a two-dimensional autocorrelation function (ACF) of the SEM images. The ACF statistically characterizes the spatial pattern within an image by comparing grey values at various positions (pixels). The function has a maximum value at zero lag (distance) and decays exponentially in all directions with increasing lag. The rate of decay is a quantitative measure of texture heterogeneity (Prasad et al., 2009).

Radial profiles of the autocorrelation function were computed along azimuths ranging from 0° to 180°, and the correlation length was estimated for each azimuth. The correlation length is taken to be the lag value at which the correlation function falls to $1/e$ (where e is the base of the natural logarithm) of its maximum value at zero lag. Then, the textural anisotropy was quantified by the texture aspect ratio (S_{tr}), defined as the ratio between the maximum (l_{max}) and minimum (l_{min}) correlation lengths obtained over all azimuths (see, Figure 3.5B). Where:

$$0 \leq \ S_{tr} = \frac{l_{min}}{l_{max}} \times 100 \ \leq 100\,,$$

$S_{tr} \approx 100$ for randomly aligned texture (isotropic) and $S_{tr} < 100$ for textures with preferential alignment (anisotropic).

The ACF was performed, and the S_{tr} parameter was calculated using Gwyddion software (version 2.63, http://gwyddion.net/) on SEM images. The images used represented areas of $60 \times 50\ \mu m^2$ and $70 \times 60\ \mu m^2$ with pixel densities of 17 and 14 pixels per micrometre, respectively. The results of the S_{tr} calculations are plotted as a function of TOC and colour-coded with density in Figure 3.6. Each data point in Figure 3.6 represents the average S_{tr} value from multiple non-overlapping areas per sample, with error bars indicating one standard deviation around the average.

The textural anisotropy values for the overburden samples range from 52% to 78%, with an average of 70%, while those for the reservoir samples range from 62% to 79%, with an average of 71%. These findings suggest that the overburden samples exhibit a slightly higher degree of textural anisotropy compared to the reservoir samples. This contrasts with previous studies on a larger spatial scale (e.g., Shapiro, 2015; Baird et al., 2017), which indicate that the overburden formation is significantly more anisotropic than the reservoir formations (Figure 3.2). However, the small difference observed between the overburden and the reservoir samples aligns with the textures identified in SEM images (Figure 3.5A, C, and D). For example, in sample A2 from the overburden, elongated clay fabrics are clearly aligned in a sub-horizontal orientation (Figure 3.5A), yielding a S_{tr} value of 52%. In contrast, sample A6 (also from the overburden) exhibits elongated clay fabric with less pronounced alignments (Figure 3.5C), resulting in an S_{tr} value of 72%.

Additionally, while the textural anisotropy of the overburden samples is scattered and shows no correlation with either TOC or density, the reservoir samples exhibit a clear positive correlation with both TOC and density (Figure 3.6). A comparison of textural anisotropy and sample mineralogy (Table 3.2) suggests an inverse correlation between preferred clay orientation and clay volume. This observation aligns with findings in sedimentary rocks (Aplin et al., 2006; Sone and Zoback, 2013; Day-Stirrat et al., 2017), which show that below a critical clay content, clay fabric loses its preferred orientation. At this point, a framework of stiffer grains dominates the rock fabric, disrupting the spatial continuity of the clay fabric.

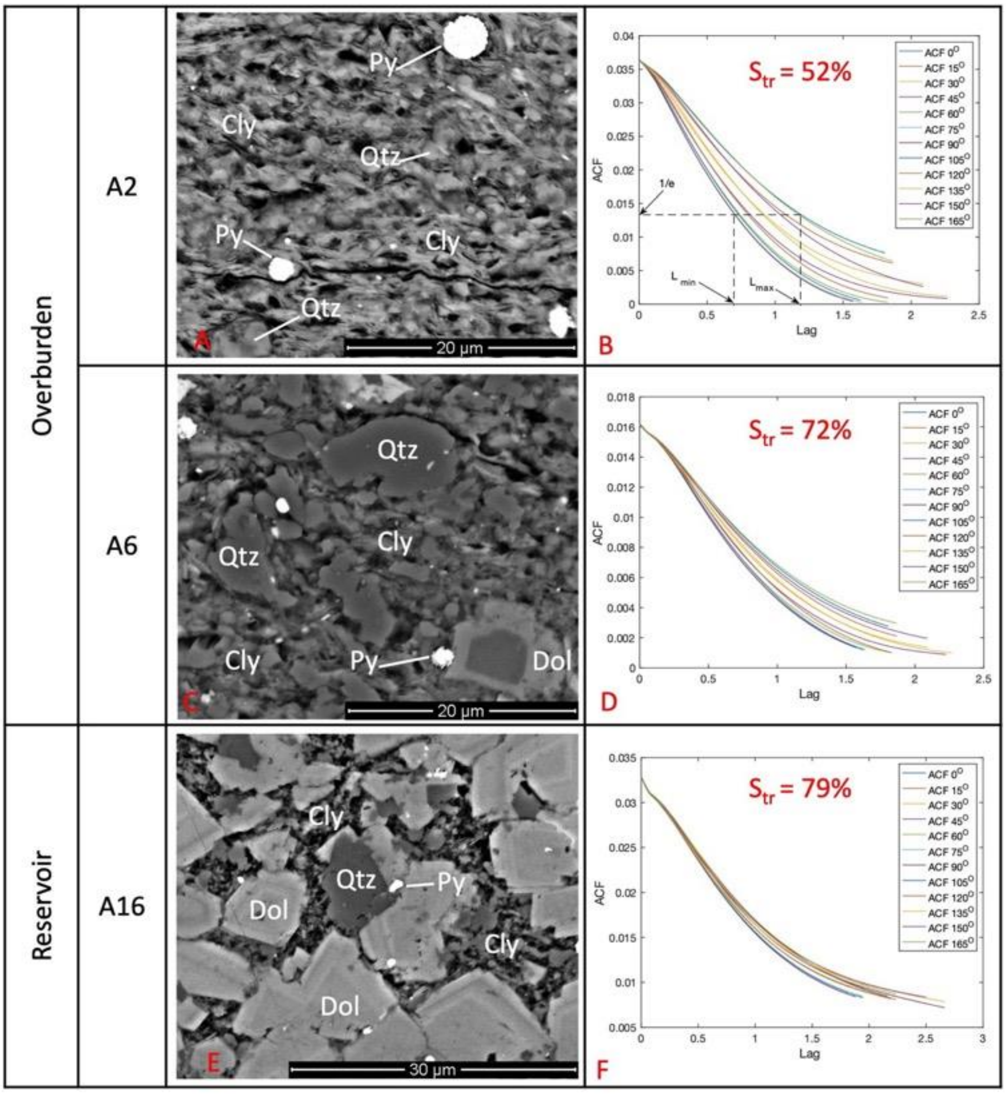

Figure 3.5. SEM images along with corresponding radial profiles of the Autocorrelation Function (ACF). (A) Overburden sample A2 displays an illite-dominated clay (Cly) matrix with scattered quartz (Qtz) and pyrite (Py) grains. (C) Overburden sample A6 exhibits a texture similar to A2, but with less pronounced alignment of clay minerals and the inclusion of dolomite (Dol) grains. (E) Reservoir sample A16 consists of angular dolomite grains with dispersed quartz grains and a minor clay/organic phase. For each of these samples, azimuthal profiles of the corresponding ACF from 0 to 180 degrees are shown in (B), (D), and (F). The lag value, where the correlation function reaches $1/e$ of its maximum value at zero lag, is used to measure the correlation length at each azimuth. The ratio between the maximum and minimum correlation lengths obtained over all azimuths provides a measure of anisotropy. A broader spread of ACF with azimuth indicates higher textural anisotropy. For example, sample A2 exhibits highly aligned, elongated clay fabrics (sub-horizontal orientation) with a lower Str value (52%), while sample A6 shows less pronounced fabric alignment and a higher Str value (72%).

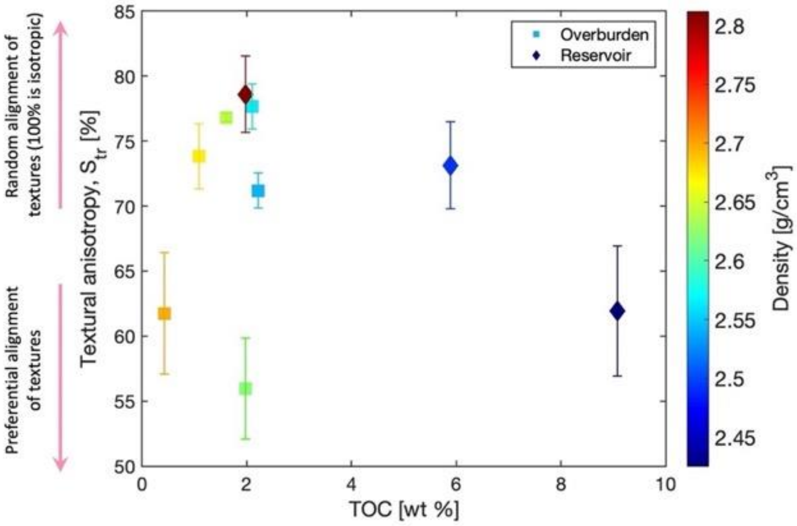

Figure 3.6. Textural anisotropy of HRB shale samples as function of TOC. The smaller the percentage on the textural anisotropy scale the more anisotropic is the sample.

3.4 Experimental techniques

This chapter focuses on the characterization of HRB shales samples in terms of their mechanical and seismic anisotropic properties. The measurements include density, total organic carbon (Section 3.3.2), ultrasonic wave velocity (compressional wave velocity, Vp and shear wave velocity Vs), elastic moduli and anisotropy (Thomsen's parameters). Detailed information about the techniques and equipment used are presented in Chapter 2. In this section, a brief description of the conducted experiments and the measured and calculated parameters is provided.

3.4.1 Triaxial loading experiments.

To evaluate the mechanical properties such as yield stress, peak stress, and static Young's modulus, as well as mode of failure (brittle vs. ductile), I conducted triaxial loading experiments on shale cores. These cores were obtained following a protocol developed during this PhD project (detailed in Chapter 2). Throughout the experimental work, cores were maintained at room temperature and humidity. The experiments were performed utilizing the Durham University triaxial apparatus with fluid flow (Dutff). Detailed description of the apparatus, including sample preparation, measurement sensors, and machine calibrations, can be found in Chapter 2.

I conducted four loading experiments on samples A12, A14 (two experiments), and A15. Samples A12 and A14 are from the Fort Simpson Formation, while A15 is from Muskwa formation (Table 3.1), which has been targeted for hydraulic fracturing. Two core plugs were manufactured from sample A14: one for an intact core loading test, and the other for a composite geometry with granite sawcut in a reactivation experiment. The results of the reactivation experiment are presented in Chapter 5. All samples were cored perpendicular to the bedding plane. The experiments conducted were Dutff 348, Dutff 350, and Dutff 351, corresponding to samples A12, A14, and A15, respectively.

3.4.2 Loading protocol, measured and calculated parameters

The loading protocol used for experiments Dutff 348, Dutff 350, and Dutff 351 was as follows: (i) first, the samples were hydrostatically compressed by gradually increasing the confining pressure to a simulated reservoir condition; (ii) then, the axial load was increased at a constant axial displacement rate of 1 $\mu m\, s^{-1}$ (equivalent to $2 \times 10^{-5} s^{-1}$ of constant axial strain) until failure, while maintaining a constant confining pressure. Yield stress is identified by a deviation from the linear trend in the axial loading curve, and failure is indicated by a peak in the recorded axial stress followed by a stress drop. The confinement pressures used were 10 MPa for experiment Dutff 348 and 80 MPa for experiment Dutff 350.

To evaluate how the static Young's modulus evolves with pressure (depth), experiment Dutff 351 was conducted using stepwise increases in confining pressure, from an initial value of 10 MPa up to 80 MPa. In this experiment, the sample was hydrostatically loaded by increasing the confining pressure (σ_3) to 10 MPa, after which axial loading (σ_1) was applied. When the axial load equalled the confining pressure, axial loading was paused, and the confining pressure was increased by 10 MPa for the next stage. This procedure was repeated until the confining pressure reached 80 MPa, at which point axial loading resumed and continued until sample failure (see Figure 3.7). These steps provided multiple measurements of the static Young's modulus at different confining pressures

Measurements of confinement pressure, fluid pressure, applied force, axial displacement, and acoustic emission were taken for all experiments. The acoustic emission data will be presented in Chapter 4. Axial stress, axial strain, and static Young's modulus were calculated using the initial cross-sectional area and length of the test specimen. In the triaxial configuration, $\sigma_3 = \sigma_2 = p_c$, where p_c is the confinement pressure. The axial stress is given by $\sigma_1 = \frac{F}{A}$, where F is the applied axial force and A is the cross-sectional area of the test sample. The applied force is corrected for machine stiffness. Differential stress is defined as the difference between the axial stress and the confinement pressure ($\sigma_1 - \sigma_3$). The axial strain is calculated as $\varepsilon = \frac{\Delta L}{L}$, where ΔL is the axial shortening and L is the initial sample length. Finally, the static Young's modulus was calculated as the slope of the linear fit in the stress-strain curve at a load range between 40% and 60% of the peak stress.

3.4.3 Wave velocity measurements and anisotropy calculations

The classical ultrasonic pulse transmission technique was used for velocity measurements under room temperature and pressure conditions. This technique involves sending a high-frequency pulse through the rock sample and measuring the time it takes for the wave to travel a known distance. For full details about the measurement technique, see Chapter 2. Five velocities were measured in three different directions.

1. Vp(0): Bedding-parallel compressional wave velocity.
2. Vsh(0): Horizontally polarized, bedding-parallel shear wave velocity.
3. Vp(45): Compressional wave velocity at 45-degree angle to bedding.
4. Vsv(90): Horizontally polarized, bedding-perpendicular shear wave velocity.
5. Vp(90): Bedding-perpendicular compressional wave velocity.

Using velocities measurements and density data (Section 3.3.2), I derived the complete dynamic elastic stiffness coefficients, dynamic Young's moduli (E1, E3), dynamic Poisson's ratios, and anisotropy parameters (Thomsen parameters: epsilon, gamma, and delta). Detailed derivation procedures, including error estimation are elaborated in Chapter 2.

3.5 Results

3.5.1 Physical properties (Vp/Vs, density)

Table 3.3 presents the results of elastic wave velocity and density measurements. The P-wave velocities parallel to the bedding plane, Vp(0), range from 5.1 $km\ s^{-1}$ to 5.7 $km\ s^{-1}$, with an average of 5.5 $km\ s^{-1}$, consistent with previous laboratory measurement on Horn River samples (Moghadam et al., 2019). The P-wave velocity perpendicular to the bedding plane, Vp(90), varies from 3.8 $km\ s^{-1}$ to 4.9 $km\ s^{-1}$, with an average velocity of 4.7 $km\ s^{-1}$. At an oblique angle, Vp(45) falls between the parallel and perpendicular values, ranging from 4.3 $km\ s^{-1}$ to 5.2 $km\ s^{-1}$, with an average velocity of 4.9 $km\ s^{-1}$. Initial observations indicate that these velocities exhibit a pattern consistent with the presumed transverse isotropy, where Vp(0) > Vp(45) > Vp(90) across all samples.

For shear wave velocities, the S-wave velocity parallel to the bedding plane, Vsh(0), ranges from 2.2 $km\ s^{-1}$ to 3.3 $km\ s^{-1}$, with an average velocity of 2.7 $km\ s^{-1}$. In contrast, the S-wave velocity perpendicular to the bedding plane, Vsv(90), ranges from 1.8 $km\ s^{-1}$ to 2.6 $km\ s^{-1}$, with an average velocity of 2.1 $km\ s^{-1}$. Wireline log measurements reported by Mo et al. (2018) and Yu and Shapiro (2014) for Horn River shales show a wider range of velocities with depth. The reported P-wave velocities range from 3.5 km/s to 6.0 km/s, while S-wave velocities range from 1.8 to 3.8 km/s. The laboratory-measured velocities are about 8% lower than the borehole logs velocities reported by Mo et al. (2018) (Figure 3.1). This discrepancy may be attributed to differences in scale and testing conditions. While laboratory measurements offer controlled insight into intrinsic rock properties, borehole logs reflect in situ conditions, including the influence of fractures, fluid content, and stress state. Additionally, variations in frequency range between laboratory (ultrasonic) and field-scale (seismic) measurements contribute to the observed differences.

Table 3.3. Measured physical properties (density, total organic carbon (TOC), and elastic wave velocities). Density figures in brackets are measurements conducted by MICP (Pers. Comm. Q. Fisher).

Source	Sample ID	FM	Bulk density [g cm^{-3}]	TOC [wt %]	Vp(0) [$km\ s^{-1}$]	Vp(45) [$km\ s^{-1}$]	Vp(90) [$km\ s^{-1}$]	Vsh(0) [$km\ s^{-1}$]	Vsv(0) [$km\ s^{-1}$]
Overburden	A2	FSMP	2.62±0.01 (2.51)	1.97	5.54±0.28	4.88±0.24	4.71±0.24	2.70±0.22	1.85±0.14
	A6	FSMP	2.67±0.01 (2.72)	1.08	5.09±0.26	4.29±0.21	3.83±0.19	2.58±0.21	1.88±0.15
	A8	FSMP	2.7±0.01	0.43	5.5±0.28	5.07±0.25	4.9±0.25	2.4±0.19	1.8±0.14
	A11	FSMP	2.64±0.01 (2.64)	1.61	5.52±0.28	5.09±0.25	4.81±0.24	3.27±0.26	2.79±0.22
	A12	FSMP	2.56±0.04	2.10	-	-	-	-	-
	A14	FSMP	2.54±0.03	2.21	5.66±0.29	-	-	2.59±0.21	-
Reservoir	A15	MSKW	2.49±0.02	5.88	5.62±0.28	5.0±0.25	4.71±0.24	2.50±0.20	1.94±0.16
	A16	OPRK	2.81±0.01 (2.83)	1.97	5.21±0.26	4.96±0.25	4.80±0.24	2.24±0.18	2.03±0.16
	A18	OPRK	2.43±0.02	9.08	5.69±0.28	5.2±0.26	4.86±0.24	2.97±0.24	2.56±0.20
	A20	EVIE	2.49±0.02 (2.50)	4.91	5.53±0.28	4.91±0.25	4.73±0.24	2.61±0.21	1.96±0.16

Overall, the measured values of P-wave and S-wave velocities are consistent with measurements of organic-rich shale (TOC > 1%) of comparable densities (Pervukhina and Rasolofosaon, 2017). They show a positive correlation between wave velocity and density, reflecting the effect of compaction and burial, which simultaneously increases density and wave velocity.

3.5.2 Mechanical strength and static young's modulus

Figure 3.7 shows an example of the stress-strain evolution for a triaxial loading experiment, specifically experiment Dutff 351 on sample A15 from the Muskwa Formation (reservoir), which has a density of 2.49 g cm^{-3} and a TOC of 5.88%. The yield and peak stresses are calculated as indicated on the curve. Numbers circled in red show the confining pressure, and the markers on the stress-strain curve indicate the sections used to calculate the static Young's modulus.

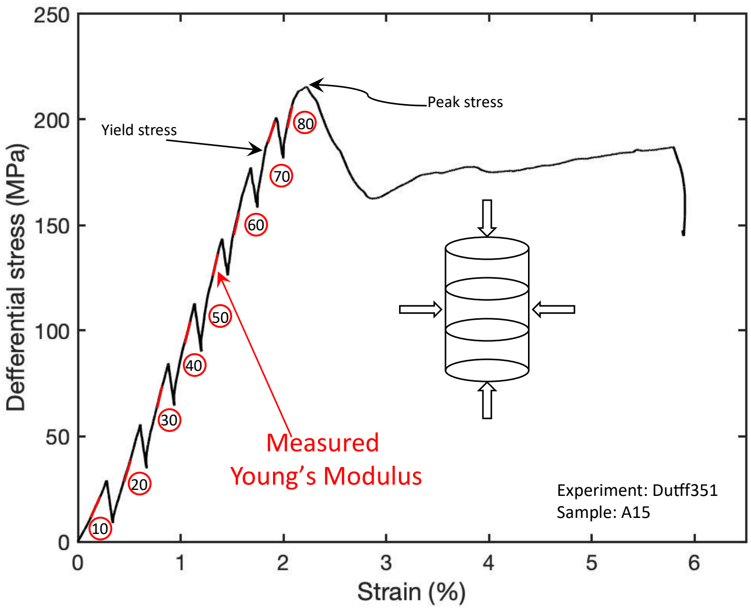

Figure 3.7. An example of a triaxial loading experiment, in which the confining pressure was increased stepwise from 10 MPa to 80 MPa without unloading between stages. At each pressure level, axial loading was applied until the axial stress equalled the confining pressure, after which the next confining pressure increment was introduced. The red mark on the stress-strain curve indicates the portion used to calculate the static Young's modulus (refer to the text for details).

Table 3.4 provides a summary of the triaxial loading results for all the experiments. The yield stress for the Fort Simpson Formation samples (overburden), A12 and A14, is 340 MPa and 270 MPa, respectively, when loaded at confining pressures of 10 MPa and 80 MPa. The peak stress is 347 MPa for sample A12 and 380 MPa for sample A14. Sample A12 has a density of 2.56 g cm^{-3} and a total organic carbon (TOC) content of 2.10%, while sample A14, which comes from a slightly deeper depth (Table 3.1), has a slightly lower density of 2.54 g cm^{-3} and a higher TOC of 2.21%. As for the Muskwa Formation sample A15 (reservoir), when loaded at pressures ranging from 10 MPa to 80 MPa, it exhibited lower yield and peak stresses of 190 MPa and 215 MPa, respectively.

For the static Young's moduli, the overburden samples exhibit values of 57 GPa and 67 GPa when loaded at confining pressure of 10 MPa and 80 MPa, respectively. The static Young's modulus for the reservoir sample ranges from 11 GPa to 38 GPa for the same pressure range.

These results underscore the pressure sensitivity of the static Young’s modulus, highlighting a generally higher modulus in overburden shales compared to the reservoir ones (Figure 3.8).

Table 3.4. Measured mechanical strength and static Young’s modulus.

Sample No.	Fm	Test conditions		Mechanical properties			
		Confining Pressure (MPa)	Strain rate $(\mu m\ s^{-1})$	Yield Stress (MPa)	Peak Stress (MPa)	Static Young’s Modulus (GPa)	Failure Mode
A12	FSMP	10	2x10^-5	340	347	57	brittle
A14	FSMP	80	2x10^-5	270	380	67	brittle
A15	MSKW	10,20,30,40, 50, 60, 70,80	2x10^-5	190	220	11,16,20, 24, 35, 38, 28, 24	brittle

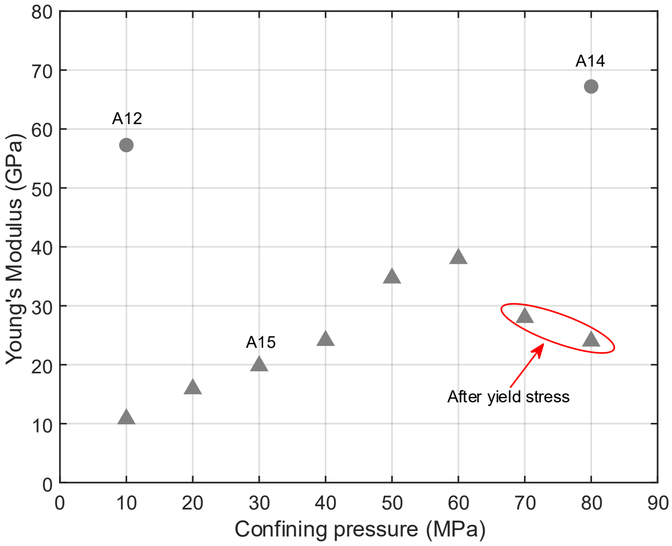

Figure 3.8. Static Young’s modulus versus confining pressure. The triangular markers all belong to sample A15 (see Figure 3.7 for details).

Moghadam et al. (2019) conducted unconfined compressive strength (UCS) tests on Horn River samples cored parallel to the bedding plane. They reported an UCS ranging from 20 MPa to 125 MPa and a static Young’s modulus ranging from 20 GPa to 38 GPa, on average. When I interpolate the results of this study to ambient confining pressure, the values are higher than those reported by Moghadam et al. (2019). Consequently, the calculated static Young's moduli are higher than the values previously reported in measurements of samples from Horn River shale formations at 0 MPa confining pressure and loaded parallel to the bedding plane, as expected.

3.5.3 Dynamic stiffness coefficients, Young’s moduli, and Poisson’s ratios

Experimental uncertainties in the stiffness coefficients' calculations were estimated through constituent parameter decomposition using partial derivatives. Additional details about the parameters and decomposition procedures can be found in Chapter 2. The estimated uncertainty falls within the range of 1.4% to 4% of the calculated values. Figure 3.9 plots dynamic stiffness coefficients (c44, c66, c13, c11, and c33) as functions of TOC. Solid markers correspond to overburden samples and open markers show reservoir samples. The stiffness coefficients are relatively invariant with TOC, although there is a small decrease in the coefficient of the reservoir samples compared to that of the overburden samples. The results indicate that all these shales are more compressible perpendicular to bedding than parallel to bedding, i.e., c11 > c33.

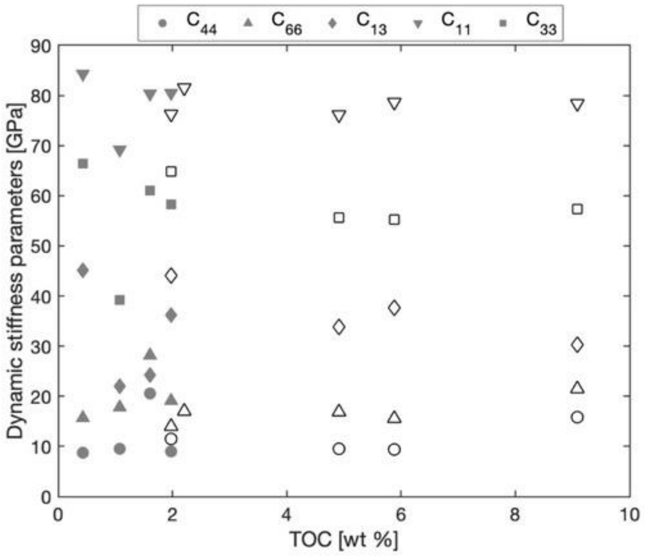

Figure 3.9. Dynamic stiffness coefficients as function of TOC. The maximum uncertainty is 4%. Solid markers correspond to overburden samples and open markers show reservoir samples.

Dynamic Young’s modulus values (E1 and E3) derived from stiffnesses coefficients are shown in Figure 3.10. E1 values, representing the dynamic Young’s modulus parallel to the bedding plane, range from 39 to 70 GPa. Once again, these values are higher than those reported by Moghadam et al. (2019), which were in the range of 30 to 59 GPa. Similarly, in line with static measurements, the overburden samples exhibit higher E1 values compared to the reservoir samples. The range for overburden samples is 44 to 70 GPa, while for the reservoir samples, the range is 39 to 57 GPa. For the dynamic Young’s modulus values perpendicular to the bedding plane E3, the range spans from 29 to 50 GPa. Among the overburden samples, E3 varies between 29 and 50 GPa, while the reservoir samples exhibit a narrower range of 32 to 42 GPa.

Figure 3.10 depicts the relationship between E1 and E3 for all the samples, colour-coded with TOC. To the best of the author's knowledge, no laboratory measurements of both E1 and E3 data have been published for Horn River shales. Nonetheless, these findings align with previous measurements conducted on highly layered shale (depicted as grey crosses in Figure 3.10). These shales originate from a gas-producing shale play with porosities of approximately 2-6% and TOC of 1-3% (Higgins et al., 2008). All samples exhibit elastic anisotropy, where the ratio between E1 and E3 is greater than one (e.g., the dashed line in Figure 3.10 represents a ratio of one). Interestingly, there appears to be no observable correlation between E1/E3 values and the TOC of these samples. It should be noted that the number of samples is limited to draw a firm conclusion.

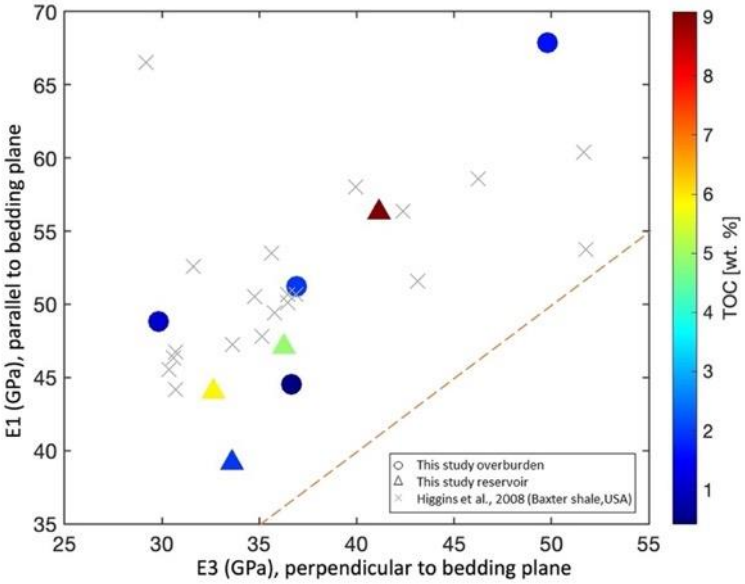

Figure 3.10. Relationship between dynamic Young's moduli E1 and E3. The colour coding represents TOC. The crosses are data from Higgins et al. (2008), and the dashed line indicates a 1:1 ratio between E1 and E3.

The corresponding dynamic Poisson's ratios, calculated from the elastic wave velocity and density measurements, are presented in Figure 3.11. The Poisson's ratios of the overburden samples range from 0.20 to 0.41, with an average of 0.32. The reservoir samples exhibit a narrower range (0.27 to 0.41) compared to the overburden samples, with an average value of 0.36. The results for the overburden show considerable scatter, making it difficult to draw any definitive inferences. However, the reservoir samples show an inverse correlation with TOC. Additionally, there seems to be anisotropy in Poisson's ratio for both the overburden and reservoir samples. The value of the horizontal Poisson's ratio, v13, is larger compared to the vertical Poisson’s ratio, v31. This anisotropy is consistent with the observations in the dynamic Young’s moduli (see Figure 3.10), which arises from the symmetry of the elastic compliance of a VTI medium: $\frac{\nu 13}{\nu 31} = \frac{E1}{E3}$.

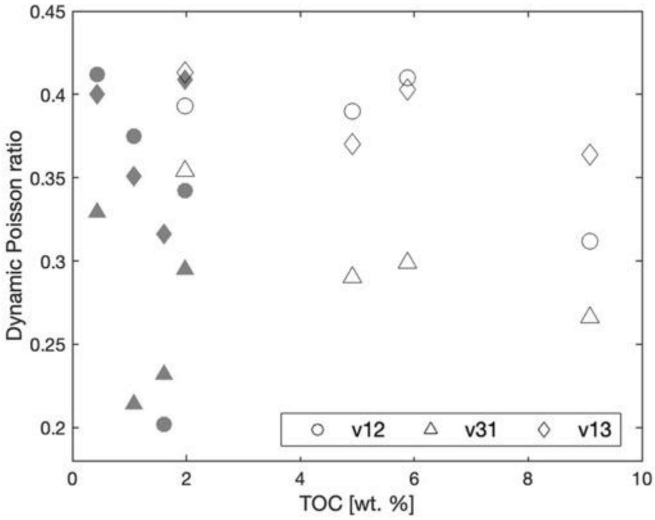

Figure 3.11. Dynamic Poisson ratio. Solid markers correspond to overburden samples and open markers show reservoir samples.

Poisson’s ratios and the dynamic Young’s moduli are crucial for hydraulic fracturing treatment design. In particular, the Poisson’s ratio is essential for estimating horizontal stress magnitude and the extent of lateral fracture propagation. When combined with a relatively extensive dataset of dynamic Young’s moduli obtained from wireline log measurements (Figure 3.1), the calculated Poisson’s ratios will provide a significant constraint in reservoir characterization.

3.5.4 Seismic anisotropy

The dynamic stiffness coefficients presented in the previous section are used to derive the Thomsen anisotropy parameters: epsilon (ε), gamma (γ), and delta (δ), with the results displayed in Figure 3.12. Parameters ε and γ denote P- and S-wave anisotropy, respectively, and reflect the fractional differences in velocities between vertical and horizontal directions. In contrast, δ does not have a clear physical interpretation and tends to dominate the near-vertical P wave response in weakly anisotropic material. The Horn River samples show substantial anisotropy in both the P- and S-wave velocities, characterised by a general decrease in anisotropy with increasing TOC (Figure 3.12).

For overburden samples, S-wave anisotropy (γ) ranges from 0.19 to 0.57, with an average of 0.40. In contrast, the reservoir samples show S-wave anisotropy ranging from 0.11 to 0.38, with an average value of 0.25. While the overburden sample results scatter, the reservoir samples exhibit a sharp decreasing trend with TOC. This is due to the narrow variation in TOC among the overburden samples compared to the large variation in TOC within and across the reservoir formations. As for P-wave anisotropy (ε), the overburden samples show values ranging from 0.14 to 0.38, averaging 0.22. The reservoir samples, in contrast, exhibit anisotropy between 0.09 and 0.21, averaging 0.17 (Figure 3.12). P-wave anisotropy of the overburden samples scatters, similar to the S-wave anisotropy. However, the P-wave anisotropy of reservoir samples does not vary with TOC. The delta (δ) parameter consistently exhibits a moderate increase with TOC for both the overburden and reservoir samples, suggesting that it is more sensitive to TOC variations compared to γ and ε (Figure 3.12).

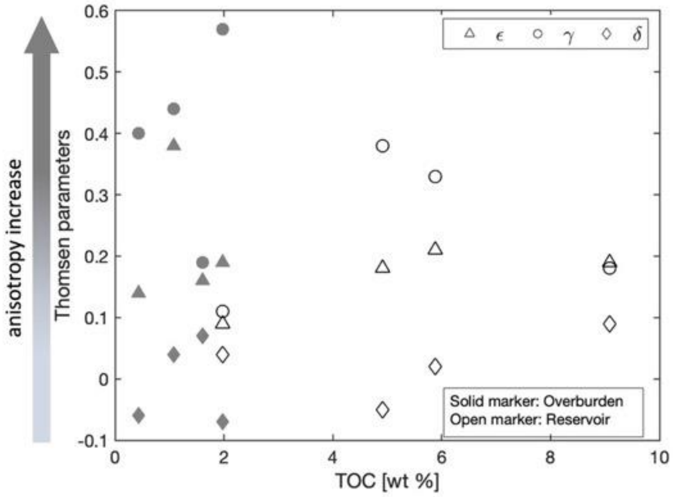

Figure 3.12. Thomsen anisotropy parameters as function of TOC. Solid markers correspond to overburden samples and open markers show reservoir samples.

The pronounced anisotropy of the Horn River shales is evident across multiple scales, from microscale measurements using nanoindentation (Charlton et al., 2023) to larger field-scale observations from microseismic data. For instance, Baird et al. (2017) estimated anisotropy in the Horn River shales using S-wave splitting (SWS) measurements in microseismic data acquired during hydraulic fracture stimulation. They reported anisotropies of 0.46, 0.33 and 0.01 for γ, ε, and δ, respectively, in the overburden formation, and notably documented a sharp decrease in anisotropy magnitude from the overburden to the reservoir (Figure 3.2). Similarly, inversions of microseismic data recorded in downhole arrays shows anisotropy values as high as 0.7, 0.4 and 0.2 for $\gamma, \varepsilon,$ and δ, respectively, in the clay-rich overburden of the Fort Simpson formation. In the organic-rich formation of Muskwa and Otter Park, γ and ε have decreased to as low as 0.2, while δ has shown no variation (Yu and Shapiro, 2014).

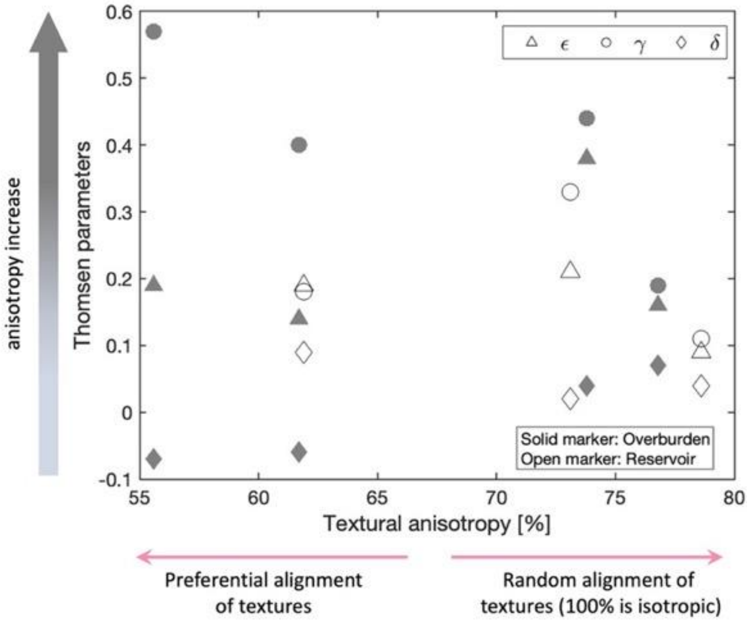

Figure 3.13. Cross-plot of Thomsen anisotropy parameters and textural anisotropy measured from SEM images.

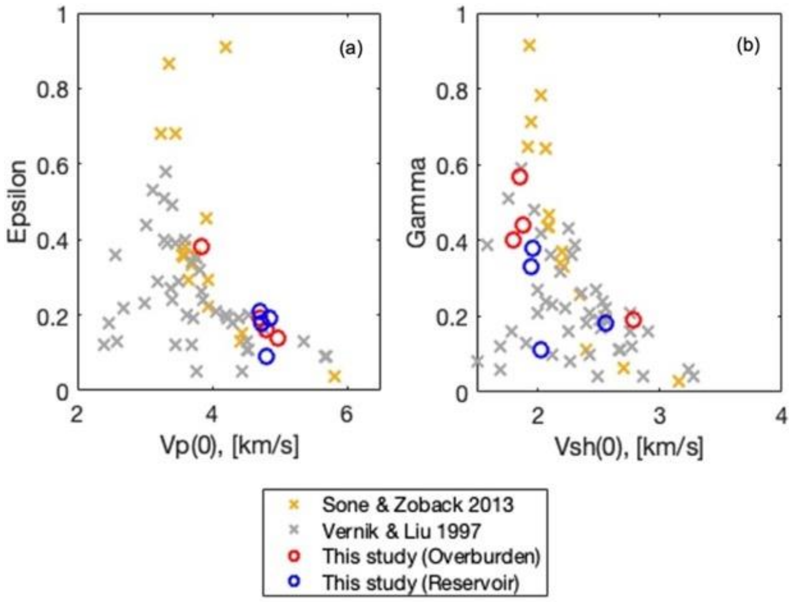

Figure 3.14. Comparison of anisotropy parameters with P-wave and S-wave velocities measured parallel to the bedding plane (Vp (0), Vsh (0)). (a) Epsilon versus Vp (0). (b) Gamma versus Vsh (0). Crosses are data from previous studies (Vernik and Liu, 1997; Sone and Zoback, 2013).

These multiscale observations of anisotropy in the Horn River shales offer considerable insights, validating homogenization models and facilitating the upscaling of mechanical properties from grain scale to core and basin scales. Additionally, the measured Thomsen anisotropy parameters (ε and γ) appear to correlate with the textural anisotropy quantified using SEM images (Figure 3.13). This relationship suggests that a more pronounced alignment of sample's texture corresponds to higher values of ε or γ.

Figure 3.14 shows a comparison of anisotropy parameters and P- and S-wave velocities measured parallel to the bedding plane. As documented in previous laboratory measurements of shale anisotropy (Sone and Zoback, 2013), there is a clear correlation between ε and γ and Vp (0) and Vsh (0) in my dataset. For the ε and Vp (0) correlation, there is an overlap of the overburden and reservoir samples, consistent with the scattering seen in Figure 3.12, suggesting weak sensitivity with TOC. When this study's results are compared with data from the literature (depicted as crosses in Figure 3.14a), the mature shales of the HRB show a well-constrained trend. In contrast, the γ and Vsh (0) correlation shows more scattering and is distributed over a larger range reflecting stronger dependency on the TOC (Figure 3.14b).

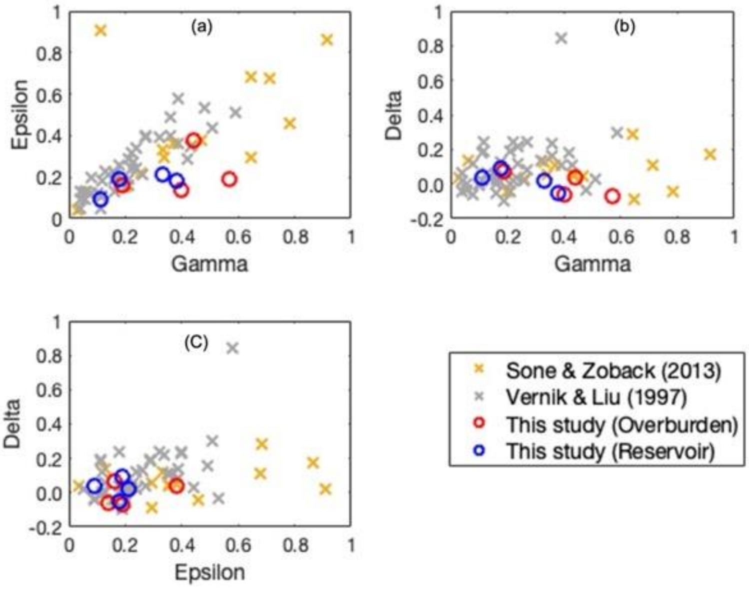

Figure 3.15. Cross-plot between Thomsen's anisotropy parameters: (a) epsilon and gamma, (b) delta and gamma, (c) delta and epsilon. Crosses are data from previous studies (Vernik and Liu, 1997; Sone and Zoback, 2013).

A comparison of the Thomsen's anisotropy parameters ε; γ; and δ is shown in Figure 3.15. As observed in previous studies, epsilon and gamma nearly have a one-to-one correlation, although this study's results tend to lean toward the lower end of this correlation (Figure 3.15a). The range of values I obtain for delta falls within the lower range of reported by Vernik and Liu (1997) and Sone and Zoback (2013). Notably, I do not observe a strong correlation of delta with the other anisotropy parameters, which is consistent with findings from previous studies (Vernik and Liu, 1997; Sone and Zoback, 2013).

3.6 Discussion

3.6.1 Effect of shale composition on anisotropic properties

The results presented in the previous sections quantify the seismic anisotropy magnitude of HRB shales. Seismic anisotropy in shales stems from two primary sources. The first is intrinsic or fabric anisotropy, which results from the preferred orientation of anisotropic minerals within the rock's lattice structure (Vernik and Liu, 1997). The second source is extrinsic anisotropy, originating from the alignment of geological features such as fractures, cracks, pores, and grain boundary contacts, including the material filling these features (Sayers, 2005; Allan et al., 2016).

XRD results of HRB shales reveal a substantial contrast in mineral composition and TOC between the overburden and reservoir samples (see Tables 3.2 and 3.3). This contrast corresponds to a decrease in anisotropy parameters. In the reservoir samples, carbonates dominate, with minor occurrences of quartz and illite, and a high average TOC of 5.46 % wt. Notably, the strongly anisotropic overburden (Fort Simpson) contains a much higher proportion of clays compared to the quartz-rich Muskwa and the carbonate-rich Otter Park and Evie formations. Previous studies on mudstones suggest that factors such as maturity (e.g., the illite-smectite transition) and clay content govern the preferred orientation of clay fabrics and, consequently, anisotropy (Aplin et al., 2006; Day-Stirrat et al., 2010; Day-Stirrat et al., 2017). For these mature shales, the SEM images and textural anisotropy results show sub-horizontal preferential orientation of clay fabrics (Figure 3.5 and Figure 3.6).

Charlton et al. (2023), on a microscale, measured the elastic anisotropy—defined as the ratio between E1 and E3—using nanoindentation techniques on Horn River shales. Their findings revealed that the clay fabrics within the overburden shale exhibit significant anisotropy, with anisotropy levels reaching as high as 1.8. In contrast, the clay content in the reservoir formation displayed lower anisotropy (E1/E3 = 1.3), which may be attributed to a more random orientation of particles. The correlation between clay contents and anisotropy has been observed in shales from gas-producing reservoirs (Sayers, 2013; Sone and Zoback, 2013). This correlation is primarily results from the fact that clays and other phyllosilicate minerals inherently possess significant intrinsic anisotropy due to their platy nature (Johnston and Christensen, 1995), whereas quartz and carbonates rarely exhibits sufficient lattice-preferred orientation (LPO) to make a substantial contribution to the overall anisotropy (Yu and Shapiro, 2014).

Table 3.5. Elastic constants used for ODF model.

Mineral	C11	C33	C44	C66	C12	C13	Reference
Quartz	86.6	106.1	57.8	39.95	6.7	12.6	Mavko, 2009
Illite	179.90	55.00	11.72	70.03	39.84	14.50	Katahara,1996
Chlorite	181.76	106.77	11.42	62.50	56.77	20.34	
Kaolinite	171.52	52.63	14.76	66.32	38.88	27.11	

The contribution of anisotropy arising from LPO can be estimated by averaging single-crystal elastic constants based on their volume fraction and crystal Orientation Distribution Functions (ODFs) (Kendall et al., 2007). To begin, I consider a grain-scale shale domain where all clay platelets are aligned, while other minerals, primarily quartz, exhibit random orientations. Using the mineral proportions, I can determine the effective anisotropic elastic tensor of this domain by combining the single-crystal elastic constants of constituent minerals, using the Voigt-Reuss-Hill averaging method. Subsequently, I introduce disorder into the alignment of these domains by averaging over an appropriate ODF. For Horn River shales, I consider a building block of rock aggregate composed of 60% clays (36% illite, 8% chlorite, and 16% kaolinite), and 40% quartz. Table 3.5 displays the elastic constants of the constituent minerals used in the model.

Although I lack petrofabric data to directly estimate the ODF of the clays, I can simulate the impact of clay alignment across various plausible textures using the principles outlined in (Sayers, 1994; Sayers, 2005) and the simplified matrix equations from (Johansen et al., 2004). The underlying assumption of the theory is that both the local shale domains and the resulting ODF exhibit transverse isotropy, enabling characterization with two expansion coefficients of generalized Legendre functions: W_{200} and W_{400}. The ODF or texture of the clay platelets is delineated by their location within the (W_{200}, W_{400}) plane. In scenarios where $W_{200} = W_{400} = 0$, the clay platelets are randomly oriented, resulting in an isotropic shale. Conversely, when clays are perfectly aligned, W_{200} and W_{400} reach their maximum values ($W_{200}^{max} \approx 0.04005$ and $W_{400}^{max} \approx 0.05373$), yielding pronounced anisotropy. The effective anisotropic stiffness tensor is computed using the Voigt approximation, from which the resulting Thomsen parameters can be determined. While all combinations of W_{200} and W_{400} up to their maximum values are theoretically possible, practical considerations suggest that disorder in clay platelet orientation tends to diminish W_{400} more rapidly than W_{200}, given that W_{400} is a higher-order moment of the ODF (Sayers, 2005). Consequently, it is expected that the texture of natural shales would predominantly occupy the region in the (W_{200}, W_{400}) plane defined by $\frac{W_{400}}{W_{200}} \leq \frac{W_{400}^{max}}{W_{200}^{max}}$.

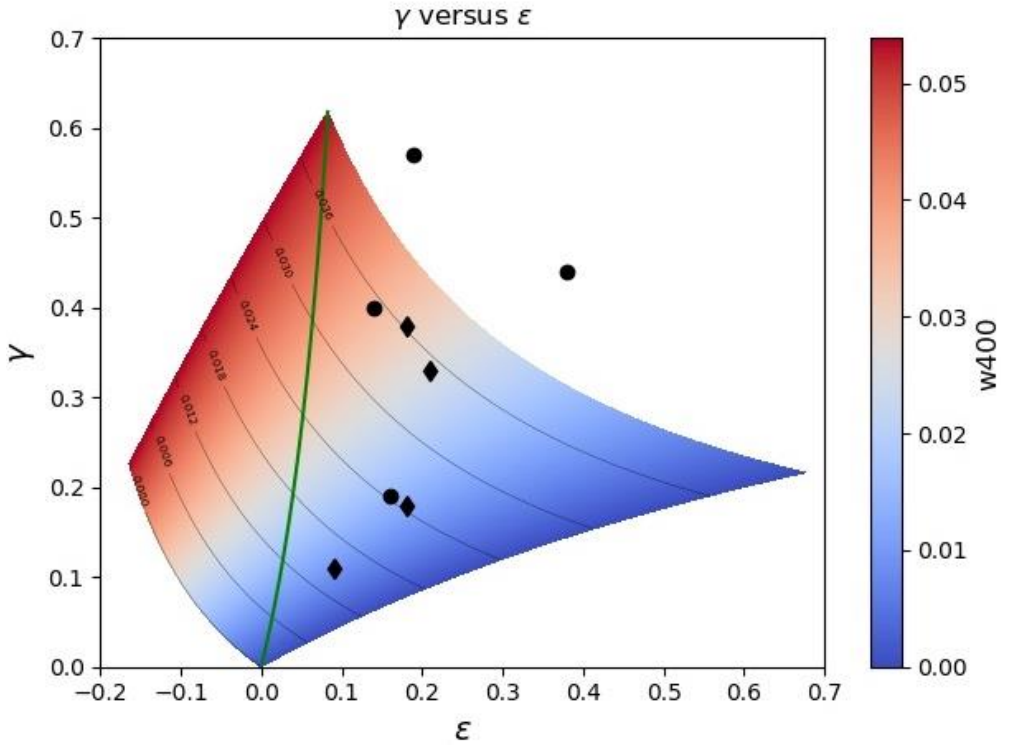

Figure 3.16. Plot of Thomsen's ε versus γ for varying coefficients W_{400} (colour) and W_{200} (thin isolines) of the ODF of clay platelets for a model composed of 60% clays (36% illite, 8% chlorite, and 16% kaolinite), and 40% quartz. The experimentally measured anisotropy of Horn River shales is superimposed on the plot. Circular markers represent overburden samples, and diamond markers represent reservoir samples. The green line indicates textures where W_{400} / $W_{200} = W_{400}^{max}$ / W_{200}^{max}. Natural textures are expected to plot to the right of this line.

Figure 3.16 illustrates the possible range of anisotropies (ε and γ) for all values of W_{200} and W_{400}, based on the procedures outlined by Pervukhina and Rasolofosaon (2017). The green line in the plot represents textures where $\frac{W_{400}}{W_{200}} = \frac{W_{400}^{max}}{W_{200}^{max}}$, suggesting that natural shale textures fall to the right of this threshold. The anisotropy results (ε and γ) obtained from measurements in this study are superimposed on the plot, with circular markers denoting overburden samples and diamonds markers representing reservoir samples. The first observation is that the clay platelet texture aligns well with the plotted field and satisfies the condition $\frac{W_{400}}{W_{200}} \leq \frac{W_{400}^{max}}{W_{200}^{max}}$, indicating its plausibility. This suggests that a significant portion of the anisotropy can be attributed to the lattice-preferred orientation (LPO) of intrinsically anisotropic clay minerals. However, it is important to note that some experimental data points from the overburden samples lie outside the plane predicted by the theoretical model based on elastic stiffnesses derived from the elastic properties of the domain. This indicates that the measured anisotropy cannot be fully explained by the LPO alone. Additionally, the elastic stiffnesses at the core scale may differ from those at mineral-scale domain within the same shale (e.g., Charlton et al., 2023).

Cracks, fractures, and microfractures, along with factors such as crack density, orientation, and connectivity, have been cited as contributors to anisotropy in shales (Vernik and Nur, 1992; Sone and Zoback, 2013). Microcracks can form due to failures in microstructure, often taking ellipsoidal shapes characterised by half lengths, a and w, where $w \ll a$. These features typically align parallel to the bedding plane, as cracks tend to develop along the shale's weaker planes (Vernik, 1993). However, they may also exhibit a preferred orientation at different angles, including perpendicular to the bedding plane, influenced by factors such as stress history, mineralogy, and TOC (Ougier-Simonin et al., 2016).

On a larger field scale, evidence of a horizontal transverse isotropy (HTI) overprint has been observed alongside predominately VTI in the Horn River shales. This phenomenon is attributed to a NE-striking vertical fracture set parallel to the maximum horizontal compressive stress (Baird et al., 2017). Studies in rock physics modelling and laboratory research, such as work by Allan et al. (2016), suggest that cracks aligned with bedding planes could exert a more pronounced influence on the VTI anisotropy in thermally mature organic-rich shales. This effect arises due to the conversion of load-bearing organic matter into oil and gas within layered shales, leading to a notable increase in horizontally aligned pores.

At present, the contribution of microfractures to the observed anisotropy and whether they account for anisotropy not attributable to the LPO effect cannot be definitively ascertained. SEM images (Figure 3.5) confirm the presence of sub-horizontal fractures and boundary contacts between the clay minerals. In these mature, fine-grained, low-porosity shales, such fractures appear to have formed as a result of organic matter maturation and are filled with bitumen, which subsequently underwent further maturation, releasing gas and generating organic matter porosity. The interconnectedness of pores and microcracks also governs permeability, influencing fluid diffusion during deformation. Incorporating detailed microstructural analyses would provide a more comprehensive understanding of how these features influence the anisotropic behaviour of fine-grained, low-porosity shales.

3.6.2 Implications for hydraulic fracturing operations in HRB

The geomechanical and seismic anisotropy characterization conducted in this study provide insights into the causes of observed anisotropy and the relationship between the composition and mechanical properties of the HRB Shales. This contributes to an enhanced understanding of induced seismicity due to hydraulic fracturing. The elastic moduli—Young's modulus and Poisson’s ratio—are the principal parameters used to evaluate the potential for successful hydraulic stimulation in low-permeability reservoirs. A high Young's modulus and low Poisson's ratio characterise brittle rock, whereas a low Young's modulus and high Poisson's ratio indicate more ductile behaviour (Rickman et al., 2008).

Figure 3.17 shows a cross-plot of Young's modulus and Poisson's ratio of the HRB shales from various studies. Data from Dong et al. (2017b) are derived from wireline logs of density and P-wave, while Teklu et al. (2018) and Moghadam et al. (2019) data are obtained through laboratory measurements. Also shown in Figure 3.17 is data from the organic-rich shale formations of the Perth Basin, Western Australia (Labani and Rezaee, 2015).

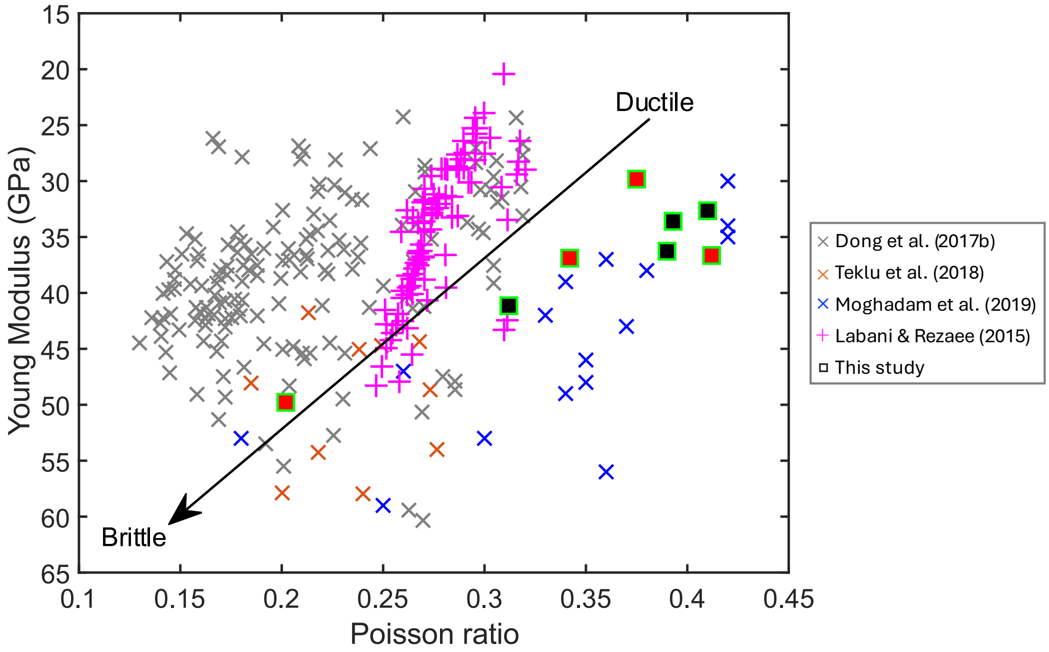

Figure 3.17. A cross-plot of Young's modulus and Poisson's ratio. High Young's modulus and low Poisson's ratio values indicate more brittle rock. In this study, overburden samples are represented by red-filled square symbols, while reservoir samples are shown with black-filled square symbols. The plot includes data derived from wireline logs of Vp and Vs (Labani and Rezaee, 2015; Dong et al., 2017b) alongside data from laboratory measurements. Note that the Young's modulus and Poisson's ratio values are generally higher in wireline logs and laboratory measurements under confinement compared to laboratory measurements conducted at ambient pressure. This discrepancy is primarily attributed to the consistently lower Vs values recorded in core samples, likely caused by pressure release during core retrieval.

Brittleness, an empirical relationship between Young's modulus and Poisson's ratio (e.g., Rickman et al., 2008), reflects the potential for creating open fractures during failure. This property varies across the overburden and reservoir units, as well as within the reservoir units themselves, primarily influenced by quartz and clay content. For instance, the Evie Member is recognized as the most brittle formation, making it highly suitable for hydraulic fracturing, followed by the Muskwa Formation (Dong et al., 2017b; Teklu et al., 2018; Moghadam et al., 2019). In contrast, the thick Fort Simpson Formation acts as an effective fracture barrier due to its high clay content. This clay-rich composition likely facilitates fracture closure through creep (e.g., Charlton et al., 2023) and provides a mechanical contrast that inhibits hydraulic fractures in the reservoir from propagating into the overburden formation.

The dependence of brittleness on the quartz and clay has been observed in several shale gas reservoirs. For example, in the Woodford shale system of west Texas, Upper Devonian in age, Aoudia et al. (2010) showed that Young's modulus and Poisson's ratio are most strongly influenced by clay and quartz content and, to a lesser extent, TOC. In addition, Labani and Rezaee (2015) showed that in the Perth Basin, Western Australia, the composition of the rock, particularly the quartz and clay content, significantly affects the rock mechanical properties and brittleness, while the quantity and maturity of organic matter have a less prominent impact. They highlight those geochemical parameters like TOC and thermal maturity influence rock properties at a nanoscale level, but their effect on macro-scale rock mechanical properties such as Young's modulus and Poisson's ratio is limited. Consequently, shale composition is a more critical factor than geochemical parameters for determining the potential intervals for hydraulic fracturing in gas shale layers.

As shown in the previous section, the anisotropy observed in HRB shales is primarily intrinsic, stemming from the lattice-preferred orientation of constituent clay minerals. Seismic wave anisotropy can significantly influence how stress is transmitted, distributed, and accumulated, thereby affecting both the spatial distribution and magnitude of induced earthquakes. Numerous studies have reported sequential, unilateral, and bilateral migration of microseismic event hypocentres during hydraulic fracturing of reservoir units in the Horn River formations (Woo et al., 2017; Yousefzadeh et al., 2018; Kettlety et al., 2019). This asymmetric growth in microseismicity is not uncommon and may be driven by gradients in the in-situ stress conditions or variations in geomechanical properties. In the Western Canadian Sedimentary Basin, the tectonic settings produce a net differential horizontal stress oriented northeast (Beaudoin et al., 2011). At HRB reservoir depth, the stress regime is classified as a strike-slip regime in the Anderson classification scheme, with $S_{Hmax} > S_V > S_{Hmin}$ (Kettlety et al., 2019).

The observed microseismicity—primarily representing shear slip along pre-existing faults and fractures—induces stress changes in the surrounding rock. Typically, increasing compressive stress leads to higher seismic velocities by closing pre-existing fractures and pore spaces, particularly those oriented perpendicular to the applied stress (e.g., Wang, 2002; Dewhurst and Siggins, 2006; Sarout and Guéguen, 2008). However, the effect of compressive stress on anisotropy is more nuanced. While fracture closure may indeed reduce directional dependence of elastic properties, compressive loading can also promote the formation of new microcracks, especially along weak planes or bedding-parallel orientations, potentially enhancing anisotropy. The net effect depends on multiple interrelated factors, including the magnitude and direction of the applied stress, the orientation of pre-existing anisotropy (e.g., bedding or aligned minerals), and the mechanical behaviour of the shale at the grain scale (e.g., Ougier-Simonin et al., 2016). Furthermore, the scale at which anisotropy is measured (core, plug, or field) can influence the observed trends. Therefore, while the intrinsic anisotropy in HRB shales stems from mineral alignment, changes during loading reflect a balance between fracture closure and new microcrack formation—processes that are themselves governed by stress magnitude, direction, and geological fabric.

3.7 Conclusion

In this chapter, I have presented the experimental characterization of the geomechanical properties and seismic anisotropy of HRB shales. A complete set of dynamic transversely isotropic (TI) stiffnesses for HRB shales was quantified using benchtop ultrasonic velocity measurements, and the Thomsen anisotropic parameters ($\varepsilon, \gamma, and\ \delta$) were determined. The results show that HRB shales exhibit high anisotropy in both P- and S-wave velocities, with anisotropy decreasing as clay content decrease. P-wave anisotropy reaches up to 38%, while S-wave anisotropy is as high as 57%, primarily due to the preferential alignment of clay minerals. A comparison with data from other organic-rich shales shows that the studied samples exhibit relatively high anisotropy, even with their comparatively low organic content.

In addition to anisotropy characterization, yield strength and peak stress were measured through triaxial loading tests conducted at confinement pressures ranging from 10 MPa to 80 MPa, representative of typical reservoir conditions. These tests provided stress-strain behaviour and static Young's modulus, revealing that static Young's modulus is pressure-sensitive, with overburden samples being stronger than reservoir samples. The HRB samples exhibited brittle failure under all tested pressure conditions.

The results indicate that the primary factors influencing these properties are mineralogy, diagenesis, and organic matter. These findings provide valuable insights into the geomechanical behaviour of HRB shales, which are critical for various applications. The anisotropy parameters, Young's moduli, and Poisson's ratios are particularly relevant for hydraulic fracture design, wellbore stability analysis, and in-situ stress determination. Notably, the core-scale anisotropy results align with field-scale anisotropy estimates derived from microseismic data (Baird et al., 2017) and with mineral-grain-scale anisotropy measurements obtained through nanoindentation (e.g., Charlton et al., 2023). This alignment is crucial for scaling geomechanical and anisotropy properties from gain-scale models to core-scale, reservoir-scale, and basin-scale characterizations.

4 Temporal and spatial evolution of acoustic emission and seismic parameters of Horn River shales during shear faulting

4.1 Introduction

4.1.1 Hydraulic fracturing, faulting and induced microseismicity

Hydraulic fracturing (HF) is a technique that involves injecting high-pressure fluid into low-permeability shale gas reservoirs to create a connected fracture network. This network enhances the porosity and permeability of the shale formations. Fracturing processes within the stimulated reservoir volume generate microseismic events, or "good microseismicity", because they indicate the effectiveness of the fracturing operation in increasing the porosity and especially the permeability of the tight reservoir, resulting in an increased hydrocarbon production rate (Schultz et al., 2020b).

Microseismic events confined within the stimulated reservoir typically have a magnitude of Mw ≤ 3 (Li et al., 2019). These artificially created microseismic events, or “good microseismicity,” do not produce ground motion and are generally not felt at the surface (Rubinstein and Mahani, 2015; Verdon and Budge, 2018). Figure 4.1 shows the microseismicity associated with hydraulic fracturing operations in major North American shale basins, indicating that, although differences exist among these shale reservoirs (Warpinski et al., 2012), the maximum seismicity induced by thousands of hydraulic fracture stimulations within the target formation is below M 1.0 (Zhao et al., 2018). However, microseismicity or seismic events that occur beyond the stimulated reservoir volume, often with larger magnitudes due to the development or reactivation of pre-existing faults located outside the reservoir (Figure 4.4), poses a significant geohazard risk for society (Lei et al., 2017; Wang et al., 2017; Wang et al., 2020a).

As HF deforms rock through the creation and opening of fractures, a myriad of hydromechanical processes influence both hydraulic fracture propagation and damage evolution, controlling the dimensions of hydraulic fractures and associated seismicity. Understanding the processes that lead to microcrack initiation and propagation within shales during HF is crucial for mitigating induced seismicity and optimizing fracturing practices (Atkinson et al., 2020; Igonin et al., 2021). Shear faulting is a critical geological process that involves the sliding of rock layers along fractures or faults (Thompson et al., 2009; Ougier-

Simonin et al., 2016), significantly affecting both natural seismicity and HF efficiency in shale formations (Wu et al., 2017).

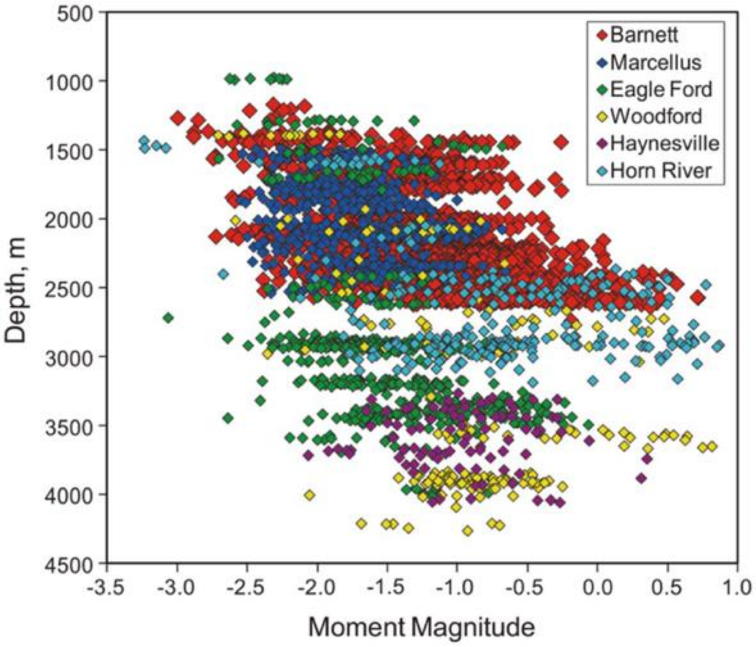

Figure 4.1. Microseismic magnitudes recorded in hydraulic fracturing operation in major North American shale basins. Each data point represents the maximum microseismicity stimulated by a hydraulic fracture treatment (Zhao et al., 2018).

Laboratory experiments provide a controlled environment to simulate and understand the micromechanical processes leading to seismic events observed in the field. By replicating subsurface stress conditions within the reservoirs, these studies allow for a detailed observation of fracture mechanics, shedding light on the initiation, propagation, and coalescence of fractures that precede seismic disturbances. During HF, changes in the stress state can cause brittle damage and fracturing in rocks, releasing mechanical energy as elastic waves detected as microseismic events. The initiation and development of fractures in stressed rock have been extensively studied in the laboratory settings using various techniques (Lockner et al., 1991; Lockner et al., 2002; Thompson et al., 2009; Ougier-Simonin et al., 2016).

One approach involves observation of the microstructure of samples via techniques such as optical microscopy or scanning electron microscopy (SEM) (Milner et al., 2010). Another method monitors the hypocentre distribution of acoustic emission (AE) events generated by microcracking activity (Stanchits et al., 2006; Goebel et al., 2013; Goodfellow and Young, 2014; Kwiatek et al., 2014). The advantage of using AE compared to microstructural observations is that the latter are limited to still images of faulting after the faulting event has happened, which can be 2D or 3D and range from nanometre to millimetre or centimetre scales. AE, on the other hand, enables the real-time study of faulting and fracturing as it evolves from onset to termination and samples a 3D volume through events location within the test specimen. Additionally, AE allows for the quantitative analysis of seismic parameters such as frequency-magnitude distribution, *b*-value, and their evolution in time as faulting progresses. Furthermore, by analysing the characteristics and distribution of these microseismic events, one can infer the onset of crack initiation, coalescence, propagation, and the potential for sudden structural failures (Vinciguerra et al., 2004; Benson et al., 2007).

4.1.2 Hydraulic fracturing induced seismicity in the HRB: a case study

The Horn River Basin (HRB), a prominent part of the Western Canadian Sedimentary Basin (WCSB) (Figure 4.2A), has gained significant attention due to its substantial hydrocarbon resources potential. The marketable dry gas resource in this region is estimated to exceed 70 trillion cubic feet (2.0 × 10^{12} m^3) (Schultz et al., 2020b). The HRB comprises three distinct overpressured, organic-rich shale formations: Muskwa, Otter Park, and Evie (Figure 4.2B). These are overlain by the Fort Simpson shale, a clay-rich shale with low organic content, and underlain by the Keg River carbonate (Dong et al., 2017b). The stratigraphical and geological settings of the HRB are presented in Chapter 3. Exploration and hydraulic fracturing activities began in 2006, peaking in 2011 (Figure 4.3B).

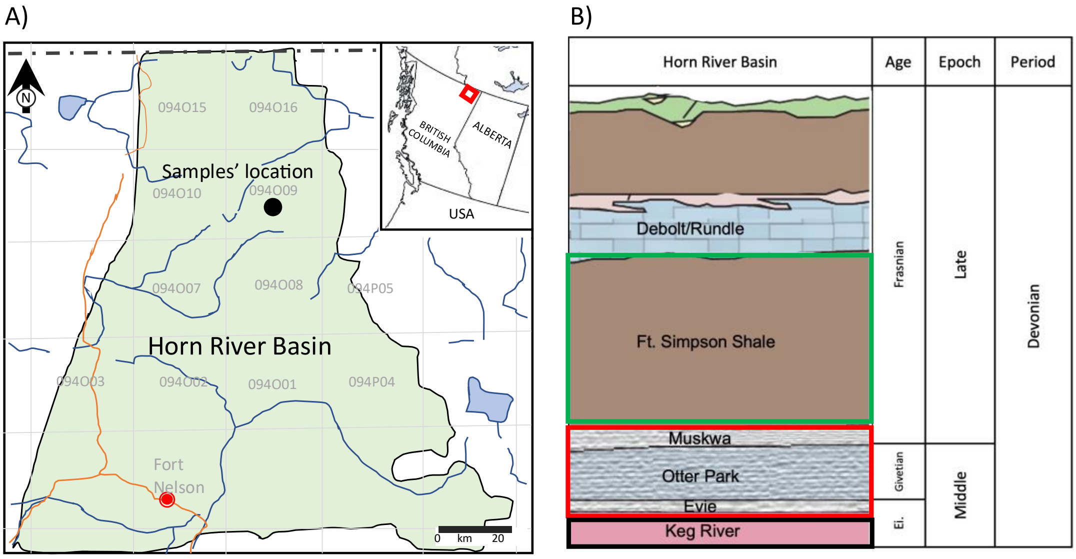

Figure 4.2. (A) Map showing the location of the HRB in British Columbia and the samples well location; (B) Stratigraphic column of HRB shales. Assembled from Dong et al. (2015), and Mo et al. (2018).

Since the start of HF operations, an increase in both the seismicity rate and average magnitude, rising from M 2.9 to 3.6, has been observed in the HRB region (Figure 4.3) (Schultz et al., 2020b). This rise in seismic activity has raised concerns among governments and local communities about various environmental and public safety issues, particularly, the potential for increased seismic hazards from larger earthquakes induced by HF outside the target reservoir (Figure 4.4). For instance, multiple earthquakes with magnitudes exceeding 3 have been recorded in the HRB, leading to the implementation of traffic light protocols (TLP), which require operators to enact control measures when a specified magnitude is recorded (Wang et al., 2017; Schultz et al., 2018).

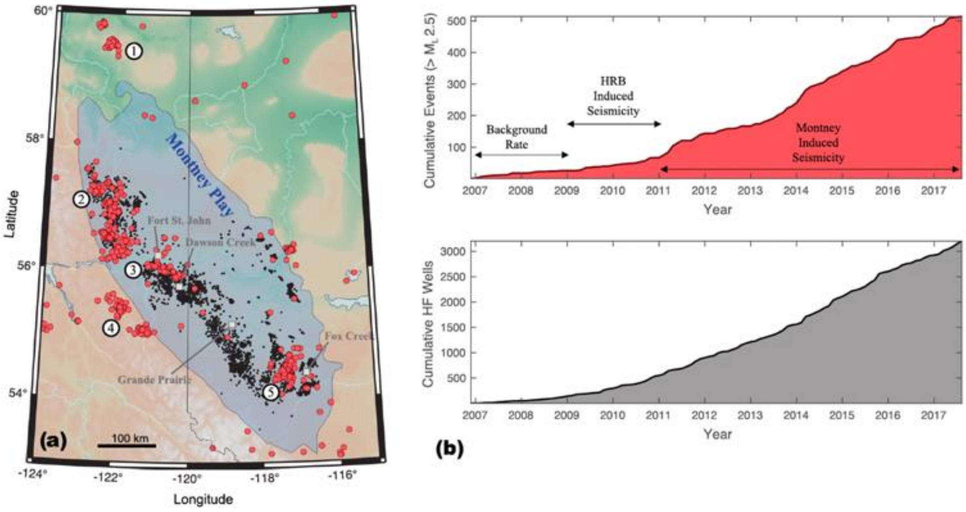

Figure 4.3. Locations and timings of HF-induced events in British Columbia (BC). (a) A map showing seismicity in BC (red circles). This map includes larger seismic events (ML ≥ 2.5) recorded from October 2006 to September 2017. The seismicity cluster in Horn River Basin is labelled as number 1. (b) Graphs showing cumulative seismicity in BC (upper panel) and the number of horizontal HF wells in BC (lower panel). The cumulative seismicity graph shows changes in the seismicity rate, transitioning from background levels to increased activity during the development of the HRB and then development of the Montney play. The number of hydraulically fractured wells in BC show a relatively steady rate starting in 2010 (Schultz et al., 2020b).

Additionally, a comprehensive analysis of microseismicity in the region indicates that a key seismic event recurrence parameter, the *b*-value — representing the relative abundance of small versus large earthquakes — is estimated to be 1.21. This value exceeds the typical *b*-value of natural tectonic earthquakes, which is around 1, suggesting a physical correlation between HF operations and induced seismicity in the area (Farahbod et al., 2015). Verdon and Budge

(2018) analysed the spatial distribution of over 232,000 events detected during hydraulic stimulation in the HRB. They reported several larger magnitudes (up to Mw 1.3), which exceed the typical magnitudes observed during hydraulic fracturing of shale gas reservoirs, where magnitudes are generally below Mw 0 (Figure 4.1).

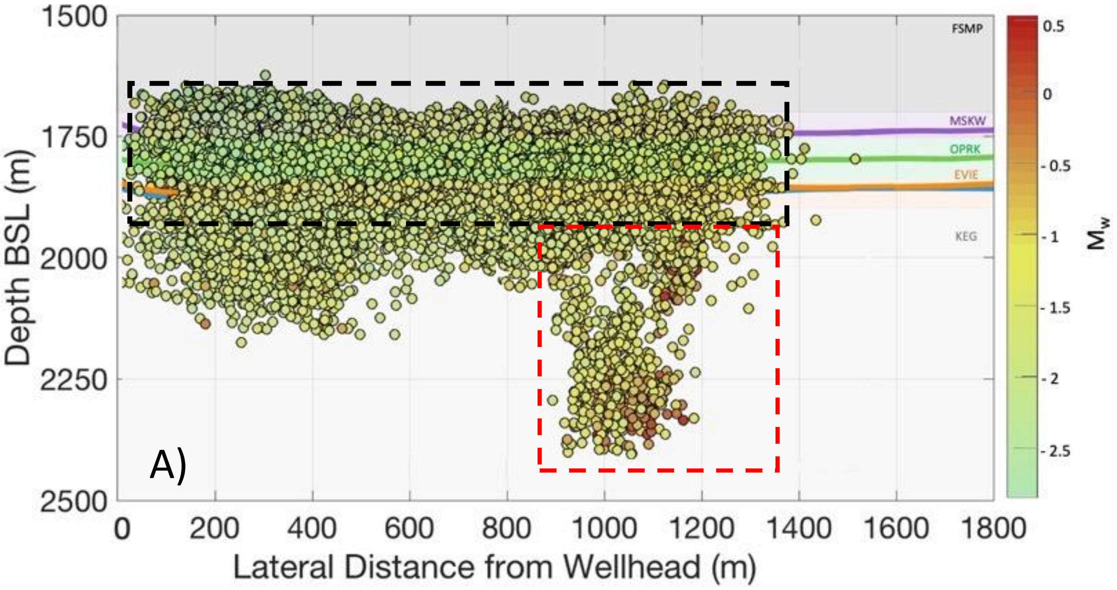

Figure 4.4. Cross-section view of events recorded during hydraulic fracturing in the HRB. Events are colour-coded by moment magnitude (Mw). Three reservoir units— Muskwa, Otter Park, and Evie— are targeted for hydraulic fracturing stimulation (solid horizontal lines). The dashed black box indicates the area of "good microseismicity" within the stimulated reservoir volume. Higher-magnitude events are recorded below the target formations, outside the reservoir volume (red dashed box). Modified from Kettlety et al. (2019).

Kettlety et al. (2019) investigated the role of elastic stress transfer in a microseismic dataset from the HRB. They quantified cumulative stress release from microseismic events associated with seismicity confined within the stimulated reservoir formations, finding magnitudes between −2 < Mw < −1 and a *b*-value > 1.5, which are likely due to fracturing processes. However, for events outside the target reservoir in the underburden (Figure 4.4), they identified magnitudes ranging from 0.0 ≤ Mw < 0.5 and a *b*-value ≈ 1.0, suggesting interaction with pre-existing faults. Snelling et al. (2013) examined *b*-values for events induced by HF within the reservoir formations, finding that different target intervals in the Horn River shales responded differently to hydraulic stimulation. For example, using events recorded in six wells (three completed in the Muskwa and three in the Evie formation), they found that *b*-values in the Muskwa formation range from 1.9 to 2.8 (Figure 4.5), while values in the Evie formation were distinctly lower, between 1.0 and 1.4. These observations support findings that lower *b*-values are generally associated with events recorded in the lower formations beneath the target reservoir. Elevated *b*-values around 2.0 are associated with hydraulic fracturing processes, whereas *b*-values approaching 1.0 suggest potential fault reactivation.

The exploitation of hydrocarbon resources in the HRB, specially through hydraulic fracturing (HF), requires a comprehensive understanding of the mechanical behaviour and seismic responses of shales under shear stress. This chapter presents the results and analyses of controlled laboratory deformation experiments on Horn River (HR) shales. Intact shale cores were triaxially loaded beyond the failure point under subsurface stress and pore pressure conditions, while the associated microseismic activity was recorded using AE monitoring. The key objective was to characterise the microseismic response of HR shales and to correlate the evolution of the AE rate, *b*-value, and P-wave velocity with the progressive shear-induced degradation leading to macroscopic failure.

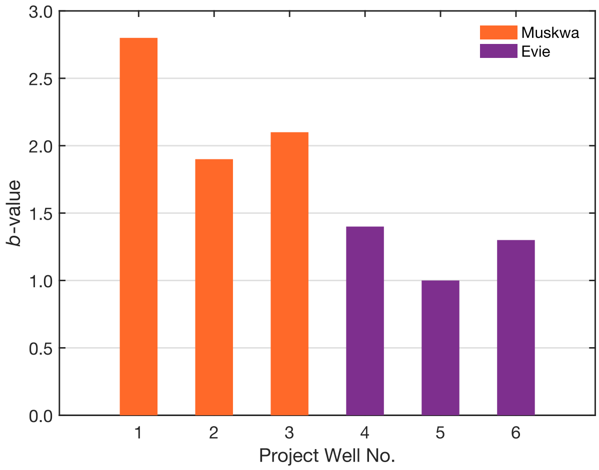

Figure 4.5. *b*-values variation in the target reservoir formations of the HRB (Snelling et al., 2013).

The insights gained from these laboratory experiments have broader implications for HF practices and seismic hazards management. By connecting the laboratory-scale observations of AE during shear faulting with larger-scale seismic phenomena observed in the field, this study aids in the development of safer and more effective fracturing techniques that minimize structural impacts and address societal concerns. Moreover, through a comprehensive analysis of AE data and fracture mechanics, this research contributes to a deeper understanding of the geomechanical responses of shales, enhancing our ability to manage and optimize resource extraction while mitigating the risks associated with subsurface fluid injection activities.

This chapter focuses on studying micro-fracturing in intact shale samples from the HRB, with particular attention to precursory signs of major failure events during HF. The following chapter (Chapter 5) will address safety issues related to larger, induced seismic events triggered by the reactivation of larger faults in the underburden.

4.2 Experimental techniques

In this section, a brief description of the experiments conducted, and the parameters measured and calculated is provided. Detailed information about the techniques and equipment used are presented in Chapter 2.

4.2.1 Triaxial loading experiments.

Shale core plugs from the Horn River Basin were subjected to failure tests using the Durham University Triaxial Apparatus with Fluid Flow (Dutff). See Chapter 2 for a detailed description of the apparatus, including measurement sensors and machine calibrations. The HRB consists of organic-rich shale units from the Horn River Formations, specifically the Muskwa, Otter Park and Evie formations. These units have been targeted by hydraulic fracturing for shale gas extraction. They are overlain by the clay-rich shale of the Fort Simpson Formation (Dong et al., 2015). The petrological and mineralogical characteristics of the Formations, as well as the physical properties of the samples, are presented in Chapter 3.

Two samples from the Fort Simpson Formation and one sample from Muskwa Formation were used for the triaxial loading experiments, where sharp contrasts in elastic anisotropy and seismic response have been reported (Yu and Shapiro, 2014; Baird et al., 2017). The samples were kept at room temperature and humidity throughout the experimental work. Figure 4.6 shows the samples assembly, including a shale core plug, a piezoelectric sensor, the acoustic emission recording system, and examples of mechanical and AE data recorded.

Table 4.1. Samples used for the triaxial loading experiments.

Sample No.	Experiment No.	Depth (m)	Bulk density [g cm^{-3}]	TOC [wt % C]	Formation
A12	Dutff 348	2571.9	2.56	2.10	Fort Simpson
A14	Dutff 350	2575.9	2.54	2.21	Fort Simpson
A15	Dutff 351	2589.5	2.49	5.88	Muskwa

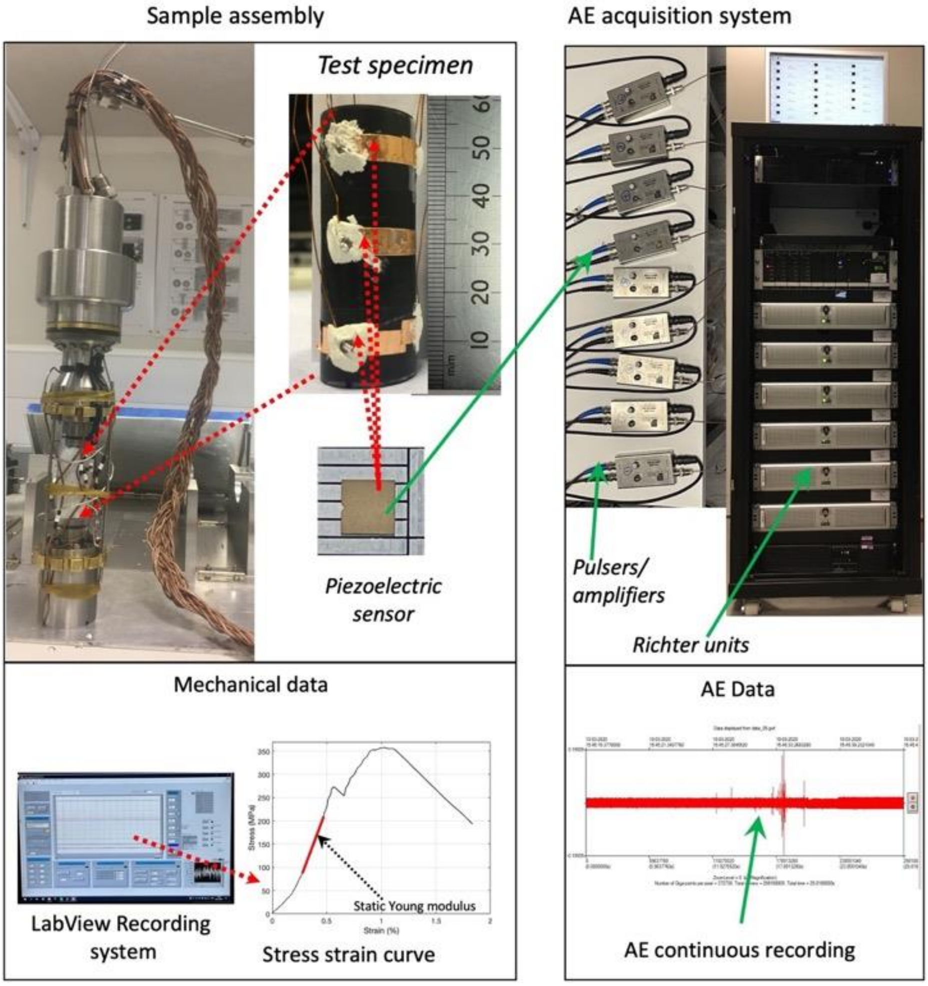

Figure 4.6. A photograph of the sample assembly with the sample jacketed in PVC and mounted, and a shale core plug with piezoelectric sensor attached. The AE recording system and graphs of examples of the mechanical and AE data recorded.

During triaxial loading experiments to failure, nine piezoelectric (PZT) sensors were installed along the sample circumference located on three different planes, evenly distributed in each plane (Figure 4.7C). The first plane is at 50% height of the specimen, and the other two planes are located 10 mm from the top and bottom of the specimen (Figure 4.7C). See Chapter 2, for a detailed description of the sensors, including installation procedures, connections, soldering, and assembly sealing mechanism. After sensors instrumentation, the specimen is wrapped with a Teflon tape and jacketed into a PVC tube to isolate it from the silicone oil confining medium used in the pressure vessel. The Teflon tape facilitates the specimen's insertion and minimises friction with the PVC. A hole is made on the PVC tube wall to allow extraction of sensors lead wires, which is backfilled with Loctite Hysol 9455 flexible epoxy. Then, the jacketed specimen is mounted on the sample assembly and inserted into the pressure vessel of the triaxial loading apparatus. Signals from the sensors are transmitted in and out of the pressure vessel through twelve narrow boreholes drilled in the top part of the assembly.

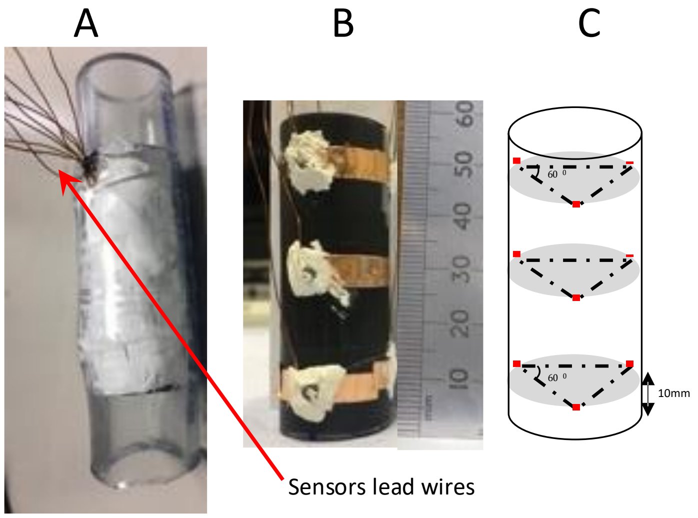

Figure 4.7. A) A shale sample inserted into a PVC tube with sensor lead wires extracted. B) A shale core with attached piezoelectric sensors. C) Schematic shows the locations of the sensors.

4.2.2 Loading protocol, measured and calculated parameters

The loading protocol consists of three main stages: (i) an isotropic loading to subject the specimen to a confinement pressure simulating reservoir pressure condition, (ii) differential stress loading at a constant axial shortening rate of 1 µm s^{-1} until sample failure, and (iii) fluid injection at a constant pore pressure during the post-macroscopic failure stage, to reactivate the newly formed faults.

Three experiments were conducted at confining pressures ranging from 10 MPa to 80 MPa and pore pressures from 0.01 MPa to 50 MPa. For each experiment, I measured confining pressure, fluid pressure, applied force, and axial shortening. The applied force was corrected for machine stiffness. Using the known initial cross-section area and length of the test specimen, axial stress and axial strain were calculated. For detailed calculation procedures of the experimental parameters and corrections see Chapter 3, Section 3.4.2.

4.2.3 Acoustic emissions data recording and processing

In addition to measuring the mechanical parameters, acoustic emissions (AE) are recorded using a Richter high-frequency (10 MHz) acquisition system. The signals from the piezoelectric sensors are digitized using Richter units at 16-bit resolution and sampled at a 10

MHz, continuously streamed, and stored on a hard drive for processing (see Chapter 2, Section 2.6). The AE data is processed post-acquisition, and AE rate, events' hypocentre, magnitude, *b*-value, fractal dimension (D-value), and P-wave velocity evolution are calculated. The processing involves filtering and running a search algorithm to identify and extract discrete events (see Chapter 2, Section 2.6). For each extracted event, the P-wave arrival time is determined using short-term/long-term averaging routine. The Simplex algorithm is then utilized to locate the events' hypocentre. Once each event is located, a location magnitude is calculated. For a cluster of located events, the *b*-value, P-wave velocity, and D-value are estimated. The acquisition system is operated using InSite-Lab software, a proprietary of ITASCA. For further details about the acquisition system and post-acquisition processing of the AE data see Chapter 2, Section 2.6.

4.2.4 Post-deformation computerized tomography (CT) scan

After the loading experiments, the fractured samples were imaged using an X-ray computed tomography (CT) scanner. This technique employs X-rays to create a 3D image of a sample by stacking cross-sectional 2D X-ray attenuation projections. A threshold segmentation based on image intensity (grayscale) values was applied, enabling the visualization and analysis of fracture distribution, fault geometry, and the damage zone within the sample's volume. The images have a voxel size of 300 × 300 × 300 µm. Segmentation procedures and visualization were performed using Avizo® software (see Chapter 2, Section 2.8). To preserve the initial state of the deformed samples and to minimize damage during scanning process, the samples were wrapped in Sellotape after extraction from the Triaxial loading apparatus.

4.3 Results

A total of three triaxial loading experiments were conducted on intact core samples of Horn River Shales, at room temperature, with confining pressures ranging from 10 MPa to 80 MPa and pore pressures from 0.01 MPa to 50 MPa. During each experiment, the samples were loaded to failure while continuous acoustic emission monitoring was conducted.

4.3.1 Mechanical data

4.3.1.1 Experiment Dutff 348 (sample A12)

This experiment was conducted at a confining pressure of 10 MPa, under room temperature and humidity conditions without pore fluid pressure. During the loading of the sample to failure, three distinct deformation stages are identified, each characterised by a specific stress and slip evolution (Figures 4.8 and 4.11). In the first stage, the sample undergoes linear elastic deformation until it reaches the yield stress of 350 MPa (Figure 4.8). At approximately 0.5 % strain, a sudden small stress drop of 18 MPa was observed, likely due to a minor fault slip of 50 µm (vertical component of slip) along a pre-existing fault (Figure 4.11). Following this small slip event, the sample continues to undergo elastic deformation until it reaches the yield stress, when the sample transitions into the pre-failure stage (pink area in Figure 4.8).

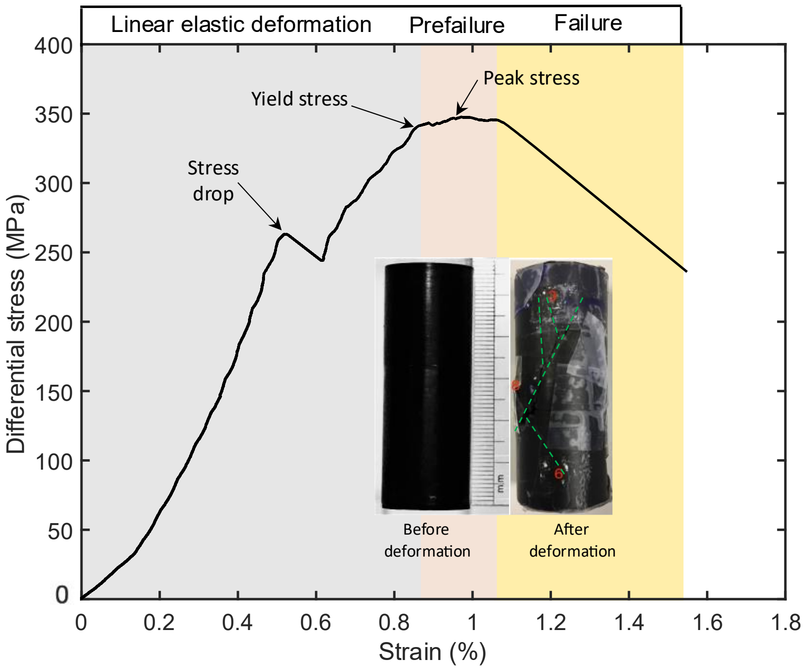

Figure 4.8. Stress vs. strain evolution for experiment Dutff 348 conducted at 10 MPa confining pressure. No fluid injection after the macroscopic failure of the sample. Three deformation stages are identified: 1) linear elastic deformation stage (grey coloured area); 2) prefailure stage (pink coloured area), and 3) failure stage (yellow coloured area). The insert shows the sample before and after deformation.

In the pre-failure stage, the sample starts weakening and accumulate significant amount of strain under almost constant stress, with only a small stress increase towards the peak stress value (Figure 4.8). Finally, during the following failure stage, a sudden stress drop of 150 MPa is observed, corresponding to a vertical component of slip of 300 µm (Figure 4.11) along the newly formed fault in the sample (yellow area in Figure 4.8). Details of the stress drop phase show that failure of the sample occurred in two stages, beginning with a gradual slow decrease of stress and slow slip before a sudden fast stress drop and slip on the newly created fault (Insert in Figure 4.11).

4.3.1.2 Experiment Dutff 350 (sample A14)

This experiment was conducted under room temperature, with a confining pressure of 80 MPa and a pore pressure up to 0.04 MPa. It followed the same loading protocol as Experiment 348, continuing until macroscopic failure. Following failure, fluids were injected at pressure into the sample to investigate any role played by pore pressure in the reactivation of the newly formed fractures. As with Experiment Dutff 348, three distinct deformation stages were identified for sample Dutff 350: a linear elastic deformation stage, followed by pre-failure and failure stages (Figure 4.9). In the first stage, the sample undergoes linear elastic deformation until the yield stress of 260 MPa is reached (Figure 4.9). Loading beyond the yield point shows a deviation of the loading curve from the linear trend, indicating that the sample transitions into the pre-failure stage when its starts weakening (Figure 4.9). The weakening continues until the sample reaches a peak stress of 380 MPa. At this peak stress, macroscopic failure occurs as shown by an abrupt stress drop of 15 MPa (Figure 4.9) and a 50 µm of slip (vertical component of slip) along the newly created fault (Figure 4.12).

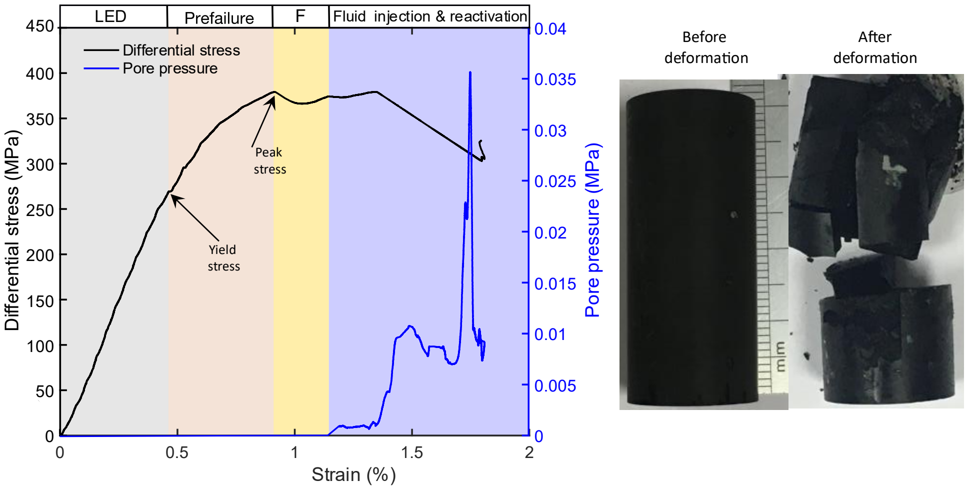

Figure 4.9. Stress vs. strain, and pore pressure evolution for Dutff 350. Similar to Dutff 348, three loading stages are identified. After macroscopic failure, fluid is injected into the newly formed fault. Pictures on the right shows the sample before and after deformation. LED: linear elastic deformation; F: Failure.

During further loading after stress drop and failure, the sample undergoes slip hardening (Figure 4.9). In the subsequent phases of the experiment, fluids were injected in the sample at pore pressure of 2 kPa (Figure 4.9). It takes about 90 seconds for the sample to become completely saturated. After saturation of the sample, continuous fluids injection in the sample triggered a spontaneous slow slip lasting 140 s, which is characterised by 120 μm of slip (vertical component of slip) and a slow stress drop of 45 MPa (Figure 4.12). During the fluid induced slow slip event, pore fluid pressure initially increased and then started to drop until the end of the slip event (Figure 4.9). The pore pressure evolution indicates that an early phase of shear compaction was followed by shear dilation during the slow slip event.

4.3.1.3 Experiment Dutff 351 (sample A15)

This experiment was conducted under room temperature conditions, with a maximum confining pressure (Pc) of 80 MPa and a pore pressure of up to 50 MPa. Unlike Experiments Dutff 348 and 350, a different loading protocol was adopted: the Pc was increased in steps of 10 MPa until the target confining pressure of 80 MPa was reached (Figure 4.10). After each 10 MPa increase in confining pressure, the sample was loaded axially until the differential stress equalled the confining pressure. At that point, axial loading was paused, and the confining pressure was increased by 10 MPa for the next step. Once the target Pc of 80 MPa was reached, the confining pressure was held constant, and the sample was loaded to failure (Figure 4.10). Following macroscopic failure, fluids were injected into the sample at pressure to investigate any role played by pore pressure in the reactivation of the newly formed fractures (Figure 4.10).

Similarly to what observed in Experiments Dutff 348 and 350, three deformation stages were identified for Experiment Dutff 351: a linear elastic deformation stage, followed by pre- and failure stages. The first phase of linear elastic deformation lasted up to yield point of 190 MPa differential stress, corresponding to a Pc of 70 MPa. Loading beyond the yield point shows a deviation of the loading curve from the linear trend, indicating that the sample transitions into the pre-failure stage when its starts weakening (Figure 4.10). The weakening continues until the sample reaches a peak stress of 215 MPa, at Pc = 80 MPa (Figure 4.10). After the peak stress, macroscopic failure occurs as shown by an abrupt stress drop of 55 MPa and 190 μm of slip (vertical component of slip) along the newly created fault (Figure 4.13).

Following the macroscopic failure event, fluid is injected into the sample which is saturated within 40 s. Once the sample is saturated, the pore fluid pressure is maintained at 5 MPa and the sample is loaded for 10 minutes without any noticeable variation in stress, apart from the gradual stress increase suggesting that the fault is locked (Figure 4.10). After 10 minutes of loading, the pore fluid pressure is increased and, when it reaches 45 MPa, a spontaneous slow slip event is triggered, lasting 70 s with 10 μm of slip (vertical component of slip) and a slow stress drop of 7 MPa (Figure 4.13). During the fluid induced slow slip event, pore fluid pressure is decreased to 10 MPa. During this imposed transient pore pressure decrease, I observe an evolution of the slip velocity from an initial lower velocity of 0.14 μm s^{-1}

to a faster slip velocity of 1.22 µm s^{-1} (Figure 4.13). Subsequently, pore fluid pressure is increased and maintained at 50 MPa until the end of the experiment. The increase in pore pressure did not trigger any further spontaneous fluid induced slip events.

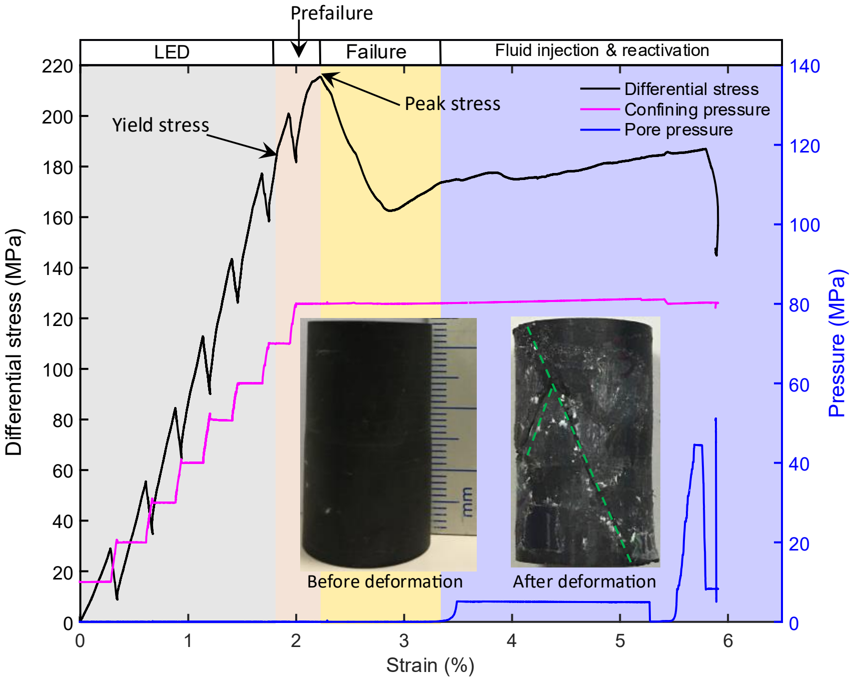

Figure 4.10. Evolution of stress-strain, confining pressure, and pore fluid pressure during experiment Dutff 351. The sample was loaded under stepwise increases in confining pressure from 10 MPa to 80 MPa, in increment of 10 MPa, without unloading between stages. See the text for details. As Dutff 348 and Dutff 350, three loading stages are identified. The insert shows pictures of the sample before and after deformation.

4.3.2 Acoustic emission data

Acoustic emission (AE) data was processed by running a triggering algorithm to identify and extract discrete events (e.g. Section 4.2.3). The algorithm triggered 300, 285 and 96 events for experiments Dutff 348, Dutff 350, and Dutff 351, respectively. I then performed a visual inspection of the triggered dataset, which allowed to identify a few events as electrical noise, and others with a too low signal-to-noise ratio (SNR). These events were manually removed from the dataset, leaving only events that could be reliably located within the volume of the specimen, which were used in my further analyses. This selection procedure resulted in a total of 120, 156 and 23 events for experiments Dutff 348, Dutff 350 and Dutff 351 respectively (Figures 4.11, 4.12 and 4.13).

Using velocity models derived from benchtop measurements for each sample (Chapter 3), the hypocentres and relative magnitude of the AE events were calculated (Figures 4.11, 4.12 and 4.13) with the Simplex algorithm in InSite software (Chapter 2, Section 2.6.2). The average hypocentre location error for the whole dataset is ±3 mm, calculated using an average of six sensors per event. This location error is estimated based on uncertainties in picking the arrival time of the first phase and experimental measurements of the sensors' locations.

In all figures, AE events are shown as spheres within a semi-transparent model of the test specimen. The colour of each sphere represents the relative time of occurrence (green for early events, red for later ones), while the size of the spheres corresponds to event magnitude. The recorded event magnitude ranges are as follows: for experiment Dutff 348, –4.65 to –2.84; for Dutff 350, –3.10 to –1.70; and for Dutff 351, –3.58 to –2.72. Note that these are relative magnitudes, as explained in the Methods chapter. They are calculated from the recorded signal amplitude (Section 2.6.2.4) and are specific to the sensor configuration used in each experiment. Therefore, in the discussion that follows, I refer to magnitudes in qualitative terms.

4.3.2.1 Linear elastic deformation stage

During the linear elastic deformation stage, all samples recorded either very modest microseismic activity or no microseismicity, as shown by the small cumulative number of microseismic events (Figures 4.11, 4.12, and 4.13). This stage is typically characterised by minor adjustments within the material, where only minimal strain is accommodated by small-scale cracking, without any major faulting or fracture development. The only exception to this trend was a small peak of acoustic emissions recorded during a minor slip event, which occurred in the early stages of the linear elastic deformation of experiment Dutff 348 (Figure 4.11A). This isolated increase in AEs suggests that a localized, small slip event temporarily disrupted the otherwise stable elastic linear deformation. The AEs locations indicate that these events were distributed with relatively small magnitude compared to events observed in later deformation stages (Figures 4.11B and 4.13B). Subsequently, the rate of seismicity remained relatively stable, at a very low level throughout the rest of the linear elastic deformation stage (Figures 4.11 and 4.13). This steady, low-level activity aligns with linear elastic behaviour, where stress-induced microcracks remain scattered and unconnected.

Overall, the few events recorded during the linear elastic deformation stage can be interpreted as resulting from sparse, distributed microcracking scattered within the sample (Figures 4.11B and 4.13B). These small-scale cracks are likely caused by minor internal stress adjustments and do not indicate any significant failure processes or precursors to larger-scale deformation.

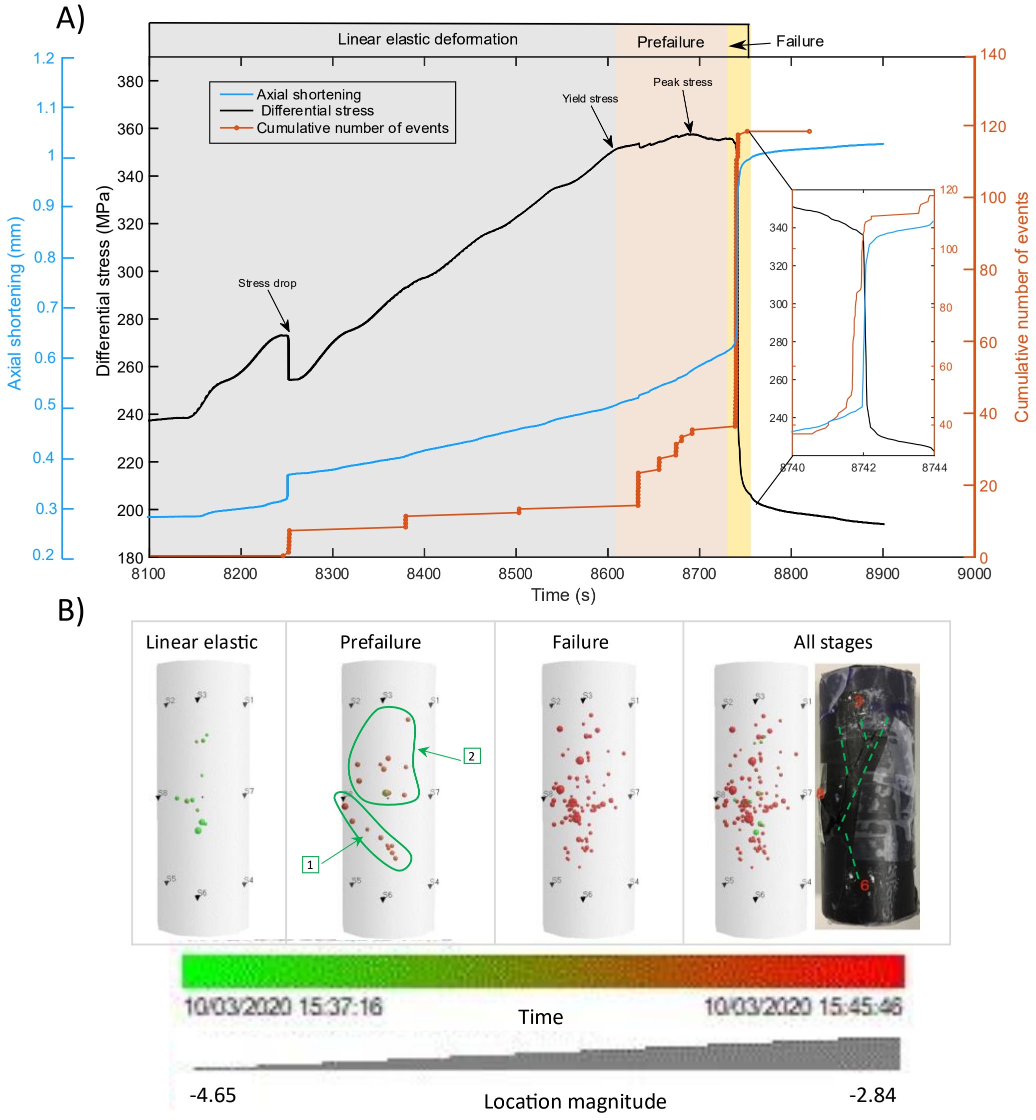

Figure 4.11. A) Evolution of differential stress, axial shortening, and cumulative number of AE events for Experiment Dutff 348. B) Snapshot showing the spatial and temporal distribution of microseismic events corresponding to the three identified deformation stages. The post-deformation image of the sample shows the formation of a main fault with a dip of approximately 30 degrees relative to the specimen's axis. Three minor faults branch off from the main fault, each dipping at about 30 degrees to the main fault (green dashed lines).

4.3.2.2 Pre-failure stage

From the onset of the pre-failure stage, all samples show a marked increase in the rate of AE, which indicates a notable uptick in AE activity compared to the preceding linear elastic phase. After this initial surge, the AE rate stabilizes at a constant level, persisting through much of the pre-failure stage until the approach of the failure stage (Figures 4.11, 4.12, and 4.13). This temporary plateau in AE activity suggests a period of semi-stable crack growth, where the rate of microcracking remains steadily higher than in the linear stage, but does not yet trigger immediate, large-scale failure. The spatial distribution of these AEs reveals that they are still widely spread throughout the sample (Figures 4.11B, 4.12B, and 4.13B), with individual events showing moderate magnitudes compared to those observed during the linear elastic deformation stage. However, there are early indications of localization, with some AEs beginning to align along an incipient fault plane (Figure 4.11B).

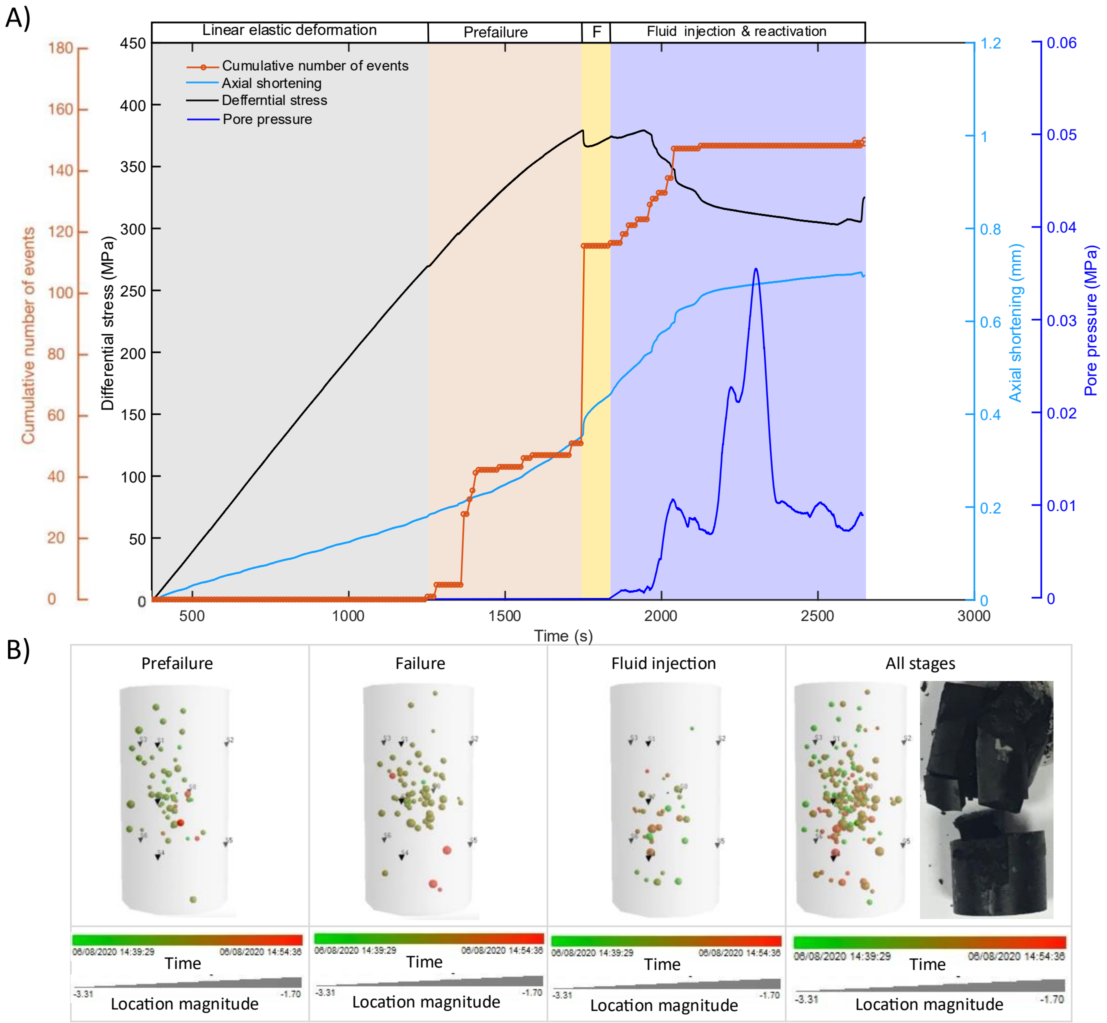

Figure 4.12. A) Evolution of differential stress, axial shortening, and cumulative number of AE events for Experiment Dutff 350. B) Snapshot showing the spatial and temporal distribution of microseismic events corresponding to the identified deformation stages. Note that the time scale is relative to each deformation stage.

In general, the increasing number of AE events recorded during the pre-failure stage, along with their evolving spatial, temporal, and magnitude characteristics, can be interpreted as evidence of coalescing microcracks and the progressive development of the final rupture plane (Figures 4.11, 4.12, and 4.13).

4.3.2.3 Failure stage

Upon reaching the failure stage, all sample show a sharp and sudden increase in the emission rate detected during the rapid stress drop phase of the macroscopic failure events (Figures 4.11, 4.12, and 4.13). The spatial distribution of AEs during this stage highlights the clustering of events along the fully developed rupture plane (Figures 4.11, 4.12, and 4.13). A sudden, sharp increase in the microseismicity rate indicates the coalescing of microcracks and acceleration of the final rupture plane. The insert in Figure 4.11A demonstrates that, contrary to the stress drop and fault slip, the exponential microseismic emission occurred in two distinct phases. In the first phase, an accelerating emission rate precedes the main failure event, while in the second phase the emission rate remains high without a preceding acceleration, suggesting that the macroscopic failure event may have consisted of multiple failure events, rather than a single one.

This pattern suggests that the primary failure may involve successive, discrete slip events along the fault, each contributing to the overall macroscopic stress drop observed during failure. Unfortunately, this distinction was not captured in the mechanical data, possibly due to the difference in sampling rates, as the microseismic emission was recorded at a higher rate (10 MHz) compared to the mechanical data (10 Hz), which may be insufficient to resolve the rapid fluctuations in stress associated with sub-events within the overall failure process.

4.3.2.4 Fluid-induced fault reactivation and microseismicity

After the failure stage, a series of slip events were spontaneously triggered in samples Dutff 350 and Dutff 351 by injecting fluids at a range of pore pressures (Figures 4.12 and 4.13). The fluid injection process induces pore pressure changes that appear to reactivate pre-existing fractures, initiating further deformation within the samples. In the case of sample Dutff 350, AE rates start to increase soon after fluid injection and sample saturation at a modest pore pressure of 2 kPa (Figure 4.12). After saturation of the sample and as soon as pore pressure is increased to 10 kPa, a slow slip event is triggered which produces a sharp increase in the AEs number (Figure 4.12A). The spatial distribution of AEs during this stage shows that these are localized, small-magnitude events dispersed throughout the sample. The fluid injection appears to have reactivated isolated fractures formed during the previous stages of the deformation process.

In the case of sample Dutff 351, when fluid was injected, three moderate magnitude events were recorded at the base of the conjugate fault (Figures 4.13B and 4.17). In general, the increasing number of AEs during fluid injection reflects the progressive influence of pore pressure on fault stability, where the presence of fluid reduces the effective stress along fault planes.

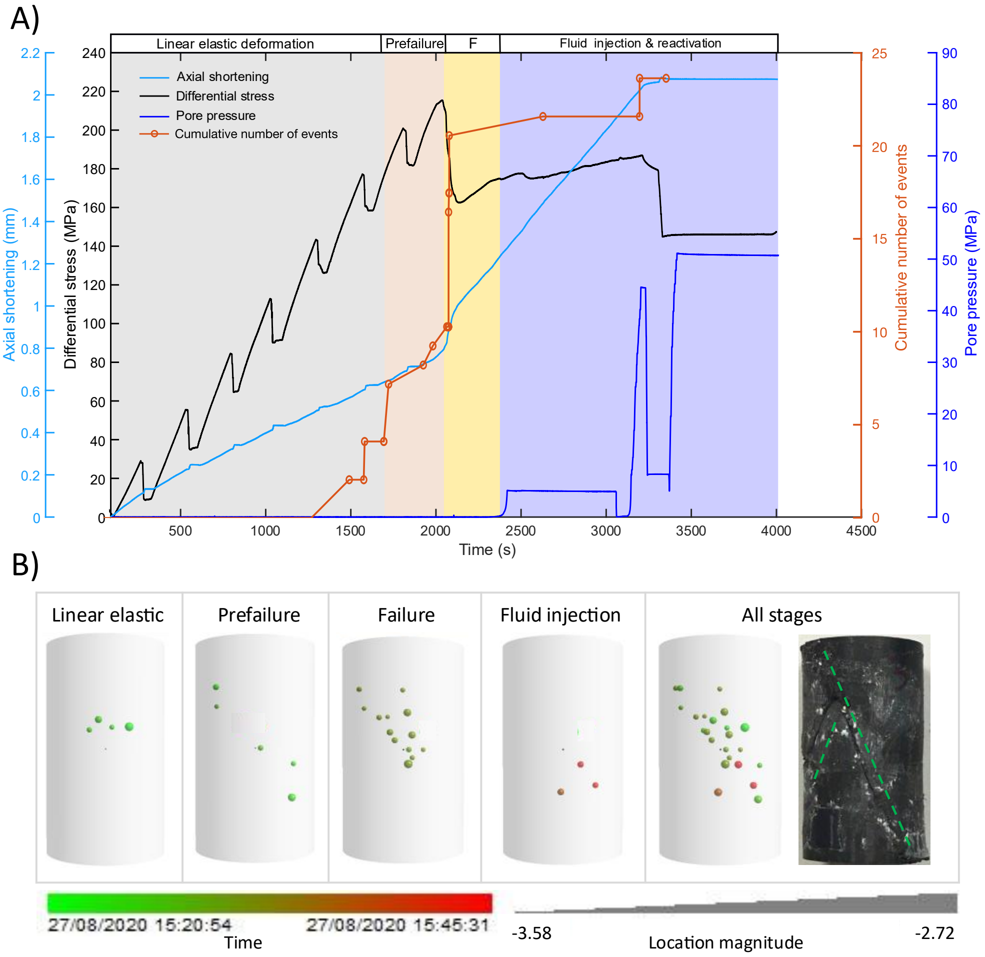

Figure 4.13. A) Evolution of differential stress, axial shortening, and cumulative number of AE events for Experiment Dutff 351. B) Snapshot showing the spatial and temporal distribution of microseismic events corresponding to the three identified deformation stages. The post-deformation image of the sample shows the formation of a main fault with a dip of approximately 45 degrees relative to the specimen's axis. A minor fault branches off from the main fault, dipping about 30 degrees relative to the main fault (green dashed lines).

4.3.3 Post-mortem CT scan data

Figure 4.14 shows 3D reconstructed greyscale images of samples from experiments Dutff 348, 350 and 351, respectively. A 2D cross-sectional view, looking at the centre of the samples, is displayed in Figures 4.14B, 4.14D and 4.14F. The bedding planes are clearly visible in the images of sample Dutff 348; however, they are less visible in samples Dutff 350 and Dutff 351. All three samples were loaded perpendicular to the bedding planes. Sample Dutff 351 contains minerals inclusions (white dots in Figure 4.14F) dispersed across the sample, with more dispersed inclusions in sample Dutff 350, and nonvisible in sample Dutff 348.

A close examination of the Dutff 348 image reveals the formation of a primary crack, and the failure mode is mainly shear faulting (Figures 4.14A and 4.14B). Multiple minor cracks branch off the primary crack at the top of the sample, likely due to heterogenous stress concentration around the edge of test sample. The overall orientation of the crack system is striking at an angle of approximately 30 degrees to the core axis. A conjugate crack formed at the bottom of the primary crack and terminated in the lower half of the sample with some minor branching.

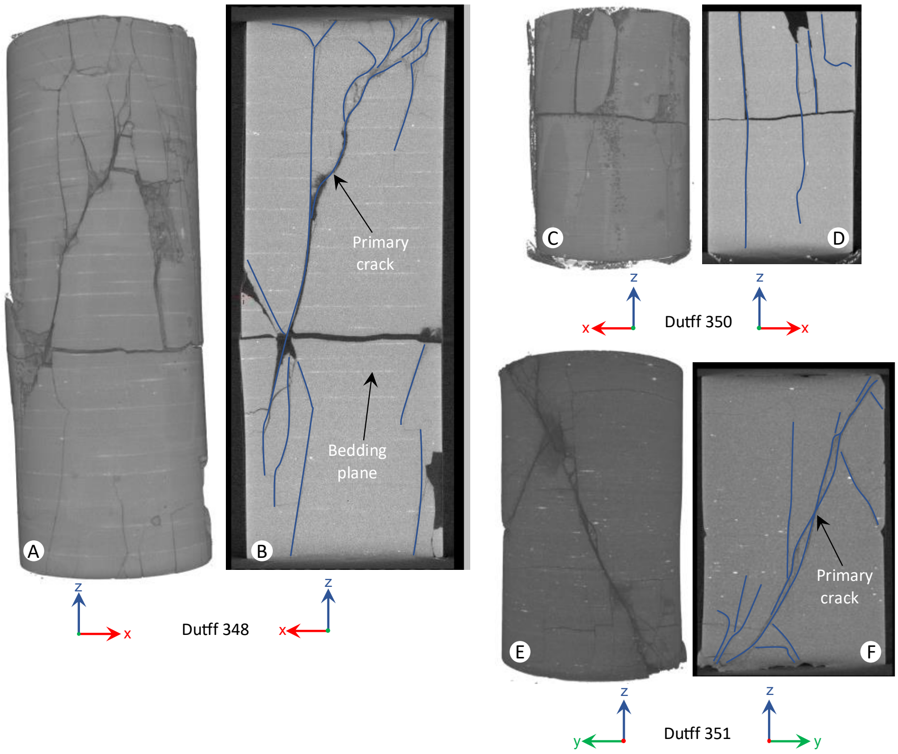

Figure 4.14. Reconstructed 3D grayscale images from X-ray scans. The brighter areas in Dutff 348 are bedding planes showing inclusion of a higher density minerals. B, D, and F are 2D cross-sectional view looking at the centre of the samples. The axes animations indicate the viewing plane.

For sample Dutff 350, three subvertical cracks formed with little branching or associated damage (Figures 4.14C and 4.14D). The cracks initiate at the top part of the sample and propagate downward, terminating in the lower half of the sample. The final failure mode is shear failure with a small amount of axial tension splitting. During failure of sample Dutff 351, a primary crack developed across the sample, striking at 45 degrees to the vertical axis. Multiple fault-jogs-like structures with expanded damage zones are observed along the primary crack (Figure 4.14F). Similar to sample Dutff 348, the primary crack in Dutff 351 branched at the top and bottom ends of the sample but was more tortuous with a more complex morphology (Figures 4.14E and 4.14F). A shorter conjugate crack formed and was displaced by the main fault, not reaching the end of the sample but terminating in the middle/upper part of the sample (Figure 4.14E).

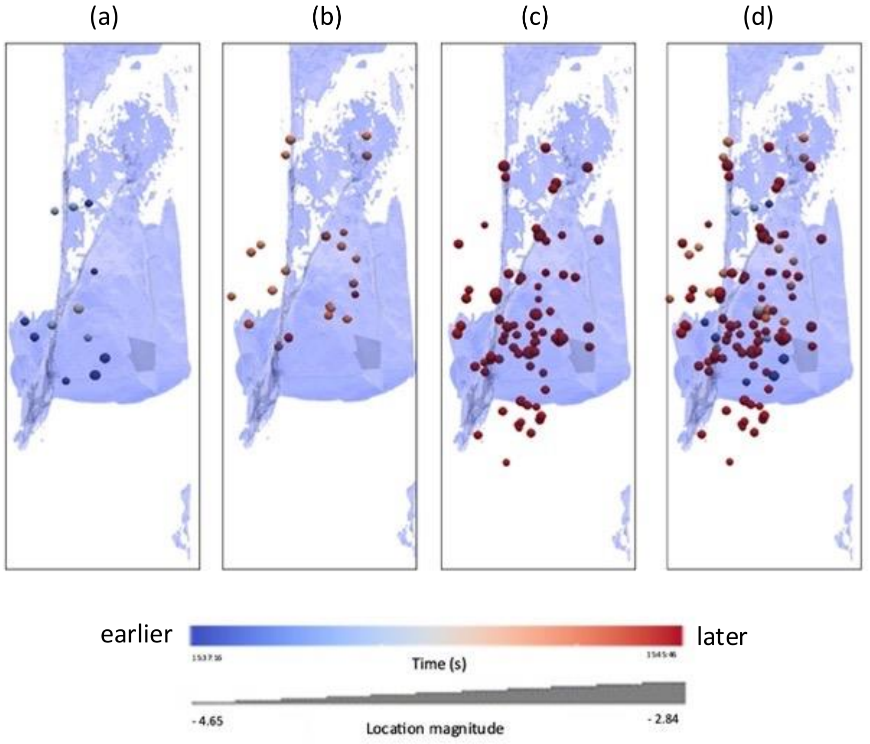

Figure 4.15. Snapshot of spatial and temporal distribution of microseismic events corresponding to the three identified deformation stages (see Figure 4.8). a) linear elastic deformation, b) prefailure, c) failure stage, and d) all three stages together.

A threshold segmentation method is used to extract the 3D crack morphology from the reconstructed CT scan images. The temporal spatial distribution of the located AE events (see the previous section for location process) was superimposed onto the 3D fracture geometries for each of the samples (Figures 4.15, 4.16, and 4.17). The 3D fracture geometries are represented with a light-blue background, while the AE events are depicted as spheres. The colour of the spheres indicates the relative time of occurrence (green for early, red for later), and their size represents the relative magnitude of the events. During the extraction of samples

Dutff 348 and Dutff 350 from the loading apparatus, they split along the foliation planes (see scan images in Figures 4.14A and 4.14C). These artefacts appear as horizontal fracture planes on the 3D fracture morphology and are excluded from further discussion.

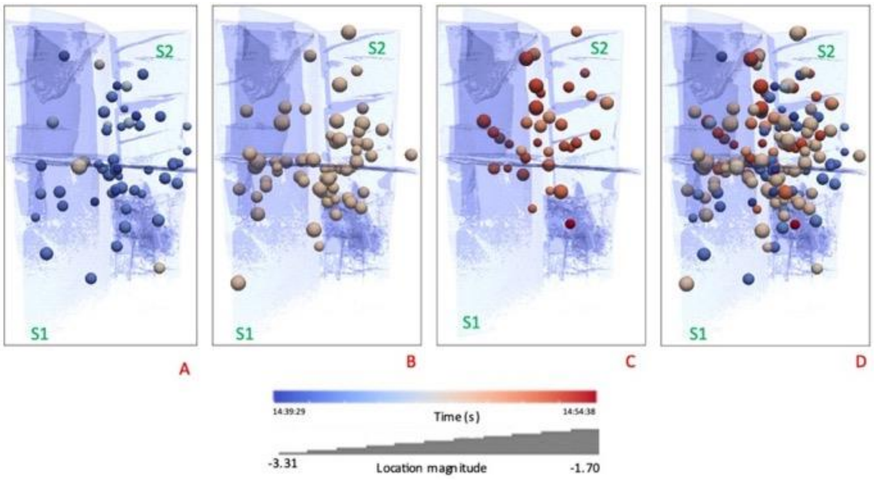

Figure 4.16. Snapshot of spatial and temporal distribution of microseismic events of experiment Dutff 350. a) prefailure, b) failure, c) fluid injection stages and d) all stages together (see Figure 4.9).

Figure 4.15 shows snapshots of the spatial and temporal distribution of event hypocentres for the linear elastic deformation, pre-failure and failure stages of experiment Dutff 348. The 3D fracture morphology shows the formation of two conjugate structures. The spatial distribution of the located events during the three loading stages are distributed along the two imaged planar structures. During the linear elastic deformation stage, a predominance of distributed seismic events of low magnitude is observed. The events concentrated along the lower part of the structure, where the conjugate fracture began to appear. In the pre-failure stage, the events were distributed in the sample and showing moderate magnitudes, with no clear pattern of strain localisation and incipient fault plane initiation. The events propagated upward both on the primary and the conjugate faults. When the failure stage finally reached its peak, large magnitude, localised events occurred. However, the events occurring during the failure stage do not localise on a single plane; rather, they are localised in multiple weakness planes around the edge of the sample. This suggests that shear faulting could have been initiated simultaneously on multiple planes. Then, the main through-going fault plane took over the minor faults and accommodated most of the rock shortening at the end of the macroscopic failure event.

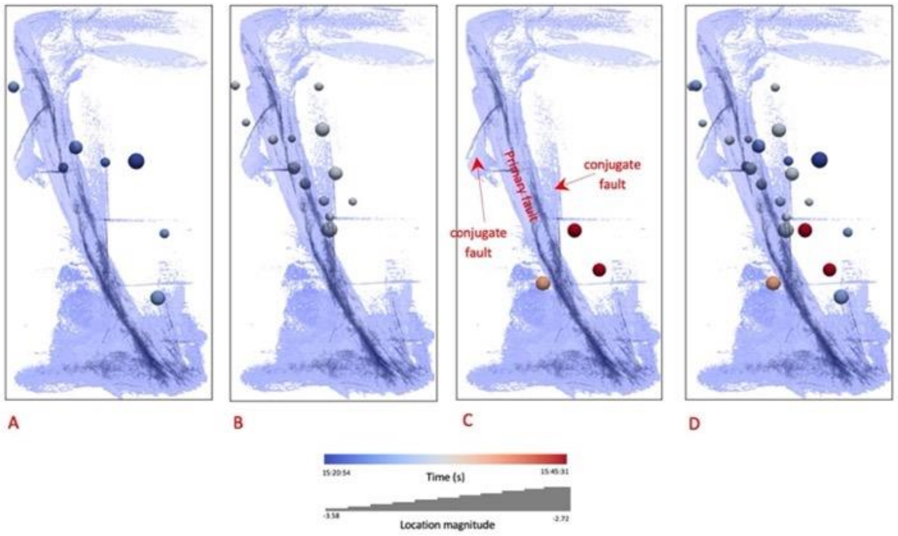

Figure 4.17. Snapshot of spatial and temporal distribution of microseismic events of experiment Dutff 351. a) prefailure, b) failure, c) fluid injection stage and d) all three stages together (see Figure 4.10).

The 3D fracture morphologies of sample Dutff 350 is different than for sample Dutff 348. In sample Dutff 350, two subvertical structures formed at approximability 90 degrees to each other (S1 and S2 in Figure 4.16). The temporal spatial distribution of events of pre-failure, failure and fluid injection stages of Dutff 350 are superimposed on the 3D geometry of the structures in Figure 4.16. The temporal and spatial evolution of events suggests that S1 and S2 developed concurrently. During the pre-failure stage, distributed, small magnitude events occurred along the two planar structures (Figure 4.16A). In the failure stage, distributed, moderate magnitude events were recorded along the edge of the sample. This suggests the structures stated at the centre and propagated toward the edge of the sample (Figure 4.16B). During fluid injection, localised, small magnitude events occurred along the pre-existing damage plane. The fluid injection appears to have reactivated isolated fractures formed during the previous stages of the deformation process.

The 3D fracture geometry, along with the temporal and spatial distribution of events of sample Dutff 351, is displayed in Figure 4.17. The deformation of this sample is accommodated by a primary fault trending approximately 45 degrees to the core axis. The damage band associated with the primary fault is narrow, in the centre of the sample, and expands toward the top and bottom of the sample. Two conjugate faults formed on the footwall and the hanging wall of the primary fault. The two conjugates are sub-parallel to each other, and the footwall fault terminates at the edge of the sample, while the fault on the hanging wall terminates at the upper part of the sample. As mentioned earlier, the microseismic response of this sample differs from that of sample Dutff 348 and Dutff 350. In the pre-failure stage, distributed, moderate magnitude events were recorded on the upper part of the primary fault (Figure 4.17A). As the deformation process proceeded and the sample transitioned into the failure stage, localised, moderate magnitude events occurred (Figure 4.17B). The location of the events suggests that the faulting started in the upper part of the sample and propagated downward. A few large magnitude events were recorded along the conjugate faults, suggesting that they developed at this stage. When fluid was injected, three moderate magnitude events were recorded at the base of the conjugate fault (Figure 4.17C).

4.3.4 Seismic parameters

The AE dataset was used to determine the evolution of the P-wave velocity, *b*-values, and D-values during the loading experiments to failure.

4.3.4.1 P-wave velocity

The P-wave velocity (Vp) in each loading stage is estimated by analysing the cluster of located events in that stage (see Section 2.6.2.3 in the Methods chapter for details). The error bar in the estimated the estimated P-wave velocity is calculated based on the average location error, weighted by the average distance between the source location and the sensors used. Figure 4.18 shows the normalised percentage change of P-wave velocity in experiments Dutff 348 and Dutff 350. The absolute change in velocity, as well as the number of events in each cluster used for the velocity estimation, is presented in Appendix A. The same colour scheme as in Figure 4.8 has been used to indicate the loading stages during the experiments.

In experiment Dutff 348, the P-wave velocity (Vp) begins to decrease during the pre-failure stage (Figure 4.18). This reduction trend continues for both experiments throughout the pre-failure stage, with a further significant drop in velocity during the macroscopic failure stage (Figure 4.18). For sample Dutff 348, the initial P-wave velocity (as measured on a benchtop) drops by 2% during the linear elastic deformation stage, which I interpret as due to the formation of small number of distributed fractures in the sample volume (Figure 4.11B). The velocity further reduces by 3% during the pre-failure stage, when more distributed fractures form as shown by the AEs dataset (Figure 4.11B). In the failure stage, the wave velocity significantly decreases, sustaining a 6% reduction during the stress drop phase associated with macroscopic failure in the sample.

Experiment Dutff 350 shows a similar P-wave reduction trend with distributed deformation and failure as Dutff 348, but with a larger percentage reduction. In experiment Dutff 350, the P-wave velocity decreases by 9% during the pre-failure stage, which is three times the reduction observed in Dutff 348 at the same deformation stage (Figure 4.18). The reduction continues, reaching 11% and 12% during the macroscopic failure and fluid induced fault reactivation stages, respectively.

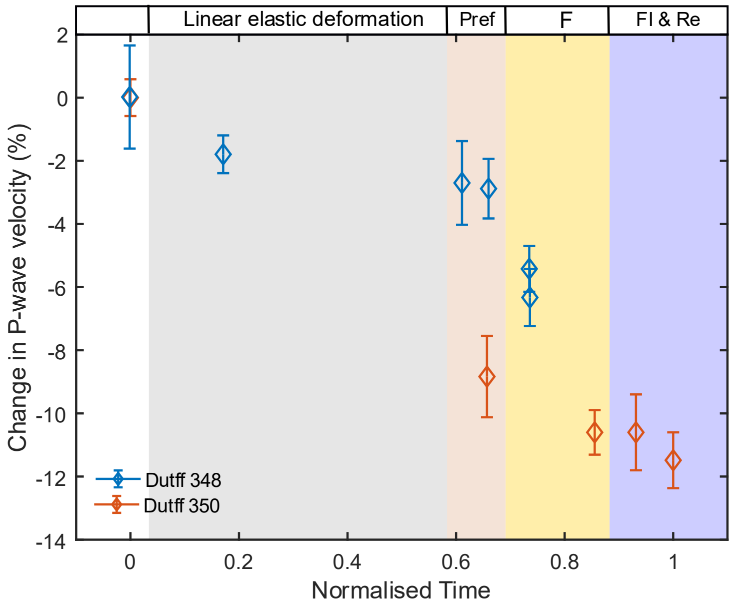

Figure 4.18. P-wave velocity change during deformation compared to initial velocity. The data point at time 0 represents the benchtop measurement (see Chapter 3 for details). The colour code is the same as in Figure 4.8. Abbreviations: Pref - prefailure, F - failure, FI - fluid injection, and Re - reactivation.

4.3.4.2 *b*-value and D-value

The seismic *b*-value, which characterises the relative proportion of small- to large-magnitude events within a cluster, is estimated using the maximum likelihood method (Aki, 1965). The same cluster of events used for P-wave velocity estimation are used for *b*-value calculation in experiments, except during the fluid injection stage, where the two clusters are combined (Figure 4.19). The standard deviation (uncertainty) in the *b*-value is estimated using the formulation of Shi and Bolt (1982) (see Section 2.6.2.4, Chapter 2).

For experiment Dutff 348, the b-value ranges from 2.00 $\pm$ 0.12 to 1.30 $\pm$ 0.10, with an average of 1.54 $\pm$ 0.13. In experiment Dutff 350, the *b*-value ranges from 2.50 $\pm$ 0.20 to 0.90 $\pm$ 0.03, with an average of 1.63 $\pm$ 0.15, across all three loading stages for both experiments. Experiment Dutff 351, which is loaded at confining pressures ranging from 10 MPa to 80 MPa, shows smaller *b*-values, starting at 1.3 during the prefailure and dropping to 1.1 during the failure stage. An evolution trend similar to that of the P-wave velocity is also observed in the *b*-values for all experiments during the main deformation stages leading up to sample failure (Figure 4.19).

During the linear elastic deformation and pre-failure stages, the ratio of large-magnitude events to the total number of events is relatively low, resulting in a higher *b*-value. In contrast, during the macroscopic failure and fluid induced fault reactivation stages, there is a noticeable increase in the proportion of larger-magnitude events, leading to a lower *b*-value.

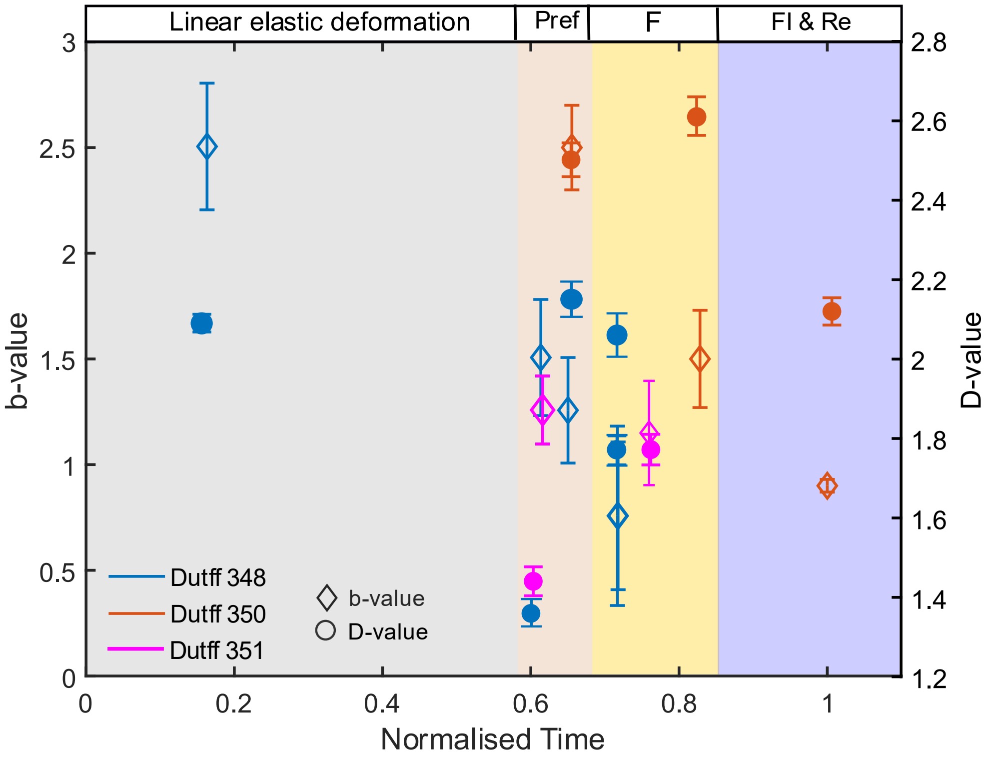

Figure 4.19. Evolution of *b*-value and D-value during deformation for experiments Dutff 348, Dutff 350, and Dutff 351. The *b*-values are represented by diamond markers, and the D-values by circle markers. The abbreviations are the same as in Figure 4.18.

The D-values are determined from the slope of the linear regression of the integral correlation of event hypocentres (see the Methods Chapter for details). The D-value reflects the spatial distribution and clustering of events (Hirata et al., 1987): a D-value close to 1 indicates a linear distribution, 2 represents a planar distribution, and 3 suggests a volumetric uniform distribution. The uncertainty in the D-value is estimated based on the uncertainty in the linear fit (Section 2.6.2.4, Methods Chapter).

In these experiments, D-values range from 1.36 ± 0.03 to 2.61 ± 0.05, reflecting changes in the fractal dimension associated with each deformation stage. In experiment Dutff 348, during the linear elastic deformation stage, a D-value of 2.09 ± 0.02 was observed. This value decreased to 1.36 ± 0.03 towards the end of the elastic deformation stage, before recovering to 2.15 ± 0.04 at the start of failure, and then dropping further to 1.77 ± 0.04 in the later prefailure stage. For sample Dutff 350, the behaviour was more complex: the D-value was 2.50 ± 0.4 during the prefailure stage, increased slightly to 2.61 ± 0.05 during failure, and subsequently decreased to 2.12 ± 0.03 during fluid injection-induced failure. In sample Dutff 351, a D-value of 1.44 ± 0.04 was recorded during prefailure, increasing to 1.77 ± 0.04 during the failure stage.

4.4 Discussion

4.4.1 Faults structure evolution during loading to failure

The evolution of fault zone structures under increasing differential axial load is crucial for understanding changes in seismic and physical properties during failure. These experiments reveal distinct stages of deformation —linear elastic, pre-failure, and failure—each displaying a different seismic response. The schematic model (Figure 4.20) illustrates the evolution of cracks and failure in the Horn River shale core plugs, where the maximum principal stress is oriented perpendicular to the bedding plane. For these fine-grained, low-porosity shales, no compaction is expected during the linear elastic stage.

In the early stages of differential axial loading, microcracks nucleate within the shale core plug, corresponding to the linear elastic deformation stage (Figures 4.11, 4.12, and 4.13). These microcracks are typically oriented perpendicular to the direction of minimum compressive stress (Dewhurst et al., 2008; Bonnelye et al., 2017b). Their orientation and distribution are significantly influenced by bedding planes (e.g., Vernik and Liu, 1997). As stress increases, the density of microcracks grows, forming a network of interconnected cracks that begins to coalesce, as shown by the AE recordings (Figures 4.11B, 4.12B, and 4.13B). With continued loading, these initially isolated microcracks propagate and interact, and evolve into larger fracture networks. The fractures increasing align in a more systematic manner, aided by the pre-existing structural weaknesses within the shale, such as bedding planes and intrinsic anisotropies (Vernik, 1993). The rising crack density and connectivity progressively reduce the mechanical integrity of the material, making it more susceptible to further deformation and eventual failure (Figures 4.8, 4.9, and 4.10).

High-resolution CT scan images reveal the complex 3D geometry and connectivity pattern of faults (Figures 4.14 - 4.17), resulting in an irregular, stair-step fault geometry (Figure 4.14F). In the early stages of loading and fault growth, the linkage of overstepping fractures leads to the formation of dilational jogs (Sibson, 2000). These jogs have significant implications for fluid pressure redistribution in low-permeability formations, as they can act as localized fluid conduits (Giorgetti et al., 2016; Cappa et al., 2018).

Samples from the Fort Simpson formation (experiments Dut348 and Dutff 350) and Muskwa formation (experiment Dutff 351) show distinct mineralogical and geochemical characteristics (see Chapter 3), but similar macroscopic mechanical behaviour (Figures 4.8, 4.9, and 4.10). This contrasts with findings from a previous study, where micromechanical data indicated differences in elastic modulus and hardness, as determined through micro-indentation, due to variations in mineralogy (e.g., Charlton et al., 2023). The Fort Simpson is characterised by a clay matrix with granular inclusions of detrital quartz, while the Muskwa is silica-rich, with quartz forming through recrystallization of biogenic opal. The observed differences between microscopic and macroscopic behaviour can be attributed to stress concentrations occurring at mineral interfaces, which facilitate the nucleation and growth of microcracks that ultimately evolve into macroscopic failure with faults.

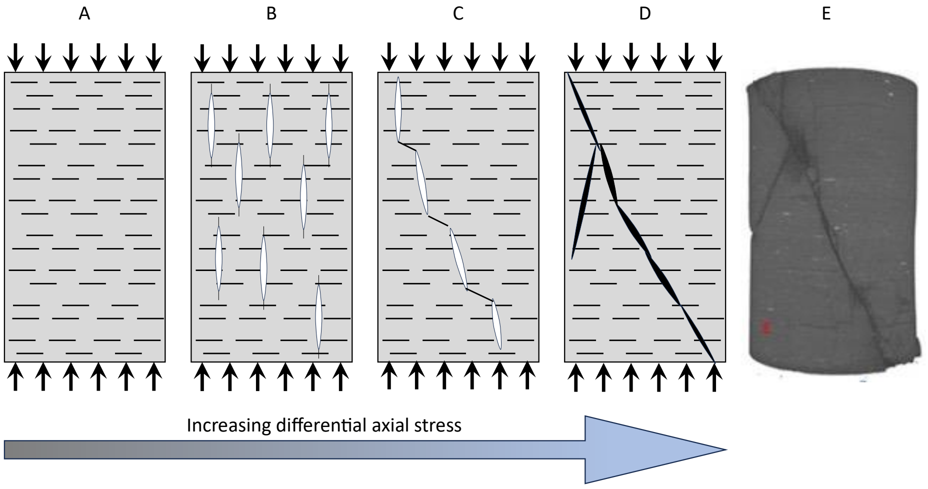

Figure 4.20. Schematic model of the evolution of cracks and failure as a function of differential stress acting perpendicular to the bedding planes (A-D). Modified from Dewhurst et al. (2008). (E) CT scan image of a shale sample loaded to failure (Experiment Dutff 351).

The stress drop during the macroscopic failure corresponds to the abrupt release of stored elastic energy and the rapid propagation of shear fractures. This phenomenon is consistent with previous studies on brittle rocks and their failure mechanisms under similar loading conditions (Lockner et al., 1992; Thompson et al., 2009). The substantial weakening and deformation observed prior to failure suggests progressive fracture linkage and strain localization leading to the formation of a throughgoing shear fault (Figure 4.8). Understanding the processes that lead from microscale distributed fracturing to localized macroscale failure is essential for predicting the mechanical response of shale formations and any diagnostic precursory change in properties that can occur during subsurface operations such as hydraulic fracturing.

AE data further reveal the progression of damage. The cumulative AE event counts increase with stress, highlighting the acceleration microcracking leading to macroscopic failure (Figures 4.11, 4.12 and 4.13). The spatial distribution of AE events, concentrated around the eventual fault plane, emphasize the localization of microcracking in the high-stress region. The progression from distributed microfractures to a macroscopic fault is marked by an increase in AE magnitude during the later stages of deformation, when a larger, throughgoing fault forms (Figures 4.11, 4.12 and 4.13), consistent with observations by Ougier-Simonin et al. (2016).

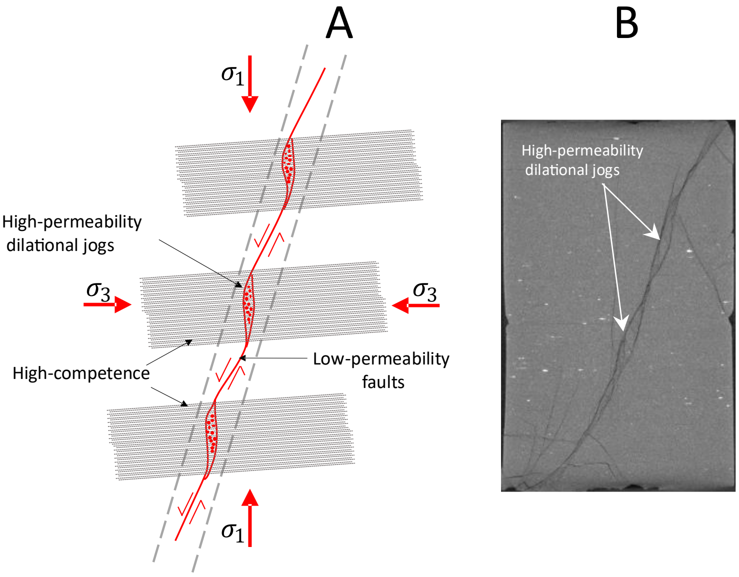

Figure 4.21. A) Schematic demonstrating the role of competence layering on brittle failure mode, modified from Sibson (2000). B) Cross-section of the sample shown in Figure 4.12E displaying dilational jogs.

4.4.2 Fault structure controls the evolution of physical and seismic parameters

The structural evolution of faults critically influences the physical properties and seismic responses of shale samples under stress (Figures 4.18 and 4.19). During the linear elastic deformation stage, microcracks initiate perpendicular to the bedding planes and are sparsely distributed throughout the deforming volume (Figure 4.20). The increased microcrack density leads to a gradual rise in structural porosity, causing a slight reduction in P-wave velocity (Figure 4.18). The low microseismic activity observed during the initial linear elastic deformation stage is consistent with previous studies on shales (Sarout et al., 2017).

As the pre-failure stage progresses, the AE rate rises significantly, reflecting intensified fracturing activity. AE events locations reveal increasing microcrack interactions and the development of a distributed fracture network, correlating with reductions in P-wave velocity (Figures 4.11, 4.12 and 4.13). During the failure stage, the AE rate peaks, and events locations show the formation of a connected macroscopic fault during the stress drop phase, accompanied by the largest observed decrease in P-wave velocity (Figure 4.18).

A notable feature is the evolution of seismic parameters, *b*-value, and D-value, during progressive deformation leading to macroscopic failure (Figure 4.19). In these experiments, the *b*-value decreases from 2.50 ± 0.20 during the elastic loading stage to 0.90 ± 0.03 at failure (Figure 4.19). The *b*-value inversely correlates with the relative proportion of small to large AE events, with lower *b*-values indicating a greater proportion of relatively large-magnitude events in a cluster. The observed evolution suggests that the *b*-value can serve as a proxy for the transition from diffuse microcracking and microseismicity within the rock volume to the formation of a macroscopic, throughgoing fault associated with larger-magnitude events (Figures 4.11, 4.12 and 4.13). A declining *b*-value highlights the increasing dominance of larger AE events, reflecting the growth and linkage of microcracks. This trend is a well-documented precursor to macroscopic faulting and has been reported in various geological materials during progressive loading to failure (Vinciguerra et al., 2004; Benson et al., 2007).

Similarly, the D-value evolves from approximately 2.61 ± 0.24 during the linear elastic stage to 1.36 ± 0.17 at failure. High initial D-values reflect a three-dimensional distribution of fractures throughout the rock volume, while decreasing D-values indicate increasing event clustering and the development of shear localization along the fault plane (Figures 4.11, 4.12, and 4.13). The reported uncertainties, indicated by the error bars in Figure 4.19, reflect the statistical variability associated with the estimation of these parameters. Although the observed trends in *b*- and D-values evolution are robust and consistent with fault growth and microcrack coalescence, the individual values are subject to sampling limitations, event detection thresholds, and fitting uncertainties. These factors can influence the absolute values but do not affect the broader trends observed

Comparison with field data show similar trends. For example, in the Horn River Basin, multiple studies have documented variations in *b*-values across the basin (Roche et al., 2015) and within the reservoir units (Muskwa, Otter Park, and Evie) (e.g., Snelling et al., 2013). These variations are attributed to formation layering, in-situ stress variations, and the reactivation of pre-existing faults. For instance, Roche et al. (2015) reported a significant decrease in *b*-values with depth, starting from 2.94 in the Fort Simpson formation and decreasing to an average of

2.30 in the Muskwa and the upper section of the Otter Park. The *b*-value then drops further to an average of 1.45 in the lower section of the Otter Park and the Evie members, respectively. Lowest *b*-value, averaging 1.10, was observed in the Keg River Formation. Roche et al. (2015) suggest that these changes in *b*-value correlate with variations in in-situ stress and the reactivation of pre-existing faults in the deeper formations.

A similar trend was reported by Kettlety et al. (2019), who found b-values greater than 1.50 for microseismicity within the stimulated reservoir volume and around 1.0 for microseismicity in the Key River Formation, which was associated with the reactivation of pre-existing faults. Additionally, Snelling et al. (2013) identified b-value variations within the reservoir formations (Figure 4.5). They showed that higher b-values are associated with dip-slip events exhibiting a non-double-couple component of failure, characteristic of hydraulic fracturing-induced microseismicity (Wang et al., 2018). In contrast, lower b-values are linked to strike-slip events with a stronger double-couple component of failure, typically mapped along pre-existing geologic features.

The D-value trends observed here also contrast with relatively constant D-values (~ 2.0) reported by Roche et al. (2015) across depth in the Horn River basin, which suggest a more stratified two-dimensional fracture distribution rather than progressive shear localization. This highlights the role of rock fabric and layering in controlling seismic events distribution patterns. Overall, the evolution of b- and D-values, provides important insights into the progressive transition from distributed microcracking to localised faulting, both in laboratory experiments and in natural settings.

4.4.3 Implications for microseismic monitoring.

The results presented here highlight critical indicators that mark the transition from distributed micro-fracturing and microseismicity within the deforming sample to the development of larger fractures that evolve into fully formed faults, culminating in larger magnitude induced seismic events.

These findings have significant implications for microseismic monitoring during hydraulic fracturing (HF) operations. The correlation between deformation stages and AE characteristics (Figures 4.18 and 4.19) provides a framework for predicting seismic responses during HF operations. The observed increase in microcracking activity and the evolution of associated seismic parameters —such as AE event magnitude and rate, *b*-value, D-value, and P-wave velocity— serve as potential indicators of fault activation and likelihood of larger seismic events. However, resolving the simultaneous occurrence of “good microseismicity” (distributed, controlled seismicity) and larger runaway seismic events remains a challenging (Atkinson et al., 2020).

Insights from the *b*-value analysis are particularly relevant for assessing seismic hazard associated with hydraulic fracturing. A decreasing *b*-value is a sign of increased likelihood of larger seismic events, which can inform the implementation of traffic light protocols (TLP) to mitigate induced seismicity risks (Schultz et al., 2018). By integrating AE monitoring with real-time seismic data, operators can make informed decisions to adjust injection rates, pressures, and volumes, thereby preventing the activation of large faults beyond the reservoir volume and minimizing impacts on the surrounding environment and infrastructure. Additionally, real-time monitoring of *b*-values and P-wave velocity offers a quantitative approach to tracking the evolving fracture mechanics and identifying the transition from micro-fracturing to macroscopic failure.

4.5 Conclusion

Three distinct deformation stages were identified for HRB shales loaded to failure under reservoir conditions, each exhibiting a unique acoustic emission (AE) response. A strong correlation was observed between AE rates, magnitudes, and microcracking activity before and during shear faulting. During the linear elastic deformation stage, a few small-magnitude AE events recorded, corresponding to sparse microcracking scattered throughout the sample. In the prefailure stage, both AE rate and magnitude increased, reflecting the coalescence of microcracks and the progressive development of the final rupture plane.

During the macroscopic failure stage, a sharp and sudden rise in AE rate was observed during the rapid stress drop phase, with AE events clustering along the fully developed rupture plane. The temporal, spatial, and magnitude distributions of AE events indicate that this sharp increase in microseismicity rate during failure is associated with the acceleration of microcrack coalescence and the final formation of the rupture plane. These correlations provide a valuable tool for predicting the onset of macroscopic failure, which is critical for seismic risk mitigation.

Systematic changes in the seismic parameters, including the *b*-value, D-value, and P-wave velocity, were also observed during progressive deformation leading to failure and faulting. The *b*-value decreased with microcracking, indicating the dominance of relatively larger-magnitude AE events within clusters. Similarly, the P-wave velocity decrease as the microcrack density increased. Meanwhile, the D-value reflected the localization and clustering of AE events as the final rupture plane developed. These variations in seismic parameters serve as indicators for sample degradation and can be used to forecast the onset of macroscopic failure. Therefore, proactive risk mitigation strategies can be implemented based on real-time observation and monitoring of theses diagnostic changes.

The observed correlation between AE characteristics and fracture evolution offers valuable insights for managing induced seismicity and optimizing HF practices. Furthermore, these findings corroborate observations from field-scale operations in the Horn River Basin. Integrating laboratory and field data has the potential to develop robust models for accurately predicting and mitigating the impacts of HF-induced seismicity.

5 Fault reactivation and induced seismicity during fluid injection

5.1 Introduction

5.1.1 Fluid injection during industrial activity and seismicity

Industrial activities involving fluid injection, such as hydraulic fracturing (Li et al., 2019; Schultz et al., 2020b), wastewater disposal (Ake et al., 2005; Keranen et al., 2013), enhanced geothermal systems (Majer et al., 2007), and carbon sequestration (Zoback and Gorelick, 2012; Verdon and Stork, 2016), are well-established causes of induced seismicity. For example, Hydraulic fracturing (HF), a process involving the injection of high-pressure fluid into low-permeability shale gas reservoirs to create fractures and increase permeability, can lead to two types of microseismic events: (1) microseismicity contained within the thin, stimulated shale layers, and (2) larger runaway magnitude events resulting from the reactivation of pre-existing faults within the basement and the overburden beneath and above the target shale formations (Kettlety et al., 2019; Amini et al., 2022).

Figure 5.1 provides a schematic of shale gas resource plays targeted by an injection borehole for hydraulic fracturing. The potential reactivation of larger, pre-existing faults within the basement and the overburden above and below the target shale formations poses a significant risk during industrial activities involving subsurface fluid injection. The influence of pre-existing faults on induced seismicity risk is evident in several geo-energy projects worldwide.

For example, wastewater injection in Oklahoma triggered a Mw 5.8 earthquake in 2016, causing widespread damage and injuries (Yeck et al., 2017). In November 2017, a Mw 5.5 earthquake occurred in Pohang, South Korea, during high-pressure fluid injection for an enhanced geothermal system (EGS) (Yeo et al., 2020). This large, runaway slip event occurred due to reactivation of a previously unmapped fault below the injection site. The earthquake resulted in extensive injuries, including dozens of hospitalizations and one fatality, displaced more than 1,700 people into emergency housing, and caused over $75 million US in direct damage to over 57,000 structures, with an estimated total economic impact exceeding $300 million US (Ellsworth et al., 2019). In Basel, Switzerland, an EGS project in 2006 induced an ML 2.6 event at peak injection pressure of about 30 MPa. The economic costs of this earthquake and the subsequent aftershocks surpassed $9 million US (Grigoli et al., 2017).

Hydraulic fracturing in tight shale gas formations has also led to significant induced seismic events due to fault reactivation (Igonin et al., 2021). In the Sichuan Basin, China, HF operations in 2018 triggered a M 5.7 event, leading to economic losses, injuries, and fatalities (Lei et al., 2017; Atkinson et al., 2020). The Western Canada Sedimentary Basin (WCSB) has similarly experienced a marked increase in large-magnitude (M > 3) seismic events (Schultz et al., 2020b). Between 2003 and 2010, only 10 events of M > 3 were recorded, compared with 58 such events between 2011 and 2019. This includes the largest HF-induced event in Canada, a Mw 4.6 near Fort St. John in the Montney play in 2015 (Figure 5.3). The event's hypocentre was within 1 km of an active injection well and occurred five days after injection began. The reactivated fault was optimally oriented within the regional stress field, with a b-value of 0.78 for the sequence (Wang et al., 2021).

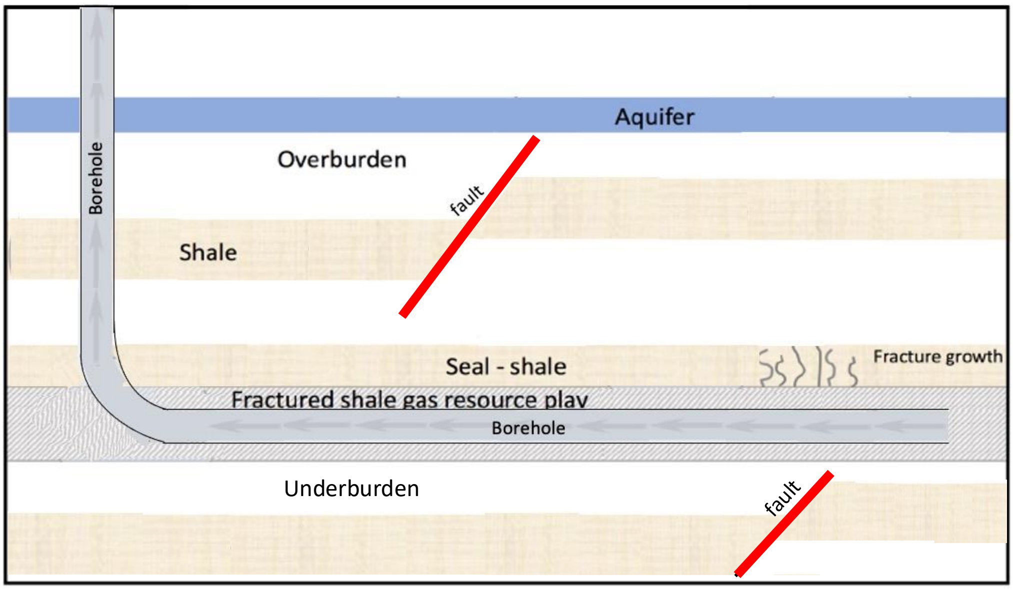

Figure 5.1. Schematic showing shale gas resource play targeted by injection borehole for hydraulic fracturing. Pre-existing faults located outside the reservoir that potentially can be reactivated resulting in large magnitude seismic event. Not to scale.

The Horn River Basin (HRB) is a prominent shale gas play in the WCSB, consisting of the highly siliceous, organic-rich Muskwa Formation, the carbonate- and organic-rich Otter Park Formation, and the organic-rich Evie Formation that has variable amounts of clay, quartz, and carbonate. These formations are overlain by the thick, clay-rich shales of the Fort Simpson Formation and underlain by the tight platform carbonates of the Keg River Formation (Maghsoudi et al., 2018). Figure 5.2 shows an example of microseismicity during hydraulic stimulation of the Muskwa, Otter Park, and Evie formations. Most events are small in magnitude (Mw < -1), and because they are contained within the reservoir units, are deemed to be "good microseismicity" that enhances the permeability and productivity of the shale (black dashed box in Figure 5.2A). However, larger magnitude events were detected below the target reservoir in the underburden (red dashed box in Figure 5.2A).

Analysis of these microseismic event hypocentres revealed reactivation of pre-existing faults, with clusters of events forming planar features that extend approximately 400 meters below the injection wells, mapping onto pre-existing faults in the underlying Keg River carbonates (Figure 5.2B). Magnitude-frequency analysis reveals that microseismic events confined within the stimulated reservoir formations have magnitudes between −2 < Mw < −1 and a b-value > 1.5, whereas events occurring in the underburden (Figure 5.3 B), have magnitudes ranging from 0.0 ≤ Mw < 0.5 and a b-value ≈ 1.0, indicating fault reactivation (Kettlety et al., 2019). This chapter focuses on the larger seismic events associated with the reactivation of pre-existing faults in the underburden.

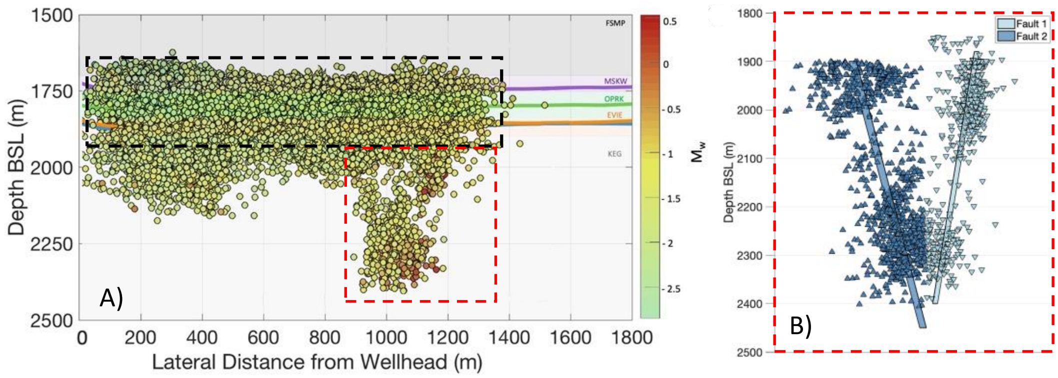

Figure 5.2. (A) Cross-sectional view of event hypocentres recorded during hydraulic stimulation of the Muskwa, Otter Park, and Evie formations in the HRB. Events are color-coded by moment magnitude (Mw). Higher-magnitude events occur in the basement below the stimulated reservoir formations (highlighted by the red dashed box), while lower-magnitude events, or “good seismicity,” are mostly contained within the stimulated reservoir volume (outlined by the black dashed box). (B) Pre-existing faults associated with the higher-magnitude events shown in the red dashed box in (A). Modified from Kettlety et al. (2019).

Fluid injection alters the subsurface stress regime by increasing pore pressure and reducing the effective normal stress on faults (Atkinson et al., 2020). This process can bring faults closer to failure conditions, particularly when they are critically stressed or optimally oriented within the stress field (see Chapter 1, Section 1.1.1). This mechanism is especially relevant in high-permeability formations where pressure changes can propagate quickly.

Additionally, fluid injection induces changes in the stress field of the rock matrix, increasing shear stress on faults and potentially triggering slip even without direct hydraulic connection (Schultz et al., 2020b; Moein et al., 2023). The creation of new fractures or the extension of existing ones can form pathways that connect to pre-existing faults located either inside or outside the reservoir (Figure 5.1), allowing fluid to migrate and increase pore pressure along these faults, potentially leading to their reactivation.

Natural fluid flow in the upper crust can also influence faulting and earthquake processes (Miller et al., 2004; Di Luccio et al., 2010). For instance, the 1997 Umbria–Marche seismic sequence in the Northern Apennines, Italy, began with two mainshocks (Mw 5.7 and Mw 6, separated by 9 hours) and was followed by a series of aftershocks lasting more than a month (Miller et al., 2004). The mainshocks nucleated in a Triassic evaporite unit overlaying compartments of carbon dioxide (CO2) at near-lithostatic pressure. The aftershock sequence was driven by the coseismic release and propagation of the trapped CO2. The pressure pulse reduced the effective normal stress on incipient slip planes and triggered aftershocks.

5.1.2 Managing induced seismicity hazard

Fluid injection during industrial operations routinely causes small magnitude events (M < 3) and can also produce larger, felt earthquakes (M > 3). Safety risks associated with induced seismicity cause public unrest, affecting the social acceptability and broad development of deep geo-energy resources. Hence, managing induced seismicity hazard is of paramount importance, especially the hazard posed by major seismic events (M > 3).

Methods used to predict the maximum magnitude of an induced event are based on empirical scaling relationships between total injected volume of fluids and maximum seismic moment (Shapiro et al., 2011; McGarr, 2014; Galis et al., 2017) (Figure 5.3). Traffic Light System (TLS) protocols apply a deterministic approach to manage the hazard of induced seismicity by maintaining net injection volumes below a certain threshold value, so that shaking nuisance or risk of damage can be avoided (Kendall et al., 2019; Atkinson et al., 2020). Unfortunately, current mitigation strategies based on microseismicity monitoring have met with only limited success (Ellsworth et al., 2019; Kwiatek et al., 2019), and felt induced events cannot be confidently predicted in advance of operations. At present, it is not possible to confidently forecast the occurrence, or the maximum size, of an induced event.

Triggered runaway ruptures challenge the hypothesis that the maximum magnitude of induced events is solely governed by the volume of the injected fluids (Figure 5.3). The reactivation of pre-existing faults is influenced by geological factors such as lithological heterogeneity, tectonic stress level, and fault orientation, as well as operational parameters like injection pressure, rate, and volume of fluids (Keranen and Weingarten, 2018; Cebry et al., 2022). Laboratory experiments have simulated fluid injection in heterogeneous fault zones, revealing that variations in rock properties affect fault stability and seismic response (Guglielmi et al., 2015). Regions with contrasting lithologies can experience uneven stress buildup, leading to more frequent and intense seismic events.

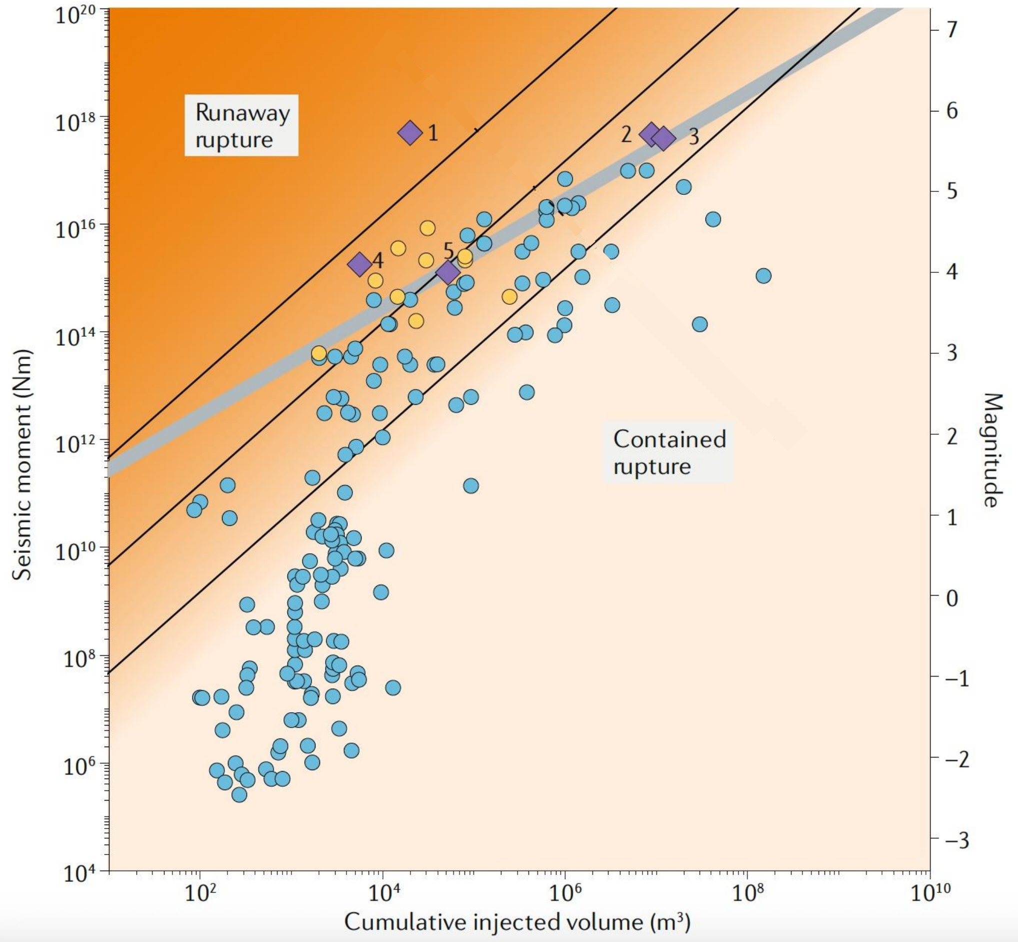

Figure 5.3. Relationship between cumulative injected volume and seismic moment. Purple diamonds indicate proposed cases of runaway rupture: Pohang, Korea (enhanced geothermal system) (diamond 1), Pawnee, Oklahoma, USA (wastewater disposal) (diamond 2), Prague, Oklahoma, USA (wastewater disposal) (diamond 3), Fort St. John, Canada (hydraulic fracturing) (diamond 4) and Fox Creek, Canada (hydraulic fracturing) (diamond 5). Grey and black lines illustrate the scaling relationship between cumulative volume and total seismic moment as proposed by McGarr (2014) and Galis et al. (2017), respectively. Background colours represent the nature of triggered activity relative to injected volume: events in the pale orange–white zone align with mechanisms where magnitude scales with cumulative volume, while events in the orange zone exceed volume-based predictions. The intermediate region represents ambiguous rupture types. Modified from Atkinson et al. (2020).

Studies have also shown that the stress state and the orientation of faults within the stress field are primary influencers on the initiation of fault slip as well as the maximum magnitude of the induced event (Martínez-Garzón et al., 2016; Wiseall et al., 2018). Additionally, numerical models have provided insights into how fluid pressure propagates differently through heterogeneous materials, influencing the timing and magnitude of induced earthquakes (Cappa and Rutqvist, 2011; Ciardo and Rinaldi, 2021). In addition, operational design parameters are critical too in controlling fault slip activation and earthquake nucleation. The influence of these parameters on fault slip behaviour has been extensively reported in seismological studies and laboratory experiments. For example, Wang et al. (2020b) demonstrated that fault slip propagation is primarily controlled by the fluid pressurization rate rather than the injection pressure.

Conversely, French et al. (2016) found that fluid pressurization is less effective at initiating accelerated slip events compared to mechanical changes in the fault normal stress. Kettlety et al. (2019) investigated the role of elastic stress transfer in the reactivation of pre-existing faults, concluding that interaction with pressurized fluid was required to initiate failure, rather than stress change alone. However, these investigations underscore the importance of considering both lithological heterogeneity and injection pressure when evaluating the seismic risks of industrial fluid injection practices. It is vital to comprehend what causes a fault to begin to slip, the mechanisms driving the transition from aseismic to seismic slip (i.e., initiation of dynamic rupture), and how large the resulting seismic event will grow (i.e., how far dynamic rupture is sustained). These factors help inform the maximum event magnitude and potential for runaway ruptures.

In this chapter, I will explore how fluid injection pressure and lithological heterogeneity affect the initiation and termination of fluid-induced rupture. To achieve this, a field injection operation is simulated in the laboratory using a composite sample with an intact reservoir rock sample from HRB placed on top of a pre-existing fault, simulating a basement fault structure below the reservoir. The sample is triaxially loaded to a critical stress state and pore pressure conditions corresponding to those encountered at 2 km depth, and fluid is injected through a borehole into the fault to cause its reactivation and propagation into the reservoir.

During the experiments, acoustic emission activity is monitored to characterize and image the progressive slip along the fault system, allowing the deciphering of the sequence of structural events associated with the reactivation. By focusing on the roles of rock heterogeneity and injection pressure, I aim to deepen our understanding of the mechanisms driving induced seismicity and to provide valuable data for enhancing the safety and effectiveness of industrial fluid injection practices. Insights into the conditions that promote or inhibit fault reactivation will inform the development of risk mitigation strategies for fluid injection operations. These results complement the work in Chapter 4, which characterises the microseismic response to fluid stimulation of intact HRB shales.

5.2 Experimental techniques

5.2.1 Reactivation experiment in triaxial loading apparatus

Two composite samples were used for the reactivation experiments. The first composite sample consisted of a Westerly granite (WG) sawcut overlain by an intact cylinder of WG (Figure 5.4d), simulating a brittle, homogeneous fault system. The second composite sample consisted of a WG sawcut, representing a pre-existing fault in the basement, overlain by an intact shale core from HRB, which represents the top reservoir seal (Figure 5.5). This configuration simulates a fault system with a heterogeneous lithology.

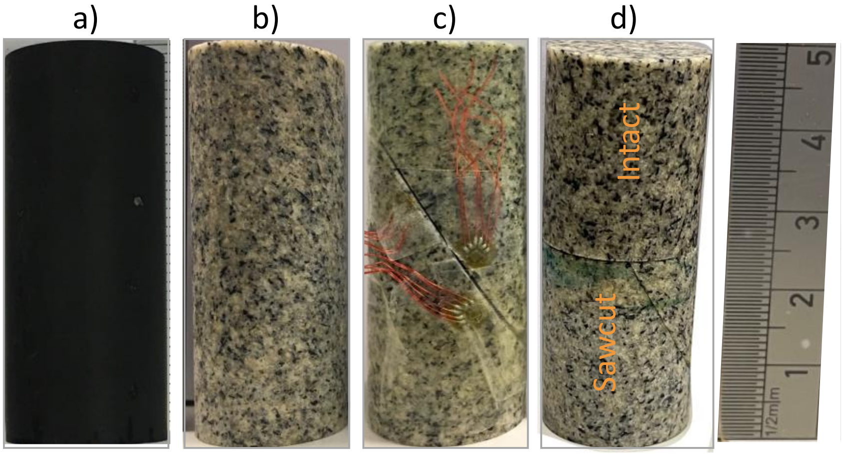

Figure 5.4. End-member components tested: (a) intact shale (Chapter 4, Experiment Dutff 348), (b) Intact Westerly granite, (c) WG sawcut, and (d) a composite sample with intact WG on top of a WG sawcut. Mechanical results are presented in the Results section below.

The shale core was manufactured following a protocol developed during this PhD, as described in Chapter 2. It was sourced from the same block as Sample A14 (Experiment Dutff 348), reported in Chapter 4. This shale originates from the Fort Simpson Formation, a clay-rich unit that acts as fracture barrier for the underlying organic-rich formations of Muskwa, Otter Park and Evie, which are targeted by fracking operations (Charlton et al., 2023). The shale sample has a density of 2.54 g cm^{-3}, a TOC of 2.21%, and is currently buried to a depth of 2575.9

meters. For detailed information on the petrophysical and mechanical properties of the shale core, see Chapter 3, and for its microseismic response, refer to Chapter 4.

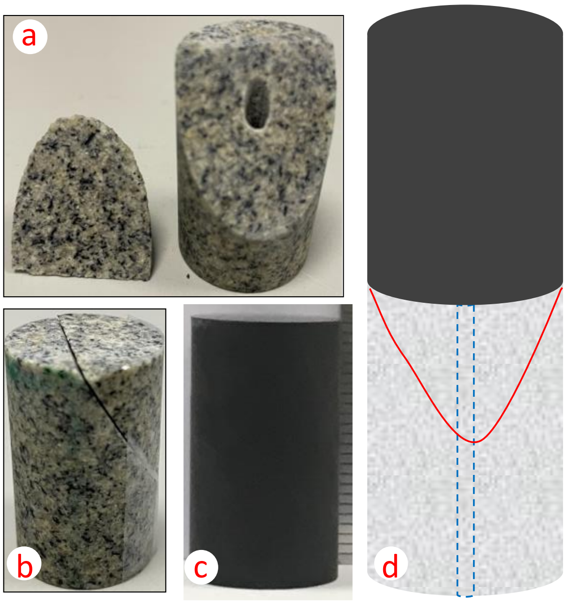

Figure 5.5. Components of a composite sample with intact shale on top of a WG sawcut: (a) granite sawcut with a drilled borehole for fluid injection, (b) assembled granite sawcut, (c) intact shale core, and (d) schematic showing the assembly of the composite sample.

The Westerly granite was selected to represent the brittle basement rock due to its well-documented mechanical, petrophysical, and microseismic response properties (Goodfellow et al., 2015). The WG is analogous to the carbonates of the Keg River Formation, which underlie the Muskwa, Otter Park and Evie formations (Figure 5.2 A). Detailed preparation of the WG sawcut is outlined in Chapter 2 (Section 2.3.2). The reactivation experiments were conducted using the Durham University triaxial apparatus with fluid flow (DUTFF). Detailed description of DUTFF's capabilities are provided in Chapter 2. The shale composite sample was instrumented with eleven piezoelectric (PZT) sensors: six on the shale core and five on the granite sawcut (Figure 5.6). For a detailed description of the sensors, including installation procedures, wire connections, soldering, and assembly sealing mechanisms, see Chapter 2. Following sensor installation, the procedures outlined in Section 4.2.1 were followed to wrap, jacket, and mount the composite sample on the sample assembly.

Before conducting the composite shale and WG sawcut experiment, the individual components (intact shale, intact WG, WG sawcut, and the composite WG with intact WG; Figure 5.4) were tested separately to characterize their mechanical behaviour. These baseline tests of the end-member components provided essential data for interpreting the results of the composite shale sample experiment.

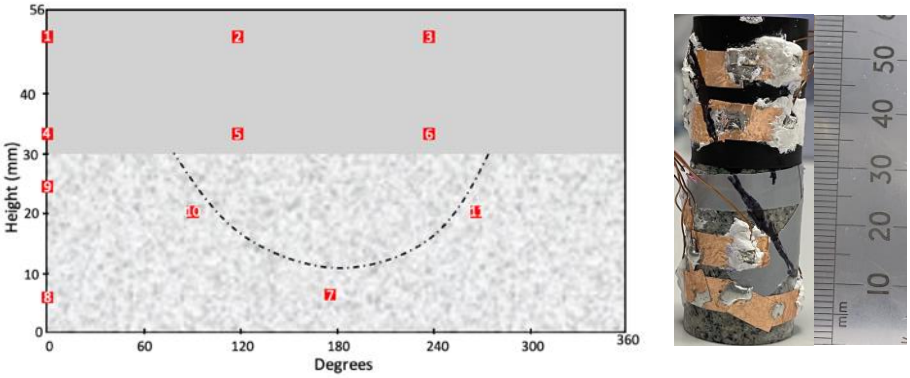

Figure 5.6. Map of PTZ sensor locations on the composite sample plotted against sample height and angles around the circumference. The dashed curve represents the edge of the pre-existing fault plane. The image on the right shows the composite sample with attached sensors.

5.2.2 Loading protocol, measured and calculated parameters

The loading protocol consists of four main stages:

1- **Isotropic loading stage:** The confining pressure is increased to subject the composite sample to a confinement pressure simulating reservoir pressure conditions.

2- **Pore fluid saturation stage:** Deionized water is injected simultaneously from both the upstream and downstream, maintaining a fluid pressure of 5 MPa to saturate the pre-existing fault. After a minimum of 30 minutes, the fault is considered saturated.

3- **Mechanical loading stage:** Differential stress (the difference between the axial stress and the confining pressure) is applied at a constant axial shortening rate of 1 µm s^{-1} until a critical stress level is reached. This critical stress is 80% of the shear strength of the pre-existing granite sawcut, which was determined from previous loading experiments shown later in the results section. The differential loading is applied under drained conditions (i.e., fluid pressure is not maintained constant).

4- **Fluid loading and cyclic reactivation stage:** fluid is injected at pressure (ranges from 8 MPa min^{-1} to 50 MPa min^{-1}, with an average rate of 30 MPa min^{-1}) to reduce the effective stress and the shear strength of the WG sawcut, inducing the sawcut fault reactivation.

After each reactivation event, indicated by a stress drop, the fluid is extracted to bring the fluid pressure back to 5 MPa. The sawcut fault is then mechanically loaded back to the critical stress level. At this point, fluid injection is resumed to induce fault reactivation again. This cyclic reactivation process is repeated multiple times. During the final cycle, the fluid pressure is maintained at the level at which reactivation occurred, with continuous monitoring of the fault system behaviour. Throughout the experiment, measurements are taken for confining pressure, fluid pressure, applied force, and axial displacement. The applied force is corrected for machine stiffness, and axial stress and axial shortening are calculated. The fault slip is then determined by resolving the axial shortening on the fault plane. Finally, the fault slip rate is calculated by differentiating the fault slip over time.

5.2.3 Acoustic emissions data recording and processing

Similar to the triaxial loading experiments conducted in Chapter 4, acoustic emission (AE) is continuously recorded for the reactivation experiment. The AE recording and processing procedures are the same as those described in Chapter 4 (Section 4.3.2).

5.3 Results

First, I present the mechanical properties of the individual components of the composite samples (e.g., intact shale, intact Westerly granite, and Westerly granite sawcut), followed by the results of the reactivation experiment on the composite sample with intact WG overlying the Westerly granite sawcut. Characterising the mechanical behaviour of these end-member components is essential for interpreting the observed responses during the fluid injection reactivation experiment on the composite shale sample atop the Westerly granite sawcut.

5.3.1 Mechanical data

5.3.1.1 Intact shale, intact Westerly granite, and Westerly granite sawcut

Figure 5.7 shows the stress versus strain curves for samples shown in Figure 5.4 A, B, and C. The experiments performed on intact shale and intact Westerly Granite (WG) samples indicated brittle behaviour at confining pressures of 10 MPa (Figure 5.7A). The shale sample yielded at 350 MPa, with a sudden stress drop at peak stress of 357 MPa and a strain of 1.0%. The intact Westerly granite yielded at 210 MPa, with a sudden stress drop at a peak of 267 MPa. Young’s moduli for the shale and WG, calculated from the linear elastic part, are 57 GPa and 46 GPa, respectively. These strength parameters indicate that the Fort Simpson shale sample from the HRB is stronger than WG when loaded to failure at 10 MPa confinement pressure. For the

WG sawcut, failure occurred at 20 MPa and 70 MPa for loading at 10 MPa and 50 MPa confining pressures, respectively (Figure 5.7B).

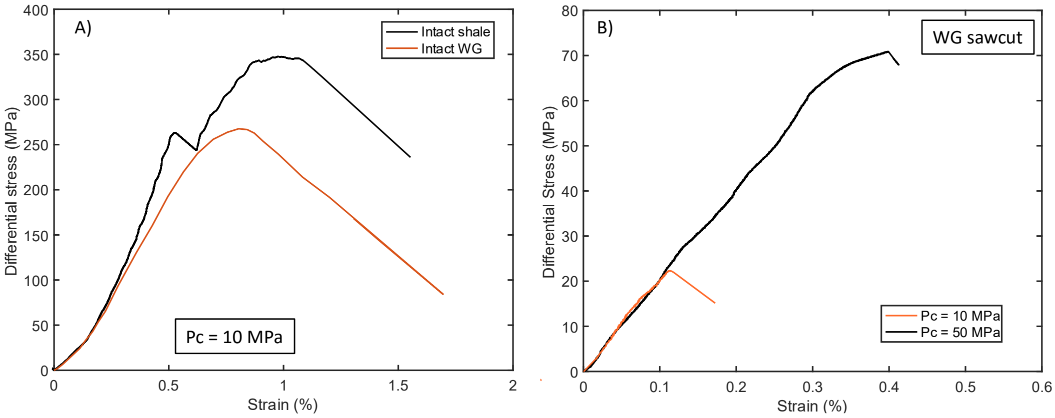

Figure 5.7. Differential stress vs strain graphs for end-member components of the composite test. A) Intact shale and intact WG samples loaded at 10 MPa confining pressure. B) Westerly granite sawcut loaded at 10 MPa and 50 MPa.

5.3.1.2 Composite reactivation experiment: intact WG and WG sawcut

Figure 5.8 shows the stress versus strain curve for a composite WG sawcut and intact WG (sample shown in Figure 5.4 d). The WG composite also exhibits brittle behaviour, yielding at 130 MPa, with a sudden stress drop at a peak stress of 190 MPa and a strain of 0.7% (Figure 5.8A). A post-mortem picture of the sample reveals that the sawcut fault was reactivated and propagated into the top intact WG component, forming a fault (Figure 5.8B). Images taken under plane-polarized light (PPL) and crossed-polarized light (XPL), shown in Figure 5.8C (top and bottom, respectively), reveal the formation of a single fault plane.

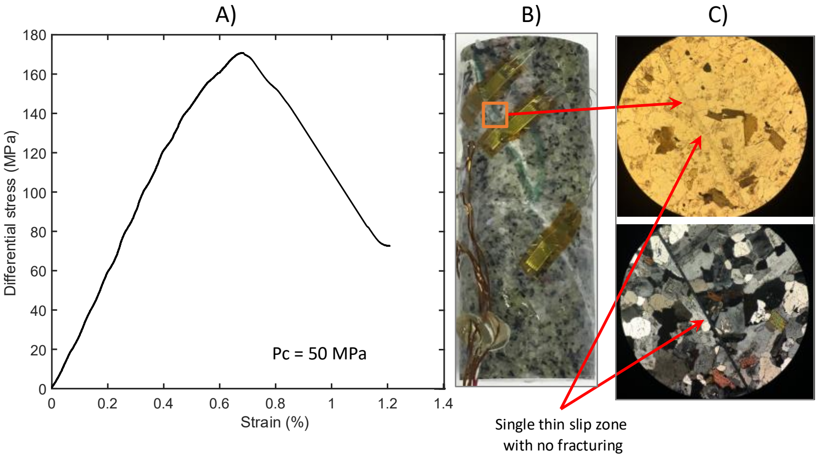

Figure 5.8. Differential stress vs. strain curve for a composite sample (intact WG on top of a WG sawcut). The plane-polarized light (PPL) and crossed-polarized light (XPL) images are courtesy of Nicola De Paola.

5.3.1.3 Composite reactivation experiment: intact shale and WG sawcut

In the first loading cycle, after the application of 60 MPa confining pressure and 5 MPa pore pressure, the sample is mechanically loaded to a critical stress level, which is 80% of the WG sawcut shear strength (cycle 1 and following mechanical loading cycles highlighted by the light grey area in Figures 5.9 and 5.11). At this stress level, pore pressure is increased by injecting fluid into the sample during cycle 2 (cycle 2 and following fluid injection/extraction cycles highlighted by light green area in Figures 5.9 and 5.11). As a result, the effective pressure reduces, and the sample fails at a pore pressure of 17 MPa, resulting in a large stress drop of 40 MPa, with slip of 30 µm at 3 µm s^{-1} (Figure 5.9, Cycle 2a). Fluid injection was halted immediately after the stress drop phase of failure, when the fault had stabilized with no further stress drop observed. Subsequently, fluid injection was resumed until a fluid pressure of 40.5 MPa, when further failure occurred resulting in another large stress drop (Cycle 2b). After this failure event the fault stabilized, and the fluid was extracted to conclude cycle 2.

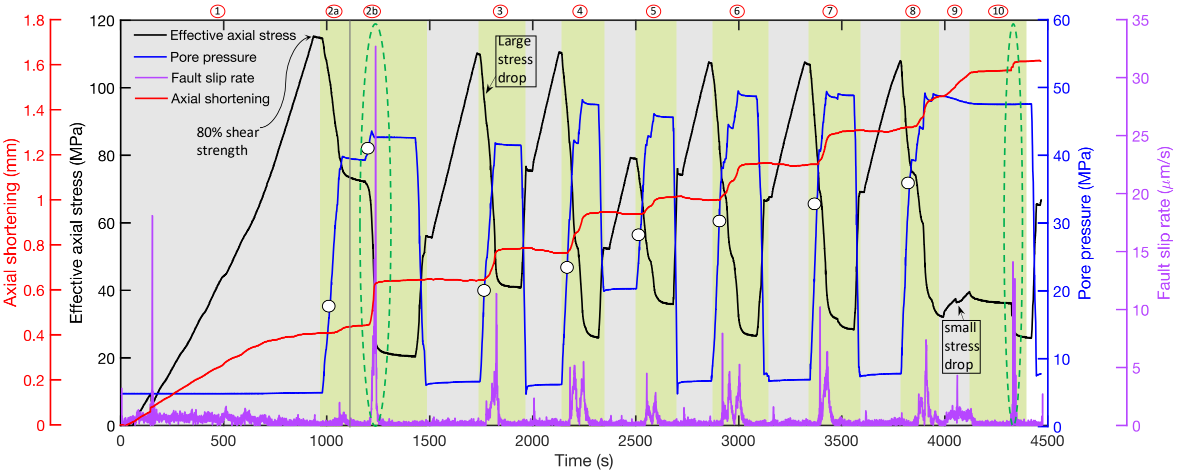

Figure 5.9. Evolution of stress, pore fluid pressure, axial shortening, and slip rate during the reactivation experiment. The light grey background represents the mechanical loading stage, while the light green background indicates the fluid injection/extraction stage (see text for description). The white circles on the pore fluid curve indicate pore pressure level at the onset of fault slip. The dark green dashed ellipses highlight episodes that are shown in detail in Figure 5.10 A and B, respectively.

The cyclic mechanical loading to 80% of the WG shear strength and fluid injection to trigger fault reactivation was repeated during 9 more cycles (Figure 5.9). In all cycles, slip events occurred during the fluid injection phase following the mechanical loading of the sample to 80% of the WG sawcut shear strength. The stress drop magnitude associated to these cyclic slip events steadily increased, ranging from 40 MPa to 83 MPa (Figure 5.9). Fault slip consistently initiated at a higher fluid pressure level in all cycles where mechanical loading preceded the fluid injection (see white circles on the pore fluid curve in Figure 5.9).

After the fluid induced slip event in cycle 8, in cycle 9, mechanical loading was resumed without reducing the fluid pressure (i.e., fluid was not extracted) producing a slip event at a lower effective stress (~40 MPa) with only a small stress drop of 1.5MPa. At the end of Cycle 9, mechanical loading was halted, allowing the fault to begin relaxing. About 30 minutes later, an additional slip event was recorded, indicating that an instantaneous instability occurred (Cycle 10 in Figure 5.9). In contrast to the consistent increase in the magnitude of the stress drop and fluid pressure level at the onset of slip during subsequent reactivation cycles, the fault slip rate showed no clear trend during the cycles, with the only exception of the second slip event (Cycle 2b) when it increased from 3 µm s^{-1} to 34 µm s^{-1} (Figure 5.10).

5.3.2 Slip event mechanical characteristics

In Cycle 2b, the slip event shows a complex evolution of stress during stress drop, characterised by four distinct phases (Figure 5.10 A). During the first Phase A0 of fluid injection pore pressure increases up to 40.5 MPa, while the fault remains locked, and the axial stress slightly reduces due to sample relaxation. As fluid injection continues during the following Phase A1, pore pressure increases to 42.6 MPa and fault slip initiates by slow creep at a slip rate of less than 5 µm s^{-1}, accompanied by a gradual stress drop of 10 MPa and 50 µm of slip (Figure 5.10A). This was followed by an acceleration of slip to a peak slip rate of 34 µm s^{-1} associated with a sudden stress drop of 30 MPa and 120 µm of slip (Figure 5.10A). Finally, a deceleration and relaxation phase occurred during Phase A3 at slow slip rate (< 5 µm s^{-1}), after which the fault locked again. This pattern of fault slip initiation by slow creep following fluid injection, and acceleration to dynamic slip (i.e., sudden increases in slip rate with simultaneous sudden drops in stress) is consistently observed during slip events occurring in all cycle 3 to 8, with the only difference being a lower maximum slip rate sustained (Figures B.1-B.8 in Appendix B).

During the last reactivation cycle 10, when pore pressure was kept constant during, fault slip consisted of multiple slip events, each characterised by a dynamic slip phase (Figure 5.10B). This behaviour contrasts with single slip events characterised by multiple phases observed during Cycles 2a to 8 (Figure 5.10A, Appendix B, Figures B.1 -B.8).

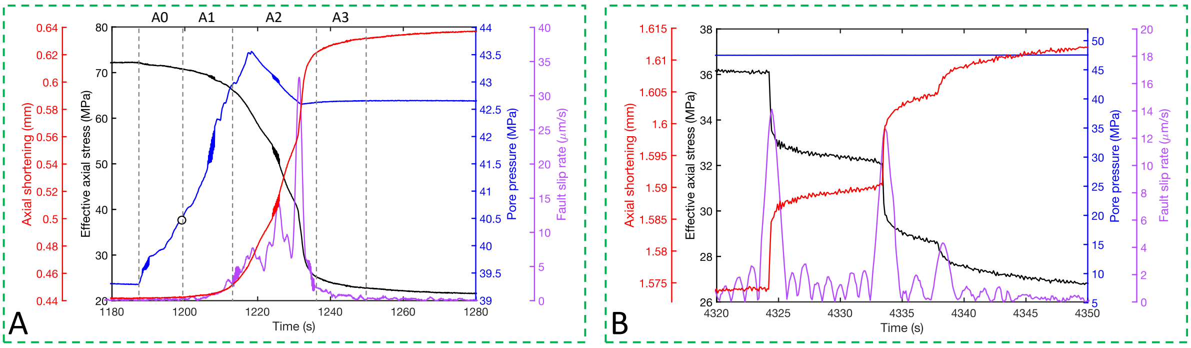

Figure 5.10. A) Slip event in Cycle 2b: The fault starts slipping at a slow rate, accelerates to dynamic slip and then deceleration to steady slip. B) Slip event in Cycle 10: multiple slips at slow slip rates (< 5 µm s^{-1}).

5.3.3 Acoustic emission data

Based on the average velocity model derived from benchtop measurements — 5.7 km s^{-1} for the shale and 6 km s^{-1} for Westerly granite — a simplex algorithm was used, implemented in the Insite Seismic Processor software (Itasca), to locate and estimate the relative magnitude of the AE events recorded during the reactivation experiments (see details in Chapter 2, Section 2.7.2). The uncertainty in the source location for all events is approximately ±3 mm. In Figure 5.11B, the AE events are shown as spheres within a semi-transparent model of the composite rock specimen: granite is depicted in off-white and shale in light grey. The colour of the spheres indicates the relative time of occurrence (green for earlier events, red for later ones), while their size scales with the magnitude of the events. The recorded events range in magnitude from –3.8 to –1.69 across all reactivation cycles. These are relative magnitudes, as described in the Methods chapter. They are calculated from the recorded signal amplitude (Section 2.6.2.4) and are specific to the sensor configuration used in this experiment. According, in the discussion that follows, magnitudes are referred to in qualitative terms.

A strong correlation is evident between the plane of the sawcut fault and the spatial distribution of AE hypocentres. During linear elastic deformation in the first cycle (Cycle 1), AE activity is very low, with a slight increase observed as peak stress is approached (Figure 5.11A). AE activity begins to rise sharply toward the end of Cycle 1, when sample is loaded at 80% of the WG sawcut shear strength. During this stage, small-magnitude events located along the pre-existing sawcut, showing the pre-existing fault in the granite was reactivated (Figure 5.11B). During mechanical loading (Cycle 1), no events were recorded in the intact shale sample.

During the first fluid injection phase (Cycle 2a and 2b), AE activity increases significantly (Figure 5.11 A), with microseismic events illuminating the development of a new, conjugate fault in the granite during Cycle 2a (Figure 5.11B). During Cycle 2b, microseismic events mainly locate along the newly formed conjugate fault, which was then reactivated after forming in Cycle 2a. A small amount of microseismic events is also located along the pre-existing WG sawcut and at the base of the shale sample, showing that the conjugate fault in the underlying granite started to propagate upward into the intact shale (Figure 5.11B). Overall, the fluid induced fault pattern imaged by AEs location is very complex, when compared to that shown by WG sawcut and intact WG composite sample (Figure 5.8).

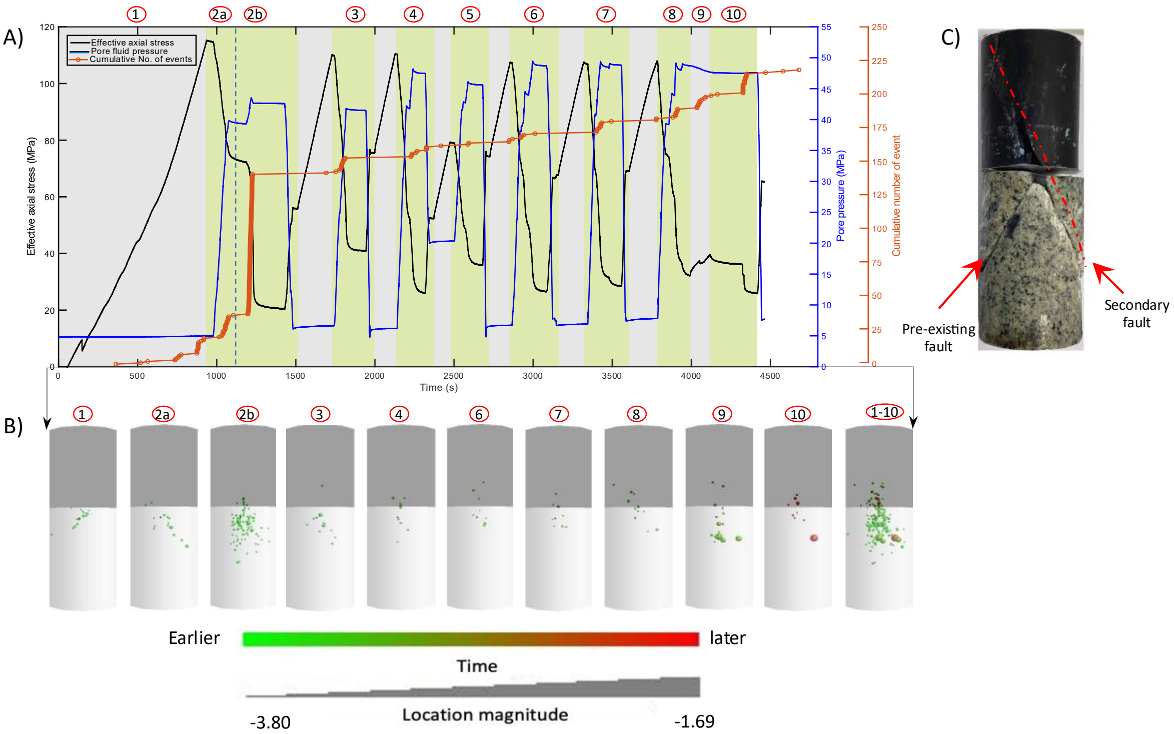

Figure 5.11. A) Effective axial stress, fluid pressure, and cumulative number of events plotted as a function of time across multiple reactivation cycles. The emission rate remains steady during the reactivation stage. Reactivation at high fluid pressure results in a higher emission rate compared to reactivation at lower fluid pressure (Cycle 8). B) The spatial and temporal evolution of microseismic events. The magnitude of the events increases progressively with each successive reactivation cycle. C) A post-mortem picture of the test specimen, showing creation of a conjugate fault that propagated into the top seal.

From Cycle 3 through Cycle 10 AE activity is recorded for each stress drop associated with fluid induced slip events (Figures 5.11 A and B). During Cycles 3 to 10, the spatial distribution of AE hypocentres is mainly localised along the newly formed conjugate fault in the Westerly granite basement, but it gradually migrated in time from the basement granite into the top seal shale (Figure 5.11B). This observation suggests that the conjugate fault was reactivated and propagated upward into the top seal shale, during repeated slip events (Figure 5.11B). The growing in size of the reactivated conjugate fault is also supported by the observation that progressively larger-magnitude events, localized along the fault, were recorded (Figure 5.11B). In particular, the largest slip events along the conjugate fault were recorded during the late Cycles 9 and 10, when AEs illuminated the development of a mature fault propagating from the basement into the upper seal shale (Figure 5.11B).

5.3.4 Evolution of seismic parameters

The temporal variation of P-wave velocity, D-value and seismic *b*-value during the reactivation cycles are shown in Figures 5.12 and 5.13. The P-wave velocity is estimated using the cluster of events that occur in each cycle (See Chapter 2 for details about the methods adopted). The uncertainty in the estimated P-wave velocity is calculated based on the average location error, weighted by the average distance between the source location and the sensors used.

On average, the P-wave velocity shows dependence on the progressive development of fracturing and faulting in each reactivation cycle. With a reference benchtop measured value of 5700 ± 80 m s^{-1}, during the first 2 reactivation cycles 1 to 2, the P-wave velocity decreases abruptly to values of 5450 ± 170 m s^{-1} and 4950 ± 100 m s^{-1}, respectively (Figure 5.12). This sharp reduction in P-wave velocity coincides with the formation of the new conjugate fault in the Westerly granite sample through Cycles 2a and 2b (Figure 5.11B). During Cycles 3 to 9, when the conjugate fault is reactivated multiple times with small magnitude events, the P-wave velocity stays relatively constant with values ranging between 4700 ± 150 and 5200 ± 124 m s^{-1}, with the only exception of an outlier high value during cycle 4 (Figure 5.12). Interestingly, the lowest value of P-wave velocity of 4700 ± 69 m s^{-1} is obtained during the last Cycle 10 (Figure 5.12), when the largest magnitude events were recorded along a fully developed fault propagating from the granite basement into the top seal shale (Figure 5.11B).

The fractal dimension, or *D*-value, is obtained from the linear regression of the integral correlation of AE event hypocentres (See Chapter 2 for details about the methods adopted). The uncertainty in *D* value is derived from the uncertainty of the linear fit (Section 2.6.2.4). In general, a D-value close to 1 indicates a linear distribution, 2 represents a planar distribution, and 3 suggests a volumetric uniform distribution. Therefore, analysing the temporal evolution of the D-value can provide insights into changes in the underlying fracture patterns.

In the reactivation experiment, D-values range from 1.03±0.03 to 1.96±0.03 (Figure 5.12). A correlation is observed between the temporal evolution of D-values and the evolving fault pattern, as imaged by AE hypocentre locations (Figure 5.11B). Specifically, the D-value increases from 1.57±0.04 in Cycle 1 to 1.96±0.03 in Cycle 2a (Figure 5.12). The initial D-value is consistent with microseismic activity localized along a pre-existing fault (Figure 5.11B). The rise in D-value during Cycle 2a can be attributed to a more planner fracturing, associated with the formation of a new conjugate fault in the lower Westerly granite sample (Figure 5.11B). In subsequent cycles, the D-value gradually decreases, reaching an average of 1.03±0.03 in Cycles 9 and 10 (Figure 5.12). This reduction reflects a more clustered distribution of AE hypocentres, indicating increasingly localised fracturing along the fault structure. This trend aligns with the development and reactivation of a throughgoing fault, as shown by AE event locations in Cycles 9 and 10, which extend from the Westerly granite basement into the overlying seal shale sample (Figure 5.11C).

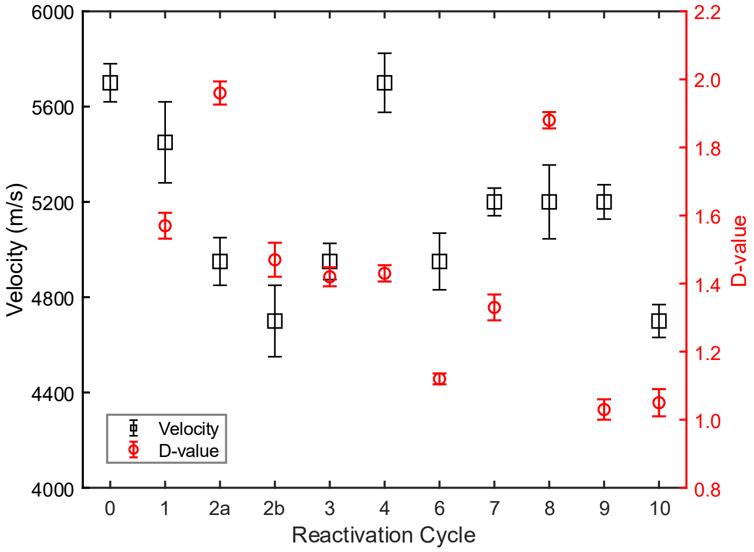

Figure 5.12. The fractal dimension (D-value) of event hypocentres and velocity variation for each reactivation cycle. Velocity measured at the benchtop is shown as at cycle zero.

When interpreting the *D*-value results, it is important to consider the scale and statistical coverage of the recorded events. While the theory of fractals assumes scale invariance for self-similar structures, in this experiment the scale range is limited to 3–50 mm, constrained by the location error ($\pm 3\ mm$) and sample size. Strictly speaking, I found the fractal structure in the band of 3-50 mm, and the fractal dimension changes during fracturing, suggesting that the patterns of microcrack distribution varies during the fracturing process in this experiment.

The seismic *b*-value, which characterises the relative proportion of small- to large-magnitude events within a cluster, is estimated using the maximum likelihood method (Aki, 1965). The standard deviation (i.e., uncertainty) in the b-value is calculated following the formulation of Shi and Bolt (1982); see the Methods chapter for further details.

Based on the evolution of fracturing and fault reactivation imaged by microseismic event locations during Cycles 1 to 10, b-values were calculated for five main clusters of AE events (Figure 5.13A). Cluster 1, recorded during Cycle 1 when the WG sawcut was reactivated, yields a *b*-value of 1.32 ± 0.06. Cluster 2 consists of AE events recorded during Cycle 2a, when an incipient conjugate fault plane began forming in the Westerly granite block, has a b-value of 1.19 ± 0.09. Cluster 3, representing events from Cycle 2b during the formation of the new conjugate fault, shows the highest b-value at 1.80 ± 0.13. Cluster 4, covering Cycles 3–8 during repeated reactivation of the new conjugate fault, has a b-value of 1.20 ± 0.17. Finally, Cluster 5, recorded during Cycles 9 and 10 when the conjugate fault became fully developed and extended from the granite basement into the overlying seal shale, exhibits the lowest b-value of 0.60 ± 0.07.

Figure 5.13B illustrates the temporal evolution of the b-value based on the cumulative number of AE events across all reactivation cycles. In the early cycles (1–2), the higher b-values suggest a dominance of smaller-magnitude events. However, as the fault system evolves, particularly with the upward propagation of the fault into the shale and the establishment of a continuous fault structure, the occurrence of larger-magnitude events becomes more frequent. This shift results in a systematic decrease in the b-value (Figure 5.13A–B), reflecting the maturation of the fault and a change in the underlying rupture dynamics, consistent with the observed fault geometry and AE spatial distribution (Figure 5.11B).

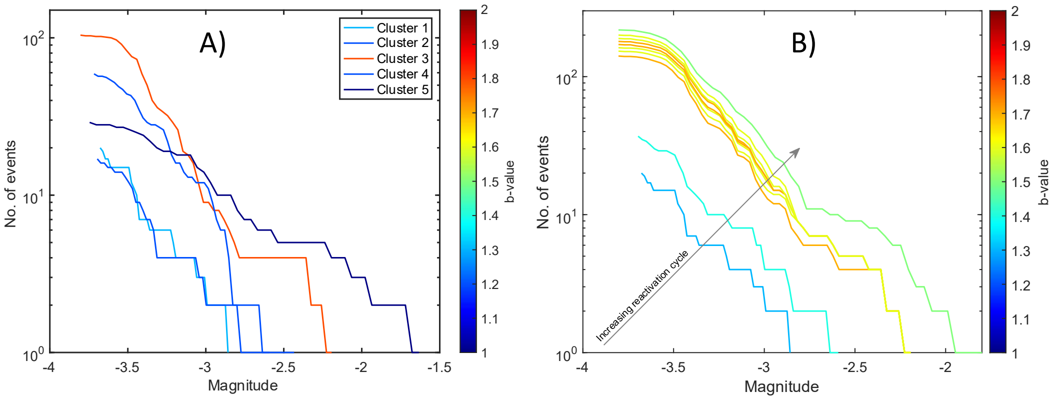

Figure 5.13. The frequency-magnitude distribution for event clusters recorded in the reactivation experiment. In Figure 5.13A, each line corresponds to events cluster, with the colour scale indicating the *b*-value obtained for each cluster. In Figure 5.13B, each line representing the cumulative number of events recorded in all previous cycles.

5.4 Discussion

5.4.1 Heterogeneous mechanical properties control the complexity of reactivated fault patterns.

The experimental results demonstrate that the reactivation of pre-existing faults due to fluid injection is critically influenced by the interplay between mechanical loading, fluid pressure, and fault zone heterogeneity. A key observation is that fault slip behaviour strongly depends on the stress state and the evolving fault structure during repeated reactivation cycles (Figures 5.9 and 5.11).

Fluid injection reduces the effective normal stress on the fault plane, promoting fault slip (Figure 5.9). This observation aligns with the effective stress principle, where increased pore pressure within the fault zone reduces the clamping force that holds the fault in place, ultimately triggering seismic events. However, the contrasting mechanical properties of granite and shale (Figure 5.7) in the composite sample significantly influenced the spatial, temporal and magnitude distribution of seismicity. During the late stages of loading of Cycle 1, acoustic emission location shows the reactivation of the pre-existing fault in the lower saw cut sample, as this is the mechanically weaker component of the composite sample (Figures 5.7 and 5.11). However, due to the high strength of the intact shale, the reactivated fault locked and could not propagate into the overlying shale sample (Figure 5.11). During fluid injection in cycle 2, a significant stress drops is associated with the development of a new conjugate fault in the Westerly granite saw cut sample (Figure 5.11). This complex behaviour can be explained by the lower mechanical strength of granite compared to shale (Figure 5.7).

Acoustic emission (AE) data show that this newly formed conjugate fault in the granite evolved into a fully connected fault plane, propagating from the basement into the top seal during subsequent reactivation cycles (Figure 5.11, Cycles 3 -10). The observed complexity of the time and space evolution of the fault pattern underscores the critical role of lithological variation in stress redistribution and fracture growth. These findings suggest that mechanical heterogeneity contribute to complex fault development and complex seismic sequences.

5.4.2 The role of fluid injection during fault reactivation

Stress drops increased steadily across reactivation cycles, ranging from 40 MPa to 83 MPa (Figure 5.9). The increasing stress drops with repeated slip events is consistent with the observation of progressive fault growth and linkage throughout the reactivation cycles shown by the acoustic emissions location, increasing magnitude of main events and decreasing D-values (e.g., fault maturation, Manighetti et al., 2021). Notably, the critical fluid pressure required to trigger fault slip did not vary significantly during fault growth in the successive reactivation cycles (Figure 5.9). After initial reactivation at pore fluid pressure of 40.5 MPa during Cycles 2-3, fault growth and propagation from the granite into the overlying shale sample during Cycles 4-10 occurred at relatively constant values of pore fluid pressure of 30 MPa (Figure 5.9). Interestingly, the slip rate exhibited no clear trend, varying between 3 µm s^{-1} and 34 µm s^{-1}. This variability suggests that slip dynamics are influenced by factors beyond fluid pressure, which was maintained roughly constant during cycles 4-10.

The distinct behaviour observed in the final cycles (9 and 10) emphasizes the complexity of fault development and growth during progressive reactivation of pre-existing faults in the underburden. In Cycles 9 and 10, reactivation slip events with progressively higher magnitude occurred without significant fluid pressure variation during mechanical loading and spontaneous slip with no loading, respectively (Figure 5.11). These observations highlight how events magnitude is controlled by fault growth and linkage from the granite into the overlying shale sample, rather than by pore pressure and volume variations.

Overall, our observations highlight the complex interplay between dynamic fracturing and rock strength during fault growth and linkage from a pre-existing fault in the underlying basement, under relatively constant regime of pore fluid pressure and injected volume.

5.4.3 Evolution of seismic parameters during fluid induced seismic sequences

The contrasting mechanical properties of granite and shale within the composite sample significantly influenced the evolution of seismic parameters. Early reactivation cycles showed pronounced stress drops and fracture formation concentrated in the weaker granite compared to the stronger shale. Over time, microseismic activity migrated into the overlying shale top seal (Figure 5.11), emphasising the impact of lithological heterogeneity on stress redistribution and fracture propagation. This migration pattern has also been observed in field studies of induced seismicity in the Horn River Basin (e.g., Kettlety et al., 2019; Figure 5.2).

As reactivation progressed, slip increased, and the fault matured, becoming more efficient at stress release (Marone, 1998). For comparison, stress drops for induced events in the Western Canadian Sedimentary Basin (WCSB) averaged 7.5 ± 0.5 MPa, with values ranging from 0.2 to 98 MPa for events magnitudes between M 2.3 and 4.4 (Holmgren et al., 2019). Stress drops for both natural earthquakes and induced seismicity are relatively magnitude-invariant (Allmann and Shearer, 2009).

In the early Cycle 2, distributed, small-magnitude AE events were observed, consistent with the formation of a new fracture plane in the Westerly granite sample. As reactivation cycles progressed, AE activity localised on the established fault plane, characterised by larger magnitude seismic events. This transition mirrors the transition from distributed fracturing, when intact rocks are first broken, to more localised fault slip on a mature throughgoing fault developed during repeated reactivation. The AE data further revealed increased microseismic activity during fault slip, particularly following fluid injection (Figure 5.9). Early AE activity (e.g., Cycles 2a and 2b, Figure 5.9) corresponded with new fracture plane formation, while later cycles indicated reactivation of existing fault planes (Figure 5.10B). Similar trends have been documented in laboratory studies; for example, Goebel et al. (2012) observed AE activity linked to microfracture development and fault slip in granite sawcut samples.

The spatial and temporal distribution of AE events correlated strongly with both pre-existing fault planes and newly formed fractures (Figure 5.11B). Initially, reactivation and seismicity were concentrated in the brittle granite, but subsequent cycles demonstrated increasing involvement of the shale top seal, during the progressive development of a throughgoing fault. This behaviour aligns with field observations where seismicity migrates through heterogeneous formations due to variations in rock properties (Zoback and Gorelick, 2012). The complex migration of AE hypocentres from the basement granite to the shale emphasizes the role of lithological heterogeneity and injected fluids at pressure in shaping the spatial distribution of seismicity.

P-wave velocity data showed a clear dependence on the fracturing process (Figure 5.12). During initial reactivation cycles, P-wave velocity decreased due to increased damage in the fault zone, as new fractures formed (Cycles 2a and 2b, Figure 5.9). In later cycles, partial recovery of velocity was observed, suggesting a healing or stabilization process within the fault. These findings are consistent with previous laboratory experiments, which reported P-wave reductions coinciding with AE activity during fracturing, followed by partial recovery during periods of reduced activity (Lei et al., 2000; Stanchits et al., 2011).

The *b*-value is relatively low *b* = 1.32 ± 0.06 and 1.19 ± 0.09 during the first two Cycles 1 and 2, respectively, likely due to highly localised slip along the pre-existing sawcut fault and the newly conjugate fault formed in the Westerly granite sample (Figure 5.13B). During the following cycles, the *b*-value increases to *b* = 1.80 ± 0.13, during distributed damage and fracturing when the main fault was growing and propagating from the Westerly granite sample into the overlying shale. During the final Cycles 9 and 10, when a throughgoing fault is well developed from the granite into the shale and slip events record the largest magnitudes, the *b*-value decrease to lower values b = 0.6 ± 0.07 (Figure 5.13A). These observations align with field studies where *b*-value drops were documented before the reactivation of pre-existing faults (Farahbod et al., 2015; Kettlety et al., 2019). Additionally, connections between asperity regions triggering major slip events and low *b*-values have been reported (Goebel et al., 2012). Such spatial and temporal *b*-value variations hold promise as precursors to fault slip on large, throughgoing faults in fluid injection scenarios.

The fractal dimension of the AE hypocentres evolved throughout the experiment, reflecting changes in the spatial distribution of seismicity. During the initial reactivation Cycles 1 to 2, the D-value increased, indicating a more complex, three-dimensional distribution of microseismic events as the granite pre-existing sawcut fault locked and more distributed fracturing accompanied the development of a new conjugate fault in the granite (Figure 5.12). In later cycles (3-8), the D-value was slightly decreasing although some fluctuations were observed in accord with the complexity shown by the developing fault from the granite into the shale (Figures 5.11, 5.12). During the final reactivation cycles 9 and 10, a marked decrease of the D-value close to 1 was observed, suggesting a more planar distribution of seismicity, consistent with the reactivation of a well-established, throughgoing fault plane from the granite into the shale (Figures 5.11 and 5.12). This pattern mirrors the findings of Keranen et al. (2014), who observed changes in the spatial distribution of induced seismicity during ongoing fluid injection, indicating a shift in fault geometry and behaviour over time.

5.4.4 Implications for hazard management of fluid induced seismicity

In the reactivation experiments, the reactivation of the fault system occurred when stress loading was only 80% of the fault strength. This experimental observation may suggest that controlled fluid extraction could stabilize faults. In fact, fluid extraction following reactivation allowed mechanical reloading of the fault without immediate slip, indicating a temporary stabilization of the fault system (Figure 5.9, Cycles 2b to 8). These observations support current practice in many Traffic Light Systems (TLS), where fluid extraction (bleeding off) is used to mitigate induced seismicity risks during hydraulic fracturing operations (Atkinson et al., 2020; Moein et al., 2023). However, these practices do not always meet with successful application and prevent seismic events (Figure 5.3), as evidenced by field studies documenting induced large events even after fluid injection has ceased up to a few months (Ellsworth et al., 2019; Shapiro et al., 2021).

However, the occurrence of instantaneous instability during a fluid retention phase (Figure 5.9, Cycle 10), marked by an increased rate of AE activity (Figure 5.10A), highlights a critical challenge. Residual stress redistribution along a well-developed, throughgoing fault can trigger delayed fault reactivation even after fluid injection has stopped, a behaviour observed in a few field case studies (Kao et al., 2018; Clarke et al., 2019). This behaviour complicates TLS implementation and underscore the need for robust monitoring and dynamic risk assessment frameworks.

The cyclic reactivation observed in this study underscores the potential for repeated fault slip under continuous fluid injection and retention, emphasizing the need for long-term monitoring and adaptive management strategies. Post-mortem analysis and AE monitoring reveals secondary conjugate faulting, further illustrating the complexity of fault interactions in heterogeneous formations. Fluid injection not only reactivates existing faults but can also produce new fracture networks that propagate into adjacent rock layers, increasing seismic hazard potential (Figure 5.3).

Monitoring seismic parameters, such as *b*-value, D-value, and P-wave velocity, offers valuable tools for assessing fault zone evolution during fluid injection operations – such as the growth and propagation of throughgoing faults beyond the reservoir volume. For example, reductions in *b*-value and P-wave velocity can provide early indicators of stress accumulation and fault plane evolution, enabling proactive mitigation strategies to prevent large, induced events (e.g., Fryer et al., 2019; Schultz et al., 2021).

These findings highlight the importance of integrating seismic parameter monitoring into fluid injection operations. By leveraging tools such as *b*-value trends, P-wave velocity, and D-value shifts, operators can enhance their ability to predict and manage seismic risks, contributing to safer and more effective resource extraction practices.

5.5 Conclusion

This study provides significant insights into the mechanics of fault slip and induced seismicity through detailed laboratory experiments. A key finding is that the pattern of reactivated faulting is strongly influenced by fault heterogeneity, in particular rock strength. The results also reveal a close relationship between the evolving fault structure and the magnitude of slip events.

The rate of microseismicity always increased just before and during phases of fault slip and stress drop, suggesting that acoustic emission (AE) patterns could serve as early indicators of impending slip events. Notably, the *b*-value, reflecting the size distribution of seismic events, emerged as a potential predictive indicator of the development and reactivation of a major throughgoing fault, whose size exceeds that of the reservoir and has the potential to grow into a runaway rupture. This finding holds practical implications for anticipating fault reactivation, particularly in fluid injection scenarios. Additionally, changes in P-wave velocity and fractal dimension (D-value) were identified as markers of evolving fracturing and faulting processes, and seismicity patterns, emphasizing the importance of monitoring these parameters to assess fault stability and manage seismicity risks.

In summary, this study enhances our understanding of the intricate interplay between mechanical properties, fluid pressure, and fault evolution in shaping induced seismicity patterns. The findings are critical for developing effective seismic hazard mitigation strategies in industrial applications such as hydraulic fracturing, geothermal stimulation, and wastewater disposal. By integrating seismic parameter analysis with experimental observations, this research provides valuable insights for managing induced seismicity hazards and improving operational safety.

6 Discussion and conclusions

6.1 Introduction

This chapter synthesizes the main findings presented in Chapters 3, 4, and 5, integrating them to address the overarching research questions set out in Chapter 1. The primary aim of this thesis was to advance our understanding of the key factors that trigger fluid-induced seismicity, a phenomenon increasingly associated with industrial activities such as hydraulic fracturing, enhanced geothermal stimulation, and wastewater disposal. The thesis specifically investigates the critical controls and interactions that lead to seismic events induced by fluid injections in shale unconventional reservoirs.

The central research questions explored in this thesis include the role of pore fluid in fracturing and faulting processes, its control over the reactivation and slip mode of pre-existing faults, the detection of systematic variations in seismic parameters preceding major induced events, and the potential for improving microseismic monitoring strategies. To address these questions, the research employs a combination of laboratory techniques, including the development of protocols for obtaining and handling shale core samples and the execution of triaxial loading experiments with acoustic emission monitoring to simulate and analyse the conditions under which fluid injections trigger seismic activities.

In this chapter, the findings from these studies are integrated to provide insights into their geological significance, directly addressing the main aims and objectives of the thesis. The discussion also highlights the broader implications of these findings for geohazard management strategies in fluid injection operations. Finally, the chapter concludes with a reflection on the remaining unanswered questions and suggestions for further research directions.

6.2 Key controls on fault slip modes

The triaxial loading experiments in Chapter 4 and 5 demonstrated that fault slip is facilitated through reduction in effective stress by increasing pore fluid pressure. For example, in experiment Dutff 350 and Dutff 351, a progressive increase in pore pressure triggered slip events as the fluid pressure reduced the clamping force on the newly created fracture plane (Figures 4.9 and 4.10). A reduction of 0.01 MPa and 5 MPa in the effective stress induced slip in Dutff 350 and Dutff 351, respectively. This result aligns with field studies from the Horn River Basin, such as those by Wang et al. (2016) and Schultz et al. (2017), which showed that increased pore pressure from fluid injection is a primary cause of induced seismicity in many hydraulic fracturing operations across the basin.

Lithological differences also emerged as a key factor influencing fault slip modes, affecting how different formations respond to loading and fluid injections. Samples from the Fort Simpson Formation, a clay-rich shale, are more ductile than those from the Muskwa Formation (Chapter 3) and Figures 4.8, 4.9, and 4.10. This reflects the mineralogical differences between formations, with the Fort Simpson shale acting as a fracture barrier due to its ductile nature (Figure 3.15). Furthermore, the contrast in elastic anisotropy and mechanical strength of the shale emphasized how lithological differences influence failure, fractures propagation and seismicity distribution.

The composite sample experiment (Chapter 5), which consisted of a Westerly granite sawcut to simulate a pre-existing fault in the underburden and an intact shale core from the Fort Simpson Formation, exhibited contrasting behaviours under fluid injection. The shale, which is mechanically stronger (Figure 5.7), acted as a fracture barrier (Chapter 3 and 4). In contrast, the pre-existing fault in the granite displayed more brittle, seismic slip (Figure 5.11), consistent with a more brittle failure under stress.

This difference in behaviour stems from the mechanical properties of the materials: the clay-rich Fort Simpson Formation exhibited slow, aseismic slip, while the granite experienced abrupt, seismic failure. These findings underscore the importance of considering lithological differences when assessing the seismic hazards of fluid injection activities. Field observations in formations such as the Fort Simpson shale and the Western Canadian Sedimentary Basin, documented by Dong et al. (2017b) and Baird et al. (2017), further illustrate how mechanical heterogeneity influences fault propagation during hydraulic fracturing. Similarly, Schultz et al. (2016) and Goebel and Brodsky (2018) demonstrated that variations in lithological properties significantly affect the distribution of induced seismicity during fluid injection.

The experiments also provided valuable insights into the transition between aseismic and seismic slip. In the pre-failure stage, a steady increase in AE activity indicated slow, aseismic slip, as observed in Chapter 4 (Figures 4.11, 4.12, and 4.13). However, as the differential stress increased, the AE rate sharply rose, signalling the onset of seismic slip (Figure 5.10). Similar transitions from slow creep to sudden slip have been documented in laboratory studies by Lei et al. (2000), who found that AE monitoring can detect precursors to failure. This transition is significant because it suggests that fluid injection can push faults through different slip regimes depending on the stress state and material properties. Duboeuf et al. (2017) also observed that aseismic slip could evolve into seismic slip during high-pressure fluid injection.

The results from experiment Dutff 348 (Figure 4.8), where no fluid injection was used, showed that without increased pore pressure, faults remain stable even under high differential stress. This suggests that carefully managing fluid injection pressure could help minimize the risk of triggering seismic slip. Injection protocols that increase pore pressure gradually are likely to result in more stable, aseismic slip, while rapid pressure increases may lead to abrupt seismic events, as suggested by French et al. (2016).

6.3 Implications for natural and fluid induced earthquakes

The findings from this research have broader implications for understanding both natural and fluid-induced seismicity. The laboratory experiments demonstrated that fluid injections can reduce the effective stress on faults, a process analogous to natural mechanisms such as fluid migration from deep aquifers or magma intrusion into fault zones (Elsworth et al., 1996; Danré et al., 2022). These findings suggest that the same mechanisms driving fluid-induced earthquakes are likely at play in some natural earthquakes, where fluids migrate into fault zones, reducing the effective normal stress and triggering slip.

The progressive fault reactivation observed in Chapter 5 (Figure 5.11) is consistent with seismic events observed in industrial contexts, such as earthquakes induced by hydraulic fracturing in the Western Canadian Sedimentary Basin (WCSB). Atkinson et al. (2020) demonstrated that fluid injection in the WCSB caused fault reactivation and induced earthquakes, with similar mechanisms of pore pressure build-up reducing effective stress and triggering seismicity. The results of this thesis provide a laboratory-scale model for understanding how fluid injections lead to fault reactivation, offering valuable insights into the physical processes driving fluid-induced seismicity.

The transition from aseismic to seismic slip observed in the laboratory experiments mirrors the field behaviour of induced seismicity, where fluid injections can initially result in small, undetectable slips before triggering larger seismic events as the pressure continues to build and pore fluids may migrate into pre-existing major fault zones outside the reservoir (Guglielmi et al., 2015). The results from the reactivation experiment (Figure 5.9), where fluid injection progressively reactivated the fault at higher pore pressures, provide a laboratory-scale model of fluid-induced earthquakes observed in the field (Atkinson et al., 2015; Schultz et al., 2017). Study like that by Verdon and Budge (2018), focusing on hydraulic fracturing in the Horn River basin, have similarly demonstrated how increasing pore pressure leads to seismicity.

Additionally, the contrast between aseismic slip in ductile formations and seismic slip in brittle formations mirrors observations from subduction zones, where the interface between plates may exhibit aseismic creep in some areas and generate large earthquakes in others. Studies like Saffer and Tobin (2011), Luo and Liu (2021), and Stanislowski et al. (2022) have observed these dual behaviours in the Cascadia subduction zone, offering a real-world analogue to the slip behaviours observed in this study's laboratory experiments.

6.4 Implications for geohazards management and mitigation systems of fluid induced seismicity

The findings of this thesis have implications for the management and mitigation of fluid-induced seismicity. By understanding the key controls on fault slip modes, it becomes possible to develop more effective mitigation strategies to reduce the risk of induced seismic events. This work underscores the importance of monitoring various seismic parameters—AE activity, b-value trends, and P-wave velocity variations — as critical indicators for assessing fault stability and predicting major seismic events during fluid injection operations. Together, these parameters provide a detailed picture of fault behaviour under changing stress conditions, contributing to the development of more robust and comprehensive strategies for monitoring and mitigating fluid-induced seismicity.

The AE data collected in Chapter 4 highlight the close relationship between AE activity and evolving stress conditions on faults during loading and fluid injection. In the pre-failure stage, AE activity increased steadily, corresponding to the creation of distributed fractures and slow, aseismic slip (Figures 4.11, 4.12, and 4.13). As differential stress rose and the fault approached critical stress levels, AE activity spiked sharply, indicating the coalescence of fractures into an incipient fault plane and signalling the onset of seismic slip. This distinct seismic response, in terms of AE activity, could serve as a precursor to fault slip, providing an early warning signal before major seismic events occur. Similar conclusions have been drawn by researchers who demonstrated the use of AE monitoring to predict fault failure (e.g., Verdon and Budge, 2018; Clarke et al., 2019). Additionally, the clear correlation between AE activity and fault reactivation observed in Chapter 5 (Figure 5.11) further corroborates AE's potential as a real-time indicator of fault instability.

Incorporating AE data into traffic light systems (TLS), as suggested in previous work (e.g., Schultz et al., 2021), could significantly enhance the ability to monitor and mitigate the risk of induced seismicity in real time. The steady increase in AE activity observed before failure indicates that microseismic monitoring can provide real-time insights into the evolving state of stress on a fault, allowing operators to adjust fluid injection rates or halt operations when seismic activity reaches critical levels. For example, in Chapter 5, progressively higher magnitude microseismic events recorded as the reactivated fault grow from the underburden to fully developed and major events that involve the (re)activation of major faults beyond the reservoir size.

The b-value, which represents the frequency distribution of earthquake magnitudes, emerged as another critical parameter for predicting fault stability. In this study, the b-value consistently decreased before major slip events (Chapters 4 and 5), indicating that larger seismic events were becoming more likely. This finding aligns with field observations, such as those by Atkinson et al. (2015), who found that a declining b-value often precedes significant seismic events. The b-value's predictive capability makes it a valuable tool for assessing seismic hazard in fluid injection contexts, where fluid pressures may gradually destabilise a fault over time. Incorporating b-value trends into TLS frameworks will enhance their predictive capabilities. A declining b-value, particularly when combined with increased AE activity, could signal an impending seismic event, prompting pre-emptive actions such as pressure reductions or operational shutdowns. This approach would allow for more effective seismic hazard management, especially in regions with known fault systems or lithological heterogeneity.

In addition to AE activity and b-values, the P-wave velocity variations observed during the experiments provided important insights into the dynamic nature of fault zones. As documented in Chapters 4 and 5, P-wave velocity decreased during fracturing, indicating fault damage and increased fracture density, but partially recovered afterward, suggesting a healing or stabilisation process (Figure 5.12). This cyclic behaviour — of fault damage followed by partial healing — has significant implications for understanding how faults respond to repeated fluid injections over time. The ability to track P-wave velocity changes in real time could offer valuable information about the structural integrity of the fault zone. A sudden drop in P-wave velocity may indicate increased damage and impending slip, while a recovery phase might suggest fault stabilisation. By integrating P-wave monitoring into existing seismic hazard frameworks, operators could gain clearer insights into the fault's evolving condition, helping to anticipate when a fault is most susceptible to reactivation.

The integration of AE activity, b-value trends, and P-wave velocity variations into traffic light systems (TLS) offers a comprehensive approach to seismic risk management. TLS frameworks, which are currently used to monitor and control fluid injection operations, would greatly benefit from the real-time data provided by these parameters, enhancing their predictive capabilities. For example, AE monitoring can give immediate feedback on the stress evolution within the fault, while b-value trends serve as an indicator of increasing seismic hazard. Additionally, tracking P-wave velocity can help operators assess the structural integrity of the fault zone and detect signs of damage or healing. Together, these tools allow for a more nuanced approach to managing fluid-induced seismicity, enabling operators to take proactive measures, such as adjusting injection rates or temporarily halting operations to prevent large seismic events.

In summary, this thesis contributes to the growing body of evidence that AE activity, b-value trends, and P-wave velocity variations are useful tools for understanding and managing fluid-induced seismicity. Incorporating these parameters into TLS and other monitoring frameworks can significantly enhance real-time hazard management, enabling more precise control over injection operations and reducing the risk of inducing larger seismic events.

6.5 Further research

Fluid-induced seismicity remains a complex and multifaceted challenge. The data and findings presented in this thesis provide a foundation for further studies and highlight key areas of research that could enhance our understanding of fluid-induced seismic processes. Further work based on this thesis should focus on the aspects briefly reported below.

First, while the experiments in this thesis examined short-term fault reactivation under controlled conditions, field-induced seismicity often occurs over much longer timescales. Long-term studies that monitor fault behaviour over extended periods are necessary to understand how faults evolve under prolonged fluid injection. Additionally, laboratory conditions may not fully capture the complexity of real-world fault systems. Future research should aim to scale these findings to field observations by incorporating more heterogeneous materials and larger-scale experiments. Field studies will be crucial in validating laboratory results and providing insights into fault reactivation processes at larger scales.

Second, to explain the temporal and spatial clustering and migration of seismicity observed during the reactivation experiments, it is important to consider fracture orientation, stress, and pore pressure heterogeneity as key drivers controlling seismicity evolution. My results highlight the limitations in forecasting seismic migration during fault reactivation due to limited knowledge of stress heterogeneity in the host rock.

Third, while this thesis focused primarily on the mechanical effects of fluid injections, the roles of fluid chemistry and mineralogical changes warrant further exploration. Fluids with varying chemical compositions may interact with fault minerals differently, potentially altering the fault's frictional properties and response to injections.

Finally, the laboratory experiments suggested that parameters such as b-value and AE activity could serve as precursors to seismic slip. Future research should aim to validate these findings through field-based monitoring to determine whether similar trends can be observed in real-time during industrial fluid injection operations.

6.6 Conclusion

This thesis advances the understanding of fluid-induced seismicity by elucidating the key controls on fault slip modes and the conditions under which fluid injections trigger seismic events. The findings have important implications for both natural and induced earthquakes, offering new insights into how pore pressure and lithological differences influence fault behaviour. The research also provides recommendations to enhance the predicative capabilities of current TLS by incorporating key seismic parameters, improving the management of seismic risks related to fluid injection. While several questions remain unanswered, the work presented here lays a strong foundation for further research aimed at better understanding and mitigating the risks associated with fluid-induced seismicity.

References

Ake, J., Mahrer, K., O'connell, D. & Block, L. 2005. Deep-injection and closely monitored induced seismicity at Paradox Valley, Colorado. *Bulletin of the Seismological Society of America,* 95(2)**,** 664-683, https://doi.org/10.1785/0120040072.

Aki, K. 1965. Maximum likelihood estimate of b in the formula log N= a-bM and its confidence limits. *Bull. Earthquake Res. Inst., Tokyo Univ.,* 43**,** 237-239.

Allan, A. M., Clark, A. C., Vanorio, T., Kanitpanyacharoen, W. & Wenk, H.-R. 2016. On the evolution of the elastic properties of organic-rich shale upon pyrolysis-induced thermal maturation. *GEOPHYSICS,* 81(3)**,** D263-D281, https://doi.org/10.1190/geo2015-0514.1.

Allmann, B. P. & Shearer, P. M. 2009. Global variations of stress drop for moderate to large earthquakes. *Journal of Geophysical Research: Solid Earth,* 114(B1)**,** https://doi.org/10.1029/2008JB005821.

Amini, A., Eberhardt, E., Rogers, S., Venables, S. & Gaucher, M. 2022. Empirical and numerical investigation into the influence of fluid injection volume and rate on induced seismicity in the Montney Formation, northeastern British Columbia. *Journal of Petroleum Science and Engineering,* 213**,** 110423, https://doi.org/10.1016/j.petrol.2022.110423.

Aoudia, K., Miskimins, J. L., Harris, N. B. & Mnich, C. A. 2010. Statistical Analysis of the Effects of Mineralogy On Rock Mechanical Properties of the Woodford Shale And the Associated Impacts For Hydraulic Fracture Treatment Design. 44th U.S. Rock Mechanics Symposium and 5th U.S.-Canada Rock Mechanics Symposium. ARMA-10-303.

Aplin, A. C., Matenaar, I. F., McCarty, D. K. & Van Der Pluijm, B. A. 2006. Influence of Mechanical Compaction and Clay Mineral Diagenesis on the Microfabric and Pore-Scale Properties of Deep-Water Gulf of Mexico Mudstones. *Clays and Clay Minerals,* 54**,** 500-514, https://doi.org/10.1346/CCMN.2006.0540411.

Astm 2009. Standard test methods for laboratory determination of density (unit weight) of soil specimens. *Standard D7263-09***,** https://doi.org/10.1520/D7263-21.

Atkinson, G. M., Eaton, D. W., Ghofrani, H., Walker, D., Cheadle, B., Schultz, R., Shcherbakov, R., Tiampo, K., Gu, J., Harrington, R. M., Liu, Y., Van Der Baan, M. & Kao, H. 2016. Hydraulic Fracturing and Seismicity in the Western Canada Sedimentary Basin. *Seismological Research Letters,* 87(3)**,** 631-647, https://doi.org/10.1785/0220150263.

Atkinson, G. M., Eaton, D. W. & Igonin, N. 2020. Developments in understanding seismicity triggered by hydraulic fracturing. 1(5)**,** 264-277, https://doi.org/10.1038/s43017-020-0049-7.

Atkinson, G. M., Ghofrani, H. & Assatourians, K. 2015. Impact of Induced Seismicity on the Evaluation of Seismic Hazard: Some Preliminary Considerations. *Seismological Research Letters,* 86(3)**,** 1009-1021, https://doi.org/10.1785/0220140204.

Bachmann, C. E., Wiemer, S., Goertz‐Allmann, B. & Woessner, J. 2012. Influence of pore‐pressure on the event‐size distribution of induced earthquakes. *Geophysical Research Letters,* 39(9)**,** https://doi.org/10.1029/2012GL051480.

Baig, A. 2014. Hydraulic fracturing-induced seismicity: an overview of recent observations and implications on development. *first break,* 32(7), https://doi.org/10.3997/1365-2397.32.7.76887.

Baird, A. F., Kendall, J. M., Fisher, Q. J. & Budge, J. 2017. The role of texture, cracks, and fractures in highly anisotropic shales. *Journal of Geophysical Research: Solid Earth,* 122(12), 10,341-10,351, https://doi.org/10.1002/2017JB014710.

Bao, X. & Eaton, D. W. 2016. Fault activation by hydraulic fracturing in western Canada. *Science,* 354(6318), 1406-1409, https://doi.org/10.1126/science.aag2583.

Beaudoin, B., Allison, J., Khalid, S. & Faurschou, K. 2011. Horn River Basin: A Study of the Behavior of Frac Barriers in a Thick Shale Package Using the Integration of Microseismic, Geomechanics and Log Analysis. Canadian Unconventional Resources Conference. SPE-147510-MS, https://doi.org/10.2118/147510-ms.

Bedford, J. D. 2017. *The kinetics and mechanics of a dehydrating system and the deformation of porous rock.* PhD thesis, University of Liverpool, UK, https://doi.org/10.17638/03009159.

Benson, P. M., Thompson, B. D., Meredith, P. G., Vinciguerra, S. & Young, R. P. 2007. Imaging slow failure in triaxially deformed Etna basalt using 3D acoustic-emission location and X-ray computed tomography. *Geophysical Research Letters,* 34(3), https://doi.org/10.1029/2006GL028721.

Birch, F. 1960. The Velocity of Compressional Waves in Rocks to 10 kbars. Part 1. *Journal of Geophysical Research,* 65, 1083-1102, https://doi.org/10.1029/JZ065i004p01083.

Bonnelye, A., Schubnel, A., David, C., Henry, P., Guglielmi, Y., Gout, C., Fauchille, A.-L. & Dick, P. 2017a. Elastic wave velocity evolution of shales deformed under uppermost crustal conditions. *Journal of Geophysical Research: Solid Earth,* 122(1), 130-141, https://doi.org/10.1002/2016jb013540.

Bonnelye, A., Schubnel, A., David, C., Henry, P., Guglielmi, Y., Gout, C., Fauchille, A.-L. & Dick, P. 2017b. Strength anisotropy of shales deformed under uppermost crustal conditions. *Journal of Geophysical Research: Solid Earth,* 122(1), 110-129, https://doi.org/10.1002/2016JB013040.

Bosman, K., Baig, A., Viegas, G. & Urbancic, T. 2016. Towards an improved understanding of induced seismicity associated with hydraulic fracturing. *First break,* 34(7), https://doi.org/10.3997/1365-2397.34.7.86051.

Brace, W. F., Walsh, J. B. & Frangos, W. T. 1968. Permeability of granite under high pressure. *Journal of Geophysical Research,* 73(6), 2225-2236, https://doi.org/10.1029/JB073i006p02225.

Brantut, N., Schubnel, A. & Guéguen, Y. 2011. Damage and rupture dynamics at the brittle-ductile transition: The case of gypsum. *Journal of Geophysical Research: Solid Earth,* 116(B1), https://doi.org/10.1029/2010JB007675.

Burlini, L., Vinciguerra, S., Di Toro, G., De Natale, G., Meredith, P. & Burg, J.-P. 2007. Seismicity preceding volcanic eruptions: New experimental insights. *Geology,* 35(2), 183-186, https://doi.org/10.1130/G23195A.1.

Butcher, A., Luckett, R., Verdon, J. P., Kendall, J. M., Baptie, B. & Wookey, J. 2017. Local magnitude discrepancies for near‐event receivers: Implications for the UK traffic‐light scheme. *Bulletin of the Seismological Society of America,* 107(2)**,** 532-541, https://doi.org/10.1785/0120160225.

Byerlee, J. 1978. Friction of rocks. *Rock friction and earthquake prediction.* Springer, https://doi.org/10.1007/BF00876528.

Cappa, F., Guglielmi, Y., Nussbaum, C. & Birkholzer, J. 2018. On the Relationship Between Fault Permeability Increases, Induced Stress Perturbation, and the Growth of Aseismic Slip During Fluid Injection. *Geophysical Research Letters,* 45(20)**,** 11,012-11,020, https://doi.org/10.1029/2018GL080233.

Cappa, F. & Rutqvist, J. 2011. Modeling of coupled deformation and permeability evolution during fault reactivation induced by deep underground injection of CO 2. *International Journal of Greenhouse Gas Control,* 5(2)**,** 336-346, https://doi.org/10.1016/j.ijggc.2010.08.005.

Cebry, S. B. L., Ke, C.-Y. & McLaskey, G. C. 2022. The Role of Background Stress State in Fluid-Induced Aseismic Slip and Dynamic Rupture on a 3-m Laboratory Fault. *Journal of Geophysical Research: Solid Earth,* 127(8)**,** e2022JB024371, https://doi.org/10.1029/2022JB024371.

Chan, J. & Schmitt, D. R. 2015. Elastic Anisotropy of a Metamorphic Rock Sample of the Canadian Shield in Northeastern Alberta. 48(4)**,** 1369-1385, https://doi.org/10.1007/s00603-014-0664-z.

Chandler, M. R., Meredith, P. G., Brantut, N. & Crawford, B. R. 2016. Fracture toughness anisotropy in shale. *Journal of Geophysical Research: Solid Earth,* 121(3)**,** 1706-1729, https://doi.org/10.1002/2015jb012756.

Chang, K. W., Yoon, H., Kim, Y. & Lee, M. Y. 2020. Operational and geological controls of coupled poroelastic stressing and pore-pressure accumulation along faults: Induced earthquakes in Pohang, South Korea. *Scientific Reports,* 10(1)**,** 2073, https://doi.org/10.1038/s41598-020-58881-z.

Charlton, T. S., Rouainia, M., Aplin, A. C., Fisher, Q. J. & Bowen, L. 2023. Nanoindentation of Horn River Basin Shales: The Micromechanical Contrast Between Overburden and Reservoir Formations. *Journal of Geophysical Research: Solid Earth,* 128(3)**,** e2022JB025957, https://doi.org/10.1029/2022JB025957.

Ciardo, F. & Rinaldi, A. P. 2021. Impact of injection rate ramp-up on nucleation and arrest of dynamic fault slip. 8(1)**,** 28, https://doi.org/10.1007/s40948-021-00336-4.

Clarke, H., Eisner, L., Styles, P. & Turner, P. 2014. Felt seismicity associated with shale gas hydraulic fracturing: The first documented example in Europe. *Geophysical Research Letters,* 41(23)**,** 8308-8314, https://doi.org/10.1002/2014GL062047.

Clarke, H., Verdon, J. P., Kettlety, T., Baird, A. F. & Kendall, J. M. 2019. Real‐time imaging, forecasting, and management of human‐induced seismicity at Preston New Road, Lancashire, England. *Seismological Research Letters,* 90(5)**,** 1902-1915, https://doi.org/10.1785/0220190110.

Culshaw, M. G. 2015. Ulusay, R (ed.), 2015. The ISRM suggested methods for rock characterization, testing and monitoring: 2007–2014. 74(4), 1499-1500, https://doi.org/10.1007/s10064-015-0780-3.

Danré, P., De Barros, L., Cappa, F. & Ampuero, J. P. 2022. Prevalence of Aseismic Slip Linking Fluid Injection to Natural and Anthropogenic Seismic Swarms. *Journal of Geophysical Research: Solid Earth,* 127, https://doi.org/10.1029/2022JB025571.

Day-Stirrat, R. J., Aplin, A. C., Kurtev, K. D., Schleicher, A. M., Brown, A. P. & Środoń, J. 2017. Late diagenesis of illite-smectite in the Podhale Basin, southern Poland: Chemistry, morphology, and preferred orientation. *Geosphere,* 13(6), 2137-2153, https://doi.org/10.1130/ges01516.1.

Day-Stirrat, R. J., Dutton, S. P., Milliken, K. L., Loucks, R. G., Aplin, A. C., Hillier, S. & Van Der Pluijm, B. A. 2010. Fabric anisotropy induced by primary depositional variations in the silt: clay ratio in two fine-grained slope fan complexes: Texas Gulf Coast and northern North Sea. 226(1), 42-53, https://doi.org/10.1016/j.sedgeo.2010.02.007.

De Barros, L., Cappa, F., Guglielmi, Y., Duboeuf, L. & Grasso, J.-R. 2019. Energy of injection-induced seismicity predicted from in-situ experiments. 9(1), 4999, https://doi.org/10.1038/s41598-019-41306-x.

De Paola, N., Faulkner, D. R. & Collettini, C. 2009. Brittle versus ductile deformation as the main control on the transport properties of low-porosity anhydrite rocks. *Journal of Geophysical Research: Solid Earth,* 114(B6), https://doi.org/10.1029/2008jb005967.

Dewhurst, D. N. & Siggins, A. F. 2006. Impact of fabric, microcracks and stress field on shale anisotropy. *Geophysical Journal International,* 165(1), 135-148, https://doi.org/10.1111/j.1365-246X.2006.02834.x.

Dewhurst, D. N., Siggins, A. F., Kuila, U., Clennell, M. B., Raven, M. D. & Nordgard-Bolas, H. M. 2008. Rock Physics, Geomechanics and Rock Properties in Shales — Where are the Links? *SHIRMS 2008: First Southern Hemisphere International Rock Mechanics Symposium*, 461-474, https://doi.org/10.36487/ACG_repo/808_39.

Dewhurst, D. N., Siggins, A. F., Sarout, J., Raven, M. D. & Nordgård-Bolås, H. M. 2011. Geomechanical and ultrasonic characterization of a Norwegian Sea shale. *Geophysics,* 76(3), WA101-WA111, https://doi.org/10.1190/1.3569599.

Di Luccio, F., Ventura, G., Di Giovambattista, R., Piscini, A. & Cinti, F. R. 2010. Normal faults and thrusts reactivated by deep fluids: The 6 April 2009 Mw 6.3 L'Aquila earthquake, central Italy. *Journal of Geophysical Research: Solid Earth,* 115(B6), https://doi.org/10.1029/2009jb007190.

Dieterich, J. H., Richards‐Dinger, K. B. & Kroll, K. A. 2015. Modeling injection‐induced seismicity with the physics‐based earthquake simulator RSQSim. *Seismological Research Letters,* 86(4), 1102-1109, https://doi.org/10.1785/0220150057.

Dong, T., Harris, N. B., Ayranci, K., Twemlow, C. E. & Nassichuk, B. R. 2015. Porosity characteristics of the Devonian Horn River shale, Canada: Insights from lithofacies classification and shale composition. 141-142, 74-90, https://doi.org/10.1016/j.coal.2015.03.001.

Dong, T., Harris, N. B., Ayranci, K., Twemlow, C. E. & Nassichuk, B. R. 2017a. The impact of composition on pore throat size and permeability in high maturity shales: Middle and Upper Devonian Horn River Group, northeastern British Columbia, Canada. *Marine and petroleum geology,* 81**,** 220-236, https://doi.org/10.1016/j.marpetgeo.2017.01.011.

Dong, T., Harris, N. B., Ayranci, K. & Yang, S. 2017b. The impact of rock composition on geomechanical properties of a shale formation: Middle and Upper Devonian Horn River Group shale, Northeast British Columbia, Canada. *AAPG Bulletin,* 101(2)**,** 177-204, https://doi.org/10.1306/07251615199.

Duboeuf, L., De Barros, L., Cappa, F., Guglielmi, Y., Deschamps, A. & Seguy, S. 2017. Aseismic Motions Drive a Sparse Seismicity During Fluid Injections Into a Fractured Zone in a Carbonate Reservoir. *Journal of Geophysical Research: Solid Earth,* 122(10)**,** 8285-8304, https://doi.org/10.1002/2017JB014535.

Eaton, D. W., Davidsen, J., Pedersen, P. K. & Boroumand, N. 2014a. Breakdown of the Gutenberg-Richter relation for microearthquakes induced by hydraulic fracturing: influence of stratabound fractures. *Geophysical Prospecting,* 62(4)**,** 806-818, https://doi.org/10.1111/1365-2478.12128.

Eaton, D. W. & Maghsoudi, S. 2015. 2b... or not 2b? Interpreting magnitude distributions from microseismic catalogs. *First Break,* 33(10)**,** https://doi.org/10.3997/1365-2397.33.10.83159.

Eaton, D. W., Van Der Baan, M., Birkelo, B. & Tary, J.-B. 2014b. Scaling relations and spectral characteristics of tensile microseisms: Evidence for opening/closing cracks during hydraulic fracturing. *Geophysical Journal International,* 196(3)**,** 1844-1857, https://doi.org/10.1093/gji/ggt498.

El-Isa, Z. H. & Eaton, D. W. 2014. Spatiotemporal variations in the b-value of earthquake magnitude–frequency distributions: Classification and causes. *Tectonophysics,* 615**,** 1-11, https://doi.org/10.1016/j.tecto.2013.12.001.

Ellsworth, W. L. 2013. Injection-Induced Earthquakes. *Science,* 341(6142)**,** 1225942, https://doi.org/10.1126/science.1225942.

Ellsworth, W. L., Giardini, D., Townend, J., Ge, S. & Shimamoto, T. 2019. Triggering of the Pohang, Korea, Earthquake (Mw 5.5) by Enhanced Geothermal System Stimulation. *Seismological Research Letters,* 90(5)**,** 1844-1858, https://doi.org/10.1785/0220190102.

Elsworth, D., Voight, B., Ouyang, Z. & Piggott, A. R. 1996. Poroelastic Response Resulting from Magma Intrusion, https://doi.org/10.1007/978-94-015-8698-6_12.

Farahbod, A. M., Cassidy, J. F., Kao, H. & Walker, D. 2014. Collaborative studies of regional seismicity in northeast British Columbia. *Can. Soc. Explor. Gephys. Rec,* 39**,** 40-44.

Farahbod, A. M., Kao, H., Cassidy, J. F. & Walker, D. 2015. How did hydraulic-fracturing operations in the Horn River Basin change seismicity patterns in northeastern British Columbia, Canada? *The leading edge,* 34(6)**,** 658-663, https://doi.org/10.1190/tle34060658.1.

Fasola, S. L., Brudzinski, M. R., Skoumal, R. J., Langenkamp, T., Currie, B. S. & Smart, K. J. 2019. Hydraulic Fracture Injection Strategy Influences the Probability of Earthquakes in the Eagle Ford Shale Play of South Texas. *Geophysical Research Letters,* 46(22)**,** 12958-12967, https://doi.org/10.1029/2019GL085167.

Fischer, G. J. 1992. Chapter 8 The Determination of Permeability and Storage Capacity: Pore Pressure Oscillation Method. *International Geophysics,* 51**,** 187-211, https://doi.org/10.1016/S0074-6142(08)62823-5.

French, M. E., Zhu, W. & Banker, J. 2016. Fault slip controlled by stress path and fluid pressurization rate. *Geophysical Research Letters,* 43(9)**,** 4330-4339, https://doi.org/10.1002/2016GL068893.

Frohlich, C. & Davis, S. D. 1993. Teleseismic b values; or, much ado about 1.0. *Journal of Geophysical Research: Solid Earth,* 98(B1)**,** 631-644, https://doi.org/10.1029/92JB01891.

Fryer, B., Siddiqi, G. & Laloui, L. 2019. Injection-induced seismicity: strategies for reducing risk using high stress path reservoirs and temperature-induced stress preconditioning. *Geophysical Journal International,* 220(2)**,** 1436-1446, https://doi.org/10.1093/gji/ggz490.

Galis, M., Ampuero, J. P., Mai, P. M. & Cappa, F. 2017. Induced seismicity provides insight into why earthquake ruptures stop. *Science Advances,* 3(12)**,** eaap7528, https://doi.org/10.1126/sciadv.aap7528.

Ge, S. & Saar, M. O. 2022. Induced seismicity during geoenergy development—A hydromechanical perspective. *Journal of Geophysical Research: Solid Earth,* 127(3)**,** e2021JB023141, https://doi.org/10.1029/2021JB023141.

Giorgetti, C., Collettini, C., Scuderi, M. M., Barchi, M. R. & Tesei, T. 2016. Fault geometry and mechanics of marly carbonate multilayers: An integrated field and laboratory study from the Northern Apennines, Italy. 93**,** 1-16, https://doi.org/10.1016/j.jsg.2016.10.001.

Goebel, T. H. & Brodsky, E. E. 2018. The spatial footprint of injection wells in a global compilation of induced earthquake sequences. *Science,* 361(6405)**,** 899-904, https://doi.org/10.1126/science.aat5449.

Goebel, T. H. W., Becker, T. W., Schorlemmer, D., Stanchits, S., Sammis, C., Rybacki, E. & Dresen, G. 2012. Identifying fault heterogeneity through mapping spatial anomalies in acoustic emission statistics. *Journal of Geophysical Research: Solid Earth,* 117(B3)**,** https://doi.org/10.1029/2011JB008763.

Goebel, T. H. W., Candela, T., Sammis, C. G., Becker, T. W., Dresen, G. & Schorlemmer, D. 2013. Seismic event distributions and off-fault damage during frictional sliding of saw-cut surfaces with pre-defined roughness. *Geophysical Journal International,* 196(1)**,** 612-625, https://doi.org/10.1093/gji/ggt401.

Goebel, T. H. W., Kwiatek, G., Becker, T. W., Brodsky, E. E. & Dresen, G. 2017. What allows seismic events to grow big?: Insights from b-value and fault roughness analysis in laboratory stick-slip experiments. *Geology,* 45(9)**,** 815-818, https://doi.org/10.1130/g39147.1.

Goodfellow, S. & Young, R. 2014. A laboratory acoustic emission experiment under in situ conditions. *Geophysical Research Letters,* 41(10)**,** 3422-3430, https://doi.org/10.1002/2014GL059965.

Goodfellow, S. D. 2015. *Quantitative analysis of acoustic emission from rock fracture experiments.* PhD thesis, University of Toronto, Canada, http://doi.org/10.13140/RG.2.2.24017.63841.

Goodfellow, S. D., Nasseri, M. H. B., Maxwell, S. C. & Young, R. P. 2015. Hydraulic fracture energy budget: Insights from the laboratory. *Geophysical Research Letters,* 42(9)**,** 3179-3187, https://doi.org/10.1002/2015GL063093.

Grigoli, F., Cesca, S., Priolo, E., Rinaldi, A. P., Clinton, J. F., Stabile, T. A., Dost, B., Fernandez, M. G., Wiemer, S. & Dahm, T. 2017. Current challenges in monitoring, discrimination, and management of induced seismicity related to underground industrial activities: A European perspective. *Reviews of Geophysics,* 55(2)**,** 310-340, https://doi.org/10.1002/2016RG000542.

Guglielmi, Y., Cappa, F., Avouac, J.-P., Henry, P. & Elsworth, D. 2015. Seismicity triggered by fluid injection–induced aseismic slip. *Science,* 348(6240)**,** 1224, https://doi.org/10.1126/science.aab0476.

Gutenberg, B. & Richter, C. F. 1944. Frequency of earthquakes in California. *Bulletin of the Seismological society of America,* 34(4)**,** 185-188, https://doi.org/10.1785/BSSA0340040185.

Hajati, T., Langenbruch, C. & Shapiro, S. A. 2015. A statistical model for seismic hazard assessment of hydraulic-fracturing-induced seismicity. *Geophysical Research Letters,* 42(24)**,** 10,601-10,606, https://doi.org/10.1002/2015GL066652.

Harbord, C. W. A. 2018. *Earthquake nucleation, rupture and slip on rough laboratory faults.* PhD thesis, Durham University, UK, http://etheses.dur.ac.uk/12725/.

Hennings, P. H., Nicot, J.-P., Gao, R. S., Deshon, H. R., Lund Snee, J.-E., Morris, A. P., Brudzinski, M. R., Horne, E. A. & Breton, C. 2021. Pore Pressure Threshold and Fault Slip Potential for Induced Earthquakes in the Dallas-Fort Worth Area of North Central Texas. *Geophysical Research Letters,* 48(15)**,** e2021GL093564, https://doi.org/10.1029/2021GL093564.

Higgins, S., Goodwin, S., Donald, A., Bratton, T. & Tracy, G. 2008. Anisotropic Stress Models Improve Completion Design in the Baxter Shale. SPE Annual Technical Conference and Exhibition. SPE-115736-MS, https://doi.org/10.2118/115736-ms.

Hirata, T., Satoh, T. & Ito, K. 1987. Fractal structure of spatial distribution of microfracturing in rock. *Geophysical Journal International,* 90(2)**,** 369-374, https://doi.org/10.1111/j.1365-246X.1987.tb00732.x.

Holmgren, J. M., Atkinson, G. M. & Ghofrani, H. 2019. Stress Drops and Directivity of Induced Earthquakes in the Western Canada Sedimentary Basin. *Bulletin of the Seismological Society of America***,** https://doi.org/10.1785/0120190035.

Hornby, B. E. 1998. Experimental laboratory determination of the dynamic elastic properties of wet, drained shales. *Journal of Geophysical Research: Solid Earth,* 103(B12)**,** 29945-29964, https://doi.org/10.1029/97JB02380.

Horne, S. A. 2013. A statistical review of mudrock elastic anisotropy. *Geophysical Prospecting,* 61(4)**,** 817-826, https://doi.org/10.1111/1365-2478.12036.

Hubbert, K. M. & Rubey, W. W. 1959. ROLE OF FLUID PRESSURE IN MECHANICS OF OVERTHRUST FAULTING: I. MECHANICS OF FLUID-FILLED POROUS SOLIDS AND ITS APPLICATION TO OVERTHRUST FAULTING. *GSA Bulletin,* 70(2)**,** 115-166, https://doi.org/10.1130/0016-7606(1959)70[115:ROFPIM]2.0.CO;2.

Igonin, N., Verdon, J. P., Kendall, J.-M. & Eaton, D. W. 2021. Large-Scale Fracture Systems Are Permeable Pathways for Fault Activation During Hydraulic Fracturing. *Journal of Geophysical Research: Solid Earth,* 126(3), e2020JB020311, https://doi.org/10.1029/2020JB020311.

Johansen, T. A., Ruud, B. O. & Jakobsen, M. 2004. Effect of grain scale alignment on seismic anisotropy and reflectivity of shales. *Geophysical Prospecting,* 52(2), 133-149, https://doi.org/10.1046/j.1365-2478.2003.00405.x.

Johnston, J. E. & Christensen, N. I. 1995. Seismic anisotropy of shales. *Journal of Geophysical Research: Solid Earth,* 100(B4), 5991-6003, https://doi.org/10.1029/95JB00031.

Kagan, Y. Y. 2007. Earthquake spatial distribution: the correlation dimension. *Geophysical Journal International,* 168(3), 1175-1194, https://doi.org/10.1111/j.1365-246X.2006.03251.x.

Kao, H., Visser, R., Smith, B. & Venables, S. 2018. Performance assessment of the induced seismicity traffic light protocol for northeastern British Columbia and western Alberta. *The Leading Edge,* 37(2), 117-126, https://doi.org/10.1190/tle37020117.1.

Kaown, D., Lee, K.-K., Kim, J., Woo, J.-U., Lee, S., Park, I.-W., Lee, D., Lee, J.-Y., Kim, H., Ge, S. & Yeo, I.-W. 2021. Earthquakes and very deep groundwater perturbation mutually induced. 11(1), 13632, https://doi.org/10.1038/s41598-021-92937-y.

Kendall, J.-M., Butcher, A., Stork, A. L., Verdon, J. P., Luckett, R. & Baptie, B. J. 2019. How big is a small earthquake? Challenges in determining microseismic magnitudes. *First Break,* 37(2), 51-56, https://doi.org/10.3997/1365-2397.n0015.

Kendall, J.-M., Fisher, Q., Crump, S. C., Maddock, J., Carter, A., Hall, S., Wookey, J., Valcke, S., Casey, M. & Lloyd, G. 2007. Seismic anisotropy as an indicator of reservoir quality in siliciclastic rocks. *Geological Society, London, Special Publications,* 292(1), 123-136, https://doi.org/10.1144/SP292.7.

Keranen, K. M., Savage, H. M., Abers, G. A. & Cochran, E. S. 2013. Potentially induced earthquakes in Oklahoma, USA: Links between wastewater injection and the 2011 Mw 5.7 earthquake sequence. *Geology,* 41(6), 699-702, https://doi.org/10.1130/g34045.1.

Keranen, K. M. & Weingarten, M. 2018. Induced Seismicity. *Annual Review of Earth and Planetary Sciences,* 46(1), 149-174, https://doi.org/10.1146/annurev-earth-082517-010054.

Keranen, K. M., Weingarten, M., Abers, G. A., Bekins, B. A. & Ge, S. 2014. Sharp increase in central Oklahoma seismicity since 2008 induced by massive wastewater injection. *Science,* 345(6195), 448-451, https://doi.org/10.1126/science.1255802.

Kettlety, T. & Verdon, J. P. 2021. Fault triggering mechanisms for hydraulic fracturing-induced seismicity from the Preston New Road, UK Case Study. *Frontiers in Earth Science,* 9, 670771, https://doi.org/10.3389/feart.2021.670771.

Kettlety, T., Verdon, J. P., Werner, M. J., Kendall, J. M. & Budge, J. 2019. Investigating the role of elastostatic stress transfer during hydraulic fracturing-induced fault activation. *Geophysical Journal International,* 217(2), 1200-1216, https://doi.org/10.1093/gji/ggz080.

Khajehdehi, O., Goebel, T. H. W., Dresen, G. & Davidsen, J. 2024. Magnitude Clustering During Stick-Slip Dynamics on Laboratory Faults. *Geophysical Research Letters,* 51(20), e2024GL109865, https://doi.org/10.1029/2024GL109865.

Kim, K.-H., Ree, J.-H., Kim, Y., Kim, S., Kang, S. Y. & Seo, W. 2018. Assessing whether the 2017 Mw 5.4 Pohang earthquake in South Korea was an induced event. *Science,* 360(6392), 1007, https://doi.org/10.1126/science.aat6081.

Kivi, I. R., Boyet, A., Wu, H., Walter, L., Hanson-Hedgecock, S., Parisio, F. & Vilarrasa, V. 2023. Global physics-based database of injection-induced seismicity. 15(7), 3163-3182, https://doi.org/10.5194/essd-15-3163-2023.

Kozłowska, M., Brudzinski, M. R., Friberg, P., Skoumal, R. J., Baxter, N. D. & Currie, B. S. 2018. Maturity of nearby faults influences seismic hazard from hydraulic fracturing. *Proceedings of the National Academy of Sciences,* 115(8), E1720-E1729, https://doi.org/10.1073/pnas.1715284115.

Kwiatek, G., Goebel, T. H. W. & Dresen, G. 2014. Seismic moment tensor and b value variations over successive seismic cycles in laboratory stick-slip experiments. *Geophysical Research Letters,* 41(16), 5838-5846, https://doi.org/10.1002/2014GL060159.

Kwiatek, G., Plenkers, K., Dresen, G. & Group, J. R. 2011. Source parameters of picoseismicity recorded at Mponeng deep gold mine, South Africa: Implications for scaling relations. *Bulletin of the Seismological Society of America,* 101(6), 2592-2608, https://doi.org/10.1785/0120110094.

Kwiatek, G., Saarno, T., Ader, T., Bluemle, F., Bohnhoff, M., Chendorain, M., Dresen, G., Heikkinen, P., Kukkonen, I., Leary, P., Leonhardt, M., Malin, P., Martínez-Garzón, P., Passmore, K., Passmore, P., Valenzuela, S. & Wollin, C. 2019. Controlling fluid-induced seismicity during a 6.1-km-deep geothermal stimulation in Finland. *Science Advances,* 5(5), eaav7224, https://doi.org/10.1126/sciadv.aav7224.

Labani, M. M. & Rezaee, R. 2015. The Importance of Geochemical Parameters and Shale Composition on Rock Mechanical Properties of Gas Shale Reservoirs: a Case Study From the Kockatea Shale and Carynginia Formation From the Perth Basin, Western Australia. *Rock Mechanics and Rock Engineering,* 48, 1249-1257, https://doi.org/10.1007/s00603-014-0617-6.

Lei, X., Huang, D., Su, J., Jiang, G., Wang, X., Wang, H., Guo, X. & Fu, H. 2017. Fault reactivation and earthquakes with magnitudes of up to Mw4.7 induced by shale- gas hydraulic fracturing in Sichuan Basin, China. *Sci Rep,* 7(1), 7971-7971, https://doi.org/10.1038/s41598-017-08557-y.

Lei, X., Kusunose, K., Rao, M. V. M. S., Nishizawa, O. & Satoh, T. 2000. Quasi-static fault growth and cracking in homogeneous brittle rock under triaxial compression using acoustic emission monitoring. *Journal of Geophysical Research: Solid Earth,* 105(B3), 6127-6139, https://doi.org/10.1029/1999JB900385.

Li, L., Tan, J., Wood, D. A., Zhao, Z., Becker, D., Lyu, Q., Shu, B. & Chen, H. 2019. A review of the current status of induced seismicity monitoring for hydraulic fracturing in unconventional tight oil and gas reservoirs. *Fuel,* 242, 195-210, https://doi.org/10.1016/j.fuel.2019.01.026.

Li, X., Lei, X., Li, Q. & Li, X. 2017. Experimental investigation of Sinian shale rock under triaxial stress monitored by ultrasonic transmission and acoustic emission. 43, 110-123, https://doi.org/10.1016/j.jngse.2017.03.035.

Lockner, D. & Byerlee, J. 1977. Hydrofracture in Weber sandstone at high confining pressure and differential stress. *Journal of Geophysical research,* 82(14), 2018-2026, https://doi.org/10.1029/JB082i014p02018.

Lockner, D., Byerlee, J. D., Kuksenko, V., Ponomarev, A. & Sidorin, A. 1991. Quasi-static fault growth and shear fracture energy in granite. *Nature,* 350(6313), 39-42, https://doi.org/10.1038/350039a0.

Lockner, D. A. & Beeler, N. M. 1999. Premonitory slip and tidal triggering of earthquakes. *Journal of Geophysical Research: Solid Earth,* 104(B9), 20133-20151, https://doi.org/10.1029/1999JB900205.

Lockner, D. A., Beeler, N. M., Lee, W. H. K., Kanamori, H., Jennings, P. C. & Kisslinger, C. 2002. 32 - Rock Failure and Earthquakes. *International Handbook of Earthquake and Engineering Seismology, Part A.* Academic Press, https://doi.org/10.1016/S0074-6142(02)80235-2.

Lockner, D. A., Moore, D. E. & Reches, Z. E. 1992. Microcrack interaction leading to shear fracture. The 33rd U.S. Symposium on Rock Mechanics (USRMS). ARMA-92-0807.

Luo, Y. & Liu, Z. 2021. Fault zone heterogeneities explain depth-dependent pattern and evolution of slow earthquakes in Cascadia. *Nature Communications,* 12, https://doi.org/10.1038/s41467-021-22232-x.

Maghsoudi, S., Baró, J., Kent, A., Eaton, D. & Davidsen, J. 2018. Interevent Triggering in Microseismicity Induced by Hydraulic Fracturing. *Bulletin of the Seismological Society of America,* 108(3A), 1133-1146, https://doi.org/10.1785/0120170368.

Mahani, A. B. 2021. Seismic b value within the Montney play of northeastern British Columbia, Canada. *Canadian Journal of Earth Sciences,* 58(8), 720-730, https://doi.org/10.1139/cjes-2020-0157.

Majer, E. L., Baria, R., Stark, M., Oates, S., Bommer, J., Smith, B. & Asanuma, H. 2007. Induced seismicity associated with enhanced geothermal systems. *Geothermics,* 36(3), 185-222, https://doi.org/10.1016/j.geothermics.2007.03.003.

Manighetti, I., Mercier, A. & De Barros, L. 2021. Fault Trace Corrugation and Segmentation as a Measure of Fault Structural Maturity. *Geophysical Research Letters,* 48(20), e2021GL095372, https://doi.org/10.1029/2021GL095372.

Manual, I. U. O. 2019. InSite Seismic Processor: User Operations Manual. Applied Seismology Consultants.

Marone, C. 1998. LABORATORY-DERIVED FRICTION LAWS AND THEIR APPLICATION TO SEISMIC FAULTING. *Annual Review of Earth and Planetary Sciences,* 26(1), 643-696, https://doi.org/10.1146/annurev.earth.26.1.643.

Martínez-Garzón, P., Kwiatek, G., Bohnhoff, M. & Dresen, G. 2016. Impact of fluid injection on fracture reactivation at The Geysers geothermal field. *Journal of Geophysical Research: Solid Earth,* 121(10), 7432-7449, https://doi.org/10.1002/2016JB013137.

Marzocchi, W. & Sandri, L. 2003. A review and new insights on the estimation of the b-value and its uncertainty. *Annals of Geophysics,* 46, 1271-1282, https://doi.org/10.4401/ag-3472.

Mavko, G. & Bandyopadhyay, K. 2008. Approximate fluid substitution for vertical velocities in weakly anisotropic VTI rocks. *Geophysics,* 74(1), D1-D6, https://doi.org/10.1190/1.3026552.

Mavko, G., Mukerji, T. & Dvorkin, J. 2009. *The Rock Physics Handbook 2ed*, Cambridge University Press, https://doi.org/10.1017/CBO9780511626753.

McGarr, A. & Barbour, A. J. 2018. Injection-Induced Moment Release Can Also Be Aseismic. *Geophysical Research Letters,* 45(11), 5344-5351, https://doi.org/10.1029/2018gl078422.

McGarr, A., Simpson, D., Seeber, L. & Lee, W. 2002. Case histories of induced and triggered seismicity. *International Geophysics Series,* 81(A), 647-664, https://doi.org/10.1016/S0074-6142(02)80243-1.

McGarr, A. F. 2014. Maximum magnitude earthquakes induced by fluid injection. *Journal of Geophysical Research B: Solid Earth,* 119(2), 1008-1019, https://doi.org/10.1002/2013JB010597.

McLaskey, G. C. & Glaser, S. D. 2012. Acoustic emission sensor calibration for absolute source measurements. *Journal of Nondestructive Evaluation,* 31, 157-168, https://doi.org/10.1007/s10921-012-0131-2.

McLaskey, G. C., Lockner, D. A., Kilgore, B. D. & Beeler, N. M. 2015. A robust calibration technique for acoustic emission systems based on momentum transfer from a ball drop. *Bulletin of the Seismological Society of America,* 105(1), 257-271, https://doi.org/10.1785/0120140170.

McLaskey, G. C., Thomas, A. M., Glaser, S. D. & Nadeau, R. M. 2012. Fault healing promotes high-frequency earthquakes in laboratory experiments and on natural faults. 491(7422), 101-104, https://doi.org/10.1038/nature11512.

McPhail, S., Walsh, W., Lee, C. & Monahan, P. 2008. Shale units of the Horn River Formation, Horn River Basin and Cordova Embayment, northeastern British Columbia. Canadian Society of Petroleum Geologists and Canadian Well Logging Society Convention.

Meléndez-Martínez, J. & Schmitt, D. R. 2016. A comparative study of the anisotropic dynamic and static elastic moduli of unconventional reservoir shales: Implication for geomechanical investigations. *GEOPHYSICS,* 81(3), D245-D261, https://doi.org/10.1190/geo2015-0427.1.

Miller, S. A., Collettini, C., Chiaraluce, L., Cocco, M., Barchi, M. & Kaus, B. J. P. 2004. Aftershocks driven by a high-pressure CO2 source at depth. 427(6976), 724-727, https://doi.org/10.1038/nature02251.

Milner, M., McLin, R. & Petriello, J. 2010. Imaging Texture and Porosity in Mudstones and Shales: Comparison of Secondary and Ion-Milled Backscatter SEM Methods. Canadian Unconventional Resources and International Petroleum Conference. SPE-138975-MS, https://doi.org/10.2118/138975-MS.

Mo, C. H., Lee, G. H., Jeoung, T. J., Ko, K. N., Kim, K. S., Park, K.-S. & Shin, C. H. 2018. Prediction of shale prospectivity from seismically-derived reservoir and completion qualities: Application to a shale-gas field, Horn River Basin, Canada. *Journal of Applied Geophysics,* 151, 11-22, https://doi.org/10.1016/j.jappgeo.2018.01.029.

Moein, M. J. A., Langenbruch, C., Schultz, R., Grigoli, F., Ellsworth, W. L., Wang, R., Rinaldi, A. P. & Shapiro, S. 2023. The physical mechanisms of induced earthquakes. *Nature Reviews Earth & Environment,* 4(12)**,** 847-863, https://doi.org/10.1038/s43017-023-00497-8.

Moghadam, A., Harris, N. B., Ayranci, K., Gomez, J. S., Angulo, N. A. & Chalaturnyk, R. 2019. Brittleness in the devonian horn river shale, British Columbia, Canada. *Journal of Natural Gas Science and Engineering,* 62**,** 247-258, https://doi.org/10.1016/j.jngse.2018.12.012.

Mousavi, S. M., Ogwari, P. O., Horton, S. P. & Langston, C. A. 2017. Spatio-temporal evolution of frequency-magnitude distribution and seismogenic index during initiation of induced seismicity at Guy-Greenbrier, Arkansas. 267**,** 53-66, https://doi.org/10.1016/j.pepi.2017.04.005.

Nelder, J. A. & Mead, R. 1965. A Simplex Method for Function Minimization. *The Computer Journal,* 7(4)**,** 308-313, https://doi.org/10.1093/comjnl/7.4.308.

Ougier-Simonin, A., Renard, F., Boehm, C. & Vidal-Gilbert, S. 2016. Microfracturing and microporosity in shales. 162**,** 198-226, https://doi.org/10.1016/j.earscirev.2016.09.006.

Perrin, C., Manighetti, I., Ampuero, J.-P., Cappa, F. & Gaudemer, Y. 2016. Location of largest earthquake slip and fast rupture controlled by along-strike change in fault structural maturity due to fault growth. *Journal of Geophysical Research: Solid Earth,* 121(5)**,** 3666-3685, https://doi.org/10.1002/2015JB012671.

Pervukhina, M. & Rasolofosaon, P. 2017. Compaction trend versus seismic anisotropy in shaly formations: Compaction trend versus seismic anisotropy. 65**,** https://doi.org/10.1111/1365-2478.12486.

Pignalberi, F., Mastella, G., Giorgetti, C. & Scuderi, M. M. 2024. Estimating Lab-Quake Source Parameters: Spectral Inversion from a Calibrated Acoustic System. *Sensors,* 24(17)**,** https://doi.org/10.3390/s24175824.

Prasad, M., Mukerji, T., Reinstaedler, M. & Arnold, W. 2009. Acoustic Signatures, Impedance Microstructure, Textural Scales, and Anisotropy of Kerogen-Rich Shale. *Proceedings - SPE Annual Technical Conference and Exhibition,* 5**,** https://doi.org/10.2118/124840-MS.

Rickman, R., Mullen, M., Petre, E., Grieser, B. & Kundert, D. A Practical Use of Shale Petrophysics for Stimulation Design Optimization: All Shale Plays Are Not Clones of the Barnett Shale. SPE Annual Technical Conference and Exhibition. SPE-115258-MS, https://doi.org/10.2118/115258-ms.

Roberts, N. S., Bell, A. F. & Main, I. G. 2015. Are volcanic seismic b-values high, and if so when? *Journal of Volcanology and Geothermal Research,* 308**,** 127-141, https://doi.org/10.1016/j.jvolgeores.2015.10.021.

Roche, V., Grob, M., Eyre, T. & Van Der Baan, M. 2015. Statistical characteristics of microseismic events and in-situ stress in the Horn River Basin. *Proceedings of GeoConvention*.

Rodríguez-Pradilla, G. 2015. Microseismic monitoring of a hydraulic-fracturing operation in a CBM reservoir: Case study in the Cerrejón Formation, Cesar-Ranchería Basin, Colombia. *The Leading Edge,* 34(8)**,** 896-902, https://doi.org/10.1190/tle34080896.1.

Ross, D. J. & Bustin, R. M. 2008. Characterizing the shale gas resource potential of Devonian–Mississippian strata in the Western Canada sedimentary basin: Application of an integrated formation evaluation. *AAPG bulletin,* 92(1)**,** 87-125, https://doi.org/10.1306/09040707048.

Rubinstein, J. L. & Mahani, A. B. 2015. Myths and Facts on Wastewater Injection, Hydraulic Fracturing, Enhanced Oil Recovery, and Induced Seismicity. *Seismological Research Letters,* 86(4)**,** 1060-1067, https://doi.org/10.1785/0220150067.

Saffer, D. M. & Tobin, H. J. 2011. Hydrogeology and Mechanics of Subduction Zone Forearcs: Fluid Flow and Pore Pressure. *Annual Review of Earth and Planetary Sciences,* 39(Volume 39, 2011)**,** 157-186, https://doi.org/10.1146/annurev-earth-040610-133408.

Sarout, J. & Guéguen, Y. 2008. Anisotropy of elastic wave velocities in deformed shales: Part 1 — Experimental results. *GEOPHYSICS,* 73(5)**,** D75-D89, https://doi.org/10.1190/1.2952744.

Sarout, J., Le Gonidec, Y., Ougier-Simonin, A., Schubnel, A., Guéguen, Y. & Dewhurst, D. N. 2017. Laboratory micro-seismic signature of shear faulting and fault slip in shale. 264**,** 47-62, https://doi.org/10.1016/j.pepi.2016.11.005.

Sarout, J., Molez, L., Guéguen, Y. & Hoteit, N. 2007. Shale dynamic properties and anisotropy under triaxial loading: Experimental and theoretical investigations. *Physics and Chemistry of the Earth, Parts A/B/C,* 32(8-14)**,** 896-906, https://doi.org/10.1016/j.pce.2006.01.007.

Sayers, C. 1994. The elastic anisotrophy of shales. *Journal of Geophysical Research: Solid Earth,* 99(B1)**,** 767-774, https://doi.org/10.1029/93JB02579.

Sayers, C. 2005. Seismic anisotropy of shales. *Geophysical prospecting,* 53(5)**,** 667-676, https://doi.org/10.1111/j.1365-2478.2005.00495.x.

Sayers, C., Den Boer, L., Dasgupta, S. & Goodway, B. 2015. Anisotropy estimate for the Horn River Basin from sonic logs in vertical and deviated wells. *The Leading Edge,* 34(3)**,** 296-306, https://doi.org/10.1190/tle34030296.1.

Sayers, C. M. 2013. The effect of anisotropy on the Young's moduli and Poisson's ratios of shales. *Geophysical Prospecting,* 61(2-Rock Physics for Reservoir Exploration, Characterisation and Monitoring)**,** 416-426, https://doi.org/10.1111/j.1365-2478.2012.01130.x.

Scholz, C. 1968. Experimental study of the fracturing process in brittle rock. *Journal of Geophysical Research,* 73(4)**,** 1447-1454, https://doi.org/10.1029/JB073i004p01447.

Schultz, R., Atkinson, G., Eaton, D. W., Gu, Y. J. & Kao, H. 2018. Hydraulic fracturing volume is associated with induced earthquake productivity in the Duvernay play. *Science,* 359(6373)**,** 304-308, https://doi.org/10.1126/science.aao0159.

Schultz, R., Beroza, G., Ellsworth, W. & Baker, J. 2020a. Risk‐informed recommendations for managing hydraulic fracturing–induced seismicity via traffic light protocols. *Bulletin of the Seismological Society of America,* 110(5)**,** 2411-2422, https://doi.org/10.1785/0120200016.

Schultz, R., Beroza, G. C. & Ellsworth, W. L. 2021. A strategy for choosing red‐light thresholds to manage hydraulic fracturing induced seismicity in North America. *Journal of Geophysical Research: Solid Earth,* 126(12)**,** e2021JB022340, https://doi.org/10.1029/2021JB022340.

Schultz, R., Corlett, H., Haug, K., Kocon, K., Maccormack, K., Stern, V. & Shipman, T. 2016. Linking fossil reefs with earthquakes: Geologic insight to where induced seismicity occurs in Alberta. *Geophysical Research Letters,* 43(6)**,** 2534-2542, https://doi.org/10.1002/2015GL067514.

Schultz, R., Skoumal, R. J., Brudzinski, M. R., Eaton, D., Baptie, B. & Ellsworth, W. 2020b. Hydraulic Fracturing-Induced Seismicity. *Reviews of Geophysics,* 58(3)**,** e2019RG000695, https://doi.org/10.1029/2019RG000695.

Schultz, R., Wang, R., Gu, Y. J., Haug, K. & Atkinson, G. 2017. A seismological overview of the induced earthquakes in the Duvernay play near Fox Creek, Alberta. *Journal of Geophysical Research: Solid Earth,* 122(1)**,** 492-505, https://doi.org/10.1002/2016JB013570.

Segall, P. & Lu, S. 2015. Injection - induced seismicity: Poroelastic and earthquake nucleation effects. *Journal of Geophysical Research: Solid Earth,* 120(7)**,** 5082-5103, https://doi.org/10.1002/2015JB012060.

Shapiro, S. A. 2015. *Fluid- Induced Seismicity,* Cambridge, Cambridge University Press, https://doi.org/10.1017/CBO9781139051132.

Shapiro, S. A. & Dinske, C. 2009. Fluid-induced seismicity: Pressure diffusion and hydraulic fracturing. *Geophysical Prospecting,* 57(2)**,** 301-310, https://doi.org/10.1111/j.1365-2478.2008.00770.x.

Shapiro, S. A., Kim, K.-H. & Ree, J.-H. 2021. Magnitude and nucleation time of the 2017 Pohang Earthquake point to its predictable artificial triggering. 12(1)**,** 6397, https://doi.org/10.1038/s41467-021-26679-w.

Shapiro, S. A., Krüger, O. S., Dinske, C. & Langenbruch, C. 2011. Magnitudes of induced earthquakes and geometric scales of fluid-stimulated rock volumes. *Geophysics,* 76(6)**,** WC55-WC63, https://doi.ogr/10.1190/geo2010-0349.1.

Shi, Y. & Bolt, B. A. 1982. The standard error of the magnitude-frequency b value. *Bulletin of the Seismological Society of America,* 72(5)**,** 1677-1687, https://doi.org/10.1785/bssa0720051677.

Sibson, R. 1992. Implications of fault-valve behaviour for rupture nucleation and recurrence. *Tectonophysics,* 211(1-4)**,** 283-293, https://doi.org/10.1016/0040-1951(92)90065-E.

Sibson, R. H. 1998. Brittle failure mode plots for compressional and extensional tectonic regimes. 20(5)**,** 655-660, https://doi.org/10.1016/S0191-8141(98)00116-3.

Sibson, R. H. 2000. Fluid involvement in normal faulting. *Journal of Geodynamics,* 29(3)**,** 469-499, https://doi.org/10.1016/S0264-3707(99)00042-3.

Skoumal, R. J., Brudzinski, M. R. & Currie, B. S. 2015. Earthquakes induced by hydraulic fracturing in Poland Township, Ohio. *Bulletin of the Seismological Society of America,* 105(1)**,** 189-197, https://doi.org/10.1785/0120140168.

Snelling, P. E., Groot, M. D. & Hwang, K. 2013. Characterizing hydraulic fracture behaviour in the Horn River Basin with microseismic data. *SEG Technical Program Expanded Abstracts 2013,* https://doi.org/10.1190/segam2013-1174.1.

Sondergeld, C. H. & Rai, C. S. 2011. Elastic anisotropy of shales. *The Leading Edge,* 30(3)**,** 324-331, https://doi.org/10.1190/1.3567264.

Sone, H. & Zoback, M. D. 2013. Mechanical properties of shale-gas reservoir rocks — Part 1: Static and dynamic elastic properties and anisotropy. *GEOPHYSICS,* 78(5)**,** D381-D392, https://doi.org/10.1190/geo2013-0050.1.

Stanchits, S., Mayr, S., Shapiro, S. & Dresen, G. 2011. Fracturing of porous rock induced by fluid injection. *Thermo-Hydro-Chemo-Mechanical Couplings in Rock Physics and Rock Mechanics,* 503(1)**,** 129-145, https://doi.org/10.1016/j.tecto.2010.09.022.

Stanchits, S., Vinciguerra, S. & Dresen, G. 2006. Ultrasonic Velocities, Acoustic Emission Characteristics and Crack Damage of Basalt and Granite. 163(5)**,** 975-994, https://doi.org/10.1007/s00024-006-0059-5.

Stanislowski, K., Roesner, A. & Ikari, M. J. 2022. Implications for megathrust slip behavior and pore pressure at the shallow northern Cascadia subduction zone from laboratory friction experiments. 578**,** 117297, https://doi.org/10.1016/j.epsl.2021.117297.

Teklu, T. W., Park, D., Jung, H. & Miskimins, J. 2018. *Integrated Rock Characterization of a Shale Gas Field in the Horn River Basin, Canada,* https://doi.org/10.15530/urtec-2018-2880467.

Thompson, B., Young, R. & Lockner, D. A. 2009. Premonitory acoustic emissions and stick‐slip in natural and smooth‐faulted Westerly granite. *Journal of Geophysical Research: Solid Earth,* 114(B2)**,** https://doi.org/10.1029/2008JB005753.

Thomsen, L. 1986. Weak elastic anisotropy. *GEOPHYSICS,* 51(10)**,** 1954-1966, https://doi.org/10.1190/1.1442051.

Trippetta, F., Collettini, C., Meredith, P. G. & Vinciguerra, S. 2013. Evolution of the elastic moduli of seismogenic Triassic Evaporites subjected to cyclic stressing. *Tectonophysics,* 592**,** 67-79, https://doi.org/10.1016/j.tecto.2013.02.011.

Verdon, J. P. & Budge, J. 2018. Examining the Capability of Statistical Models to Mitigate Induced Seismicity during Hydraulic Fracturing of Shale Gas Reservoirs. *Bulletin of the Seismological Society of America,* 108(2)**,** 690-701, https://doi.org/10.1785/0120170207.

Verdon, J. P. & Stork, A. L. 2016. Carbon capture and storage, geomechanics and induced seismic activity. 8(6)**,** 928-935, https://doi.org/10.1016/j.jrmge.2016.06.004.

Vernik, L. 1993. Microcrack-induced versus intrinsic elastic anisotropy in mature HC-source shales. *Geophysics,* 58(11)**,** 1703-1706, https://doi.org/10.1190/1.1443385.

Vernik, L. & Liu, X. 1997. Velocity anisotropy in shales: A petrophysical study. *GEOPHYSICS,* 62(2)**,** 521-532, https://doi.org/10.1190/1.1444162.

Vernik, L. & Nur, A. 1992. Ultrasonic velocity and anisotropy of hydrocarbon source rocks. *GEOPHYSICS,* 57(5)**,** 727-735, https://doi.org/10.1190/1.1443286.

Viegas, G., Baig, A. & Urbancic, T. 2017. Scaling of induced seismicity, implications for the role of geological setting on seismic hazard, https://doi.org/10.3997/2214-4609.201701674.

Vinciguerra, S., Meredith, P. & Hazzard, J. 2004. Experimental and modeling study of fluid pressure-driven fractures in Darley Dale sandstone. 31**,** 9609, https://doi.org/10.1029/2004GL019638.

Vinciguerra, S., Trovato, C., Meredith, P. G., Benson, P. M., Troise, C. & Natale, G. D. 2006. Understanding the Seismic Velocity Structure of Campi Flegrei Caldera (Italy): From the Laboratory to the Field Scale. *pure and applied geophysics,* 163(10)**,** 2205-2221, https://doi.org/10.1007/s00024-006-0118-y.

Waldron, A. R. & Camac, B. A. 2016. Microseismic monitoring of hydraulic-fracturing programs in the Cooper Basin, Australia. *The Leading Edge,* 35(1)**,** 72-76, https://doi.org/10.1190/tle35010072.1.

Wang, B., Harrington, R. M., Liu, Y., Kao, H. & Yu, H. 2020a. A Study on the Largest Hydraulic‐Fracturing‐Induced Earthquake in Canada: Observations and Static Stress‐Drop Estimation. *Bulletin of the Seismological Society of America,* 110(5)**,** 2283-2294, https://doi.org/10.1785/0120190261.

Wang, B., Verdecchia, A., Kao, H., Harrington, R. M., Liu, Y. & Yu, H. 2021. A study on the largest hydraulic fracturing induced earthquake in Canada: Numerical modeling and triggering mechanism. *Bulletin of the Seismological Society of America,* 111(3)**,** 1392-1404, https://doi.org/10.1785/0120200251.

Wang, L., Kwiatek, G., Rybacki, E., Bonnelye, A., Bohnhoff, M. & Dresen, G. 2020b. Laboratory Study on Fluid-Induced Fault Slip Behavior: The Role of Fluid Pressurization Rate, https://doi.org/10.1029/2019GL086627.

Wang, R., Gu, Y. J., Schultz, R. & Chen, Y. 2018. Faults and Non-Double-Couple Components for Induced Earthquakes. *Geophysical Research Letters,* 45(17)**,** 8966-8975, https://doi.org/10.1029/2018GL079027.

Wang, R., Gu, Y. J., Schultz, R., Kim, A. & Atkinson, G. 2016. Source analysis of a potential hydraulic-fracturing-induced earthquake near Fox Creek, Alberta. *Geophysical Research Letters,* 43(2)**,** 564-573, https://doi.org/10.1002/2015gl066917.

Wang, R., Gu, Y. J., Schultz, R., Zhang, M. & Kim, A. 2017. Source characteristics and geological implications of the January 2016 induced earthquake swarm near Crooked Lake, Alberta. *Geophysical Journal International,* 210(2)**,** 979-988, https://doi.org/10.1093/gji/ggx204.

Wang, Z. 2002. Seismic anisotropy in sedimentary rocks, part 2: Laboratory data. *Geophysics,* 67(5)**,** 1423-1440, https://doi.org/10.1190/1.1512743.

Warpinski, N. R., Du, J. & Zimmer, U. 2012. Measurements of Hydraulic-Fracture-Induced Seismicity in Gas Shales. SPE Hydraulic Fracturing Technology Conference. SPE-151597-MS, https://doi.org/10.2118/151597-ms.

Weingarten, M., Ge, S., Godt, J. W., Bekins, B. A. & Rubinstein, J. L. 2015. High-rate injection is associated with the increase in U.S. mid-continent seismicity. *Science,* 348(6241)**,** 1336-1340, https://doi.org/10.1126/science.aab1345.

Wiseall, A. C., Cuss, R. J., Hough, E. & Kemp, S. J. 2018. The role of fault gouge properties on fault reactivation during hydraulic stimulation; an experimental study using analogue faults. 59**,** 21-34, https://doi.org/10.1016/j.jngse.2018.08.021.

Wong, R. C. K., Schmitt, D. R., Collis, D. & Gautam, R. 2008. Inherent transversely isotropic elastic parameters of over-consolidated shale measured by ultrasonic waves and their comparison with static and acoustic in situ log measurements. *Journal of Geophysics and Engineering,* 5(1)**,** 103-117, https://doi.org/10.1088/1742-2132/5/1/011.

Woo, J.-U., Kim, J., Rhie, J. & Kang, T.-S. 2017. Characteristics in hypocenters of microseismic events due to hydraulic fracturing and natural faults: a case study in the Horn River Basin, Canada. 21(5)**,** 683-694, https://doi.org/10.1007/s12303-017-0021-9.

Wu, S., Ge, H., Wang, X. & Meng, F. 2017. Shale failure processes and spatial distribution of fractures obtained by AE monitoring. 41**,** 82-92, https://doi.org/10.1016/j.jngse.2017.02.015.

Wyss, M., Sammis, C. G., Nadeau, R. M. & Wiemer, S. 2004. Fractal dimension and *b*-value on creeping and locked patches of the San Andreas fault near Parkfield, California. *Bulletin of the Seismological Society of America,* 94(2)**,** 410-421, https://doi.org/10.1785/0120030054.

Yang, H., Liu, Y., Wei, M., Zhuang, J. & Zhou, S. 2017. Induced earthquakes in the development of unconventional energy resources. *Science China Earth Sciences,* 60**,** 1632-1644, https://doi.org/10.1007/s11430-017-9063-0.

Yeck, W. L., Hayes, G. P., McNamara, D. E., Rubinstein, J. L., Barnhart, W. D., Earle, P. S. & Benz, H. M. 2017. Oklahoma experiences largest earthquake during ongoing regional wastewater injection hazard mitigation efforts. *Geophysical Research Letters,* 44(2)**,** 711-717, https://doi.org/10.1002/2016GL071685.

Yeo, I., Brown, M., Ge, S. & Lee, K. 2020. Causal mechanism of injection-induced earthquakes through the Mw 5.5 Pohang earthquake case study. *Nature communications,* 11(1)**,** 2614, https://doi.org/10.1038/s41467-020-16408-0.

Yin, H. 1992. *Acoustic velocity and attenuation of rocks: Isotropy, intrinsic anisotropy, and stress-induced anisotropy.* PhD thesis, Stanford University, USA.

Yousefzadeh, A., Li, Q., Virués, C. & Aguilera, R. 2018. An Interpretation of Microseismic Spatial Anomalies, b-values, and Magnitude Analyses To Identify Activated Fracture Networks in Horn River Basin. *SPE Production & Operations,* 33(04)**,** 679-696, https://doi.org/10.2118/179153-PA.

Yu, C. & Shapiro, S. 2014. Seismic anisotropy of shale: Inversion of microseismic data. *SEG Technical Program Expanded Abstracts 2324-2329,* https://doi.org/10.1190/segam2014-1251.1.

Zhang, Q., Su, B., Chen, G., Luo, J., Zhang, J., Zhao, Q. & Ni, Y.-Q. 2025. Shear Behavior and Acoustic Emission Characteristics of Propped Rough Fractures. *Rock Mechanics and Rock Engineering,* 58(2)**,** 2089-2103, https://doi.org/10.1007/s00603-024-04263-0.

Zhao, H., Ma, F., Liu, G., Feng, X. & Guo, J. 2018. Analytical investigation of hydraulic fracture-induced seismicity and fault activation. 77(13)**,** 526, https://doi.org/10.1007/s12665-018-7708-8.

Zoback, M. D. & Gorelick, S. M. 2012. Earthquake triggering and large-scale geologic storage of carbon dioxide. *Proceedings of the National Academy of Sciences,* 109(26)**,** 10164-10168, https://doi.org/10.1073/pnas.1202473109.

Appendices

Appendix A

P-wave velocity and *b*-value evolution are estimated using clusters of events recorded during the identified loading stages. The initial P-wave velocity measured on a benchtop is shown in the top row. The background colours in the table correspond to the loading stages shown in Figures 4.8, 4.9, and 4.10.

	Experiment	Dutff 348		Dutff 350	
Benchtop measurement	P-wave velocity [m s^{-1}]	5520 ± 90		5660 ± 33	
Elastic loading	P-wave velocity [m s^{-1}]	5420 ± 33			
	b-value	2 ± 0.12			
	Event No.	14			
Prefailure	P-wave velocity [m s^{-1}]	5370 ± 73	5360 ± 52	5160 ± 73	
	b-value	1.6 ± 0.11	1.5 ± 0.10	2.5 ± 0.20	
	Event No.	11	13	54	
Failure	P-wave velocity [m s^{-1}]	5220 ± 40	5170 ± 50	5060 ± 40	
	b-value	1.3 ± 0.17	1.3 ± 0.14	1.5 ± 0.23	
	Event No.	48	34	66	
Fluid injection & reactivation	P-wave velocity [m s^{-1}]			5060 ± 68	5010 ± 50
	b-value			0.9 ± 0.03	
	Event No.			36	

Appendix B

Slip events corresponding to reactivation cycles shown in Figure 5.9. Each vertical axis is colour-coded to match its corresponding curve, and the axis label indicates the parameter being represented.

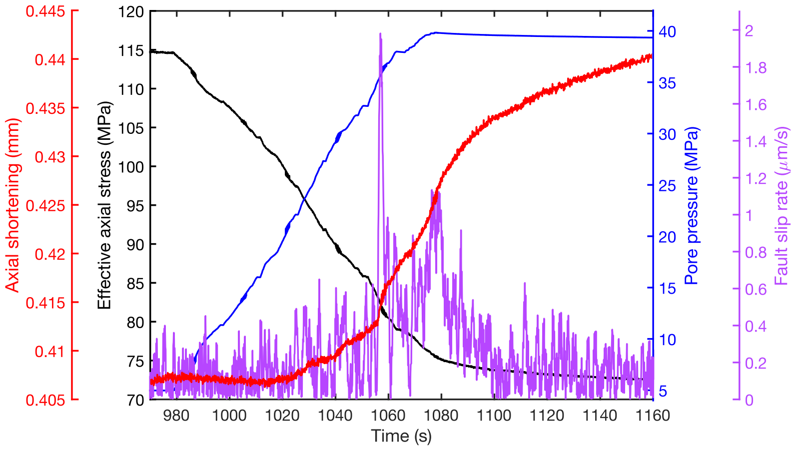

Figure B.1. Slip event of reactivation Cycle 2a.

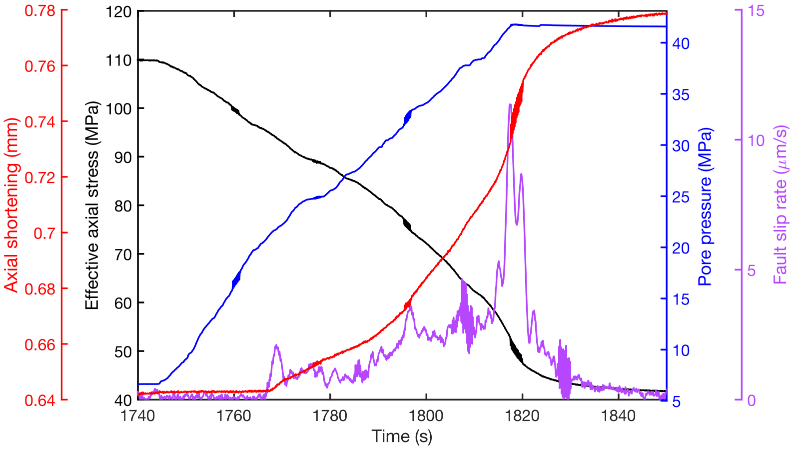

Figure B.2. Slip event of reactivation Cycle 3.

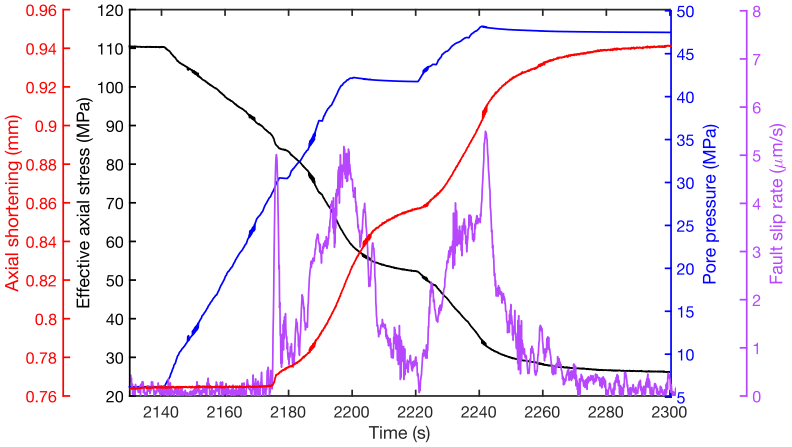

Figure B.3. Slip event of reactivation Cycle 4.

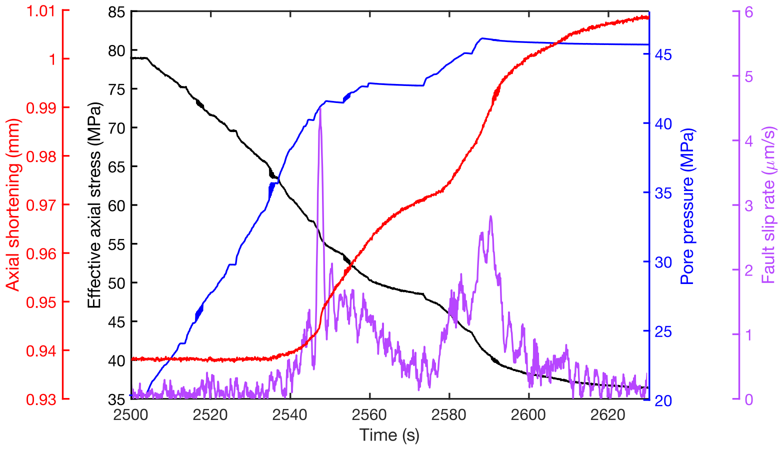

Figure B.4. Slip event of reactivation Cycle 5.

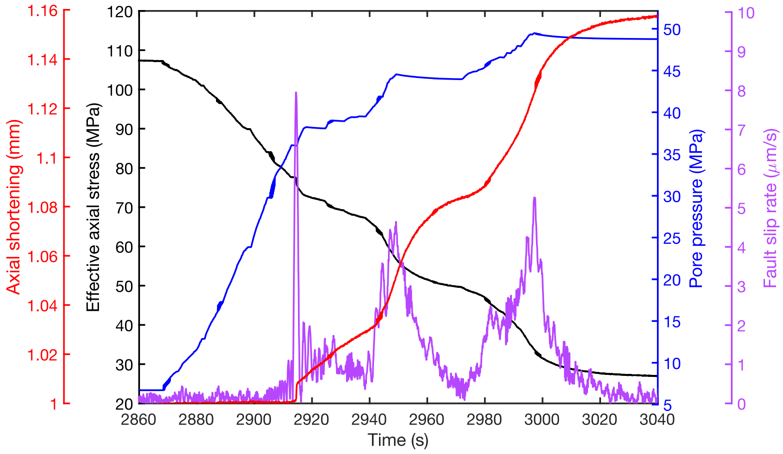

Figure B.5. Slip event of reactivation Cycle 6.

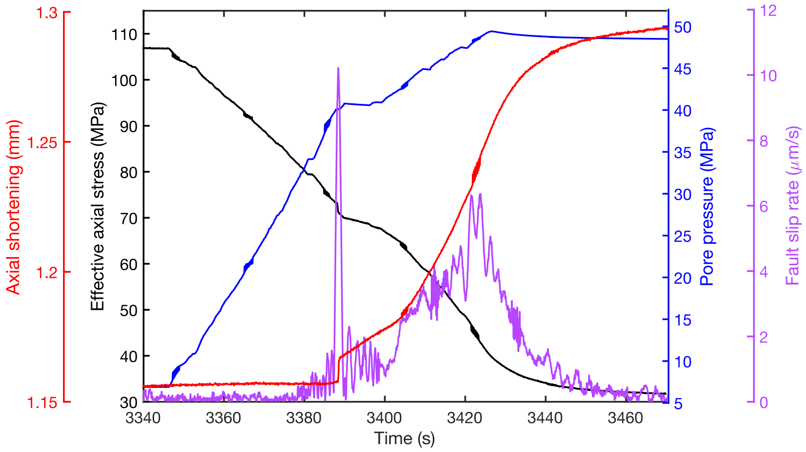

Figure B.6. Slip event of reactivation Cycle 7.

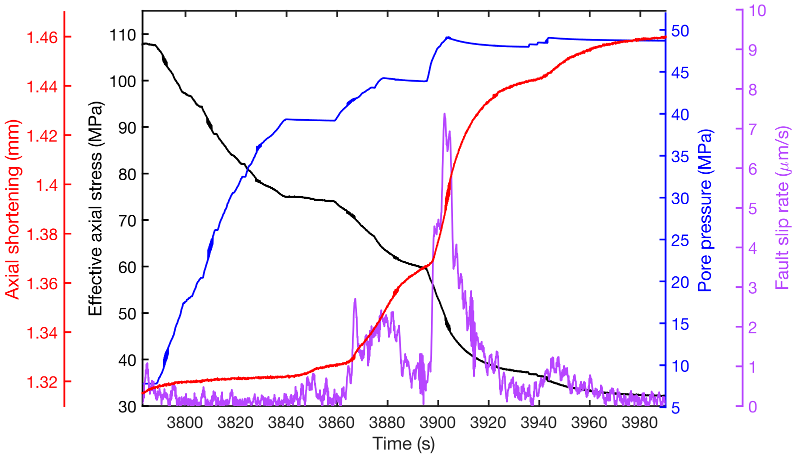

Figure B.7. Slip event of reactivation Cycle 8.

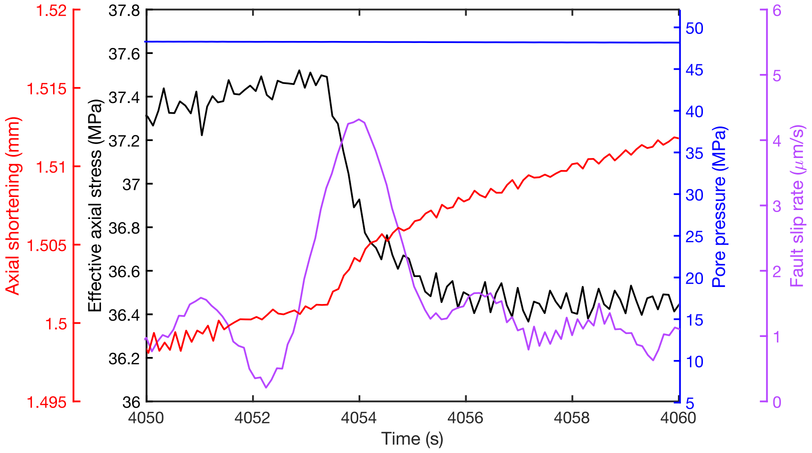

Figure B.8. Slip event of reactivation Cycle 9.